Constraining the Evolution of Galaxies over the Interaction Sequence with Multiwavelength Observations and Simulations

Constraining the Evolution of Galaxies over the Interaction Sequence with Multiwavelength Observations and Simulations

A dissertation presented

by

Lauranne Lanz

to

The Department of Astronomy

in partial fulfillment of the requirements

for the degree of

Doctor of Philosophy

in the subject of

Astronomy & Astrophysics

Harvard University

Cambridge, Massachusetts

August 2013

Dissertation Advisor: Doctor Howard A. Smith Lauranne Lanz

Constraining the Evolution of Galaxies over the Interaction Sequence with Multiwavelength Observations and Simulations

Abstract

Interactions are crucial for galaxy formation and profoundly affect their evolution. However, our understanding of the impact of interactions on star formation and activity of the central supermassive black hole remains incomplete. In the canonical picture of the interaction process, these processes are expected to undergo a strong enhancement, but some recent studies have not found this prediction to be true in a statistically meaningful sense. This thesis uses a sample of local interactions observed from the ultraviolet to the far-infrared and a suite of N-body hydrodynamic simulations of interactions to examine the evolution of star formation, stellar mass, dust properties, and spectral energy distributions (SEDs) over the interaction sequence.

First, we present the SEDs of 31 interactions in 14 systems, which we fit with stellar population synthesis models combined with a thermal dust model. We examine the differences between mildly, moderately, and strongly interacting systems. The star formation rate (SFR), dust luminosity, and the 15-25 K dust component temperature increase as the interaction progresses from moderately to strongly interacting. However, the SFR per stellar mass remains constant across the interaction stages.

Second, we create 14 hydrodynamic simulations of isolated and interacting galaxies and calculate simulated photometry in 25 bands using the SUNRISE radiative transfer

code. By comparing observed and simulated SEDs, we identify the simulation properties necessary to reproduce an interaction's SED. The best matches originate from simulated systems of similar stellar mass, infrared luminosities, dust mass, and SFR to the observed systems. Although an SED alone is insufficient to identify the interaction stage, strongly interacting systems preferentially match SEDs from times close to coalescence in the simulations.

Third, we describe a case study of a post-merger system, Fornax A, for which we constrain its parameters of its progenitors. Based on the excess dust mass in this elliptical galaxy, we estimate a spiral galaxy with a stellar mass of $(1-6)\times10^{10}\,\mathrm{M}_{\odot}$ brought in $\approx$10% of Fornax A's current stellar mass. We describe the probable two-outburst history that created the radio lobes $\sim$0.4 Gyr ago and two cavities in the X-ray emission closer to the nucleus $\sim$0.1 Gyr ago.

Contents

Acknowledgments

Before we dive into the wondrous dance of interacting galaxies, I want to thank the many people without whom this dissertation and the long process before it would not have been possible.

First and foremost, I thank my wonderful parents. Maman, you have been such an amazing support and friend. You have given me guidance, strength, laughs, hugs, and great conversations. Dad, I still remember going to that first big telescope at L'Observatoire de Haute Provence with you and your advice has helped guide me since. My siblings, Alexis and Shakoo, I thank you for listening patiently when I ramble about my passions and I hope that I have let you ramble about yours. Merci à toute ma famille pour vos bons voeux et l'amour qui m'a soutenue surtout ces derniers jours quand je finissais ma thèse.

I have had several wonderful advisors, who have shaped me as a scientist. I thank, my advisor Howard Smith for developing such a wonderful thesis project with me and for recognizing and encouraging my love of outreach. I thank John Huchra for luring me into the study of galaxies my first semester at Harvard, and Christine Jones and Bill Forman for nurturing that delight, introducing me to X-ray astronomy, and, letting me discover infrared astronomy. I thank Matt Ashby for his steadfast support and assistance, and for taking me on my first observing trip in Chile. I also thank Lee Mundy, Sidney Wolff, and Steve Strom, who introduced me to astronomical research and convinced me it was much better than particle physics.

I thank Andreas Zezas for many reasons: for his many thoughtful comments, for

helpful and insightful scientific conversations, and for helping to shape my thesis. I thank Chris Hayward, without whose simulations I would not have been able to complete a substantive part of this thesis, Ryan Hickox who taught me so much IDL and was very patient with a young graduate student, Elisabete da Cunha who helped understand MAGPHYS and worked with me to modify it to my needs, Volker Tolls who taught the love/hate relation one has with HIPE, Patrik Jonsson who taught me how to work with SUNRISE outputs, Paul Nulsen for our conversations, and Ralph Kraft for his helpful explanations of jet and AGN processes. I thank Giovanni Fazio, Steve Willner, Joe Hora, and Zhong Wang for welcoming me into the IRAC group. I thank Sarah Willis, Rafael Martinez Galarza, Andres Guzman, Dharam Vir Lal, Zhiyuan Li, Ryan Johnson, and Felipe Santos for fruitful collaborations and friendly group meetings.

I am grateful to my thesis (advisory) committee for their helpful advice. I thank Alyssa Goodman for her insights regarding the dangers of χ^2 fitting and Lars Hernquist for bringing a theorist's perspective and welcoming me to his group meeting. I thank George Helou for agreeing to be my external examiner.

Thanks to my many teachers and mentors throughout the years, especially Philip Hale, Tom Clifton, Justin Parke, Tom Cohen, and Phil Sadler. I learned so much from you and you helped instill in me a passion for teaching and for nurturing the growth of knowledge in others. I also thank David Aguilar for teaching me the joy of public speaking, and Christine Pulliam, Geneviève de Messiers, David DeVorkin, and Rich DeMidio who put together the wonderful events at which I spoke.

I am very grateful for the wonderful atmosphere of the Astronomy Department at Harvard and the Harvard-Smithsonian Center for Astrophysics. Thanks to Jean Collins,

Donna Adams, and Robb Scholten for keeping us running smoothly. Peg Herlihy has been a great help and I appreciate her extensive ability to answer my many questions and her care for our well-being. Thanks to Nina Zonnevylle for inviting me to knitting group and to Van McGlasson for conversations by the water cooler. I also thank Shaun Gallagher and Nigel Atkins for teaching me the basics of recording the colloquia.

It is at Harvard that I blossomed socially. I thank all the astronomy graduate students and pre-docs for creating such a supportive environment and for years of laughter, advice, and games. I especially thank Ben Maruca, Zach Berta, Wen-Fai Fong, Jack Steiner, Courtney Dressing, Lauren Woolsey, Elisabeth Newton, Sukrit Ranjan, Katherine Rosenfeld, Chris Faesi, Stephanie Bush, Robert Marcus, Joey Nielsen, Gurtina Besla, Alexa Hart, Sarah Willis, Kate Alexander, Pierre Christian, Ian Czekala, Jason Dittmann, Maria Drout, Doug Ferrer, Robert Harris, Luke Kelley, Ragnhild Lunnan, Meredith MacGregor, George Miller, Philip Mocz, Maxwell Moe, Laura Blecha, Diego Muñoz, Dylan Nelson, Stephen Portillo, Nathan Sanders, Laura Schaefer, Zachary Slepian, Paul Torrey, Anjali Tripathi, Yucong Zhu, Sarah Ballard, Bob Penna, Greg Snyder, Nick Stone, Joey Muñoz, Meredith Hughes, Ryan O'Leary, and Andy Friedman. I also particularly thank Sarah Rugheimer MacGregor who encouraged me to try so many new things, and Tanmoy Laskar and Bekki Dawson who have been wonderful housemates and great caretakers of my furry friend Merry when I travel. I'm grateful for the friendships that I have developed at Harvard with Katie Rose, Jonathan Ruel, Kristen Keerma, Aaron Kuan, Patrick Rich, Mary Moore, Amanda McFedries, Christian MacGregor, and Rachel Epstein. You have all helped me grow so much.

For my family

Chapter 1

Introduction

In March 2012, I had the privilege of seeing the Magellanic Clouds with the naked eye for the first time from Las Campanas Observatory in Chile. It was a beautiful sight of two galaxies in our cosmic backyard engaging in that destructive dance of interaction. Galaxy interactions are a crucial process through which galaxies form, grow, and evolve. Understanding that process provides insights into the origins of our Galaxy and the building blocks of the cosmic web around us and into the effects that our interaction with the Andromeda Galaxy will have on the Milky Way.

The study of galaxy interactions has a significant complication compared, for example, to the study of exoplanets. Whereas planets orbit stars on timescales of days to years, galaxies interact on timescales of hundreds of millions to billions of years. Observing even a tiny fraction of the evolution of a single interaction is an endeavor for many, many generations of astronomers. Therefore, in order to study the interaction process as a whole, we must either circumvent the timescale problem by using a sample of interactions captured at different stages or bypass the problem using simulated

encounters. Determining where galaxies fall on the interaction sequence is however a non-negligible problem. Relative order is often determined by the degree of morphological distortion observed in each system (e.g., Dopita et al. 2002, Toomre & Toomre 1972). However, the appearance of a system is not solely a function of interaction stage but also of the geometry of the interaction, the masses of the galaxies, metallicity, molecular gas content, and (not least) previous encounters (e.g., Di Matteo et al. 2007; Springel et al. 2005; Hopkins et al. 2006; Mihos & Hernquist 1994, 1996).

Understanding local interactions is a crucial step in constructing the detailed evolution of galaxies since the Big Bang. The James Webb Space Telescope will allow exploration of the earliest interactions, but to study how that interaction process differs from that of local encounters, we need to refine our understanding of the evolution of local galaxies over the interaction sequence and confirm the ability of simulations to reproduce realistic interactions. We also need to identify unambiguous signatures of interaction stage that can be used more accurately than morphological distortion and that do not require the same angular resolution.

Now is an excellent time to examine such questions as "Does the spectral energy distribution (SED) contain the signature of interaction stage?", "Can this signature be deciphered from the SED alone?", and "Is there a wavelength regime crucial to this code-breaking?". The past decade has seen both the success of space missions yielding rich observational archives from the X-ray to the far-infrared (FIR) and the development of computational tools to fit SEDs and simulate interactions. The work I present in this thesis takes advantage of all of these advances to improve our understanding of local interactions.

1.1 What Happens in a Galaxy Interaction?

The precise trajectory of two galaxies along the interaction sequence depends on many parameters including the geometry of the encounter, the masses of the galaxies, and their gas contents. However, interactions generally pass through certain common stages across a wide range of interaction types. Figure 1.1 shows the framework of the merger sequence defined by Hopkins et al. (2008b) for major interactions. Small groups or pairs of galaxies are attracted to each other through gravity (a-b). Depending on the geometry of the encounter, the galaxies proceed through one or more pericenter passages during which the star formation rate (SFR; shown in the upper plot) is expected to increase (c). The galaxies eventually enter a short-lived coalescence stage (d), during which gas flows to the center fueling star formation and an active galactic nucleus (AGN). The star formation activity during this stage can be so intense that the merger's infrared (IR) emission becomes bright enough to classify the system as a luminous IR galaxy (LIRG; $L \leq 10^{11}\,L_{\odot}$) or ultra luminous IR galaxy (ULIRG; $L \leq 10^{12}\,L_{\odot}$). The rapid growth of the AGN prompts a "blowout" phase (e) during which feedback from the AGN expels much of the remaining gas in the galaxy, depriving it of material out of which to form stars and revealing the previously obscured AGN (f). The post-merger remnant (f-g) gradually settles into an elliptical galaxy with little star formation or nuclear activity.

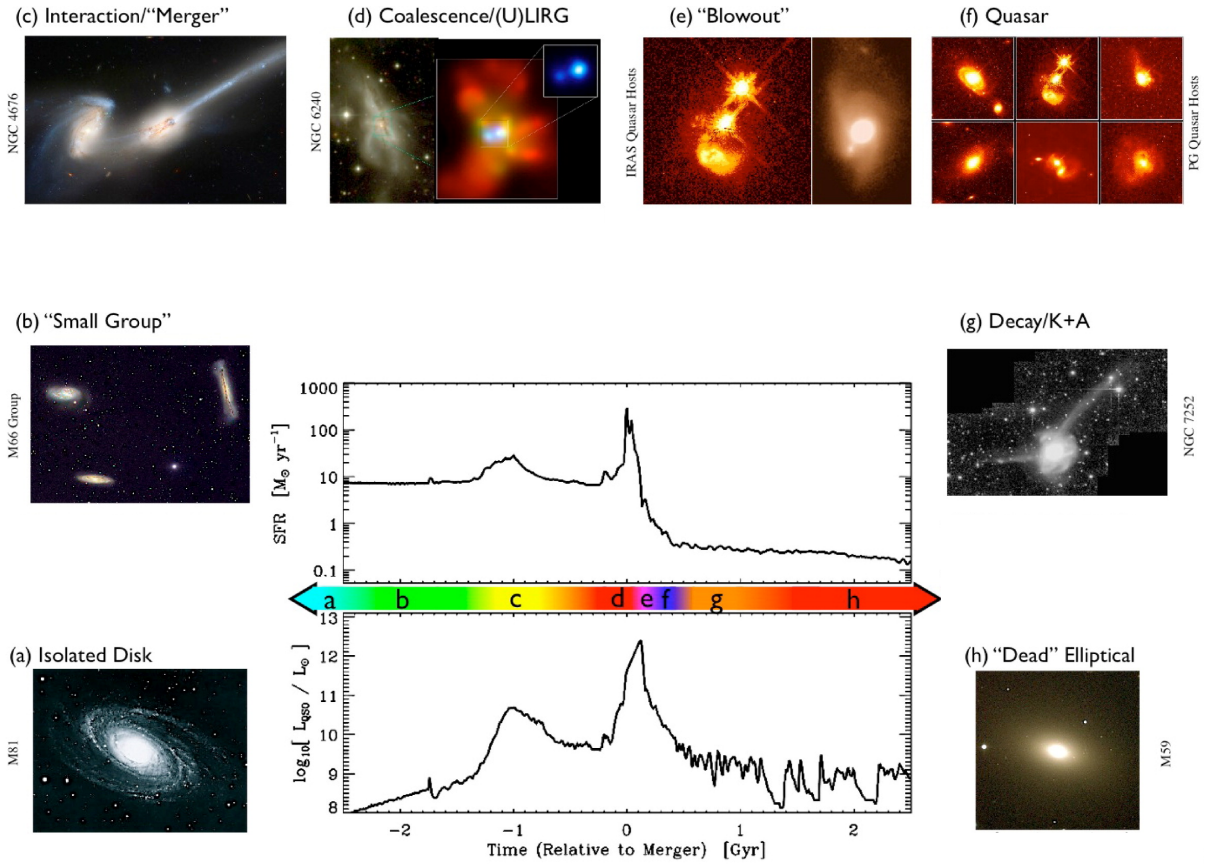

Figure 1.1: Schematic outline of the stages of a gas-rich major merger from Hopkins et al. (2008b). The two plots show the evolution of SFR (top) and AGN luminosity (bottom) over the course of the interaction

In the canonical picture of the interaction sequence, encounters can have three primary observable effects:

- **Enhancement of star formation activity:** Many local LIRGs and ULIRGS show evidence of tidal interactions (e.g., Veilleux et al. 2002). Similarly, sub-millimeter galaxies, the high-redshift counterparts of these local IR-bright galaxies, are thought to be predominantly mergers (e.g., Blain et al. 1999). Many hydrodynamic simulations of interacting galaxies (e.g., Figure 1.1; Hopkins et al. 2008b; Springel et al. 2005) predict a heightened SFR, especially during the coalescence stage. However, some recent studies have not found this to be globally true in a statistically meaningful sense (e.g. Xu et al. 2010, Yuan et al. 2012).

- **AGN activity:** Simulated interactions generally show gas inflows to the centers of galaxies (e.g., Di Matteo et al. 2005, Springel et al. 2005). In principle, the accretion of this gas converts a low-luminosity, dormant nucleus into an AGN. However, the AGN's luminosity is expected to vary widely over the course of an interaction (lower panel of Figure 1.1). Although observational studies of merging galaxies have demonstrated that, at least on a statistical level, interactions trigger an enhancement in nuclear activity, recent literature includes arguments both for and against a strong connection between nuclear activity and mergers (e.g., Li et al. 2008; Kocevski et al. 2012; Ellison et al. 2011; Scudder et al. 2012, Silverman et al. 2011).

- **Morphological distortions:** Disturbed galaxies have long been associated with mergers (e.g., Toomre & Toomre 1972). However, numerical simulations have shown that the degree of induced distortion varies greatly based on the parameters

of the interaction including the geometry of the encounter, the interaction stage, and the gas and stellar masses of the progenitor galaxies among many other properties (e.g., Hopkins et al. 2006; Hopkins et al. 2012; Mihos & Hernquist 1994, 1996; Barnes 1992; Barnes & Hernquist 1996; Sanders 1999). Figure 1.2 shows a set of composite color images in the Sloan Digital Sky Survey (SDSS) urz bands of a simulated major merger from Lotz et al. (2008). Tidal features, seen strongly in the images at 0.59 Gyr and 1.66 Gyr can have low surface brightness compared to the bulk of the galaxy, particularly in early interaction stages. Therefore, shallow observations of a system at the maximum separation after first pericenter passage (at 1.03 Gyr) can look very similar to the initial galaxies.

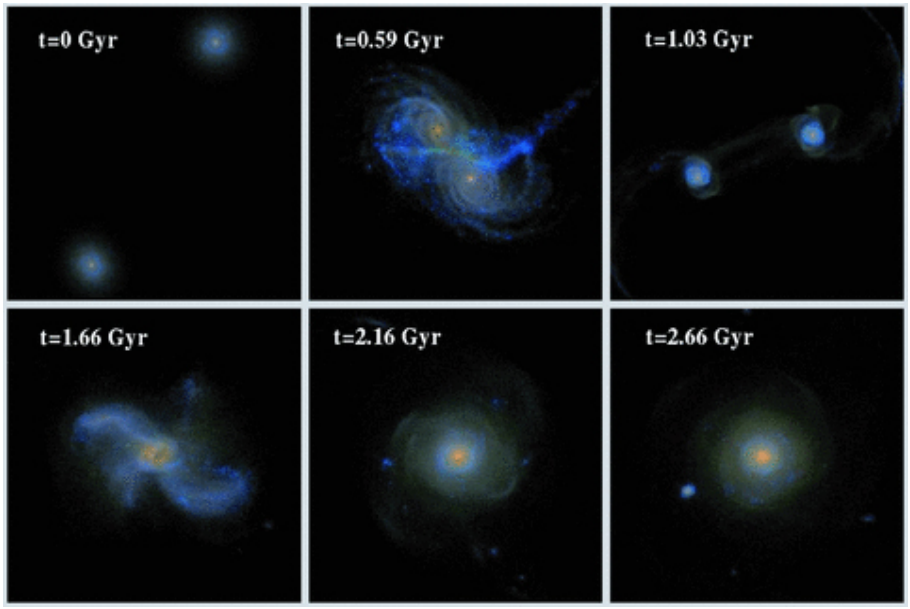

Figure 1.2: SDSS *urz* images of a simulated major merger from Lotz et al. (2008). Time since the start of the simulation is given in the upper left corner of each image. In order of increasing time, the images show: the initial state of the simulation, the first pericenter passage, the maximal separation after first passage, coalescence of the nuclei, and the post-merger system 0.5 Gyr and 1 Gyr after coalescence.

1.2 A Golden Age for the Study of Galaxy Interactions

In the past decade, two new developments have dramatically changed our ability to study galaxy interactions. The first is the success of space missions covering the spectrum from X-rays to the FIR. Together, their observations have significantly improved our understanding of star formation and accretion around galactic nuclei, processes that dominate the emission in interacting systems. The second is the development of computational codes to derive galaxy properties from SEDs, and simulate interactions as well as their emission through radiative transfer calculations.

1.2.1 A Wealth of Multiwavelength Observations

The astronomical community has been blessed with a wealth of space missions that were launched in the past decade. In the mid-infrared (MIR), the Spitzer Space Telescope was built on the legacy of the Infrared Astronomical Satellite (IRAS) and the Infrared Space Observatory (ISO). With its improved spatial resolution and its sensitive detectors at 3.6 μm-170 μm, Spitzer revealed the clumpy structure of star formation obscured by dust (e.g., Smith et al. 2007; Draine et al. 2007). Figure 1.3 shows M81 as observed by Spitzer (Willner et al. 2004). The short wavelength detectors on Spitzer provide constraints on the underlying stellar mass of the galaxy, while its 8 μm band is typically dominated by the emission of polycyclic aromatic hydrocarbons (PAH), large molecules excited by UV radiation. The 24 μm image of M81, which traces emission by small grains in star-forming regions, shows the clumpiness of embedded star formation, structure

common to many spiral galaxies.

The Herschel Space Observatory further increased our understanding of obscured star formation, revealing the structure of warm and cold dust emitting from 110 μm$-$500 μm. Its observations have demonstrated the importance of photometry at wavelengths longer than 200 μm in order not over-estimate the dust mass (Aniano et al. 2012). Magdis et al. (2012) recently proposed a method to use dust mass to estimate the molecular content of galaxies, thereby avoiding use of the uncertain CO-to-H_2 conversion factor, which would not be possible without the strides that Herschel observations have allowed us to take in understanding dust properties.

Our understanding of star formation has also been greatly enhanced by observations of unobscured star-forming activity taken with the Galaxy Evolution Explorer (GALEX). GALEX has also revealed that extended UV disks are surprisingly common in spiral galaxies (e.g. Thilker et al. 2007). The all-sky survey performed by GALEX provides a wealth of information on star formation in local isolated and interacting galaxies (e.g. de Paz et al. 2007). The Ultraviolet/Optical Telescope on Swift provides observations of many regions not observed by GALEX due to bright foreground stars.

The observations of these four telescopes, combined with ground-based optical and NIR photometry, yields SEDs with spectral coverage from the UV to sub-millimeter wavelengths. The IR photometry now available at the critical emission peak from warm luminous dust provides significant constraints on the starburst processes that heat the dust. Further, the combination of UV and IR data can provide more consistent measurements of star-forming activity, dust content, and optical depth of the star-forming regions by assuming a conservation between the energy absorbed in the UV and emitted

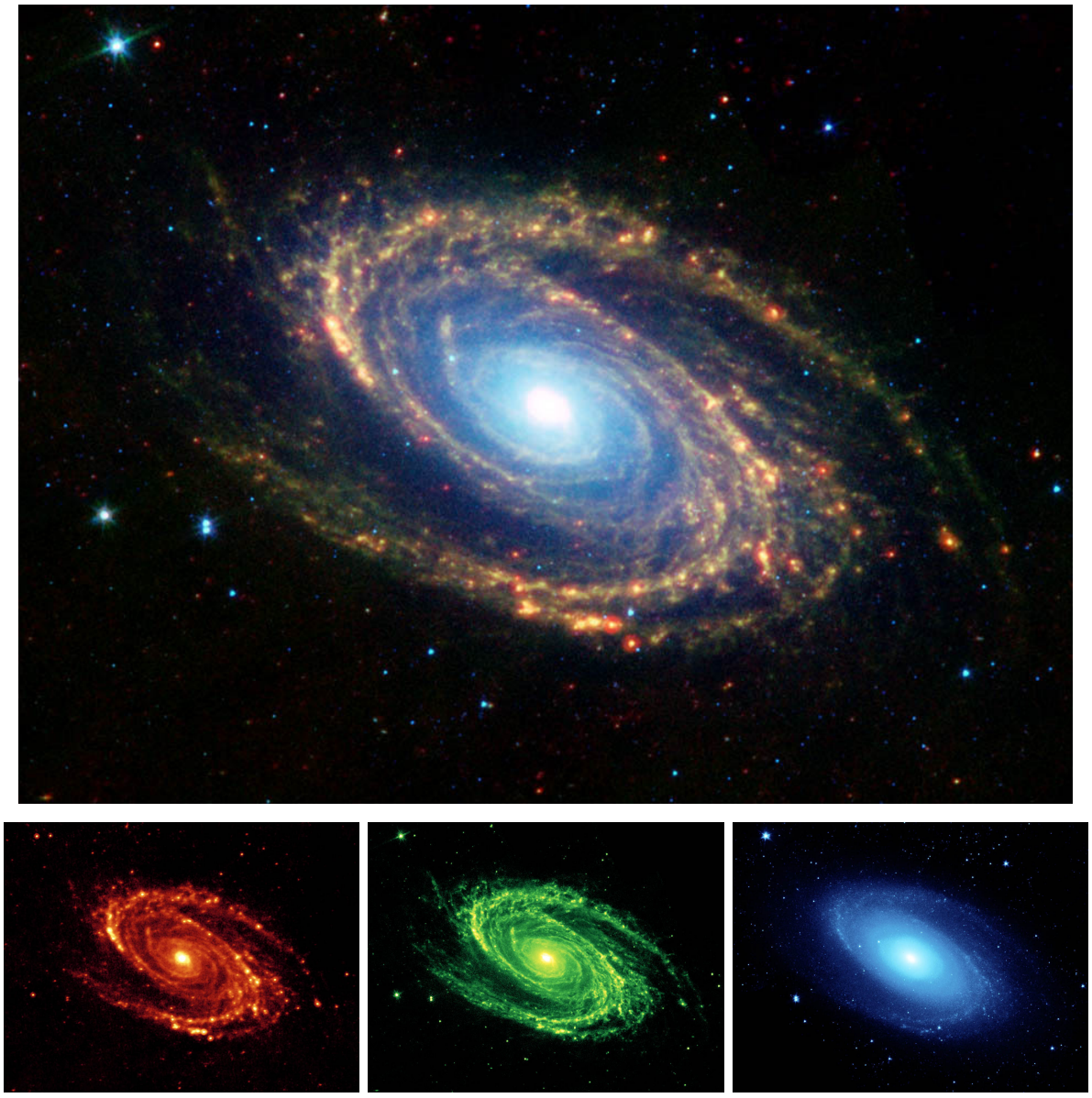

Figure 1.3: Spiral Galaxy M81 as observed by the Spitzer Space Telescope at 3.6 μm (blue), 8.0 μm (green), and 24 μm (red) (S. Wilner, priv. comm.).

in the IR.

1.2.2 Computational Tools

Modeling SEDs

A number of computational tools for fitting SEDs from the UV to the FIR and deriving the physical parameters including SFR, stellar mass, and dust properties have been developed over the past decade (e.g. MAGPHYS (da Cunha et al. 2008), CIGALE (Noll et al. 2009), GRASIL (Silva et al. 1998). While each code has its unique features, they broadly share similar methodology. Stellar galaxy spectra are created using a variety of star formation histories and models such as the single stellar population models of PEGASE (Fioc & Rocca-Volmerange 1997) or the stellar population synthesis code of Bruzual & Charlot (2003). These model spectra are then attenuated using versions of the Calzetti et al. (1994) law (e.g. CIGALE) or with radiative transfer through a dusty ISM (e.g. Charlot & Fall 2000 as in MAGPHYS). These SED-fitting codes assume a balance in the energy absorbed in the optical and UV and re-emitted by thermal dust emission in the IR. Dust emission is modeled in a variety of ways. CIGALE uses the semi-empirical templates of Dale & Helou (2002), while MAGPHYS has a four-component dust model comprised of a template for the emission of polycyclic aromatic hydrocarbons (PAH), and three modified blackbodies (β =1.5 or 2) of which two have variable temperatures of $15-25\,\mathrm{K}$ and $30-60\,\mathrm{K}$.

Simulating Interactions

Simulations of interactions have developed significantly since Toomre & Toomre created their simple models of the Antennae and other well-known systems. The increase in computing power has permitted the creation of cosmological simulations with over 10^{10} particles (e.g. "Millennium Run", Springel et al. 2005b). The development of hydrodynamic codes such as GADGET (Springel 2005) now include the effects of gas dynamics, star formation, supernovae feedback, AGN feedback, and gas heating and cooling in addition to the gravitational interaction of dark matter haloes. These codes can be applied to the simulation of individual galaxies or interactions as well as to larger cosmological settings (e.g. Hopkins et al. 2006; Mihos & Hernquist 1994, 1996; Barnes & Hernquist 1996; Cox et al. 2008).

A second important tool has been the development of radiative transfer codes to compute the predicted emission from simulated systems. Jonsson (2006, see also Jonsson et al. 2010) developed a panchromatic radiative transfer code called SUNRISE. It uses a Monte Carlo method to solve the radiation-transfer problem. SUNRISE uses the outputs of hydrodynamic simulations captured at a variety of times to generate the geometry of the problem, i.e., the relative positions of the luminous sources, the obscuring material, and the fiducial observer. Photon packages are followed from the sources through the diffuse medium whose temperature and emission is iteratively determined in each grid cell. Eventually, the propagated photons escape the medium and are captured by the observer.

1.3 Approaches to Studying Galaxy Interactions

1.3.1 Observations of Interactions

Despite many previous studies (e.g., Dahari 1985; Sanders et al. 1988; Kewley et al. 2001; Lambas et al. 2003, Surace et al. 1993), our understanding of the processes occurring during interactions remains incomplete. Our work, presented in Chapter 2, has two primary advantages over earlier studies.

Many earlier studies selected their sample galaxies in one of three ways: (1) based on the infrared brightness (e.g. Sanders et al. 1988, Kewley et al. 2001), (2) based on optical line diagnostics (e.g. Lambas et al. 2003), or (3) based on the presence of morphological distortion (e.g. Dahari 1985, Surace et al. 1993). Each methodology has its drawbacks. IR-selected samples typically select more active systems in which the enhanced star formation has heated the dust to a more luminous state. Selection based on optical spectra inherently suffer from the obscuring effects of dust, which can vary significantly with interaction stage in a given merger. Finally, selection based on morphological distortion preferentially selects systems in more evolved interaction stages. Therefore, a selection criterion not associated with either morphological disturbance or activity is critical in obtaining a sample with systems covering the full interaction sequence.

In Chapter 2, we present a sample of interactions selected based on the local density of nearby neighbors and observed with Herschel, Spitzer, GALEX, IRAS, and 2MASS. The analysis of the multiwavelength SEDs of this interacting sample also provides a handle for the examination of the evolution of the SFR, stellar mass, and dust properties

as a function of the strength of the interaction.

1.3.2 Comparison between Observations and Simulations

Simulations of interacting galaxies have to date been created with one of two goals in mind: modeling a specific system, or examining how well ensemble properties of interacting systems can be recreated. These aims in turn inform the type of observation against which these simulations are tested.

Toomre & Toomre (1972) were the first to systematically model well-known local interacting galaxies, including M51, the Mice (NGC 4676), and the Antennae (NGC 4038/4039). They created simple simulations of the motion of massless particles in the gravitational field of two masses and reproduced the tidal features seen in these systems. This methodology exemplifies the first type of study: creating simulations of specific systems in an effort to reproduce morphological distortions and, more recently, kinematic data. Privon et al. (2013) recently used Identikit (Barnes & Hibbard 2009, Barnes 2011) to create N-body simulations that reproduced the morphology and H I kinematics of NGC 5257/5258, the Mice, the Antennae, and NGC 2623. Based on these simulations, they estimated the time since first pericenter passage and until coalescence.

However, such morphological analyses suffer from an obvious bias: simulations trace mass but observations trace light. The second methodology entails the propagation of light from luminous matter in hydrodynamic simulations through a dusty interstellar medium (ISM) to one or more fiducial observers. The emission seen by those observers can then be directly compared to real observations. As discussed in Section 1.2.2, SUNRISE is an ideal tool for creating simulated SEDs. Jonsson et al. (2010) used it

to simulate the SEDs of seven isolated spiral galaxies. They examined how well these simulations reproduced the IR and optical colors found in the Spitzer Infrared Nearby Galaxy Survey (SINGS; Kennicutt et al. 2003), and found good agreement, although the full observed range was not reproduced in the simulations. Jonsson et al. (2010) also noted that the SEDs of each of their simulations was similar to the SED of at least one SINGS galaxy, demonstrating the realism of the simulated galaxies. Similarly, Snyder et al. (2013) examined mid-IR diagnostics of the AGN activity in simulations of two major mergers and found the simulations reproduced the range of parameters seen in several diagnostic diagrams (Laurent et al. 2000; Spoon et al. 2007; Veilleux et al. 2009; Lutz et al. 2004).

There has not previously been a systematic comparison of simulated and observed SEDs. Our study, presented in Chapter 3, is the first to simulate a suite of interactions between typical spirals and compare the resulting SEDs with photometry of observed interactions. This analysis permits the determination of the simulation properties necessary to reproduce the SED of an interaction and addresses the question of whether an SED is sufficient to identify the interaction stage.

1.3.3 Archeology Conducted on Post-Mergers

Leeuw et al. (2004) summarized our understanding of cold dust in local elliptical galaxies prior to Spitzer: due to the limited FIR data and the uncertain detection of emission by IRAS in these galaxies, typical dust masses were highly uncertain but unexpected amounts of dust, at least compared to optical extinction studies, had been detected in nearby bright elliptical galaxies (e.g. Roberts et al. 1991, Goudfrooij et al. 1994).

The Infrared Space Observatory (ISO) showed that in addition to this cold dust, some elliptical galaxies contain warmer dust (Ferrari et al. 2002). Spitzer allowed more widespread and precise detections of dust in early-type galaxies (e.g. Kaneda et al. 2007, Temi et al. 2007). Kaneda et al. (2007) also found a correlation between signs of interaction and the presence of excess dust in elliptical galaxies.

In Section 1.1, we discussed the activity of the AGN as one of the observable effects. While the AGN itself is most observable during or shortly after coalescence (e.g. Figure 1.1), the effects of its feedback are longer lasting and visible in many of the elliptical galaxies created by major mergers. Since the study of AGN feedback is still in its youth, a wide range of arguments have been made on its importance in galaxy evolution and the means by which the AGN affects its host galaxy. Fabian (2012) reviews the two primary modes of feedback: the radiative mode during which the AGN accretes at close to the Eddington limit and drives an outflow of gas, and the kinetic mode that acts in massive galaxies, often at the center of clusters, and in which their environment is affected through jets acting on hot gas. These powerful jets inflate bubbles of relativistic plasma which are buoyant relative to the intracluster or intracgroup medium and therefore rise. This process feeds energy back into the gas and prevents the "cooling flow" problem wherein the cooling rate of hot gas based on X-ray emission predicts a much larger reservoir of cold star forming gas at the centers of clusters than observed.

Observations with the Chandra X-ray Observatory have detected these bubbles in numerous clusters and galaxies (e.g. Dunn & Fabian 2006, 2008; Cavagnolo et al. 2011; Randall et al. 2011; Blanton et al. 2011; David et al. 2011; Forman et al. 2007). They appear as cavities in the emission and are sometimes detected in emission at radio wavelengths. Cavities undetected at high-frequency radio wavelengths are known as

ghost cavities and may be detected with low-frequency radio observations where the radio spectral aging has not affected the synchrotron emission as strongly (e.g. Giacintucci et al. 2009). The kinetic power in the jets can be estimated from the energy necessary to adiabatically inflate an observed bubble given the surrounding medium's pressure (Churazov et al. 2002). Bubbles can also be used to estimate the age of the outburst that created them, as they are assumed to rise buoyantly (Churazov et al. 2001).

In Chapter 4, we present the analysis of the post-merger galaxy Fornax A. We use the excess dust to estimate the stellar and dust mass of the smaller progenitor spiral galaxy that likely merged with an elliptical. This type of analysis to constrain merger parameters in a post-merger system had not previously been done. We detected a new pair of cavities in the extended X-ray emission of Fornax A and used the methodology described above to constrain the energies and the times of outburst events. Since then, no systematic analysis using excess dust mass to constrain merger history has been conducted. However, Kaviraj et al. (2012) recently used the dust and gas in early-type galaxies to estimate the molecular gas fractions in the accreted satellite galaxy. The use of post-merger systems therefore provides another avenue for further examination of the interaction process.

Chapter 2

Global Star Formation Rates and Dust Emission Over the Galaxy Interaction Sequence

This thesis chapter originally appeared in the literature as

L. Lanz, A. Zezas, N. Brassington, H. A. Smith, M. L. N. Ashby, E. da Cunha, G. G. Fazio, C. C. Hayward , L. Hernquist, P. Jonsson

The Astrophysical Journal, 2013, 768, 90

Abstract

We measured and modeled the spectral energy distributions (SEDs) in 28 bands from the ultraviolet to the far-infrared (FIR) for 31 interacting galaxies in 14 systems. The

sample is drawn from the Spitzer Interacting Galaxy Survey, which probes a range of galaxy interaction parameters at multiple wavelengths with an emphasis on the infrared bands. The subset presented in this paper consists of all galaxies for which FIR *Herschel* SPIRE observations are publicly available. Our SEDs combine the *Herschel* photometry with multi-wavelength data from *Spitzer*, *GALEX*, *Swift* UVOT, and 2MASS. While the shapes of the SEDs are broadly similar across our sample, strongly interacting galaxies typically have more mid-infrared emission relative to their near-infrared and FIR emission than weakly or moderately interacting galaxies. We modeled the full SEDs to derive host galaxy star formation rates (SFRs), specific star formation rates (sSFRs), stellar masses, dust temperatures, dust luminosities, and dust masses. We find increases in the dust luminosity and mass, SFR, and cold (15−25 K) dust temperature as the interaction progresses from *moderately* to *strongly* interacting and between *non-interacting* and *strongly* interacting galaxies. We also find increases in the SFR between *weakly* and *strongly* interacting galaxies. In contrast, the sSFR remains unchanged across all the interaction stages. The ultraviolet photometry is crucial for constraining the age of the stellar population and the SFR, while dust mass is primarily determined by SPIRE photometry. The SFR derived from the SED modeling agrees well with rates estimated by proportionality relations that depend on infrared emission.

2.1 Introduction

Galaxy evolution is believed to be heavily influenced by interactions between galaxies, both for local systems and for distant objects at earlier cosmological times. In the canonical view, interactions between galaxies have three primary observable effects. In

the most dramatic cases, interactions stimulate star formation in a burst of activity that is presumed to power the high infrared (IR) luminosities typically seen in such systems. Many local ultra-luminous IR galaxies ($L \geq 10^{12}\ L_{\odot}$; ULIRGs) and luminous IR galaxies ($10^{11}\ L_{\odot} \leq L \leq 10^{12}\ L_{\odot}$; LIRGs) show evidence of galaxy interactions (e.g., Veilleux et al. 2002). Similarly, their high-redshift counterparts, sub-millimeter galaxies, first detected by SCUBA and now studied extensively by the Spectral and Photometric Imaging Receiver (SPIRE) on the *Herschel Space Observatory*,[1] are thought to be predominantly mergers (e.g., Blain et al. 1999), although the relative contribution of mergers of different stages to their numbers is still an open question (e.g., Hayward et al. 2012a, 2012b).

The second effect is that interactions significantly affect the subsequent evolution of galaxies, which may lead to significant changes in their morphology. Disturbed galaxies have long been associated with mergers (e.g., Toomre & Toomre 1972). Numerical simulations of interactions (e.g., Hopkins et al. 2006; Hopkins 2012; Mihos & Hernquist 1994, 1996; Barnes 1992; Barnes & Hernquist 1996; Sanders 1999) show a variety of morphological distortions as well as variable amounts of star formation. The simulations also demonstrate the complexity of the problem: the degree of induced activity and distortion varies greatly with the parameters of the encounter, the phase of the interactions, the molecular gas content ("wetness"), and the mass of the progenitor galaxies among many other properties.

Third, the canonical picture, as seen in many simulations (e.g., Di Matteo et al.

[1] *Herschel* is an ESA space observatory with science instruments provided by European-led Principal Investigator consortia and with important participation from NASA.

2005; Springel et al. 2005a), involves merger-driven gas inflow to the central regions, resulting in heightened activity of the central supermassive black hole as well as starburst activity due to the increased central gas density and possibly turbulence. The process in principle converts a low-luminosity nucleus into an active galactic nucleus (AGN) but one whose luminosity might range widely depending on the stage of the interaction. Indeed, observations of merging galaxies over the years have tended to provide evidence supporting the conclusion that, at least on a statistical level, interactions trigger an enhancement in the formation of stars as well as nuclear activity. However, the recent literature includes works that argue both for and against a strong connection between nuclear activity and mergers (e.g., Li et al. 2008; Kocevski et al. 2012; Ellison et al. 2011; Scudder et al. 2012; Silverman et al. 2011).

Therefore, despite many previous studies (e.g., Dahari 1985; Sanders et al. 1988; Kewley et al. 2001; Lambas et al. 2003), both observational and through simulations, our understanding of the evolution of the physical activity during the course of a galaxy-galaxy interaction remains incomplete. In the past decade, two new developments have dramatically changed our understanding of star formation and accretion activity around galactic nuclei, which are the two dominant processes at work in controlling the observed emission. The first is the success of space missions, in particular, the *Spitzer Space Telescope*[2] (Werner et al. 2004) and the *Herschel Space Observatory* (Pilbratt et al. 2010) in the IR, as well as the *Galaxy Evolution Explorer*[3] (*GALEX*; Martin et al. 2005)

[2] *Spitzer* is operated by the Jet Propulsion Laboratory, California Institute of Technology under a contract with NASA.

[3] *GALEX* is operated for NASA by the California Institute of Technology under NASA contract NAS5-98034.

and *Swift* (Gehrels et al. 2004) in the ultraviolet (UV), providing photometry across the complete spectral range from UV to millimeter wavelengths. Most importantly, detailed imaging and high sensitivity photometry now available at the critical far-infrared (FIR) emission peak resulting from warm, luminous dust heated by starbursts provides crucial information regarding dust heating and embedded star formation. The combination of UV and IR observations is essential to obtain a complete census of recent and ongoing star formation by capturing both the unobscured and obscured emission from young stars.

The second development has been the success of computational codes. We have new tools for the derivation of galaxy properties including masses, star formation rates (SFRs), and interstellar medium (ISM) parameters from global fits, which allow self-consistent measurements of critical parameters combining stellar evolution models (e.g., Bruzual & Charlot 2003) with radiative transfer through a dusty ISM (e.g., Charlot & Fall 2000). A second set of tools uses sophisticated hydrodynamic computational codes to simulate interactions (e.g., GADGET; Springel 2005), while simultaneously new radiative transfer models can compute the predicted emission from these evolving interacting systems (e.g., SUNRISE; Jonsson 2006).

It is important to recognize that observational biases can be significant. Due to the long timescales of an interaction (typically $10^8 - 10^9$ years), observers rely on studies of a range of interacting systems to reconstruct a likely sequence of events. Moreover, determining the exact phase of any particular observed interaction from its morphology is uncertain at best, because the appearance of a system at a given interaction phase also depends on the specific geometry of the encounter, the masses of the galaxies, metallicity, molecular gas content, and (not least) previous interaction

histories (e.g., Di Matteo et al. 2007). Systems are ordered into an evolutionary sequence using intuition provided by simulations and physical models, which are themselves based on observations of particular systems. Selection criteria, however, can introduce a bias for more luminous, morphologically disturbed systems and, hence, toward the most active phases of interactions. Therefore, a selection criterion not associated with either morphological disturbance or degree of activity is critical for obtaining a sample containing systems throughout the full interaction sequence.

We have undertaken a program to take advantage of all these developments: full, multi-wavelength datasets of an interacting galaxy sample selected with few biases; hydrodynamic simulations; and radiative transfer modeling, in a systematic effort to better understand systems across a range of interaction stages and to iterate refinements to the various modeling and radiative transfer codes. We have chosen a representative sample of objects spanning the interaction sequence, obtained their full spectral energy distributions (SEDs), and are comparing the results against a variety of models − based on both templates/stellar evolution/radiative transfer and on diagnostic features.

This first paper of the project presents results and conclusions for a sample of 31 interacting galaxies in fourteen systems for which there are currently complete multi-wavelength data that can be used to study the variations in their star formation and dust heating. This paper is organized as follows. We describe the full Spitzer Interacting Galaxy Survey (SIGS) sample in Section 2.2 and the classification of each of the sources in the interaction sequence. Section 2.3 describes the wide range of observational photometry used to construct the SEDs. It also describes the issues associated with obtaining reliable photometry from the diverse datasets. In Section 2.4, we model the SEDs of these objects. Section 2.5 discusses the variations seen across the

interaction sequence and constraints imposed by photometry from different instruments and compares SFRs derived using the entire SED to those from relations depending on one or two wavelengths. In Section 2.6, we summarize our results.

2.2 The Spitzer Interacting Galaxy Survey (SIGS) Sample

2.2.1 Sample Description

The SIGS sample was designed to span the full range of galaxy interaction parameters by using a sample selected strictly on the basis of interaction probability rather than morphology, activity, luminosity, or other derivative indicators. The catalog includes interactions of all types, not just those that give rise to obvious morphological peculiarities and/or nuclear/starburst activity, thus minimizing morphological biases so we can address the relationships between interactions and activity. A selection criterion not dependent on visible signs of tidal interactions is important because of the dependence of the response of interacting galaxies on the relative inclinations of disks (e.g., Toomre & Toomre 1972; D'Onghia et al. 2010) and the uncertain distribution of dark matter around the galaxies (e.g., Dubinski et al. 1996, 1999). The SIGS sample was based on the Keel−Kennicutt visibly selected catalog of interacting spiral galaxies (Keel et al. 1985, hereafter K85), which selected galaxies based on the local density of nearby neighbors and consists of bright spiral galaxies having neighbors with typical projected separations of 4−5 effective radii. A criterion based on the relative recessional velocities $|\Delta v| < 600$ km s^{-1} was imposed to exclude non-associated, projected pairs.

In order to resolve structures on scales of a few hundred pc, we limited the original sample to sources closer than cz < 4000 km s^{-1}. To investigate the effects of tidal interaction, we added a complementary set to the prime sample: the K85 "Arp Sample" with the same maximum distance as the Keel−Kennicutt complete sample. This set is based on the Arp catalog of peculiar galaxies from which K85 selected all objects showing evidence of tidal interaction not strong enough to disrupt the galactic disks (i.e., it does not bias against early stage mergers). Although K85 excluded some fainter members of the interacting groups (their selection criteria required a B band magnitude of $B_T \leq 13.0$), we include them in order to obtain a complete picture of the activity in the different interacting systems.

The total SIGS sample consists of 103 individual interacting galaxies in 48 systems. The combined galaxies span the range of interaction types, luminosities, and galaxy types. SIGS is comprised primarily of spiral-spiral interactions, with some spiral-elliptical and spiral-irregular interactions. Its set of systems contains both major and minor mergers, ranging from systems likely to be in first approach (e.g., NGC 3424/NGC 3430) through close passages (e.g., M51) to final collision (NGC 3690/IC 694), and span an infrared luminosity[4] range from $1.3{\times}10^{10}$ to 5.1×10^{14} $L_{\odot}$. From this complete sample, which has a sufficiently large number of objects to allow us to study statistically the activity in interacting galaxies across a wide range of encounter parameters, we will be able to study the increase of star formation and AGN activity in interacting disk galaxies. As discussed in Section 2.1, while there have been a significant number of studies probing SFR enhancement and nuclear activity, the importance of the different

[4] $\log(L_{\rm TIR})=\log(L_{24\mu{\rm m}})+0.494{\times}\log(L_{\rm PAH\ 8\mu m}/L_{24\mu{\rm m}})+0.997$ (Boquien et al. 2010).

interaction parameters in triggering these events is not well understood. The SIGS sample provides us with the opportunity to observe a large range of galaxies, including very early interaction stages. The level and distribution of star-formation in such early stage interactions has not been systematically studied before, therefore our sample will allow us to identify the initial increase in SFR caused by the interaction, as well as identify where this enhancement is located in the galaxies (i.e., in the central region of the galaxy, along the disk, or within tidal features). Additionally, the size of our sample also provides us with the ability to probe these enhancements for all systems as a function of different interaction parameters, such as galaxy mass, mass ratio and gas content. A detailed description of the SIGS sample along with the analysis of the *Spitzer* data and a presentation of the images and the photometric results is given in N. Brassington et al. (2013, in preparation).

There are currently fourteen interacting systems from the SIGS set which have publicly available observations by all the facilities: *Herschel* (SPIRE and partial coverage with the Photodetector Array Camera and Spectrometer (PACS)), *Spitzer*, 2 Micron All Sky Survey (2MASS), and either *GALEX* or *Swift*, enabling us to model their emission from far-UV (FUV) to FIR in 28 filters when ancillary archival measurements are added. Not all galaxies have photometric data in all filters; we used as many photometric data as available, generally 15−25. These galaxies comprise the sample we examine in this paper and were selected from the SIGS sample on the basis of available SPIRE observations. They are listed in Table 2.1 along with key parameters.

Table 2.1. Sample Description

Group (1)	Galaxy (2)	R.A. (J2000) (3)	Decl. (J2000) (4)	Distance (Mpc) (5)	Interaction Stage (6)	Aperture Size (7)	Aperture Angle (8)	Aperture From (9)
1	NGC 2976	09 47 16.3	+67 54 52.0	3.75	2.0±0.0	$3\farcm57 \times 1\farcm77$	$51\fdg8$	3.6 μm
	NGC 3031	09 55 33.2	+69 03 57.9	3.77	2.0±0.4	$10\farcm11 \times 5\farcm82$	$64\fdg0$	3.6 μm
	NGC 3034	09 55 52.2	+69 40 47.8	3.89	2.0±0.4	$2\farcm87 \times 1\farcm07$	$336\fdg4$	3.6 μm
	NGC 3077	10 03 19.8	+68 44 01.5	3.93	2.0±0.5	$2\farcm12 \times 1\farcm62$	$318\fdg5$	3.6 μm
2	NGC 3185	10 17 38.7	+21 41 16.2	22.6	2.0±0.5	$1\farcm84 \times 0\farcm99$	$41\fdg9$	NUV
	NGC 3187	10 17 48.4	+21 52 30.9	26.1	3.0±0.5	$2\farcm25 \times 1\farcm04$	$338\fdg7$	NUV
	NGC 3190	10 18 05.7	+21 49 57.0	22.5	3.0±0.5	$2\farcm14 \times 0\farcm97$	$28\fdg4$	3.6 μm
3	NGC 3226	10 23 27.0	+19 53 53.2	23.3	4.0±0.5	$1\farcm29 \times 1\farcm00$	$302\fdg5$	3.6 μm
	NGC 3227	10 23 30.5	+19 51 55.1	20.6	4.0±0.5	$1\farcm89 \times 1\farcm03$	$60\fdg4$	3.6 μm
4	NGC 3395	10 49 50.0	+32 58 55.2	27.7	4.0±0.5	$1\farcm46 \times 0\farcm89$	$278\fdg9$	3.6 μm
	NGC 3396	10 49 55.2	+32 59 25.7	27.7	4.0±0.5	$1\farcm38 \times 0\farcm60$	$9\fdg6$	3.6 μm
5	NGC 3424	10 51 46.9	+32 54 04.1	26.1	2.0±0.4	$1\farcm81 \times 0\farcm59$	$17\fdg4$	NUV
	NGC 3430	10 52 11.5	+32 57 05.0	26.7	2.0±0.4	$2\farcm69 \times 1\farcm46$	$301\fdg3$	NUV
6	NGC 3448	10 54 38.7	+54 18 21.0	24.4	3.0±0.0	$1\farcm57 \times 0\farcm59$	$338\fdg6$	3.6 μm
	UGC 6016	10 54 13.4	+54 17 15.5	27.2*	3.0±0.0	$1\farcm28 \times 0\farcm67$	$329\fdg3$	3.6 μm
7	NGC 3690/IC 694	11 28 31.2	+58 33 46.7	48.1*	4.0±0.4	$1\farcm20 \times 0\farcm93$	$40\fdg6$	3.6 μm
8	NGC 3786	11 39 42.5	+31 54 34.2	41.7	3.0±0.5	$1\farcm04 \times 0\farcm57$	$340\fdg7$	3.6 μm
	NGC 3788	11 39 44.6	+31 55 54.3	36.5	3.0±0.5	$1\farcm32 \times 0\farcm41$	$84\fdg8$	3.6 μm
9	NGC 4038/4039	12 01 53.9	−18 52 34.8	25.4	4.0±0.0	$3\farcm00 \times 2\farcm33$	$304\fdg3$	3.6 μm
10	NGC 4618	12 41 32.8	+41 08 44.4	7.28	3.0±0.5	$2\farcm69 \times 2\farcm08$	$284\fdg1$	3.6 μm
	NGC 4625	12 41 52.6	+41 16 20.6	8.20	3.0±0.5	$1\farcm88 \times 1\farcm49$	$296\fdg5$	NUV
11	NGC 4647	12 43 32.6	+11 34 53.9	16.8	3.0±0.5	$1\farcm53 \times 1\farcm24$	$18\fdg6$	NUV
	NGC 4649	12 43 40.0	+11 33 09.8	17.3	3.0±0.5	$1\farcm81 \times 1\farcm33$	$34\fdg2$	3.6 μm
12	M51A	13 29 54.1	+47 11 41.2	7.69	3.0±0.5	$6\farcm86 \times 4\farcm42$	$293\fdg5$	NUV
	M51B	13 29 59.7	+47 15 58.5	7.66	3.0±0.5	$2\farcm68 \times 1\farcm95$	$18\fdg3$	3.6 μm
13	NGC 5394	13 58 33.7	+37 27 14.4	56.4*	4.0±0.5	$0\farcm89 \times 0\farcm50$	$84\fdg2$	NUV
	NGC 5395	13 58 37.6	+37 25 41.2	56.4*	4.0±0.5	$2\farcm88 \times 1\farcm08$	$87\fdg9$	NUV
14	M101	14 03 09.8	+54 20 37.3	6.70	3.0±0.5	$10\farcm00 \times 8\farcm53$	$156\fdg4$	3.6 μm
	NGC 5474	14 05 01.2	+53 39 11.6	5.94	3.0±0.5	$2\farcm53 \times 2\farcm24$	$290\fdg2$	3.6 μm

Note. — Distance moduli were obtained from Tully et al. (2008), Tully (1994), and the Extra-galactic Distance Database. The distances in Column 5 marked with * did not have distance moduli and were calculated based on heliocentric velocities, corrected per Mould et al. (2000) and assuming $H_0 = 72$ km s^{-1} Mpc^{-1}. The determination of interaction stage is described in Section 2.2.2. In Column 6 we give the median and standard deviation of the classifications by the co-authors. The parameters of the elliptical apertures are given in Columns 7 and 8 and we note whether it was determined on the *GALEX* NUV or IRAC 3.6 μm image. The angle is given degrees north of west.

2.2.2 Estimating the Interaction Phase

Toomre & Toomre (1972) were the first to systematically model and describe the morphological characteristics of interacting galaxies. Using simple simulations, they showed that tails and bridges could result from tidal forces and reconstructed the orbits that could produce the tidal features seen in some of the best known interacting systems including M51, the Mice (NGC 4676), and the Antennae (NGC 4038/4039). Their work also highlighted the close connection between observations and modeling: our classification of the interaction stages in our sample is based on theoretical descriptions of how such interactions are expected to proceed.

As Rich et al. (2012) have shown, projected distance alone is an unreliable indicator of interaction stage. We therefore used the Dopita et al. (2002) five-stage scheme to classify the interaction stage of our galaxies. By construction, our sample does not include any Stage 1 galaxies (isolated, non-interacting galaxies). Stage 2 galaxies are described as weakly interacting systems, which are close on the sky, but show minimal morphological distortion. These systems could be either before or after the first passage. Stage 3 galaxies, which we call moderately interacting, show stronger signs of morphological distortion and often tidal tails. Depending on the geometry of the encounter, these systems could be in the midst of the first or a subsequent passage. Stage 4 (strongly interacting) galaxies show strong signs of disturbance and are therefore in more evolved stage of interaction. Our sample falls into these three categories. While the SIGS sample has a Stage 5 (coalescence/post-merger systems), the sample presented in this paper does not. The SIGS sample is roughly equally divided between Stages 2−4, while the sample presented in this paper has 7, 14, and 7.

This classification method is clearly a statistical scheme in the sense that, for each individual galaxy, the classification stage does not translate directly to an interaction phase. However, since the scheme is based on morphological appearance of galaxies, it provides a direct picture of the effect of the interaction on the distributions of the stellar component of the galaxies and their star formation activity. The classification was carried out independently for each galaxy in the SIGS sample by six collaborators on the basis of appearance alone in Digitized Sky Survey (DSS) images. Stage 2 galaxies show little morphological distortion, while Stage 4 galaxies are strongly distorted. Stage 3 galaxies show some distortion in the form of tidal features, although their disks remain undisturbed. Visible DSS images are best suited for this purpose, since they trace on-going star formation as well as older stellar populations in a single image. In Appendix A, we show representative examples of the galaxies in Stages 2−4. Galaxy groups in which classifications differed by more than one stage were re-examined; the median of the classifications is used for each galaxy. Table 2.1 lists the interaction stage for all of the galaxies in our sample.

2.2.3 Comparison Non-interacting Sample

As a comparison sample of non-interacting galaxies, we used a subset of the "normal" galaxy sample of Smith et al. (2007a). Smith et al. (2007a) identified 42 galaxies from the Spitzer Infrared Nearby Galaxies Survey (SINGS; Kennicutt et al. 2003; Dale et al. 2005) of which 26 were spirals, which had not been subject to strong distortions. We were more conservative in our definition of non-interacting, by removing galaxies associated with clusters or radial-velocity groups, and we removed the three that were not observed

with SPIRE as part of the Key Insights on Nearby Galaxy: a Far Infrared Survey with Herschel (KINGFISH; Kennicutt et al. 2011). Our comparison sample is comprised of 15 galaxies: NGC 925, NGC 1291, NGC 2841, NGC 3049, NGC 3184, NGC 3521, NGC 3621, NGC 3938, NGC 4236, NGC 4559, NGC 4594, NGC 4736, NGC 4826, NGC 5055, and NGC 6946. We used the distances provided in Smith et al. (2007a) and the UV−MIR photometry given in Dale et al. 2007) and the FIR photometry given in Dale et al. (2012).

2.3 Observations and Data Reduction

The sample presented here has a complete set of near-infrared (NIR) to FIR photometry observed by 2MASS, *Spitzer*, and *Herschel* respectively, as well as near-UV (NUV) and FUV photometry observed primarily by *GALEX* and completed by the Ultraviolet/Optical Telescope (UVOT) on *Swift*. In the next sections, we describe the observations and their reduction. The observations were supplemented with mid-infrared (MIR) to FIR fluxes measured by the *Infrared Astronomical Satellite* (*IRAS*), the 70 μm and 160 μm Multiband Imaging Photometer (MIPS) detectors on *Spitzer*, and UBV fluxes from the Third Reference Catalog (RC3; de Vaucouleurs et al. 1991) where available in the literature through the NASA Extragalactic Database (NED). The MIPS 24 μm fluxes from these sources typically agree within the uncertainties with those we measure. Figures 2.1−2.6 show from left to right the *GALEX*, 2MASS, *Spitzer* Infrared Array Camera (IRAC), and *Herschel* observations of each galaxy. Some galaxies (e.g., NGC 3031 and M51A) have similar morphology from UV to FIR. In contrast, others have distinct morphological differences between the UV and IR, such as the FIR bright

spots of NGC 2976 or the extended UV disk of NGC 3430. Appendix C contains notes on the individual galaxies.

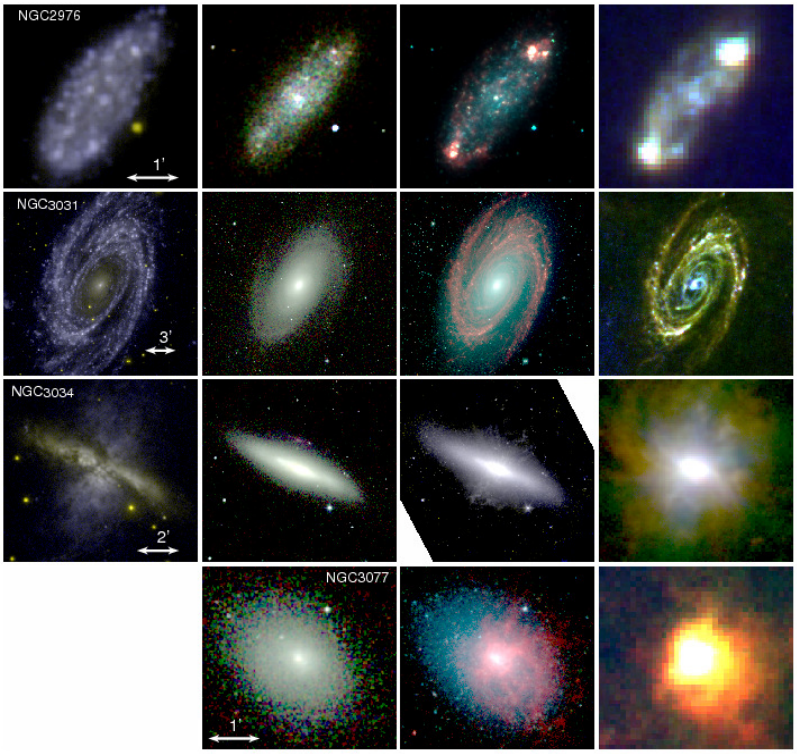

Figure 2.1: NGC 2976, NGC 3031, NGC 3034, and NGC 3077 (from top to bottom) as observed, from left to right, by *GALEX* (NUV in yellow; FUV in blue), 2MASS (J in blue, H in green, and Ks in red), IRAC (3.6 μm in blue, 4.5 μm in green, and 8.0 μm in red), and *Herschel* (PACS 75 μm in blue, PACS 170 μm in green, and SPIRE 250 μm in red). The longer wavelength IRAC observations of NGC 3034 were saturated, so 4.5 μm is shown in yellow instead. NGC 3077 was not observed by either *GALEX* or *Swift*. At the distance of these galaxies, $1' \approx 1.1$ kpc.

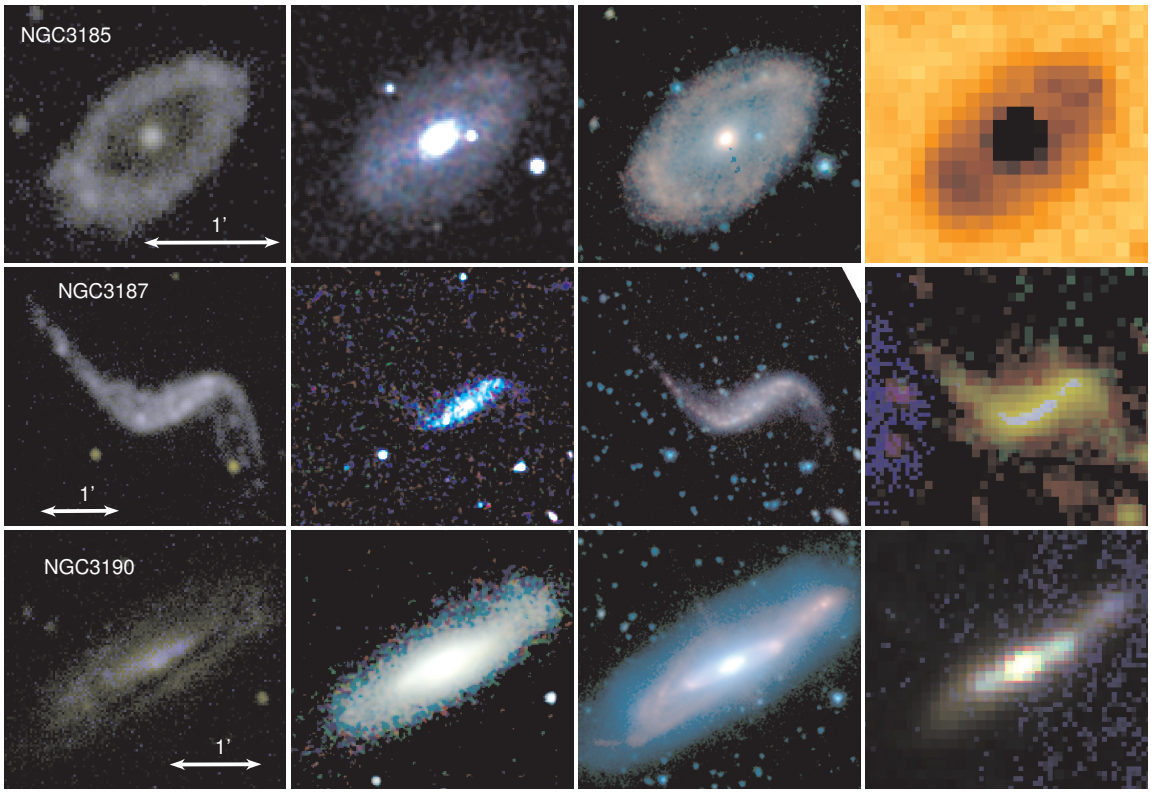

Figure 2.2: As Figure 2.1, but for NGC 3185, NGC 3187, and NGC 3190. NGC 3185 was not observed by PACS, the right image only shows the SPIRE 250 μm image in which darker pixels have higher flux.. At the distance of these galaxies, $1'$ is approximately 6−7 kpc.

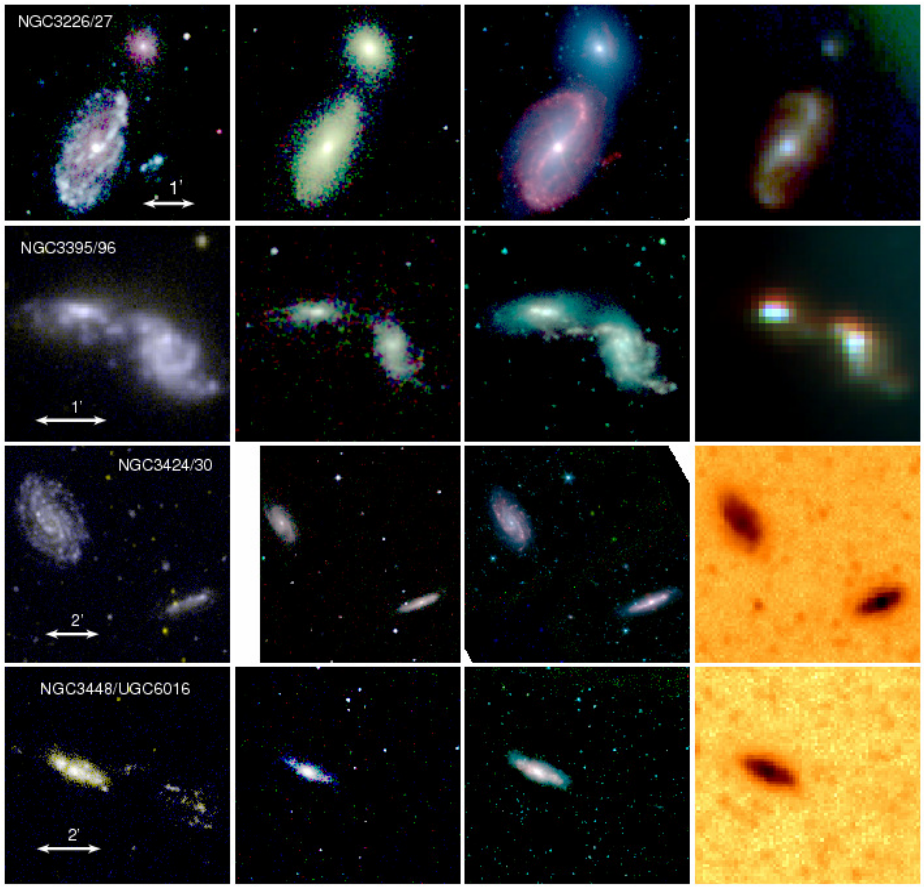

Figure 2.3: As Figure 2.1, but for NGC 3226 (upper)/NGC 3227 (lower), NGC 3395 (right)/NGC 3396 (left), NGC 3424 (right)/NGC 3430 (left), and NGC 3448 (left)/UGC 6016 (right). NGC 3226/3227 was not observed by *GALEX* but by *Swift*. Their left image show the *Swift* observations through the UVW1 filter in blue, the UVM2 filter in green, and the UVW2 filter in red. NGC 3424/30 and NGC 3448/UGC 6016 were not observed with PACS, so the right image only shows the SPIRE 250 μm image as in Figure 2.2. UGC 6016, while having significant extended diffuse emission in the UV, is not well detected in the IR bands. At the distance of these galaxies $1'$ is approximately 6−8 kpc.

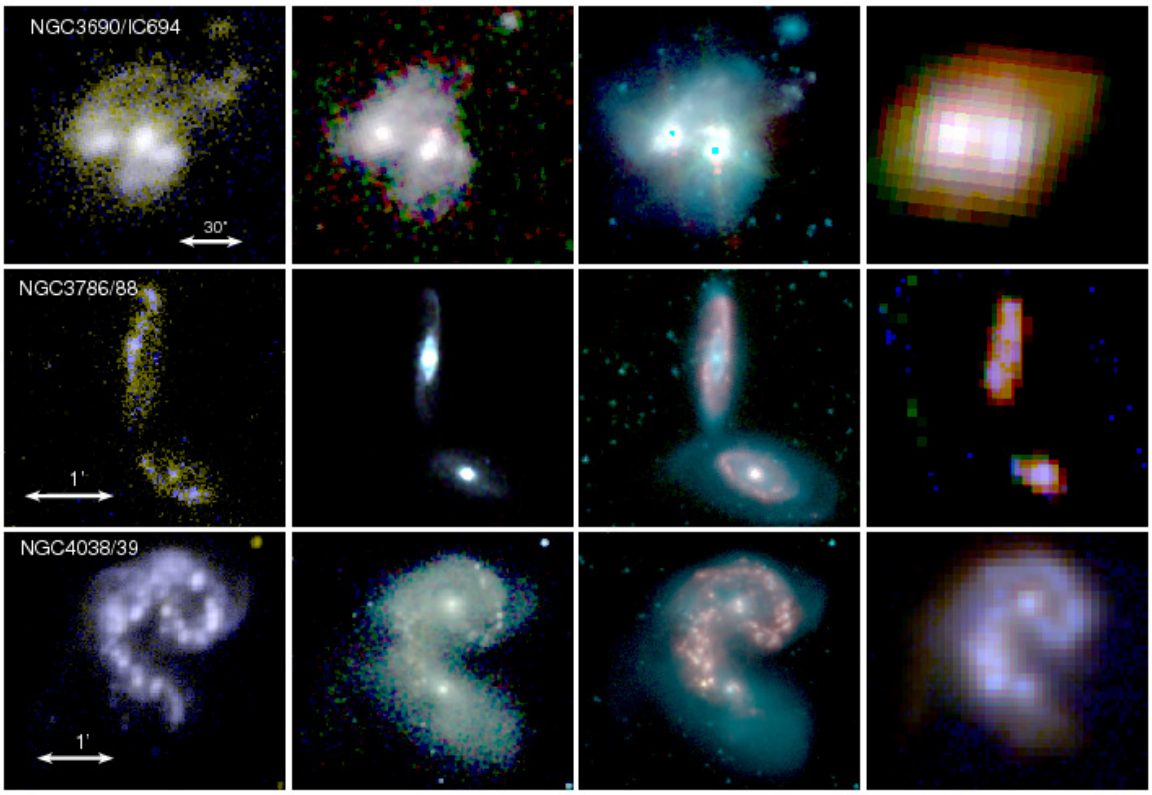

Figure 2.4: As Figure 2.1, but for NGC 3690/IC 694, NGC 3786 (bottom)/NGC 3788 (top), and NGC 4038/4039. The 8 μm IRAC image of NGC 3690/IC 694 is saturated in the nuclei of the two galaxies, resulting in the blue-green artifacts. At the distance of these galaxies, $1'$ is approximately 14 kpc (NGC 3690), 11−12 kpc (NGC 3786/3788), and 7.4 kpc (NGC 4038/4039).

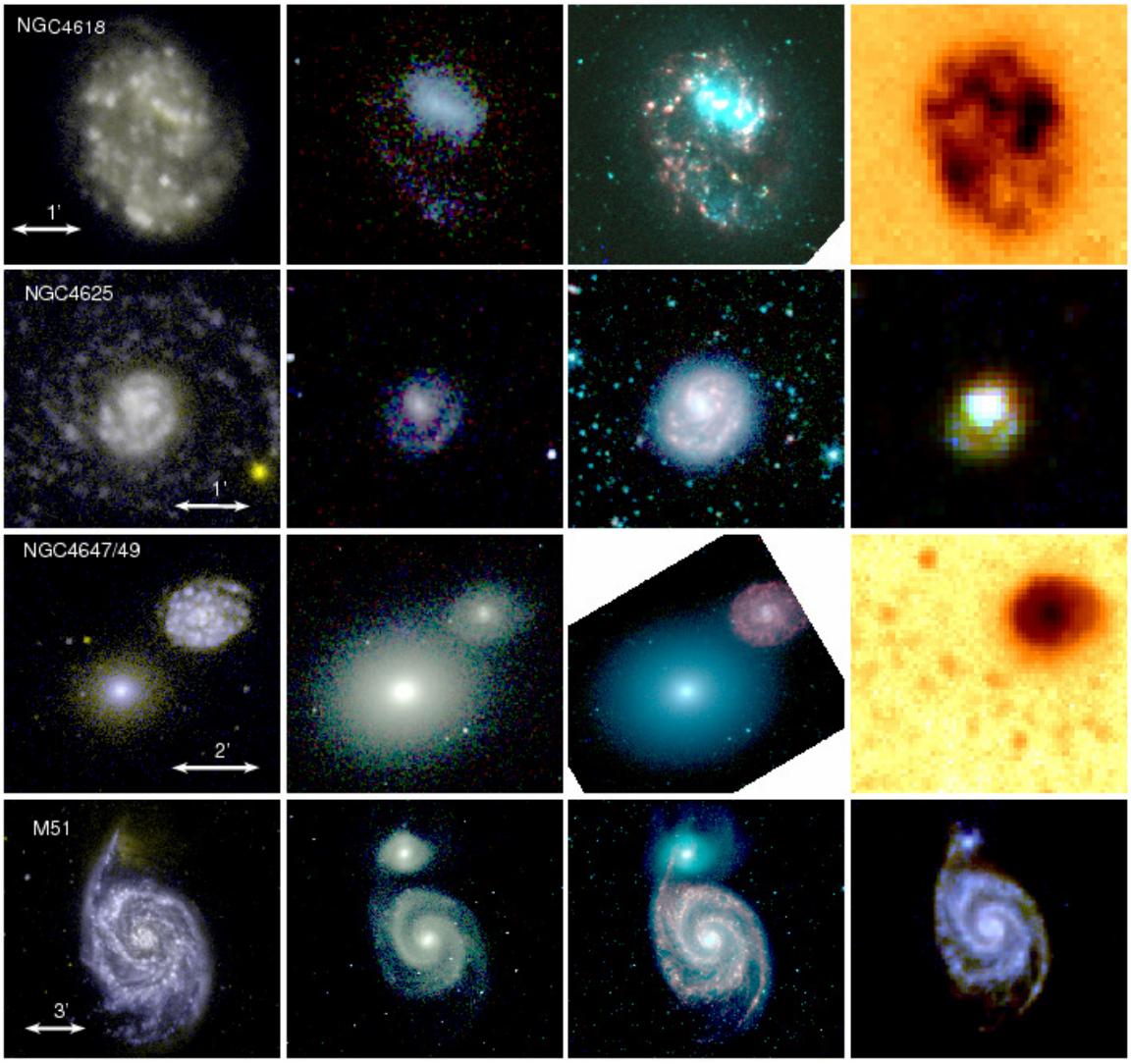

Figure 2.5: As Figure 2.1, but for NGC 4618, NGC 4625, NGC 4647 (right)/NGC 4649 (left), and M51. The right images of NGC 4618 and NGC 4647/49 only show the SPIRE 250 μm image. At the distance of these galaxies, $1'$ is approximately 2.1−2.4 kpc (NGC 4618/4625), 5 kpc (NGC 4647/4649), and 2.2 kpc (M51).

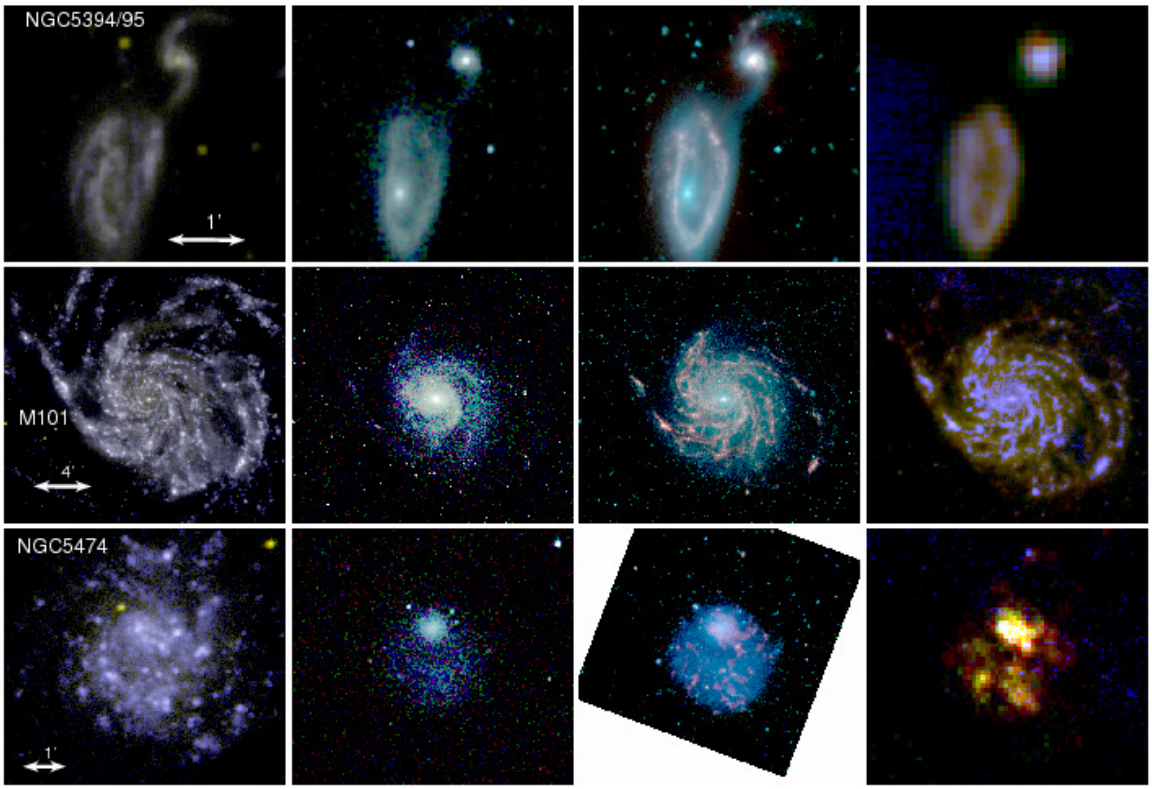

Figure 2.6: As Figure 2.1, but for NGC 5394 (top)/NGC 5395 (bottom), M101, and NGC 5474. At the distances of these galaxies, $1'$ is approximately 16 kpc (NGC 5394/5395) and 1.7−2.0 kpc (M101/NGC 5474).

2.3.1 Galaxy Distances

All of the galaxies in our sample are nearby (within 60 Mpc) and can therefore have peculiar velocities that contribute significantly to their recessional velocities. Tully et al. (2008) recently compiled redshift-independent distances for nearby galaxies with velocities less than 3000 km s^{-1} using alternate methods including Cepheids (Freedman et al. 2001), the luminosity of stars at the tip of the red giant branch (Karachentsev et al. 2006), surface brightness fluctuations (Tonry et al. 2001), and the Tully−Fisher relation (Tully & Fisher 1977). Distances to additional galaxies based on their group or cluster association are given in the Extra-galactic Distance Database[5] (EDD; R. B. Tully 2010, private communication). Twenty-six of our galaxies have distance moduli given by either Tully et al. (2008), Tully (1994), or EDD. For the five galaxies lacking distance moduli, we obtained heliocentric velocities from the PSCz catalog (Saunders et al. 2000; NGC 3690/IC 694, NGC 5394, and NGC 5395) and RC3 (UGC 6016), which we corrected to account for the velocity field of Virgo, the Great Attractor, and the Shapley supercluster, following Mould et al. (2000). Distances were then calculated assuming H_0 =72 km s^{-1} Mpc^{-1}. The distances are given in Table 2.1.

2.3.2 Infrared Photometry

Spitzer Observations

The IRAC (Fazio et al. 2004) and MIPS (Rieke et al. 2004) 24 μm observations were taken as part of a variety of programs, including the main SIGS program (PID 20140;

[5]http://edd.ifa.hawaii.edu

P.I. A. Zezas), which also observed galaxy groups that had not previously been observed. The observation parameters are given in Tables 2.2−refch2:spitzerobsmips. The IRAC Basic Calibrated Data (BCD) were retrieved from the Spitzer archive and cleaned before being coadded into mosaics with 0.″6 pixels using IRACproc (Schuster et al. 2006). The MIPS 24 μm BCDs were merged to form mosaics with 2.″45 pixels using the Mosaicker and Point Source Extractor package (MOPEX; Makovoz & Khan 2005). The reduction of these data will be described in detail in N. Brassington et al. (2013, in preparation). While the pipeline versions range from S13-S18, the difference between the pipelines are minor and do not impact significantly the photometry.[6] The pipeline version for each galaxy is given in Tables 2.2 and 2.3.

Herschel Observations

The parameters for the *Herschel* SPIRE (Griffin et al. 2010) and PACS (Poglitsch et al. 2010) observations are given in Table 2.4. The *Herschel* data were taken as part of two Science Demonstration Phase programs (P.I.s C. Wilson and S. Eales), four Key Project programs (P.I.s R. Kennicutt, S. Eales, C. Wilson, and E. Sturm), and one Guaranteed Time program (P.I. L. Spinoglio). All of the galaxies were observed by SPIRE at 250 μm, 350 μm, and 500 μm; this was part of the selection criteria of this sample. Approximately 50% of the sample were observed in all three PACS bands and an additional ∼25% were observed at 75 μm and 170 μm.

The data were retrieved from the Herschel Science Archive and processed using the calibration trees of version 8.0.1 of the Herschel Interactive Processing Environment

[6]http://irsa.ipac.caltech.edu/data/SPITZER/docs/irac/iracinstrumenthandbook/79/

(HIPE; Ott 2010). This processing was accomplished using the default pipeline scripts available through HIPE to make Large Map mode mosaics for the SPIRE data and extended source mosaics with MADmap for PACS data. We discuss additional details regarding the processing of PACS data in Appendix B.

2MASS Observations

NIR mosaics of the sample galaxies observed as part of the 2MASS (Skrutskie et al. 2006) were retrieved from the NASA/IPAC Infrared Science Archive,[7] and from the Large Galaxy Atlas (Jarrett et al. 2003) when possible. The counts measured in the images were converted to Janskys using the zero points of Cohen et al. (2003). We compared our fluxes measured in the apertures described in Section 2.3.4 to the total fluxes given in NED from Jarrett et al. (2003) and the 2MASS Extended Object Catalog and found good agreement.

Ancillary IRAS Photometry

IRAS photometry was obtained from the HIRES Atlas (Surace et al. 2004), the *IRAS* Revised Bright Galaxy Sample (Sanders et al. 2003), the *IRAS* Bright Galaxy Sample (Soifer et al. 1989), and the Faint Source Catalogue (Moshir & et al. 1990). The latter three catalogs present photometry derived from the native IRAS beam size of $2' - 5'$; this can be problematic for systems in close interaction phases. We therefore preferentially used the HIRES Atlas, which was reprocessed with $30'' - 1\farcm5$. In the one system

[7]NASA/IPAC Infrared Science Archive is operated by the Jet Propulsion Laboratory, California Institute of Technology, under contract with NASA.

where only low-resolution photometry is available and the galaxies are close enough for contamination to occur, we do not include the IRAS photometry in our analysis.

Table 2.2. Description of *Spitzer* IRAC Observations

Galaxy	PID	Date	Exposure/Band	Pipeline
NGC 2976	159	2004 Oct 29−30	30×30 s	13.2.0
NGC 3031	159	2004 May 1	240×30 s	13.0.2
NGC 3034	159	2005 May 6−9, Oct 25	120×30 s	14.0.0
NGC 3077	59	2004 Mar 8	8×12 s	18.18.0
	40204	2007 Nov 15	30×30 s	18.18.0
NGC 3185	40936	2007 Dec 23	8×12 s	18.18.0
NGC 3185/3187/3190	159	2004 Apr 28	48×30 s	13.0.2
NGC 3226/3227	3269	2004 Dec 21	2×12 s	13.2.0
	1054	2003 Nov 26	48×12 s	13.2.0
NGC 3395/3396	20671	2006 Dec 29	24×12 s	18.7.0
NGC 3424/3430	20140	2006 Jun 1	30×12 s	14.0.0
NGC 3448/UGC 6016	3247	2004 Dec 16	72×12 s	14.0.0
NGC 3690/IC 694	32	2003 Dec 18	120×12 s	13.2.0
NGC 3786/3788	3247	2004 Dec 17	46×12 s	14.0.0
NGC 4038/4039	32	2003 Dec 24	100×12 s	13.2.0
NGC 4618/4625	69	2004 May 21	10×30 s	13.2.0
	159	2004 May 18, May 21	16×30 s	13.2.0
NGC 4647/4649	69	2004 Jun 10	10×12 s	13.2.0
M51	159	2004 May 18, May 22	108×30 s	13.2.0
NGC 5394/5395	3672	2005 Jan 21	10×30 s	18.7.0
M101	60	2004 Mar 8	338×12 s	13.2.0
NGC 5474	159	2004 May 18, May 22	62×30 s	13.2.0

Table 2.3. Description of *Spitzer* MIPS Observations

Galaxy	PID	Date	Mode	Exposure Time	Pipeline
NGC 2976	159	2004 Oct 16	Scan	169.8 s	14.4.0
NGC 3031	159	2003 Nov 24	Scan	175.8 s	14.4.0
NGC 3034	159	2004 Nov 11	Scan	152.5 s	14.4.0
NGC 3077	59	2004 Mar 16	Phot	159.3 s	18.13.0
GC 3185					
NGC 3185/3187/3190	159	2004 Dec 28	Scan	173.3/156.2/176.6 s	14.4.0
NGC 3226/3227	1054	2003 Nov 24	Phot	593.4 s	14.4.0
NGC 3395/3396	20140	2005 Dec 3	Phot	226.4 s	14.4.0
NGC 3424/3430	50696	2008 Jun 21−23	Phot	220.1/542.3 s	18.13.0
NGC 3448/UGC 6016	3247	2007 Jun 19	Phot	557.8 s	14.4.0
NGC 3690/IC 694	32	2005 Jan 2	Phot	79.6 s	14.4.0
NGC 3786/3788	3247	2005 May 12	Phot	557.8 s	14.4.0
NGC 4038/4039	32	2005 Jan 25	Scan	87.1 s	14.4.0
NGC 4618/4625	69	2004 Jun 3	Phot	754.6/278.9 s	14.4.0
	159	2004 Dec 26−Jan 2	Scan	176.6/165.7 s	14.4.0
NGC 4647/4649	69	2005 Jun 26	Phot	139.4/278.9 s	18.12.0
M51	159	2004 Jun 22	Scan	175.8/174.5 s	14.4.0
NGC 5394/5395	3247	2005 Jan 25	Phot	557.8 s	14.4.0
M101	60	2007 Jun 19	Scan	176.5 s	14.4.0
NGC 5474	159	2004 Dec 26	Scan	162.1 s	18.12.0

Note. — MIPS exposures are determined differently based on the observing mode. For galaxies observed in the Phot mode, we give the total exposure time of the frames covering the galaxy. For galaxies observed in the Scan mode, we give the average observing time on the galaxy.

Table 2.4. Description of *Herschel* Observations

Galaxy	Instrument	ObsID	Date	Obs. Mode	Exposure (s)	PACS Bands
NGC 2976	SPIRE	1342192106	2010 Mar 11	Large Map	1076	
	PACS	1342207170-73	2010 Oct 26	Scan Map	3624	75 μm, 110 μm, 170 μm
NGC 3031	SPIRE	1342185538	2009 Oct 6	Large Map	5042	
	PACS	1342186085-86	2009 Oct 17	Scan Map	22208	75 μm, 170 μm
NGC 3034	SPIRE	1342185537	2009 Oct 6	Large Map	2418	
	PACS	1342209350-51	2010 Nov 10	Scan Map	6542	75 μm, 170 μm
NGC 3077	SPIRE	1342193015	2010 Mar 28	Large Map	2095	
	PACS	1342216507-10	2011 Mar 21	Scan Map	7356	75 μm, 110 μm, 170 μm
NGC 3185/3187/3190	SPIRE	1342196668	2010 May 18	Large Map	1035	
NGC 3187/3190	PACS	1342207145-48	2010 Oct 25	Scan Map	2708	75 μm, 110 μm, 170 μm
NGC 3226/3227	SPIRE	1342197318	2010 May 30	Large Map	2624	
	PACS	1342221146-47	2010 May 16	Scan Map	1178	75 μm, 170 μm
NGC 3395/3396	SPIRE	1342209286	2010 Nov 9	Large Map	999	
	PACS	1342221104-07	2011 May 16	Scan Map	2564	75 μm, 110 μm, 170 μm
NGC 3424/3430	SPIRE	1342195946	2010 May 8	Large Map	1618	
NGC 3448/UGC 6016	SPIRE	1342185539	2009 Oct 6	Large Map	1833	
NGC 3690/IC 694	SPIRE	1342199344	2010 Jun 29	Large Map	459	
	PACS	1342210600-05	2010 Nov 30	Scan Map	2462	75 μm, 110 μm, 170 μm
	PACS	134211104-05	2010 Dec 13	Scan Map	524	110 μm, 170 μm
NGC 3786/3788	SPIRE	1342223233	2011 Jun 28	Small Map	169	
	PACS	1342223319-20	2011 Jun 29	Scan Map	104	75 μm, 170 μm
NGC 4038/4039	SPIRE	1342188686	2009 Dec 29	Large Map	710	
	PACS	1342187836-39	2009 Dec 8	Scan Map	2662	75 μm, 110 μm, 170 μm
NGC 4618/4625	SPIRE	1342188755	2009 Dec 31	Large Map	1052	
NGC 4625	PACS	1342210468-71	2010 Nov 19	Scan Map	2708	75 μm, 110 μm, 170 μm
NGC 4647/4649	SPIRE	1342188778	2009 Dec 31	Large Map	4295	
M51	SPIRE	1342188589	2009 Dec 26	Large Map	1577	
	PACS	1342188328-29	2009 Dec 20	Scan Map	4422	75 μm, 170 μm
NGC 5394/5395	SPIRE	1342236140	2012 Jan 1	Large Map	1253	
	PACS	1342211285-88	2010 Dec 17	Scan Map	2200	75 μm, 110 μm, 170 μm
M101	SPIRE	1342188750	2009 Dec 30	Large Map	9443	
	PACS	1342198471-74	2010 Jun 16−17	Scan Map	38077	75 μm, 110 μm, 170 μm
NGC 5474	SPIRE	1342188751	2009 Dec 26	Large Scan	1052	
	PACS	13422077178-81	2010 Oct 26	Scan Map	2708	75 μm, 110 μm, 170 μm

2.3.3 Ultraviolet Photometry

GALEX Observations

Twenty-eight of our sample galaxies were observed by *GALEX*; three sources within the sample (NGC 3226, NGC 3227, and NGC 3077), however, were not observed due to the presence of nearby bright stars. For the galaxies with *GALEX* photometry, mosaics of the longest observations were retrieved from the Mikulski Archive for Space Telescopes using GalexView version 1.4.6. The details of those observations are given in Table 2.5. The NUV observation of NGC 3690/IC 694 was reprocessed by D. Neill at our request to correct a masking problem. We use the conversions from count rate to fluxes provided by Goddard Space Flight Center.[8]

Swift UVOT Observations

Most of the gaps in the *GALEX* coverage can be filled in with data from the *Swift* UVOT telescope, which has three UV filters that bracket the *GALEX* NUV filter in mean wavelength. Two of the three galaxies lacking *GALEX* data, NGC 3226 and NGC 3227, were observed by UVOT. Unfortunately, NGC 3077's nearby bright star exceeded the tolerances of this telescope as well. We originally planned to use existing UVOT photometry for all our sample. We obtained the raw data and exposure maps from the Swift archive for the seventeen galaxies with UVOT data and coadded the observations into one mosaic and exposure map per UV filter per interacting system. However, as described by Hoversten et al. (2011), the photon-counting nature of the *Swift*

[8]http://galexgi.gsfc.nasa.gov/docs/galex/FAQ/counts_background.html

detectors makes them vulnerable to coincidence losses, which become significant when the count rate is greater than 0.007 counts per second per pixel. We calculated count rate maps to determine where coincidence losses need to be taken into account. Due the difficulties associated with coincidence losses in extended sources, described in greater length in Appendix B, we opted only to use the UVOT data for the missing *GALEX* objects NGC 3226 and NGC 3227. We added one test case, NGC 3424, to confirm that the UVOT data yielded fluxes consistent with *GALEX* and found good agreement. The details of the observations of these three galaxies are given in Table 2.6. To convert the count rate to fluxes, we used the conversion assuming a stellar spectrum described in Breeveld et al. (2010).

Table 2.5. Description of *GALEX* Observations

Galaxy	Tilename	NUV		FUV	
		Date	Exposure (s)	Date	Exposure (s)
NGC 2976	GI2_024002_NGC2976_stream	2006 Jan 04	18113.55	2006 Jan 04	17212.50
NGC 3031	GI1_071001_M81	2005 Jan 12	29421.55	2006 Jan 05	14706.70
NGC 3034	NGA_M82	2009 Jan 31	17311.95	2009 Jan 31	11527.35
NGC 3185/3187/3190	NGA_NGC3190	2004 Jan 30	3545.80	2005 Feb 19	1299.15
NGC 3395/3396/3424/3430	GI1_078004_NGC3395	2006 Mar 23	2666.15	2006 Mar 23	1500.10
NGC 3448/UGC 6016	AIS_92	2004 Feb 4	423.00	2004 Apr 21	143.00
NGC 3690/IC 694	AIS_99	2007 Feb 13	211.00	2007 Feb 13	211.00
NGC 3786/3788	AIS_111	2007 Feb 20	103.05	2007 Feb 20	103.05
NGC 4038/4039	NGA_Antennae	2004 Feb 22	1541.30	3004 Feb 22	1541.30
NGC 4618/4625	NGA_NGC 4625	2004 Apr 5	3259.00	2004 Apr 5	3259.00
NGC 4647/4649	GI1_109003_NGC4660	2005 Apr 30	3113.25	2008 Apr 23	1624.10
M51	GI3_050006_NGC5194	2007 May 29	10216.20	2007 May 29	10216.20
NGC 5394/5395	GI1_026018_Arp84	2006 Apr 12	4268.65	2007 May 30	2811.40
M101	GI3_050008_NGC5457	2008 Apr 4	13294.40	2008 Apr 4	13293.4
NGC 5474	NGA_NGC5474	2003 Jun 19	1610.00	2003 Jun 19	1610.10

Table 2.6. Description of *Swift* UVOT Observations

Galaxy	ObsID	Date	Exposure Times (s) UVW2	UVM2	UVW1
NGC 3226/3227	00031280001	2008 Nov 4	342	249	352
NGC 3226/3227	00031280002	2008 Nov 5	704	511	346
NGC 3226/3227	00031280003	2008 Nov 12	692	424	372
NGC 3226/3227	00031280004	2008 Nov 13	744	538	372
NGC 3226/3227	00031280005	2008 Nov 21	744	522	381
NGC 3226/3227	00031280006	2008 Nov 22	763	137	381
NGC 3226/3227	00031280007	2008 Nov 25	763	531	381
NGC 3226/3227	00031280008	2008 Nov 27	763	196	246
NGC 3226/3227	00031280009	2008 Dec 2	0	0	293
NGC 3226/3227	00031280010	2008 Dec 3	274	349	126
NGC 3424/3430	00091132001	2011 Apr 16	0	0	1976
NGC 3424/3430	00091132003	2011 Jun 28	0	0	0
NGC 3424/3430	00091132004	2011 Jul 4	0	80	1315
NGC 3424/3430	00091132005	2011 Jul 7	302	0	0
NGC 3424/3430	00091132006	2011 Jul 8	0	1877	0
NGC 3424/3430	00091132007	2011 Oct 7	750	988	0
NGC 3424/3430	00091132008	2011 Oct 10	0	0	0

Note. — The *Swift* observation ID number (Column 2) and the start date of each observation (Column 3) are given for each observation of each object for which observations with minimal coincidence losses exist. Exposure times in the each filter are given in Columns 4−6.

2.3.4 Aperture and Uncertainty Determination

For consistency, we used matched apertures across all wavebands in our photometric analysis. Generally, the IR emission of galaxies is more extended that their UV emission. However, some of the galaxies are more extended in the UV than in the IR (e.g. NGC 3430). We used the SExtractor algorithm (Bertin & Arnouts 1996) to determine Kron apertures in both the NUV and the 3.6 μm IRAC images. In all cases, the larger of the two apertures was then used to measure the integrated galaxy flux at all wavelengths in order to obtain flux from a consistent area of each galaxy across our wavelength range. The size and position angle of each aperture as well as on which image it was determined is given in Table 2.1. Background regions were selected to mimic the content of background and foreground objects in the aperture on the outskirts of the galaxies. Once the aperture was selected, flux densities in the aperture and background regions were measured using the analysis tools of the SAOImage DS9 (Joye & Mandel 2003).

Due to the proximity of some members of the same interacting system, their apertures can overlap. We dealt with these situations in one of three ways. For significantly overlapping systems (NGC 4038/4039, NGC 3690/IC 694, and NGC 3395/3396), separate apertures could not be robustly determined. In these cases, we treated the combined system as a single object. Second, there were two systems (M51 A/B and NGC 5394/5495) where the aperture for the smaller galaxy was mostly contained within the aperture of the larger galaxy, but it was clear that the emission in the overlap area came from the smaller galaxy. In these cases, we subtracted the emission and area of the overlap region from that of the larger aperture. Third, there were three systems (NGC 3226/3227, NGC 3786/3788, and NGC 4647/4649) where the aperture overlapped

but without significant contamination. In these cases, we extrapolated the expected flux in the overlap area from the surface brightness in the rest of the elliptical aperture at the same radii.

The *Spitzer* fluxes required aperture corrections. We determined the effective radius of the elliptical aperture[9] and used the extended source flux corrections given in the IRAC Instrument Handbook.[10] For the MIPS 24 μm aperture corrections, we interpolated between the aperture corrections given in the MIPS Instrument Handbook.[11] The *GALEX* data were corrected for obscuration due to Milky Way dust using the extinction laws given by Wyder et al. (2005).

Uncertainties in the absolute fluxes are the sum in quadrature of a statistical uncertainty and a calibration uncertainty. The *Spitzer* bandpass uncertainties are typically dominated by the calibration uncertainty of 3% for IRAC (Cohen et al. 2003) and 4% for MIPS 24 μm (Engelbracht et al. 2007). We used a calibration uncertainty of 10% for the *GALEX* data (Center 2004) and a 5%−15% uncertainty for the *Swift* bands (Poole et al. 2008), and the statistical uncertainty is calculated using Poisson statistics. We used a 7% calibration uncertainty for the SPIRE bandpasses (Swinyard et al. 2010) and 10% for the PACS bandpasses (Paladini et al. 2012) and followed Dale et al. (2012) in calculating the statistical uncertainty. The photometry results for *GALEX*, *Swift*, and

[9] $r_{\rm eff} = \sqrt{ab}$ for semi-major axis a and semi-minor axis b

[10] http://irsa.ipac.caltech.edu/data/SPITZER/docs/irac/iracinstrumenthandbook/30/

[11] http://irsa.ipac.caltech.edu/data/SPITZER/docs/mips/mipsinstrumenthandbook/50/

2MASS; *Spitzer*; and *Herschel* are provided in Tables 2.7−2.9, respectively. When flux is not determined significantly, we provide 3σ upper limits, but we do not provide lower limits in cases of saturated images. The additional photometry from the literature is given in Table 2.10.

Table 2.7. *GALEX, Swift*, and 2MASS Photometry

Galaxy	*GALEX* FUV (mJy)	*GALEX* NUV (mJy)	*Swift* UVW2 (mJy)	*Swift* UVM2 (mJy)	*Swift* UVW1 (mJy)	2MASS *J* (mJy)	2MASS *H* (mJy)	2MASS *Ks* (mJy)
NGC 2976	24.85±2.49	38.70±3.87	...	...	...	766.4±36.6	854.5±55.6	678.3±60.2
NGC 3031	175.5±17.6	274.2±27.4	...	...	...	19730±730	23760±960	19770±810
NGC 3034	8.57±0.86	35.29±3.53	...	...	...	6614±230.	8972±322	8550.±304
NGC 3077	...	...	...	...	...	832.4±32.0	941.5±39.7	745.9±35.2
NGC 3185	2.05±0.21	2.27±0.23	...	...	...	172.5±9.6	200.0±15.5	170.9±16.9
NGC 3187	3.28±0.33	4.49±0.45	...	...	...	51.05±8.68	81.91±14.54	53.14±16.01
NGC 3190	0.40±0.04	1.81±0.18	...	...	...	626.8±22.9	792.1±30.3	684.8±27.6
NGC 3226	...	...	0.86±0.09	0.80±0.12	2.65±0.39	254.2±10.5	269.9±13.3	232.2±12.8
NGC 3227	...	...	4.37±0.47	4.10±0.60	9.47±0.46	523.9±19.9	607.5±25.4	526.7±23.4
NGC 3395/3396	19.15±1.92	27.67±2.77	...	...	...	155.1±10.5	184.1±18.8	159.4±15.5
NGC 3424	0.91±0.09	2.69±0.27	1.85±0.20	1.70±0.25	3.61±0.18	163.6±7.2	206.3±9.9	174.9±9.7
NGC 3430	8.38±0.84	12.42±1.24	...	...	...	224.4±13.2	231.7±18.2	165.7±18.3
NGC 3448	5.67±0.58	8.96±0.90	...	...	...	106.0±6.59	116.4±11.1	103.4±9.8
UGC 6016	1.20±0.13	1.34±0.14	...	...	...	< 17.2	< 23.1	< 20.5
NGC 3690/IC 694	10.15±1.03	15.70±1.57	...	...	...	222.4±9.5	300.2±14.5	285.3±13.0
NGC 3786	0.97±0.11	1.85±0.19	...	...	...	110.9±5.2	135.4±8.8	118.3±7.4
NGC 3788	1.61±0.18	2.98±0.30	...	...	...	117.6±5.0	139.8±8.3	120.5±7.0
NGC 4038/4039	34.15±3.42	55.10±5.51	...	...	...	927.6±44.7	1126±62	915.7±76.2
NGC 4618	27.69±2.77	39.19±3.92	...	...	...	326.8±30.7	318.0±50.7	245.9±45.3
NGC 4625	4.83±0.48	7.30±0.73	...	...	...	90.41±14.42	111.5±22.3	76.6±24.3
NGC 4647	4.66±047	10.00±1.00	...	...	...	473.4±21.2	528.1±25.7	441.9±28.0
NGC 4649	3.80±0.38	7.29±0.73	...	...	...	2694±94	3290.±119	2713±99
M51A	116.1±11.6	202.5±20.3	...	...	...	4285±165	5343±243	4213±255
M51B	6.75±0.68	12.65±1.27	...	...	...	1895±69	2374±91	1915±78
NGC 5394	0.61±0.06	1.48±0.15	...	...	...	62.17±2.98	77.30±4.45	66.69±5.08
NGC 5395	2.91±0.29	5.70±0.57	...	...	...	250.9±11.3	301.5±16.7	247.6±18.9
M101	338.1±33.8	452.9±45.3	...	...	...	3711±338	4279±551	3893±569
NGC 5474	19.47±1.95	25.91±2.59	...	...	...	228.7±32.0	231.9±47.7	172.4±57.9

Note. — The upper limits given are 3σ upper limits.

Table 2.8. *Spitzer* IRAC and MIPS Photometry

Galaxy	3.6 μm (mJy)	4.5 μm (mJy)	5.8 μm (mJy)	8.0 μm (mJy)	24 μm (mJy)
NGC 2976	393.2±11.8	269.1±8.1	476.6±14.3	957.7±28.7	1454±58
NGC 3031	9936±298	6146±492	5217±417	6329±506	6011±240
NGC 3034	6564±197	5223±157	...	...	...
NGC 3077	373.3±11.2	267.3±8.0	298.1±9.0	571.1±17.1	1752±53
NGC 3185	76.44±2.29	50.53±1.52	52.95±1.60	115.0±3.5	192.3±7.7
NGC 3187	22.51±0.68	16.09±0.48	26.48±0.80	62.56±1.88	91.48±3.66
NGC 3190	337.0±10.1	213.9±6.4	176.1±5.3	288.8±8.7	271.9±10.9
NGC 3226	122.2±3.7	76.34±2.29	48.92±1.47	44.26±1.33	37.10±1.48
NGC 3227	287.7±8.6	218.7±6.6	256.4±7.7	597.0±17.9	1769±71
NGC 3395/3396	87.62±2.63	61.30±1.84	145.1±4.4	423.2±12.7	1190.±48
NGC 3424	103.4±3.1	72.75±2.18	148.3±4.5	460.7±13.8	776.4±31.0
NGC 3430	116.0±3.5	78.97±2.37	110.2±3.3	372.0±11.2	434.7±17.4
NGC 3448	62.03±1.86	44.02±1.32	79.53±2.39	193.53±5.81	580.7±23.2
UGC 6016	1.52±0.05	0.90±0.03	< 8.0	2.13±0.15	4.00±0.13
NGC 3690/IC 694	293.2±8.8	347.6±10.4	841.0±25.2	...	18660±750
NGC 3786	32.61±0.98	21.07±0.63	27.69±0.83	66.39±1.99	266.5±10.7
NGC 3788	30.97±0.93	23.80±0.71	26.32±0.79	60.14±1.80	166.1±6.6
NGC 4038/4039	523.3±15.7	359.1±10.8	706.1±21.2	1757±53	6131±245
NGC 4618	152.2±4.6	97.15±2.91	157.6±4.7	327.5±9.8	394.3±15.7
NGC 4625	43.04±1.29	27.67±0.83	45.97±1.38	126.3±3.8	124.4±5.0
NGC 4647	195.3±5.9	124.3±3.7	222.2±6.9	553.0±16.6	612.9±24.5
NGC 4649	1202±36	711.6±21.4	449.6±13.5	280.0±8.4	126.9±5.1
M51A	2474±78	1662±54	3637±110.	10790±320	12520±510
M51B	965.9±37.9	632.9±28.0	667.5±25.9	1430.1±50.9	2149±94
NGC 5394	40.79±1.22	28.54±0.86	67.03±2.01	208.5±6.3	854.7±34.2
NGC 5395	141.0±4.2	95.16±2.85	143.0±4.3	404.4±12.1	444.1±17.8
M101	2373±71	1593±48	3056±92	7423±223	10610±425
NGC 5474	98.27±2.95	66.25±1.99	75.66±2.27	105.9±3.2	151.1±7.0

Note. — IRAC 5.8 μm, IRAC 8.0 μm, and MIPS 24 μm are saturated for NGC 3034, as is 8 μm for NGC 3690/IC 694. The upper limits are 3σ upper limits.

Table 2.9. *Herschel* PACS and SPIRE Photometry

Galaxy	PACS			SPIRE		
	75 μm (Jy)	110 μm (Jy)	170 μm (Jy)	250 μm (Jy)	350 μm (Jy)	500 μm (Jy)
NGC 2976	35.48±3.55	48.90±4.90	48.88±4.89	24.87±1.74	11.84±0.83	4.86±0.34
NGC 3031	67.56±6.86	...	351.5±35.2	161.5±11.3	78.75±5.51	32.98±2.31
NGC 3034	1985±198	...	1291±129	363.1±25.4	121.5±8.5	35.45±2.48
NGC 3077	22.52±3.38	32.12±4.82	23.77±3.57	8.54±0.60	3.36±0.24	1.18±0.08
NGC 3185	...	...	...	2.50±0.21	1.23±0.14	0.38±0.09
NGC 3187	2.20±0.39	5.52±0.89	3.87±0.62	2.37±0.17	1.39±0.10	0.69±0.05
NGC 3190	6.98±1.06	12.29±1.87	16.86±2.54	8.06±0.56	3.45±0.24	1.20±0.08
NGC 3226	0.22±0.05	...	2.59±0.27	0.81±0.06	0.30±0.02	0.10±0.01
NGC 3227	11.87±1.19	...	22.33±2.24	10.96±0.77	4.43±0.31	1.50±0.11
NGC 3395/3396	12.94±1.45	16.49±1.78	17.19±1.75	6.95±0.49	2.93±0.21	1.06±0.08
NGC 3424	...	...	...	8.15±0.57	3.37±0.24	1.13±0.08
NGC 3430	...	...	...	8.07±0.57	3.61±0.25	1.38±0.10
NGC 3448	...	...	...	4.68±0.33	2.11±0.15	0.84±0.06
UGC 6016	...	...	...	0.10±0.02	0.060±0.014	0.014±0.002
NGC 3690/IC 694	139.3±13.9	126.7±12.7	74.19±7.42	21.34±1.49	7.37±0.52	2.22±0.16
NGC 3786	2.30±0.25	...	3.93±0.42	1.97±0.14	0.83±0.06	0.27±0.02
NGC 3788	2.02±0.22	...	6.83±0.70	3.29±0.23	1.41±0.10	0.49±0.04
NGC 4038/4039	80.95±8.11	116.0±11.6	99.79±9.98	37.57±2.63	14.82±1.04	5.01±0.35
NGC 4618	...	...	...	8.61±0.60	4.19±0.29	1.71±0.12
NGC 4625	2.94±0.31	2.87±0.33	4.86±0.50	2.40±0.17	1.16±0.08	0.47±0.40
NGC 4647	...	...	...	11.12±0.78	4.60±0.32	1.56±0.11
NGC 4649	...	...	...	< 0.09	< 0.09	< 0.06
M51A	181.1±18.1	...	441.4±44.1	184.2±12.9	74.22±5.20	25.38±1.78
M51B	24.63±2.47	...	53.72±5.37	20.71±1.45	8.22±0.58	2.72±0.19
NGC 5394	6.04±0.61	8.31±0.83	8.27±0.83	2.95±0.21	1.06±0.07	0.33±0.02
NGC 5395	7.30±0.76	11.03±1.12	16.28±1.64	8.73±0.61	3.80±0.27	1.39±0.10
M101	97.05±14.56	265.0±39.8	373.4±56.0	172.6±12.1	79.91±5.60	31.66±2.22
NGC 5474	2.84±0.28	5.81±0.58	9.08±0.908	3.55±0.26	1.97±0.15	0.86±0.08

Table 2.10. Literature Photometry

Galaxy	Third Reference Catalogue			IRAS				Ref.	MIPS	
	U (mJy)	B (mJy)	V (mJy)	12 μm (Jy)	25 μm (Jy)	60 μm (Jy)	100 μm (Jy)		70 μm (Jy)	160 μm (Jy)
NGC 2976	85.10±10.90	200.0±25.5	314.0±40.1	0.92±0.02	1.71±0.02	13.09±0.29	33.43±0.34	(2)	20.43±4.34[a]	53.56±12.28
NGC 3031	...	2970.±83	6100.±180.	5.86±0.88	5.42±0.81	44.73±6.71	174.02±26.10	(2)	85.18±18.05	360.0±84.1
NGC 3034	259.0±23.70	812.0±70.2	1570.±137.	79.43±7.94	332.6±33.3	1480.±148	1374.±137.	(2)	...	...
NGC 3077	90.70±11.70	243.0±30.9	418.0±53.3	0.76±0.02	1.88±0.03	15.90±0.04	26.53±0.13	(2)	...	...
NGC 3185	...	27.10±1.81	49.30±4.07	0.15±0.04[b]	0.14±0.04[b]	1.43±0.09	3.67±0.22	(4)	...	...
NGC 3187	5.94±0.73	11.60±1.24	15.30±1.74	...	...	...	...		...	...
NGC 3190	16.50±1.63	60.50±5.83	126.0±12.2	0.32±0.03[c]	0.35±0.08[c]	3.19±0.35[c]	10.11±0.51[c]	(4)	5.66±1.20	15.01±3.51
NGC 3226	...	51.20±10.14	100.0±21.0	<0.27	<0.18	<0.60	...	(1)	...	...
NGC 3227	51.30±10.60	155.0±31.3	281.0±57.6	1.11±0.12	2.04±0.21	9.01±1.00	19.11±2.00	(1)	...	...
NGC 3395/3396	...	...	...	0.47±0.03	1.47±0.04	10.92±0.03	17.83±0.10	(2)	...	...
NGC 3424	...	...	...	0.59±0.04	0.94±0.04	9.03±0.09	17.03±0.21	(1)	...	...
NGC 3430	21.60±4.51	56.20±11.40	87.30±17.80	0.38±0.08	0.78±0.05	4.36±0.07	10.88±1.00	(1)	...	...
NGC 3448	22.00±2.83	43.40±5.52	55.10±7.03	0.34±0.11[b]	0.76±0.21[b]	6.74±0.35	12.17±0.47	(1)	...	...
UGC 6016	...	...	...	<0.10	<0.15	<0.50	<0.50	(1)	...	...
NGC 3690/IC 694	...	...	...	3.90±0.40	24.14±2.40	121.64±12.50	122.45±12.50	(1)	...	....
NGC 4038/4039	...	...	...	1.94±0.04	6.54±0.03	45.16±0.06	87.09±0.20	(2)	...	...
NGC 4618	70.10±2.95	139.0±5.2	178.0±6.9	0.40±0.03	0.45±0.04	4.92±0.04	13.05±0.17	(3)	...	...
NGC 4625	14.50±0.88	28.90±1.09	41.80±1.76	0.12±0.03[b]	0.19±0.04	1.20±0.13	3.58±0.25	(4)	2.06±0.44	5.42±1.28
NGC 4647	23.20±2.91	71.40±5.46	111.0±8.8	0.76±0.08	1.06±0.16	6.04±0.24	17.56±0.81	(1)	...	...
NGC 4649	...	508.0±23.9	1060.±509	0.33±0.05	<0.32	<0.24	<1.05	(1)	...	...
M51A	...	1110.±63	1650.±95	7.21±0.08	9.56±0.08[a]	97.42±0.19	221.2±0.3	(2)	147.1±31.3	494.7±113.1
M51B	89.90±6.23	282.0±18.7	551.0±37.1	0.35±0.02[a]	1.02±0.05[a]	15.22±0.80	31.33±0.37	(2)	16.31±4.61	14.86±2.97[a]
NGC 5394	5.37±1.16	14.10±2.85	22.80±4.66	0.52±0.05	1.19±0.11	5.62±1.41[b]	10.43±3.10[b]	(1)	...	...
NGC 5395	23.90±5.06	61.60±12.50	103.0±21.1	0.40±0.04	0.48±0.06	6.86±1.50	14.21±3.10	(1)	...	...
M101	...	2020.±175	2610.±248	6.20±0.93	11.78±1.77	88.04±13.21	253.0±38.0	(2)	...	...
NGC 5474	...	131.0±19.4	176.0±27.6	<0.88	<0.76	1.33±0.07	4.80±0.24	(4)	3.73±0.27[a]	10.56 ±2.47

Note. — The IRAS fluxes are from (1)the HIRES Atlas (Surace et al. 2004), (2) the IRAS Revised Bright Galaxy Sample (Sanders et al. 2003), (3) the IRAS Bright Galaxy Sample (Soifer et al. 1989), and (4) the Faint Source Catalogue (Moshir & et al. 1990) obtained through NED. The MIPS 70 μm and 160 μm data come from Dale et al. (2007) with the exception of NGC 3031 (Dale et al. 2009) and NGC 3077 (Engelbracht et al. 2008). Upper limits were not used in the fits. NGC 3786 and NGC 3788 did not have any ancillary photometry.

[a]Not included in fits because differs significantly from other measurements. [b] Not included in fits because detection is less than 4σ.
[c] Not included in fits because IRAS fluxes likely contains more than one galaxy.

2.4 SED Fitting with MAGPHYS

2.4.1 Fitting Process

To estimate SFR, specific star formation rates (sSFRs), stellar and dust masses, and dust temperatures, we used the SED fitting code MAGPHYS (da Cunha et al. 2008). MAGPHYS fits SEDs with a combination of UV−NIR stellar spectral libraries from Bruzual & Charlot (2003) and a simple, physically-motivated model for IR emission from dust developed in da Cunha et al. (2008). It models the ISM as a mix of diffuse dust interspersed with denser, warmer stellar birth clouds. MAGPHYS also includes a set of UV−NIR libraries that modify the Bruzual & Charlot (2003) population synthesis with the Bruzual (2007) population synthesis, which provides different treatment of post-asymptotic giant branch (AGB) stars. We fit our UV to FIR SEDs with MAGPHYS with and without the post-AGB modifications and found consistent results; from here on, we only use the results with the earlier Bruzual & Charlot (2003) libraries as their treatment of the post-AGB stars is more consistent with current understanding (e.g., Zibetti et al. 2013). The IR dust libraries have five components: a fixed polycyclic aromatic hydrocarbon (PAH) spectrum shape derived from the M17 SW star-forming region (Madden et al. 2006), a NIR continuum associated with the PAH emission modeled by a modified blackbody ($\beta = 1$) at 850 K, a hot MIR continuum modeled by the sum of two modified blackbodies ($\beta = 1$) at 130 K and 250 K, a warm (30−60 K) dust component modeled as a modified blackbody ($\beta = 1.5$), and a cold (15−25 K) dust component modeled as a modified blackbody ($\beta = 2$). The warm dust component is assumed to exist both in the diffuse ISM and in denser birth clouds, while the cold dust exists only in the diffuse ISM. MAGPHYS determines probability distribution functions

(PDFs) for the fitted parameters by combining UV−NIR and IR spectral libraries such that the energy absorbed in the UV/visible regime is re-emitted in the IR. It gives both the best-fit obscured SED and the associated unobscured stellar SED.

We input the measured and literature fluxes in our set of 28 filters to MAGPHYS and examined the variation in derived galaxy properties including dust luminosity, SFR, sSFR, stellar and dust mass, and dust temperatures and discuss the results below. Then we performed five additional fits: one without UV photometry, one without SPIRE photometry, one without any photometry at wavelengths $\lambda \geq 30\,\mu$m, one without either UV or SPIRE photometry, and one with only UBV, 2MASS, and IRAC photometry. For these fits for each galaxy, we examined the median and 68% confidence interval for the fitted parameters to determine the influence of the particular dataset on the value of (and constraints on) these properties, as we elaborate below. For the non-interacting galaxies, we only performed the fit with all of the available photometry.

2.4.2 SED Fits

Figures 2.7 − 2.16 show the SEDs along with the best-fit models for our interacting galaxies. The contributions of the different components of the IR model described above are also shown. The median and 68% confidence interval of these parameters are given in Table 2.11. Just as the galaxies exhibit a variety of UV versus IR morphologies (Figures 2.1−2.6), the SEDs have a corresponding range of relative UV, NIR, and FIR emission. For example, some galaxies (e.g., NGC 3190 or M51B) have very little UV flux in comparison with their visible and IR flux, while others (e.g., NGC 3187) have almost as much UV flux as IR flux. The SEDs also show a range of obscuration from the heavily

obscured galaxies (e.g., NGC 3690) to relatively unobscured galaxies (e.g., NGC 4618), or ones with extended UV disks such as NGC 3430 or UGC 6016. Appendix C briefly describes each galaxy, discussing any particular issues regarding the photometry and the SED fitting. Note in particular that fits to edge-on galaxies tend to over-estimate the amount of UV obscuration and hence the model UV fluxes tend to be too low compared to the observations.

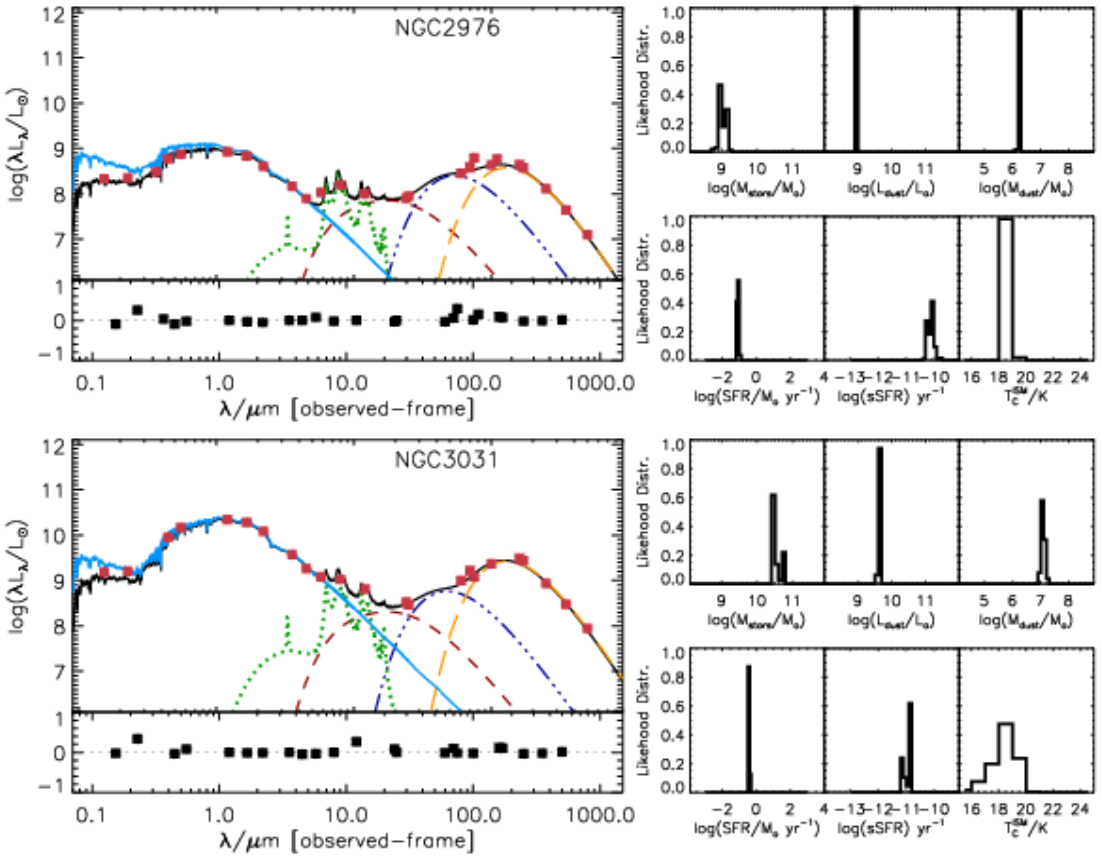

Figure 2.7: SEDs for NGC 2976 (top) and NGC 3031 (bottom) with data shown as red points, the best fit model plotted in black, and the stellar emission in the absence of dust shown in blue. The components of the infrared emission are over plotted: PAH emission (dotted, green line), MIR emission at 130 K and 250 K (red, dashed line), warm 30−60 K dust emission (dot-dashed, purple line), and cold 15−25 K dust emission (long dashed, orange line). Below the fitted SED is plotted the fractional difference between the model and data. To the right of the SED, we plot a subset of the probability distribution functions (PDFs) of the fitted parameters for (from left to right): stellar mass, dust luminosity, and dust mass (top) and SFR, sSFR, and cold dust temperature (bottom).

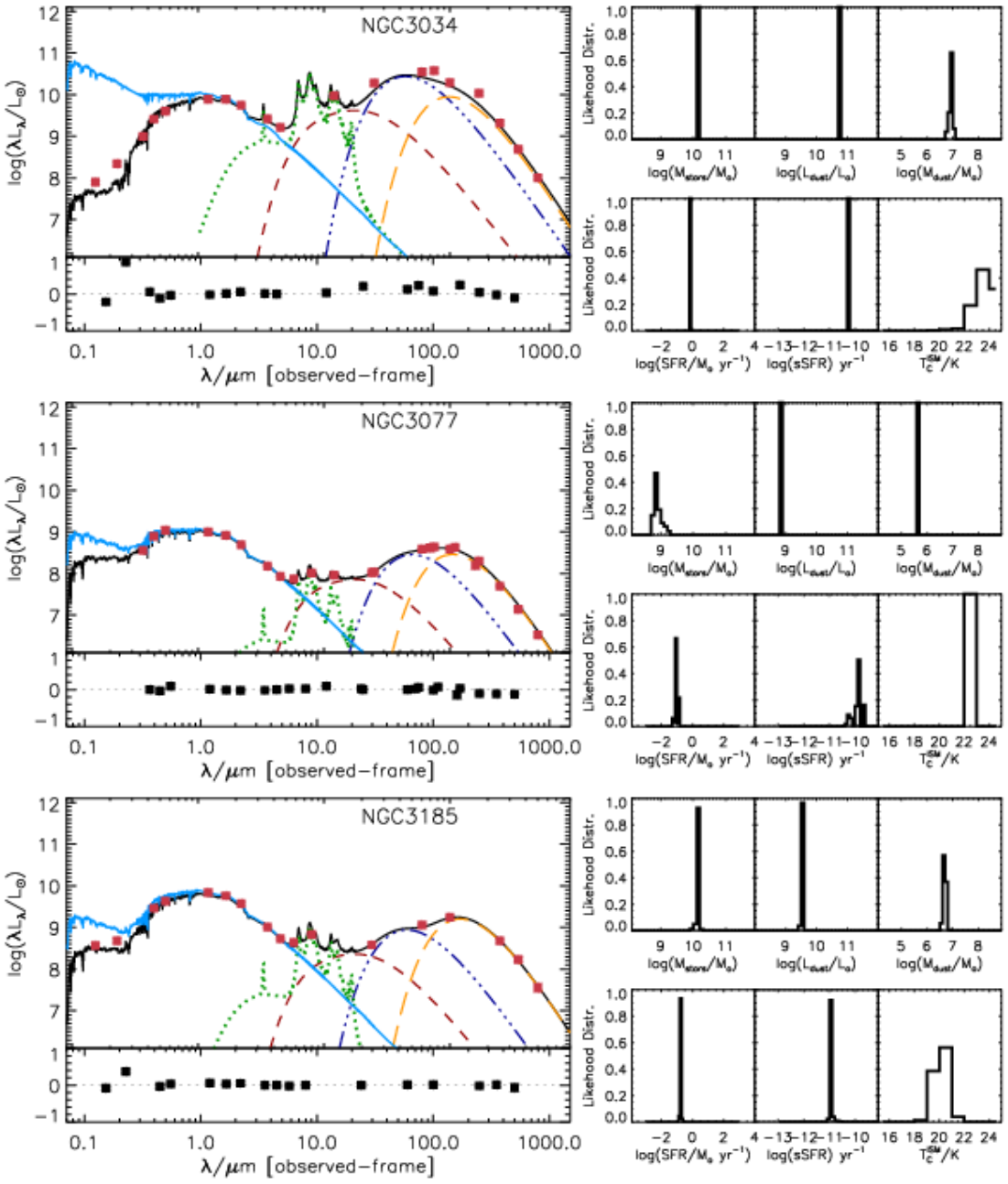

Figure 2.8: As Figure 2.7, but for NGC 3034 (top), NGC 3077 (middle), and NGC 3185 (bottom).

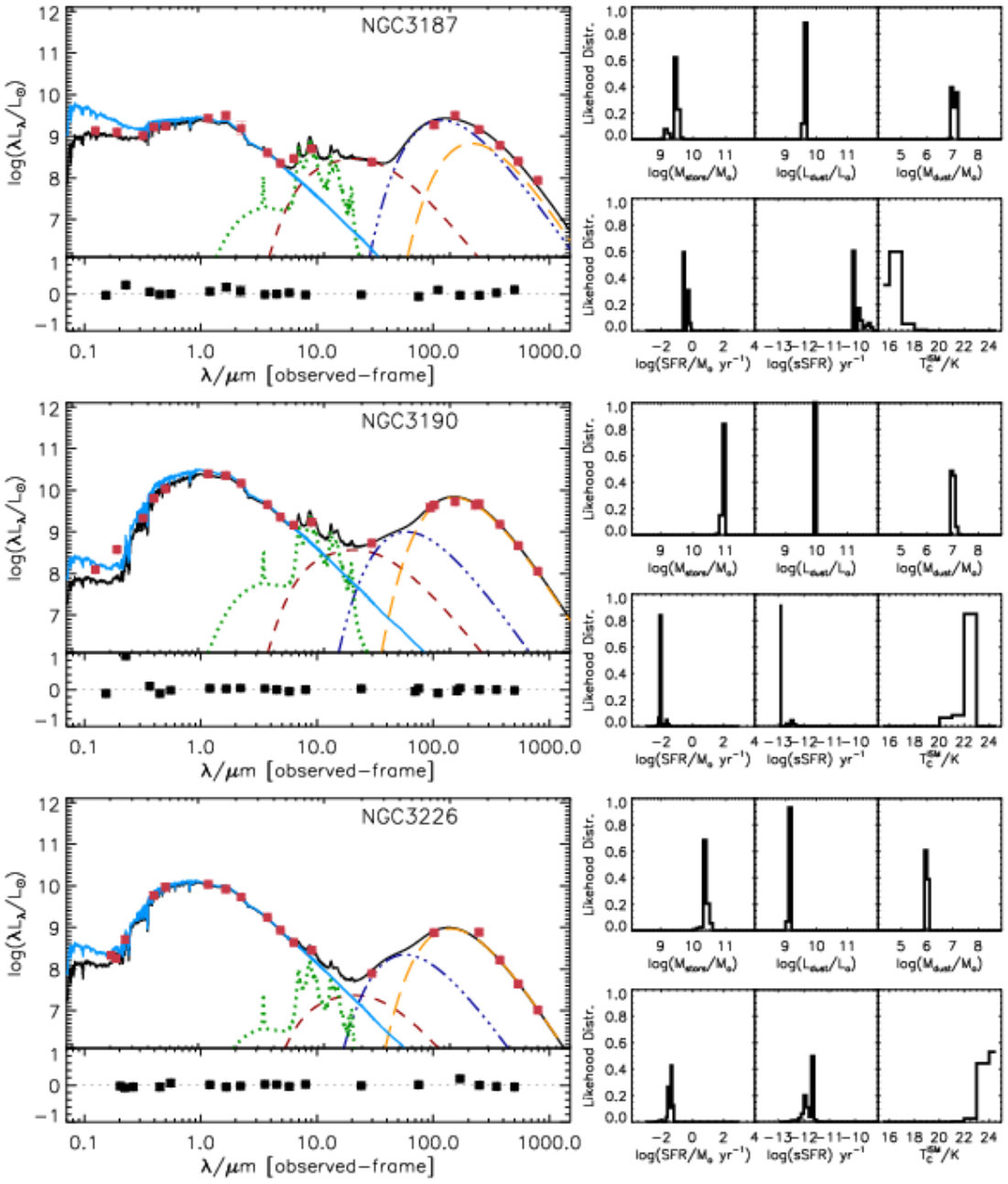

Figure 2.9: As Figure 2.7, but for NGC 3187 (top), NGC 3190 (middle), and NGC 3226 (bottom).

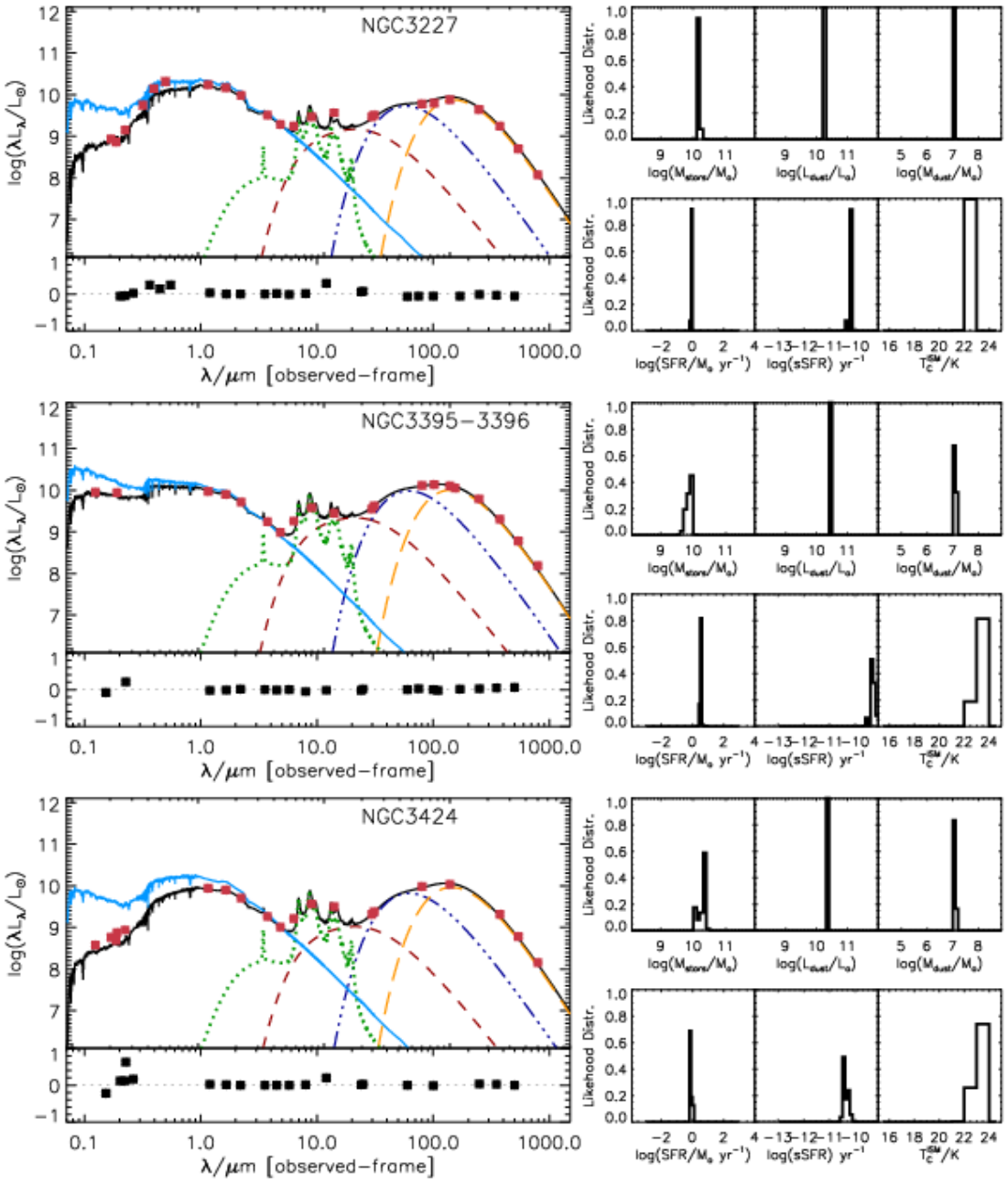

Figure 2.10: As Figure 2.7, but for NGC 3227 (top), NGC 3395/3396 (middle), and NGC 3424 (bottom).

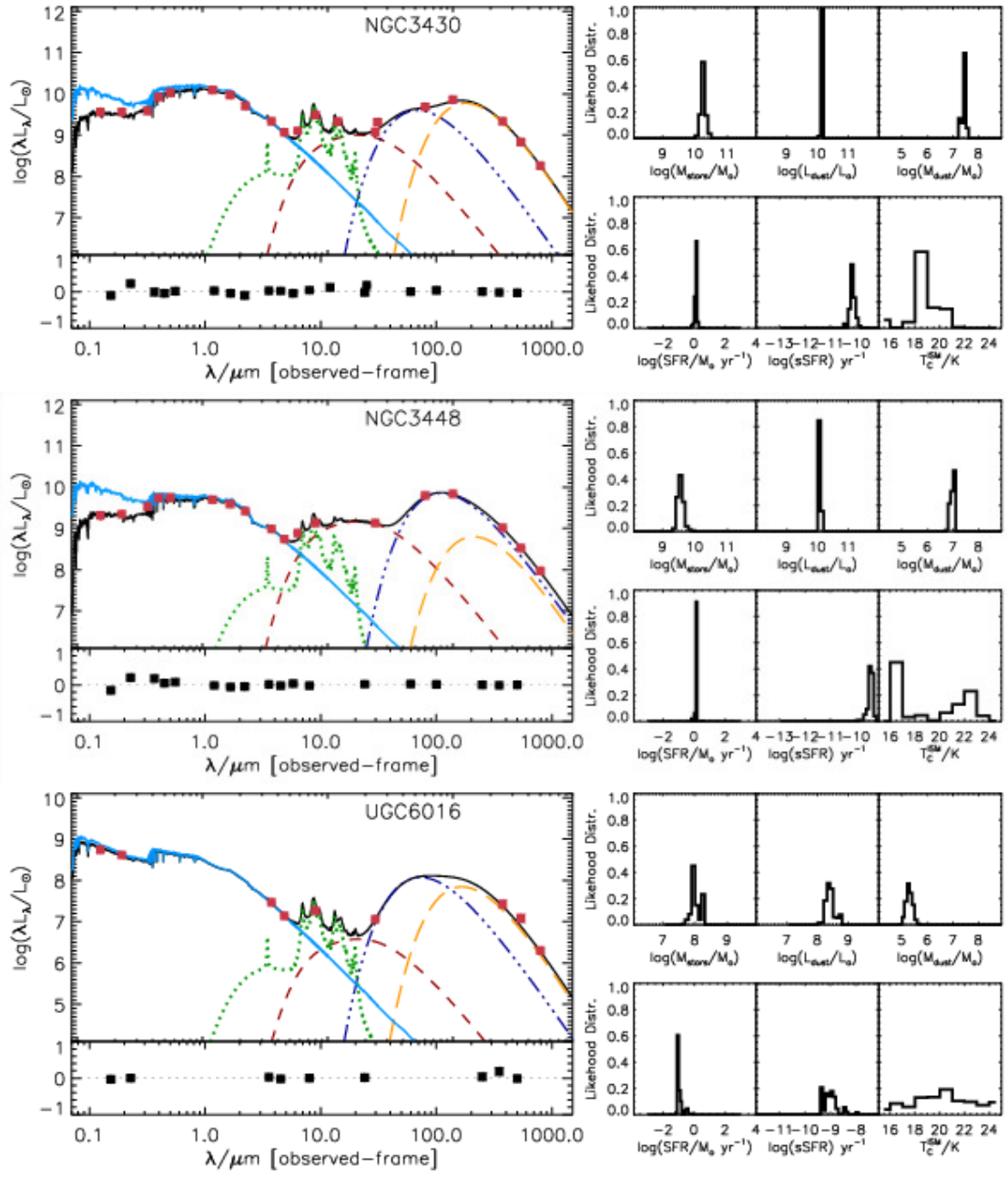

Figure 2.11: As Figure 2.7, but for NGC 3430 (top), NGC 3448 (middle), and UGC 6016 (bottom). Note that the axes of the UGC 6016 plots have smaller values than the rest of the plots.

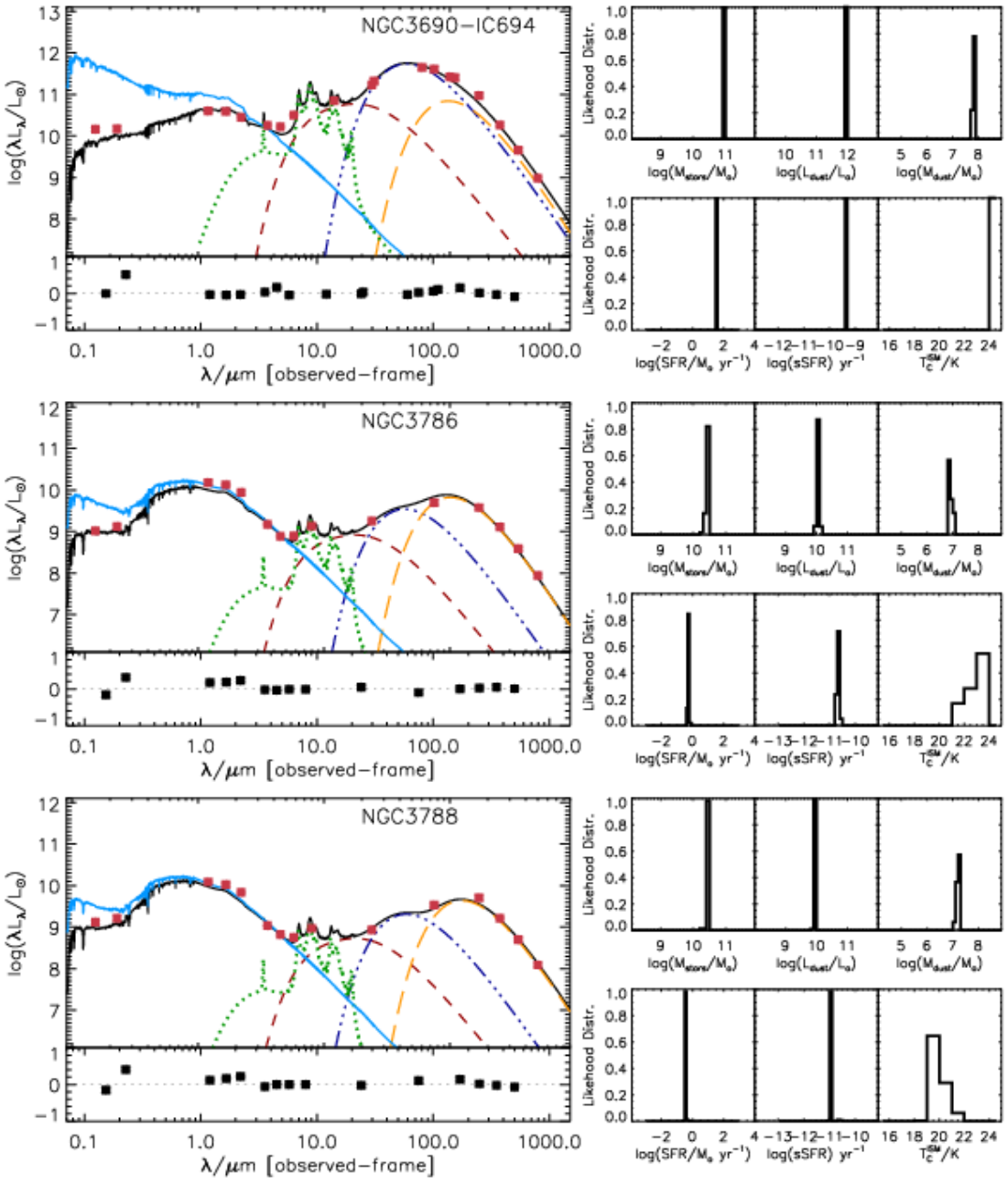

Figure 2.12: As Figure 2.7, but for NGC 3690/IC 694 (top), NGC 3786 (middle), and NGC 3788 (bottom). Note that the axes of the NGC 3690 plots have larger values than the rest of the plots.

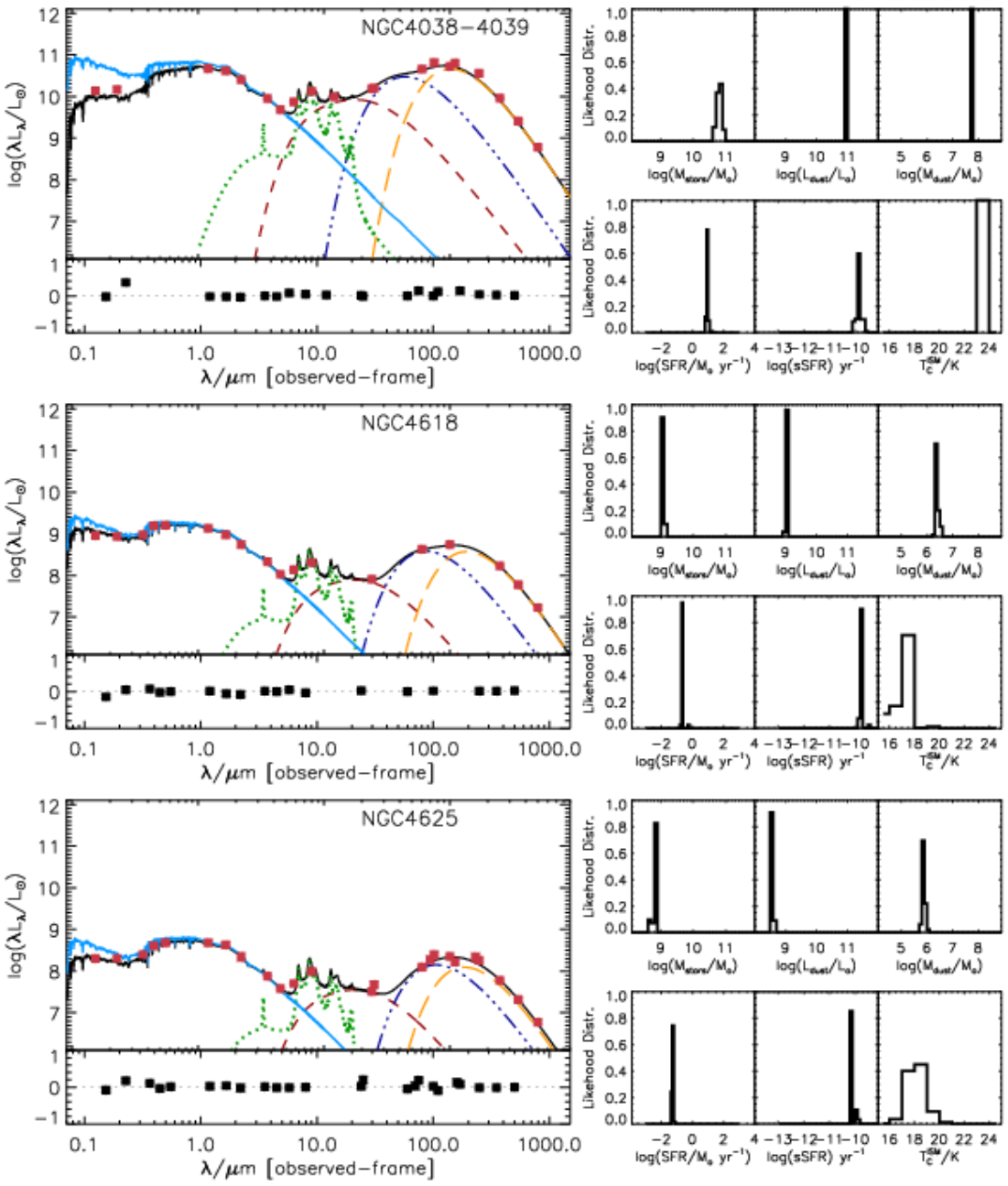

Figure 2.13: As Figure 2.7, but for NGC 4038/4039 (top), NGC 4618 (middle), and NGC 4625 (bottom).

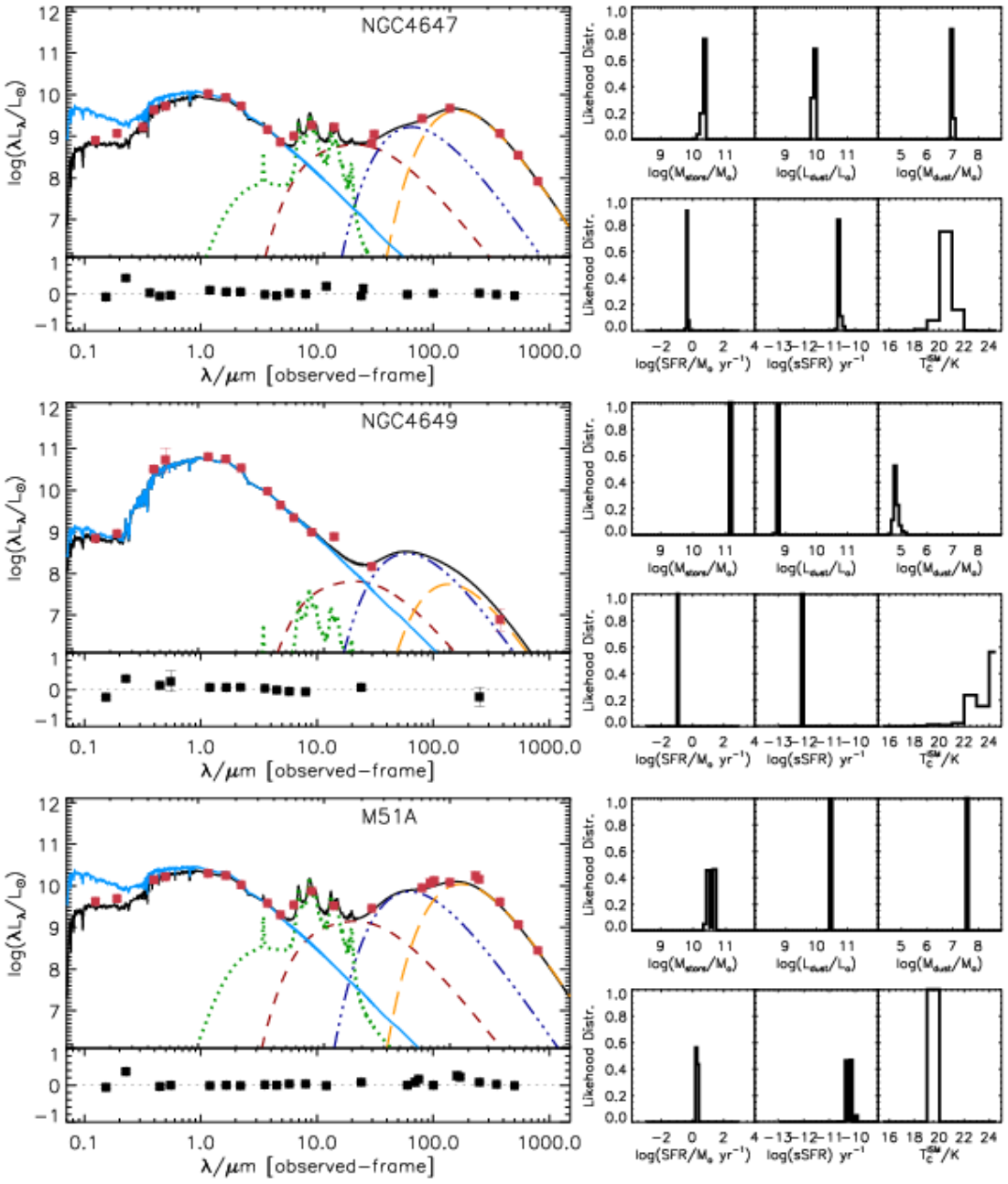

Figure 2.14: As Figure 2.7, but for NGC 4647 (top), NGC 4649 (middle), and M51A (bottom).

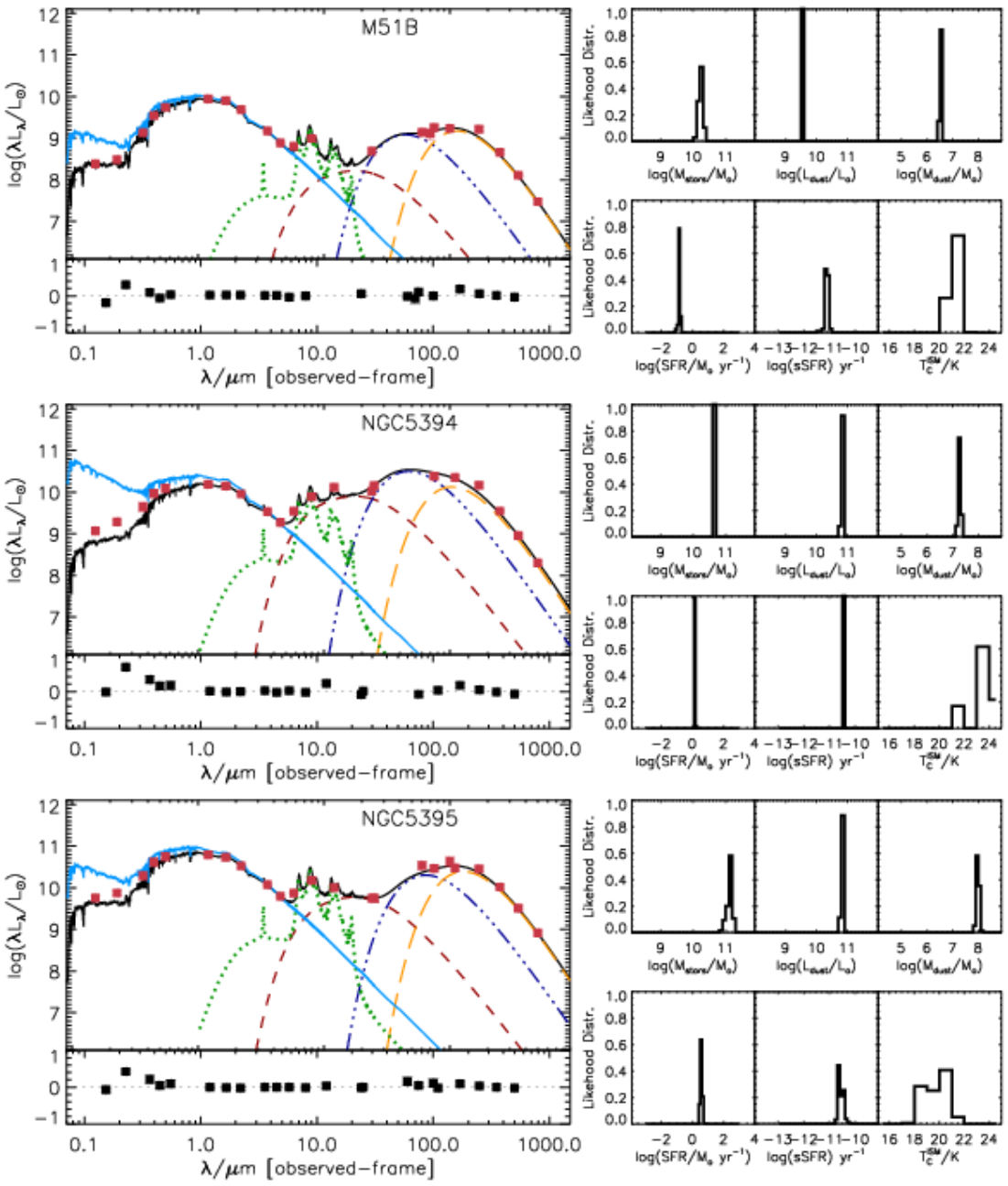

Figure 2.15: As Figure 2.7, but for M51B (top), NGC 5394 (middle) and NGC 5395 (bottom).

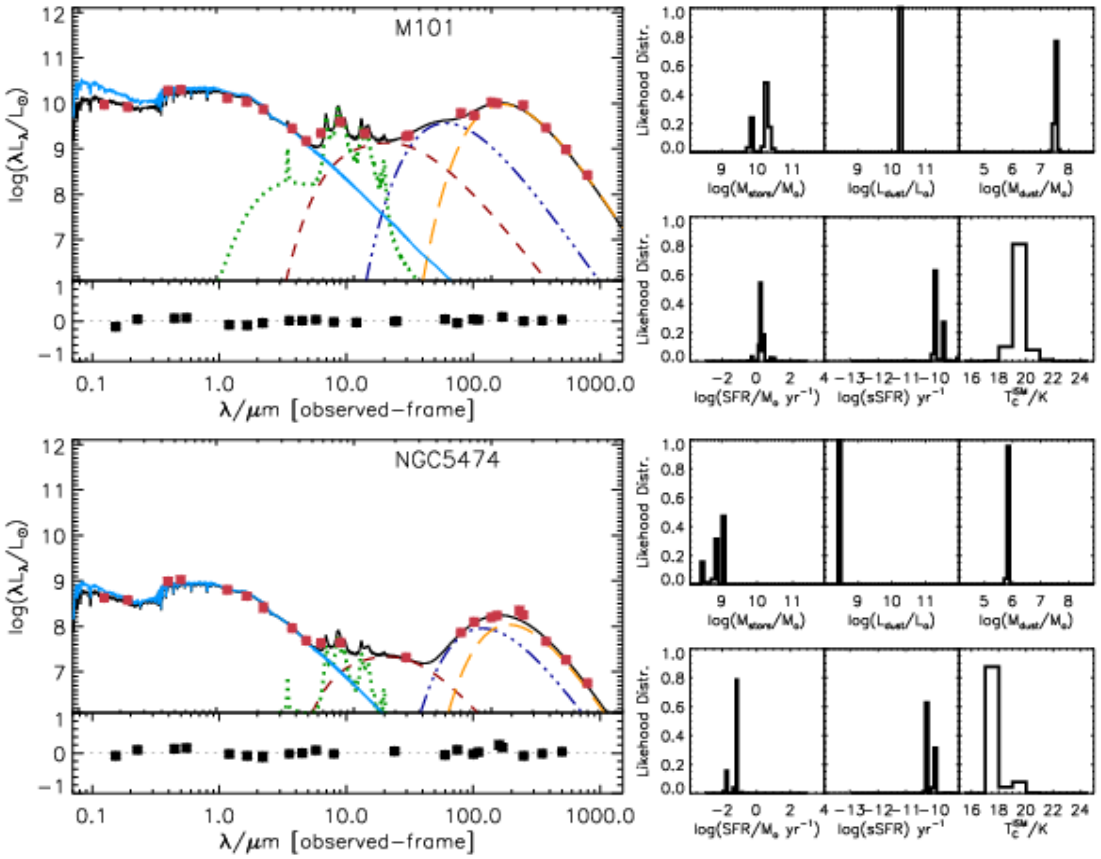

Figure 2.16: As Figure 2.7, but for M101 (top) and NGC 5474 (bottom).

Table 2.11. MAGPHYS Parameters

Name	Dust Luminosity (10^9 $L_\odot$)	Stellar Mass (10^{10} $M_\odot$)	Dust Mass (10^7 $M_\odot$)	SFR[a] ($M_\odot$ yr^{-1})	Specific SFR (10^{-11} yr^{-1})	Cold Dust Temp. (K)	Warm Dust Temp. (K)
NGC 2976	$0.86^{+0.01}_{-0.02}$	$0.10^{+0.05}_{-0.01}$	$0.17^{+0.02}_{-0.01}$	$0.084^{+0.009}_{-0.015}$	$8.51^{+0.20}_{-3.14}$	$18.8^{+0.1}_{-0.2}$	$48.6^{+3.7}_{-0.1}$
NGC 3031	$4.05^{+0.05}_{-0.05}$	$2.95^{+2.42}_{-0.07}$	$1.18^{+0.24}_{-0.15}$	$0.373^{+0.022}_{-0.044}$	$1.35^{+0.03}_{-0.59}$	$18.4^{+0.6}_{-0.9}$	$53.6^{+3.5}_{-21.2}$
NGC 3034	$54.95^{+1.28}_{-1.25}$	$1.45^{+0.03}_{-0.03}$	$0.86^{+0.09}_{-0.18}$	$0.728^{+0.008}_{-0.008}$	$5.37^{+0.13}_{-0.12}$	$23.5^{+0.8}_{-0.7}$	$51.4^{+5.6}_{-8.0}$
NGC 3077	$0.75^{+0.02}_{-0.02}$	$0.068^{+0.035}_{-0.002}$	$0.041^{+0.001}_{-0.001}$	$0.097^{+0.031}_{-0.011}$	$14.96^{+6.17}_{-8.20}$	$22.9^{+0.1}_{-0.1}$	$52.5^{+0.1}_{-0.1}$
NGC 3185	$3.29^{+0.04}_{-0.04}$	$1.45^{+0.03}_{-0.03}$	$0.49^{+0.02}_{-0.07}$	$0.183^{+0.002}_{-0.002}$	$1.20^{+0.03}_{-0.03}$	$20.2^{+0.4}_{-0.4}$	$57.8^{+1.4}_{-3.7}$
NGC 3187	$4.09^{+0.05}_{-0.05}$	$0.31^{+0.08}_{-0.04}$	$1.02^{+0.06}_{-0.05}$	$0.274^{+0.325}_{-0.003}$	$8.51^{+10.33}_{-0.11}$	$16.2^{+0.4}_{-0.3}$	$32.6^{+9.7}_{-1.7}$
NGC 3190	$8.55^{+0.82}_{-0.10}$	$8.32^{+0.39}_{-0.37}$	$1.44^{+0.03}_{-0.03}$	$0.0084^{+0.0004}_{-0.0004}$	$0.011^{+0.001}_{-0.001}$	$22.3^{+0.1}_{-0.1}$	$57.9^{+0.1}_{-0.2}$
NGC 3226	$1.40^{+0.10}_{-0.11}$	$2.29^{+0.28}_{-0.15}$	$0.10^{+0.01}_{-0.01}$	$0.045^{+0.003}_{-0.017}$	$2.14^{+0.05}_{-0.94}$	$24.1^{+0.7}_{-0.5}$	$54.4^{+4.0}_{-3.7}$
NGC 3227	$16.98^{+0.40}_{-0.39}$	$1.32^{+0.03}_{-0.03}$	$1.15^{+0.03}_{-0.03}$	$0.836^{+0.019}_{-0.019}$	$6.76^{+0.16}_{-0.15}$	$22.5^{+0.1}_{-0.1}$	$59.1^{+0.1}_{-0.1}$
NGC 3395/3396	$26.30^{+0.61}_{-0.60}$	$0.70^{+0.11}_{-0.08}$	$1.13^{+0.39}_{-0.01}$	$3.289^{+0.235}_{-0.148}$	$42.17^{+10.92}_{-0.96}$	$23.8^{+0.1}_{-1.3}$	$55.8^{+3.0}_{-0.1}$
NGC 3424	$20.42^{+0.48}_{-0.46}$	$2.04^{+0.05}_{-0.81}$	$1.14^{+0.17}_{-0.03}$	$0.753^{+0.163}_{-0.050}$	$3.80^{+2.22}_{-0.09}$	$23.3^{+0.1}_{-0.7}$	$55.4^{+0.1}_{-4.6}$
NGC 3430	$13.49^{+0.64}_{-0.61}$	$1.82^{+0.42}_{-0.23}$	$2.55^{+0.12}_{-0.35}$	$1.355^{+0.165}_{-0.188}$	$7.59^{+1.96}_{-2.22}$	$19.0^{+0.6}_{-0.8}$	$55.5^{+3.61}_{-5.1}$
NGC 3448	$11.22^{+1.37}_{-0.26}$	$0.35^{+0.07}_{-0.05}$	$0.91^{+0.12}_{-0.16}$	$1.371^{+0.065}_{-0.047}$	$37.58^{+9.73}_{-7.73}$	$18.7^{+3.9}_{-2.3}$	$32.9^{+22.2}_{-0.4}$
UGC 6016	$0.25^{+0.09}_{-0.08}$	$0.010^{+0.009}_{-0.002}$	$0.020^{+0.007}_{-0.005}$	$0.091^{+0.048}_{-0.008}$	$94.41^{+55.22}_{-47.09}$	$20.4^{+2.7}_{-2.7}$	$41.1^{+6.4}_{-7.2}$
NGC 3690/IC 694	$812.8^{+18.93}_{-18.50}$	$8.13^{+0.19}_{-0.19}$	$7.28^{+0.17}_{-1.56}$	$35.65^{+0.83}_{-0.81}$	$42.17^{+0.98}_{-0.96}$	$24.8^{+0.2}_{-0.1}$	$58.0^{+0.1}_{-4.3}$
NGC 3786	$12.59^{+0.29}_{-1.87}$	$3.02^{+0.07}_{-0.62}$	$0.72^{+0.29}_{-0.02}$	$0.612^{+0.014}_{-0.109}$	$2.14^{+0.05}_{-0.23}$	$23.8^{+0.1}_{-2.3}$	$59.6^{+0.4}_{-1.0}$
NGC 3788	$8.07^{+0.19}_{-0.09}$	$2.95^{+0.07}_{-0.07}$	$1.59^{+0.04}_{-0.27}$	$0.352^{+0.008}_{-0.004}$	$1.20^{+0.03}_{-0.03}$	$19.6^{+0.7}_{-0.1}$	$58.2^{+0.9}_{-2.0}$
NGC 4038/4039	$97.72^{+2.28}_{-2.22}$	$6.46^{+0.62}_{-1.33}$	$5.15^{+0.12}_{-0.12}$	$8.954^{+0.422}_{-0.788}$	$13.34^{+3.45}_{-2.74}$	$23.7^{+0.1}_{-0.1}$	$59.9^{+0.1}_{-0.1}$
NGC 4618	$1.04^{+0.02}_{-0.01}$	$0.11^{+0.01}_{-0.01}$	$0.25^{+0.04}_{-0.01}$	$0.225^{+0.003}_{-0.003}$	$18.84^{+0.44}_{-0.43}$	$17.7^{+0.1}_{-1.6}$	$40.8^{+0.1}_{-7.3}$
NGC 4625	$0.39^{+0.01}_{-0.01}$	$0.063^{+0.001}_{-0.001}$	$0.074^{+0.007}_{-0.004}$	$0.050^{+0.001}_{-0.001}$	$7.59^{+0.18}_{-0.17}$	$18.4^{+0.3}_{-1.3}$	$33.7^{+3.9}_{-2.8}$
NGC 4647	$8.07^{+0.19}_{-0.27}$	$2.04^{+0.05}_{-0.09}$	$0.99^{+0.02}_{-0.04}$	$0.470^{+0.011}_{-0.011}$	$2.40^{+0.06}_{-0.05}$	$20.9^{+0.2}_{-0.1}$	$52.7^{+4.3}_{-0.1}$
NGC 4649	$0.50^{+0.01}_{-0.01}$	$13.80^{+0.32}_{-0.31}$	$0.006^{+0.002}_{-0.001}$	$0.114^{+0.003}_{-0.001}$	$0.085^{+0.002}_{-0.002}$	$24.5^{+0.1}_{-1.9}$	$59.5^{+0.4}_{-1.6}$
M51A	$25.70^{+0.60}_{-0.59}$	$3.02^{+1.77}_{-0.33}$	$3.78^{+0.09}_{-0.09}$	$1.936^{+0.138}_{-0.022}$	$6.76^{+0.82}_{-2.50}$	$19.6^{+0.1}_{-0.1}$	$54.9^{+0.1}_{-0.1}$
M51B	$3.65^{+0.08}_{-0.20}$	$1.95^{+0.05}_{-0.36}$	$0.34^{+0.03}_{-0.02}$	$0.142^{+0.003}_{-0.014}$	$0.76^{+0.09}_{-0.02}$	$21.0^{+0.1}_{-0.3}$	$59.3^{+0.1}_{-5.8}$
NGC 5394	$63.10^{+1.47}_{-1.44}$	$4.79^{+0.11}_{-0.11}$	$1.77^{+0.26}_{-0.08}$	$1.538^{+0.018}_{-0.035}$	$3.39^{+0.08}_{-0.08}$	$23.2^{+1.0}_{-1.5}$	$55.6^{+1.3}_{-2.2}$
NGC 5395	$66.07^{+4.73}_{-1.50}$	$15.14^{+0.71}_{-4.42}$	$9.48^{+1.66}_{-1.22}$	$3.690^{+0.403}_{-0.513}$	$2.69^{+1.11}_{-0.55}$	$19.7^{+0.7}_{-0.8}$	$45.3^{+5.6}_{-9.7}$
M101	$18.20^{+0.42}_{-0.82}$	$1.82^{+0.47}_{-1.12}$	$3.25^{+0.31}_{-0.11}$	$1.959^{+0.905}_{-0.367}$	$11.89^{+9.25}_{-1.29}$	$19.4^{+0.3}_{-0.4}$	$58.2^{+0.8}_{-2.2}$
NGC 5474	$0.26^{+0.01}_{-0.01}$	$0.074^{+0.041}_{-0.041}$	$0.072^{+0.002}_{-0.002}$	$0.070^{+0.007}_{-0.054}$	$6.03^{+4.57}_{-0.14}$	$17.9^{+0.1}_{-0.1}$	$30.4^{+0.8}_{-0.1}$
NGC 925	$4.39^{+0.10}_{-0.10}$	$0.92^{+0.02}_{-0.52}$	$2.38^{+0.03}_{-0.08}$	$0.459^{+0.236}_{-0.010}$	$4.79^{+7.10}_{-0.11}$	$15.4^{+0.7}_{-0.1}$	$35.7^{+6.2}_{-4.9}$
NGC 1291	$2.17^{+0.05}_{-0.02}$	$6.17^{+0.75}_{-0.54}$	$0.89^{+0.14}_{-0.03}$	$0.118^{+0.014}_{-0.022}$	$0.13^{+0.08}_{-0.06}$	$17.2^{+0.1}_{-0.4}$	$57.4^{+1.9}_{-1.9}$
NGC 2841	$4.54^{+0.11}_{-0.10}$	$2.95^{+1.41}_{-0.32}$	$1.98^{+0.32}_{-0.15}$	$0.220^{+0.044}_{-0.069}$	$0.54^{+0.09}_{-0.22}$	$17.2^{+0.2}_{-0.4}$	$55.0^{+1.4}_{-1.3}$
NGC 3049	$4.29^{+0.10}_{-0.19}$	$0.11^{+0.01}_{-0.01}$	$0.66^{+0.07}_{-0.14}$	$0.459^{+0.569}_{-0.036}$	$37.58^{+63.76}_{-4.59}$	$17.3^{+1.1}_{-0.3}$	$54.9^{+1.7}_{-2.5}$
NGC 3184	$4.86^{+0.11}_{-0.11}$	$0.42^{+0.09}_{-0.07}$	$1.25^{+0.31}_{-0.12}$	$0.207^{+0.216}_{-0.087}$	$2.69^{+7.62}_{-1.57}$	$18.2^{+0.3}_{-0.7}$	$52.9^{+3.3}_{-4.3}$
NGC 3521	$21.88^{+0.51}_{-0.50}$	$4.57^{+1.05}_{-1.10}$	$3.52^{+0.43}_{-0.56}$	$0.771^{+0.104}_{-0.130}$	$1.35^{+0.49}_{-0.56}$	$19.9^{+0.5}_{-0.4}$	$50.6^{+3.4}_{-4.9}$
NGC 3621	$6.64^{+0.15}_{-0.30}$	$0.84^{+0.26}_{-0.18}$	$1.29^{+0.16}_{-0.18}$	$0.598^{+0.050}_{-0.059}$	$5.37^{+1.75}_{-1.39}$	$18.6^{+0.8}_{-0.6}$	$46.2^{+5.4}_{-9.7}$

Table 2.11—Continued

Name	Dust Luminosity ($10^9\ L_\odot$)	Stellar Mass ($10^{10}\ M_\odot$)	Dust Mass ($10^7\ M_\odot$)	SFR[a] ($M_\odot\ \mathrm{yr}^{-1}$)	Specific SFR ($10^{-11}\ \mathrm{yr}^{-1}$)	Cold Dust Temp. (K)	Warm Dust Temp. (K)
NGC 3938	$7.80^{+0.18}_{-0.18}$	$0.26^{+0.05}_{-0.01}$	$1.50^{+0.13}_{-0.10}$	$0.225^{+0.470}_{-0.005}$	$8.51^{+12.62}_{-0.19}$	$19.1^{+0.2}_{-0.4}$	$46.5^{+8.2}_{-5.6}$
NGC 4236	$0.27^{+0.01}_{-0.01}$	$0.020^{+0.001}_{-0.001}$	$0.009^{+0.001}_{-0.001}$	$0.022^{+0.001}_{-0.001}$	$10.59^{+0.25}_{-0.24}$	$24.6^{+0.1}_{-0.6}$	$48.4^{+0.8}_{-0.1}$
NGC 4559	$7.36^{+0.09}_{-0.25}$	$0.52^{+0.01}_{-0.01}$	$2.00^{+0.43}_{-0.18}$	$1.294^{+0.015}_{-0.058}$	$23.71^{+0.55}_{-0.54}$	$17.8^{+0.4}_{-1.1}$	$45.8^{+7.6}_{-8.3}$
NGC 4594	$7.28^{+0.17}_{-0.17}$	$32.36^{+0.75}_{-0.74}$	$2.77^{+0.06}_{-0.38}$	$0.032^{+0.001}_{-0.001}$	$0.011^{+0.001}_{-0.001}$	$17.8^{+0.4}_{-0.1}$	$59.1^{+0.1}_{-2.3}$
NGC 4736	$7.03^{+0.42}_{-0.24}$	$1.02^{+0.46}_{-0.05}$	$0.53^{+0.06}_{-0.06}$	$0.598^{+0.028}_{-0.033}$	$4.27^{+0.14}_{-1.76}$	$21.8^{+0.8}_{-1.0}$	$35.4^{+12.7}_{-3.0}$
NGC 4826	$4.29^{+0.10}_{-0.10}$	$3.72^{+0.27}_{-0.63}$	$0.31^{+0.05}_{-0.05}$	$0.070^{+0.016}_{-0.039}$	$0.09^{+0.03}_{-0.13}$	$23.4^{+0.9}_{-0.6}$	$58.4^{+0.8}_{-3.4}$
NGC 5055	$19.50^{+0.45}_{-0.44}$	$5.01^{+0.61}_{-1.38}$	$4.00^{+0.39}_{-0.14}$	$0.906^{+0.076}_{-0.219}$	$1.35^{+0.49}_{-0.56}$	$19.2^{+0.1}_{-0.3}$	$54.6^{+1.8}_{-6.0}$
NGC 6946	$23.99^{+0.56}_{-0.55}$	$2.19^{+0.27}_{-0.49}$	$2.77^{+0.34}_{-0.41}$	$1.629^{+0.241}_{-0.350}$	$6.76^{+1.96}_{-0.82}$	$20.7^{+0.6}_{-0.8}$	$54.9^{+2.4}_{-1.7}$

Note. — Median of the PDFs determined by MAGPHYS. The uncertainty given is the 68% confidence range.

[a] Averaged over 100 Myr

2.5 Discussion

2.5.1 Variation in SED Shape with Interaction Stage

We now discuss the shape of the SED as a function of the interaction stage. We first normalized each SED to its 2MASS *Ks* luminosity. Emission in the 2MASS *Ks* filter is dominated by the old stellar populations and hence is a good proxy for stellar mass. The comparison between the SEDs is shown in Figure 2.17. In the inset, we show the median normalized SED for each class of galaxies. The SED shapes between the three stages vary by approximately as much as the variations within a stage. However, there are some significant variations, especially in the Stage 4 SEDs compared to the Stage 2 and 3 SEDs. Stage 4 galaxies typically have more emission from the hot/warm dust than earlier interaction stages, as evidenced by the stronger $10-60\,\mu$m emission relative to their stellar mass. Further, Stage 4 galaxies tend to have more warm dust relative to their cold dust FIR emission. In contrast to this variation in the relative MIR emission, all three stages have similar ratios of NIR stellar emission to FIR emission from cold dust. We will discuss the statistical significance of these results in the next section.

These differences in the SEDs are consistent with the results of simulations, which predict that an integrated SED of an interacting system becomes hotter at merger coalescence during the peak of starburst and AGN activity (e.g., Hayward et al. 2011, 2012; Younger et al. 2009; Narayanan et al. 2010a, 2010b). However, the increase in temperature in this sample of galaxies is unlikely to be driven purely by AGN activity. None of the galaxies in our sample have mid-infrared colors indicating that they are globally dominated by AGN activity as defined in the IRAC color−color space in Stern

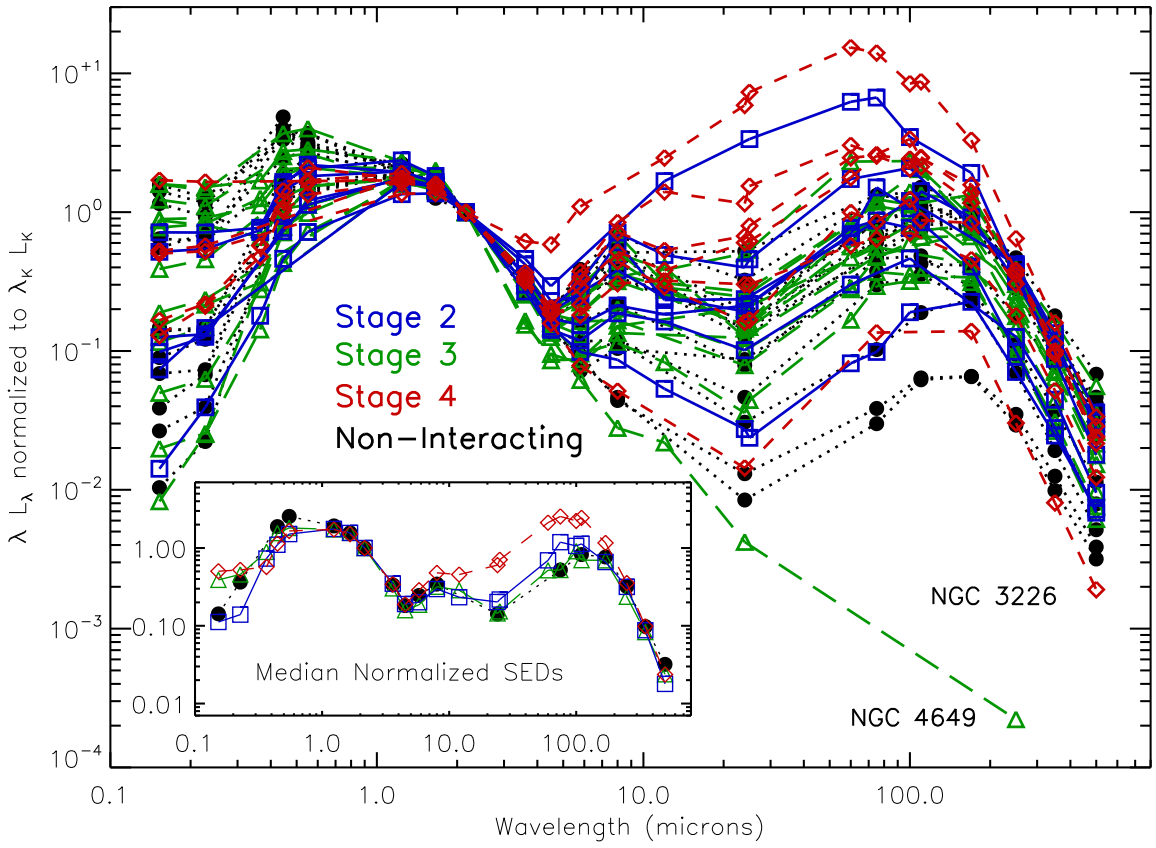

Figure 2.17: SEDs normalized to the 2MASS *Ks* band luminosity for each galaxy. Stage 2 (weakly interacting), Stage 3 (moderately interacting), Stage 4 (strongly interacting), and non-interacting galaxies are shown respectively in blue squares joined with solid lines, green triangles joined with long dashes, red diamonds joined with short dashes, and black circles joined with dotted lines, respectively. Inset, we show the median SED for each class of galaxies. These SEDs show a tendency for Stage 4 galaxies to have more hot-warm dust emission in the 10−60 μm range relative to both its cold dust emission in the SPIRE bandpasses and its stellar NIR emission, whereas the ratio of NIR to FIR emission is relatively consistent. Additionally, the more strongly interacting galaxies typically have a younger stellar population than the Stage 2 galaxies as suggested by the relative amounts of UV to NIR emission. The two labeled galaxies are elliptical galaxies.

et al. (2005; Figure 18). Further, while five of the sample galaxies are classified as Seyfert galaxies and three are classified as low-ionization nuclear emission-line region (LINER) galaxies, they are found in all three stages. We used the software DECOMPIR[12] (Mullaney et al. 2011) to estimate the AGN contribution to the $8-1000\,\mu$m and $8-35\,\mu$m emission for these nine galaxies based on the $8-500\,\mu$m photometry. We give the individual contributions in the descriptions in Appendix C; the range of the contribution to the total IR is up to 10% with some larger, more uncertain values up to 25%. Further, we do not find significant differences in the AGN contribution to either the total infrared luminosity or mid-infrared luminosity, where the Stage 4 SEDs are typically brighter, between the stages. Hence, the effect of AGN on the SEDs of the sample galaxies is modest and does not affect our conclusions.

The more strongly interacting systems demonstrate a tendency to have, on average, younger stellar populations, resulting in stronger UV emission relative to their NIR emission. Since the UV emission has only been corrected for Milky Way extinction, additional intrinsic extinction could increase this effect. Ignoring NGC 4649, a large elliptical that has very little MIR−FIR emission, the UV bands reflect this tendency and show a large amount of variation between galaxies, which is likely due to the different amounts of dust attenuation and the sensitivity of the UV to recent star formation history. Comparing to the stellar mass proxy of 2MASS *Ks*, Stage 4 galaxies typically have a 1:2 luminosity ratio between emission in the *GALEX* bands and 2MASS *Ks* band, whereas Stage 2 galaxies typically have a 1:10 luminosity ratio.

[12]http:sites.google.com/site/decompir

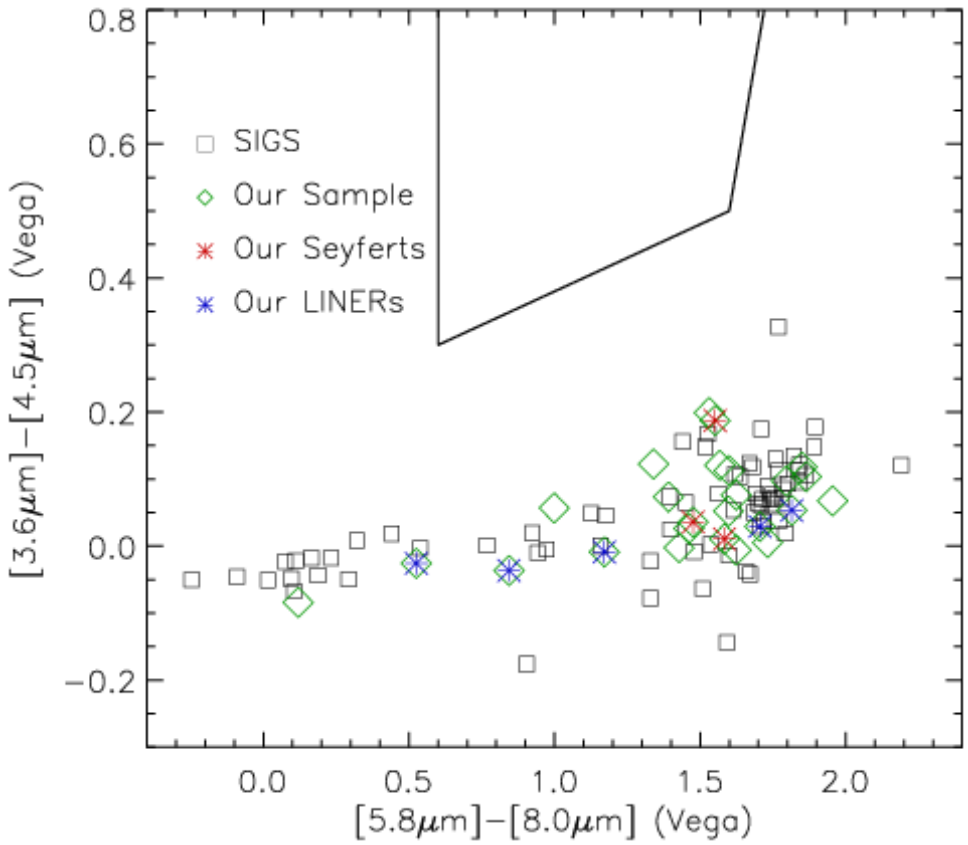

Figure 2.18: IRAC color-color plot of the SIGS galaxies (square) with our sample galaxies (diamonds) over-plotted, showing that none fall in the wedge identified by Stern et al. (2005) as galaxies hosting AGN. Our sample galaxies identified optically as Seyferts or LINERs in Keel et al. (1985) or Ho et al. (1997, 2000) and are marked with red and blue stars, respectively.

2.5.2 Variations in Galaxy Parameters with Interaction Stage

Figures 2.19 and 2.20 show the histograms and cumulative distributions for the three interaction stages defined in Section 2.2.2 for four parameters whose PDFs are shown in Figures 2.7-2.16 compared to the non-interacting galaxies. Table 2.12 gives the results of the Kolmogorov−Smirnov (K-S; e.g., Press et al. 2007) tests performed to determine the likelihood that the samples for the different stages originate from a common parent population for each parameter. With the number of galaxies in our sample, we do not have the same statistical power that the full SIGS sample will have (N. Brassington et al. 2013, in preparation).

The mass of dust is one of four parameters derived from the SED that differs with marginal statistical significance between the Stage 3 and Stage 4 galaxies ($p = 0.02$). Both the mass of warm dust and of cold dust likewise differ. The warm dust mass also differs between the Stage 4 galaxies and the non-interacting galaxies. In contrast, the distribution of dust mass in the ISM of non-interacting galaxies falls between the distributions of Stage 2/3 and Stage 4 galaxies. The dust mass in the ISM and stellar mass also each show only small increases in their median values as the interaction sequence progresses, and their cumulative distributions are not significantly different. Indeed, both the stellar mass ($p = 0.96$) and total dust mass ($p = 0.96$) for Stage 2 and Stage 3 galaxies are consistent with coming from the same populations. These trends are consistent with the SED shapes described in Section 2.5.1, where the Stage 4 SEDs typically show more emission from the hot/warm dust relative to the cold dust emission and stellar emission.

The dust luminosity (Figure 2.19, left) shows marginally statistically significant

differences between Stage 3 and Stage 4 galaxies ($p = 0.01$) and between the non-interacting galaxies and the Stage 4 galaxies ($p = 0.02$). The median dust luminosity increases with interaction stage by over an order of magnitude between Stage 2 and Stage 4. Elbaz et al. (2011) defined an "IR main sequence" of galaxies in which the ratio of total IR luminosity to 8 μm luminosity has a Gaussian distribution. We examined this ratio for our sample and found good agreement with the expected distribution. The only interacting galaxy that lies off this relation, by roughly an order of magnitude, is the large elliptical NGC 4649, as would be expected. Elbaz et al. (2011) also defined two modes of star formation: a "normal" mode exemplified by the galaxies on the IR main sequence and a "starburst" mode with excess sSFR in comparison. Our sample's agreement with the IR main sequence indicates that our set of interacting galaxies do not contain systems with significantly increased sSFR.

We also considered the evolution of the cold and warm dust temperatures. The cold dust temperature (Figure 2.19, right) is the third parameter showing evidence for differences between the Stage 3 and Stage 4 ($p = 0.01$) and between the non-interacting galaxies and the Stage 4 galaxies ($p = 0.01$). The cold dust temperature's median value varies in a similar manner to the IR luminosity, increasing between Stages 3 and 4 but relatively constant between Stages 2 and 3; the median value of the warm dust temperature is by contrast fairly constant. Only Stage 4 does not span the range of the 15−25 K cold dust temperature, while in Stage 2 and Stage 4 the warm dust temperatures are confined to the 45−60 K range. The similarity in evolutionary trend in the IR luminosity and cold dust temperature is likely due to the predominance of cold dust mass and luminosity in the total dust estimates. We might expect a similar trend to be exhibited in the temperature of the warm dust primarily present in the stellar birth

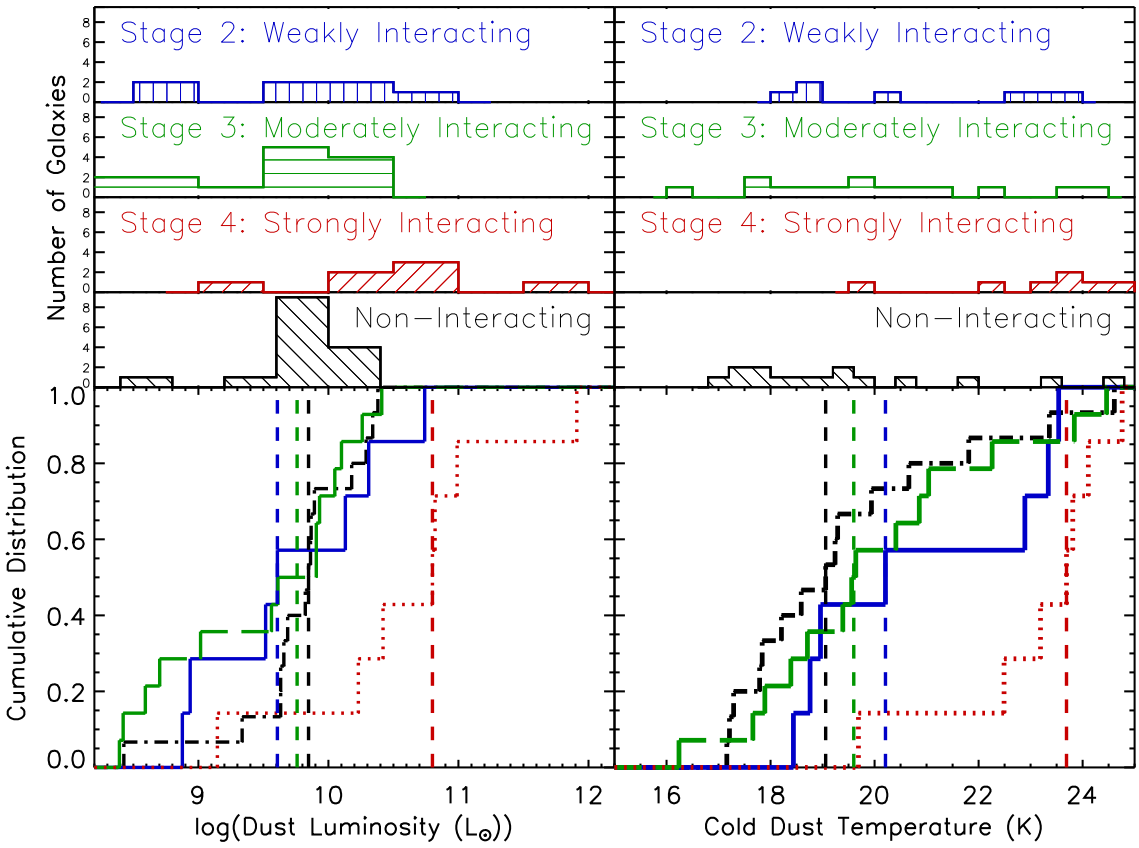

Figure 2.19: Histograms (top) and cumulative distributions (bottom) of the dust luminosity (left) and cold dust temperature (right) derived by MAGPHYS for the three interaction stages defined by the classification system of Dopita et al. (2002), where Stages 2−4 are weakly (blue, solid), moderately (green, long dashed), and strongly (red, short dashed) interacting, respectively. Non-interacting galaxies are shown in black dot-dashed lines. There is a difference in both luminosity and temperature between the Stages 3 and 4 populations and between Stage 4 and non-interacting populations as defined by a K-S Test (see Table 2.12). The vertical dotted lines give the median value for each stage. The median dust luminosity is lowest for the "weakly interacting" Stage 2 galaxies and increases by more than an order of magnitude for the "strongly interacting" Stage 4 galaxies. The 15-25 K dust temperature is noticeably higher in the Stage 4 galaxies.

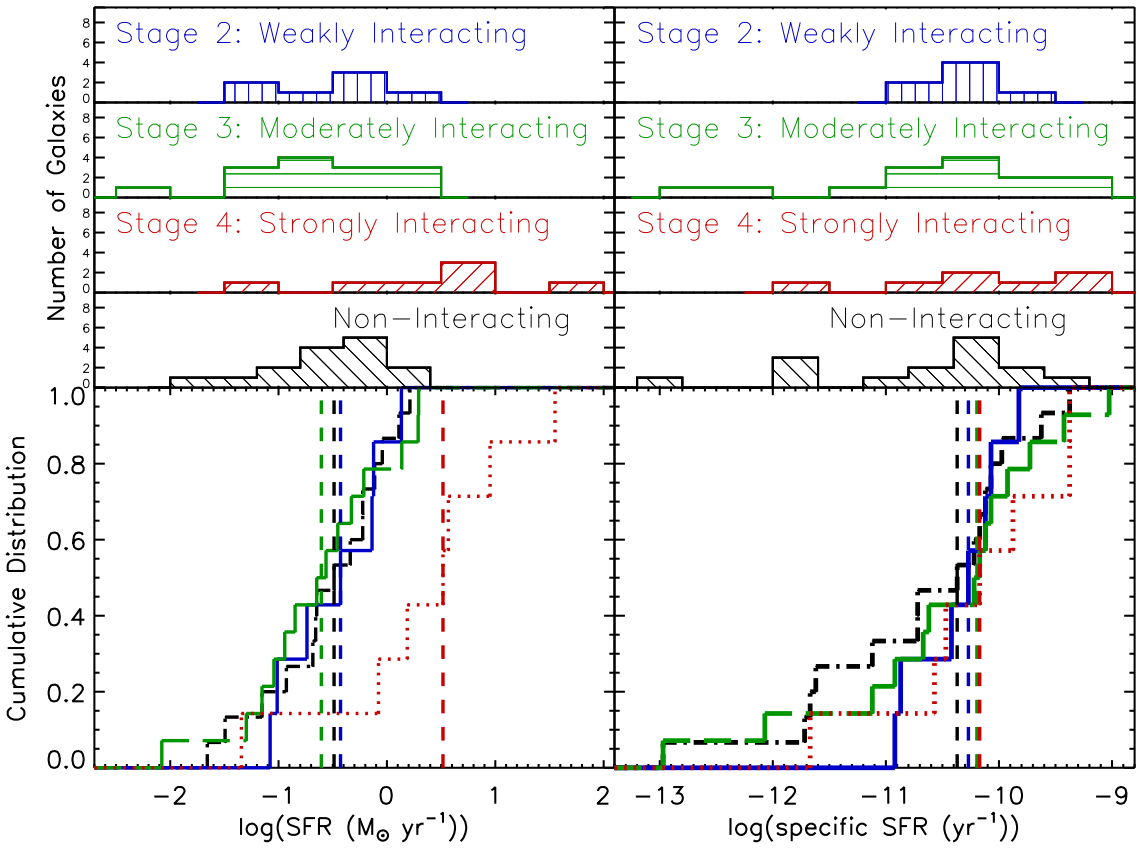

Figure 2.20: Histograms (top) and cumulative distributions (bottom) of SFR (left) and sSFR (right) derived by MAGPHYS for each interaction stage and the control sample shown with the same color and linestyles as Figure 2.19. SFR shows an increase between non-interacting through moderately interacting galaxies and the Stage 4, "strongly interacting" systems, an evolution similar to that of dust luminosity. In contrast, the sSFR distributions are very similar, as is supported by the results of the K-S tests.

clouds, however the warm dust temperature is less well constrained in MAGPHYS than the cold dust temperature. The cold dust contribution and warm dust temperature are both correlated with the warm dust mass (which drives the MIR continuum intensity and the shape of the SED). Therefore, the warm dust temperature PDFs tends to be broader, with a 68% range that is typically four to five times the size of the cold dust 68% confidence interval. However, since the cold dust mass is typically over $\sim 80\%$ of the total dust mass, the total dust mass is still fairly well constrained.

The SFR, shown in Figure 2.20 (left), shows an increase in median value with interaction stage, like the dust mass and dust luminosity, and has a marginally significant probability the same population did not yield the Stage 4 galaxies as well as the Stage 2 ($p = 0.03$), Stage 3 ($p = 0.02$), and non-interacting ($p = 0.02$) galaxies. Since the warm (30−60 K) dust, primarily heated by young stars with ages less than 10 Myr, contributes significantly to the total dust luminosity, it makes sense that these three parameters show similar evolution over the interaction stages. However, an increase in SFR between the different stages could be also attributed to our Stage 4 galaxies simply being larger with greater gas reservoirs. To test this, we also examined the evolution of sSFR over the interaction stages (Figure 2.20, right). In contrast to SFR, we do not find much difference in the median values of the sSFR, and the cumulative distributions are very similar in both width and normalization. We therefore do not see enhanced sSFR in more evolved mergers, consistent with the ratios of total IR luminosity to 8 μm luminosity being due to a "normal" mode of star formation for our whole sample. We also do not see differences between the distributions of the sSFR of the three interacting galaxy samples and of the non-interacting galaxies. Xu et al. (2010) and Yuan et al. (2012) examined star formation in a sample of local major mergers and both found that that the sSFR

distributions of galaxies in spiral-spiral interactions and non-interacting systems were unlikely to originate from the same population (based on a K-S test: $p = 0.03 - 0.04$). However, they also found a mass dependence in the enhancement of sSFR; only those galaxies with $M_* > 10^{10.5} M_\odot$ were found to have significant enhancements. Our sample shows a similar trend, but we only have six galaxies with $M_* > 10^{10.5} M_\odot$ of which one is an elliptical, and they are spread across Stages 3 and 4.

We also examined the star formation efficiency, which we define as the ratio of SFR to warm (30−60 K) birth cloud dust mass, a proxy for molecular gas mass. While the ratio of dust mass to gas mass is not necessarily the same between galaxies, this ratio provides a means of estimating the star formation efficiency under the assumption of constant gas-to-dust ratio. This star formation efficiency allows us to compare the SFR taking into account the variable gas reservoirs. We find that regardless of stage, the star formation efficiency ranges over more than three orders of magnitude and the cumulative distributions show no evidence of originating from different populations. This result agrees with the findings of Casasola et al. (2004) who found similar star formation efficiencies, defined as the ratio of FIR luminosity (a proxy for SFR) and molecular hydrogen mass, for interacting and non-interacting galaxies.

All the apparent variations with interaction stage come with a few caveats. First, with only 31 galaxies, our sample has limited statistical power to identify significant variations, especially with half the galaxies in Stage 3. Analysis of trends in SFR and sSFR with the full SIGS sample (N. Brassington et al. 2013, in preparation), which covers the stages much more uniformly, will have greater statistical power (albeit these comparisons lack the *Herschel* SPIRE data and SED analysis that provides more accurate SFR measurements). Second, our classification scheme permits us to examine

parameter variations with respect to the strength of the interaction. While this sequence crudely mimics an interaction, the dynamics of two colliding galaxies often includes multiple encounters prior to final coalescence, modifying the level of star formation at intermediate stages (e.g., Torrey et al. 2012), as well as the intensity of the final burst (e.g., Hopkins et al. 2008, 2009). As a result, interacting systems often do not progress linearly through the interaction stages defined by our classification system.

Table 2.12. K-S Probabilities

Parameter	With Non-Interacting			Between Stages		
	Stage 2	Stage 3	Stage 4	Stages 2 and 3	Stages 3 and 4	Stages 2 and 4
Dust Luminosity	0.238	0.224	**0.017**	0.767	**0.008**	0.129
Total Dust Mass	0.095	0.072	0.462	0.964	**0.022**	0.423
Stellar Mass	0.366	0.655	0.569	0.964	0.271	0.129
SFR	0.980	0.983	**0.017**	0.964	**0.022**	**0.028**
sSFR	0.569	0.953	0.606	0.964	0.768	0.883
Cold Dust Temperature	0.337	0.417	**0.006**	0.767	**0.008**	0.423
Warm Dust Temperature	0.569	0.237	0.106	0.271	0.271	0.129
Cold Dust Mass	0.095	0.072	0.462	0.964	**0.022**	0.423
Total Warm Dust Mass	0.682	0.678	**0.019**	0.767	**0.022**	0.129
Birth Cloud Warm Dust Mass	0.912	0.678	**0.019**	0.492	**0.022**	0.129
SFR/Dust Luminosity	0.238	0.224	0.999	0.492	0.271	0.883
SFR/Birth Cloud Warm Dust Mass	0.119	0.478	0.462	0.492	0.492	0.883
Dust Mass/Stellar Mass	0.644	0.916	0.857	0.767	0.271	0.423
Birth Cloud /Cold ISM Dust Mass	0.719	0.224	0.037	0.767	0.271	0.129

Note. — The probabilities given in this table are the probability that the same population yielded the compared samples, so small values indicate a common population is unlikely. The marginally significant differences are given in bold. The total dust mass is composed of warm dust in the stellar birth clouds and the diffuse ISM and cold dust in the diffuse ISM.

2.5.3 Relative Importance of Specific Data Sets in Constraining Galaxy Parameters

For each galaxy, we ran six MAGPHYS fits to measure the relative importance of UV, SPIRE, and MIR−FIR data in constraining the value of the derived SFR; stellar mass; sSFR; and dust temperatures, luminosity, and masses. We did this by comparing fits with all available data with fits using a subset of the complete dataset in order to determine if and how the absence of a particular dataset results in a systematic over- or under-estimation of these parameters. Figure 2.21 shows a representative example: the best-fit SEDs for all six fits for M101 as well as the accompanying PDFs for the parameters of interest.

As expected, the SFR is significantly constrained by UV data. This is demonstrated in Figure 2.22, where the median 68% confidence interval size is a factor of ∼4 larger in the absence of UV photometry. While stellar mass is fairly well constrained by the UBV-IRAC data alone, the absence of UV data tends to result in younger stellar population templates being selected by MAGPHYS. This effect can be seen in the differences in the UV slope and the strength of the Lyman and Balmer breaks in the various panels of Figure 2.21. When a younger stellar population template is selected, a smaller fraction of the stellar emission is assumed to originate from late-type stars, resulting in a tendency to estimate the stellar mass $\sim 10\% - 20\%$ lower than when all the data are used. This can be seen in Figure 2.23 where we plot the median fractional difference in the value of the galaxy properties for fits with incomplete data sets. UV photometry constrains both the SFR and stellar mass, and it is also the most important wavelength regime to constrain the sSFR. The absence of UV data also tends to result

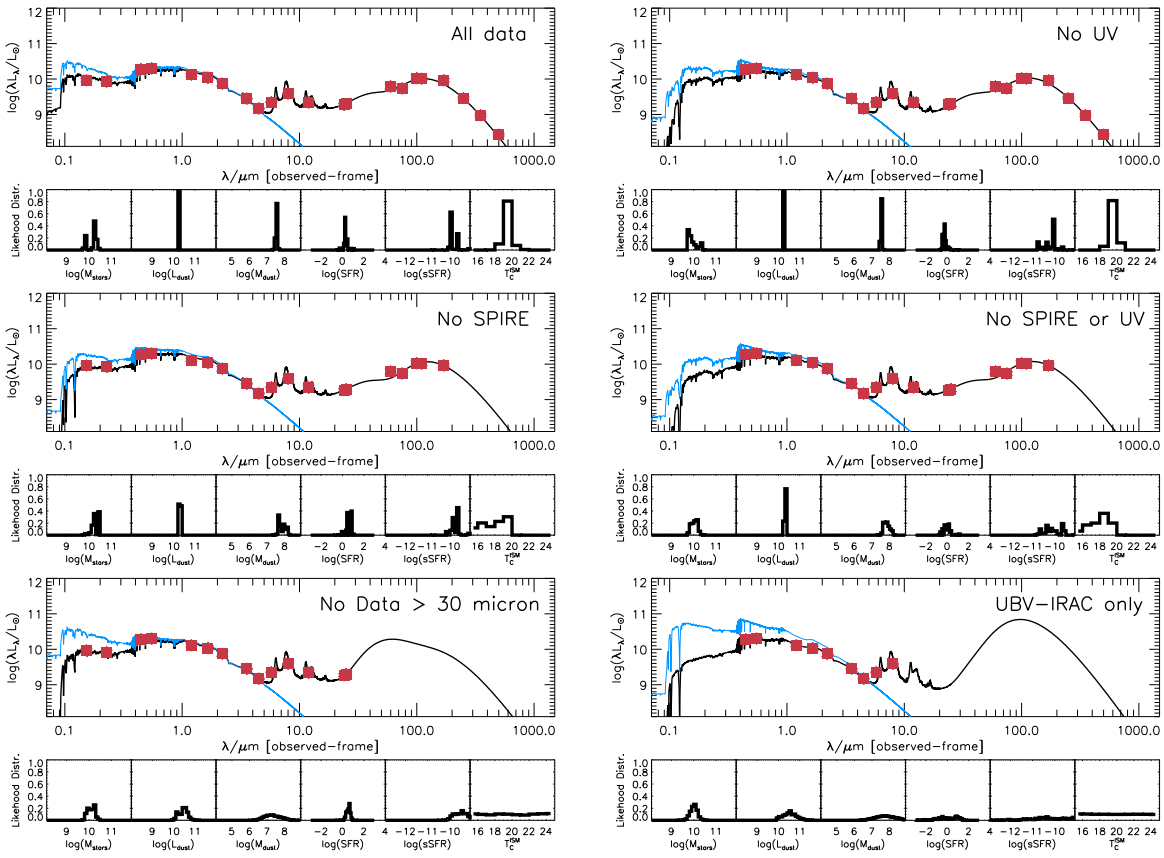

Figure 2.21: MAGPHYS fits with the six different data sets for M101, as a representative example of the set of fits done for each galaxy, showing the increasingly constrained parameters (from lower right to top left) as more data are used. UV photometry (present in the left panels) is crucial in constraining sSFR, while SPIRE data (present in the top two panels) is essential for the determination of cold dust temperature and dust mass. The lower right panel demonstrates the limited constraints that ground based photometry alone can provide.

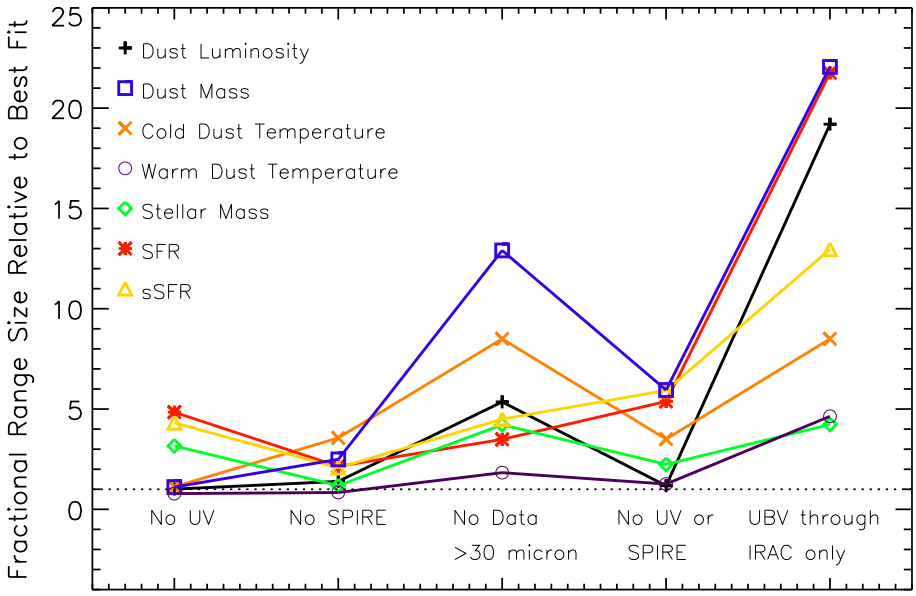

Figure 2.22: Parameter confidence intervals increase with the omission of data. Points indicate the median size of the 68% confidence interval in the probability distribution function (PDF) for each parameter for the whole set of galaxies relative to the range when all of the data are used in the fit. Using all available data, the median 68% ranges are: 6.3×10^{8} $L_{\odot}$ (dust luminosity), 1.8×10^{6} $M_{\odot}$ (dust mass), 0.80 K (cold dust temperature), 4.4 K (warm dust temperature), 2.1×10^{9} $M_{\odot}$ (stellar mass), 0.047 $M_{\odot}$ yr^{-1} (SFR), and 1.3×10^{-11} yr^{-1} (sSFR). UV data are crucial for the determination of sSFR, whereas dust luminosity, mass, and 15−25 K temperature are best constrained by SPIRE data with further constraints applied by photometry from 30 to 200 μm.

in an over-estimation of the SFR resulting in an estimate of the sSFR ∼40% higher than in fits using all available data.

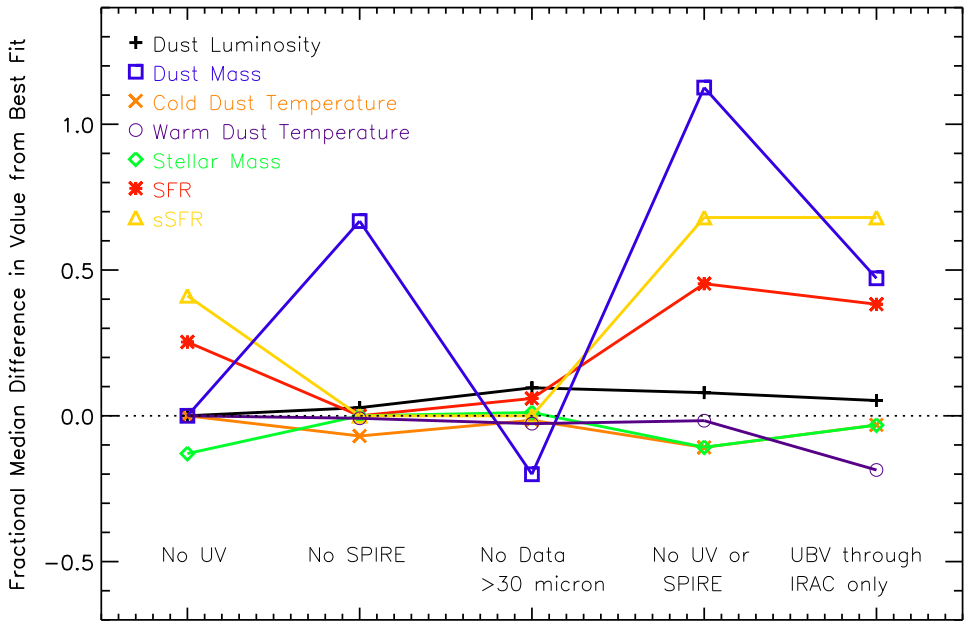

Figure 2.23: Median fractional difference for each parameter relative to its value that parameter when all of the data are used in the fit. The absence of UV data results in sSFR ∼40% higher than in fits using all the data. Dust mass, made up primarily of cold dust, is very sensitive to changes in the cold dust temperature.

Herschel data are particularly crucial in constraining the cold dust temperature. PACS data typically outline the peak of the IR emission, but in cases of the coldest dust temperatures, PACS 170 μm is typically too indeterminate and it is only in conjunction with the SPIRE 250 μm data that the cold dust temperature is reasonably constrained. In contrast, as expected, warm dust temperature is not well constrained by the SPIRE data. Dust luminosity is typically well-estimated with a combination of IRAS and PACS

data, only becoming about a factor of ∼2 more uncertain in absence of SPIRE data.

SPIRE observations are crucial for constraining the dust mass, whose 68% confidence interval would be at least a factor of three larger without SPIRE data. When MIR data at wavelengths $\lambda \geq 30\,\mu$m are likewise absent, the dust mass becomes almost completely unconstrained as the SED contains little information about the dust emission. The dust mass estimate is the most sensitive to the absence of specific datasets. Interestingly, the dust mass estimated by MAGPHYS is ∼60% higher when SPIRE data are excluded as compared with when all data are used; however, when photometry at wavelengths $\lambda \geq 30\,\mu$m is excluded, the dust mass is estimated ∼20% lower than when all data are used. The over-estimates in dust mass are correlated with the under-estimates in the cold dust temperature. Since, cold dust tends to make up the bulk of the dust mass and because cold dust mass varies as T^{-6} (assuming it is modeled as a $\beta = 2$ modified blackbody), a 5% change in the dust temperature results in a 30%−40% difference in the dust mass. Aniano et al. (2012) recently showed similar results for NGC 628 and NGC 6946, where fits undertaken only with data at wavelengths $\lambda \leq 170\,\mu$m tend to overpredict the emission in the SPIRE bands and the associated cold dust mass. When all data at wavelengths $\lambda \geq 30\,\mu$m are omitted, MAGPHYS relies primarily on more common UV−NIR dominated sources.

2.5.4 Comparison of the SFR Derived from the SED to Monochromatic and Broad-band Relations

Because the SFR is such a key physical parameter, many statistical heuristic attempts have been developed to estimate it from simple observables such as the UV flux (as

measured by *GALEX*) or Hα, the 24 μm flux, the total IR flux, and combinations of UV and MIR fluxes (e.g., Calzetti 2012). We compared the SFR derived by MAGPHYS to the expected SFR based on a wide range of relations (Figure 2.24): from the FUV relations of Salim et al. (2007) and Treyer et al. (2010), from the MIPS 24 μm emission relations of Rieke et al. (2009) and Zhu et al. (2008, as given in Calzetti et al. 2010), from the relations combining UV and 24 μm emission of Leroy et al. (2008) and Kennicutt et al. (2009), and from the total IR luminosity relation of Kennicutt (1998). We correct the FUV emission from dust using the prescription given in Salim et al. (2007) and use the dust luminosity derived by MAGPHYS for the total IR luminosity. We assume a Chabrier (2003) initial mass function (IMF) and therefore have applied correction factors of 1.06 for relations that assume a Kroupa (2001) IMF and 1.60 for relations that assume a Salpeter (1955) IMF, following Calzetti (2012) and Schiminovich et al. 2007. Figure 2.24 shows the resulting values plotted against the SFR determined by MAGPHYS.

One trend is quickly apparent: the SFRs estimated from UV photometry alone tend to be high compared with the SED-derived SFR, whereas the relations based solely or partially on IR photometry agree fairly well, at least for SFR greater than $\sim$0.1 $M_\odot$ yr^{-1}. Median differences are of $0.7-0.9 M_\odot$ yr^{-1} for the FUV relations. Interestingly, our most active galaxy, NGC 3690/IC 694, shows the inverse trend, as does a prototype starburst M82. This may indicate that the correction for dust is insufficient for these systems. The outlier of NGC 3190 (Figure 2.24) is due to the low SFR associated with the best MAGPHYS model for this galaxy that significantly underestimated its UV emission, likely due to the edge-on geometry of the system.

The apparent over-estimation of the SFR by the FUV relations is rooted in the time over which the SFR is estimated in MAGPHYS. FUV emission is dominated by star

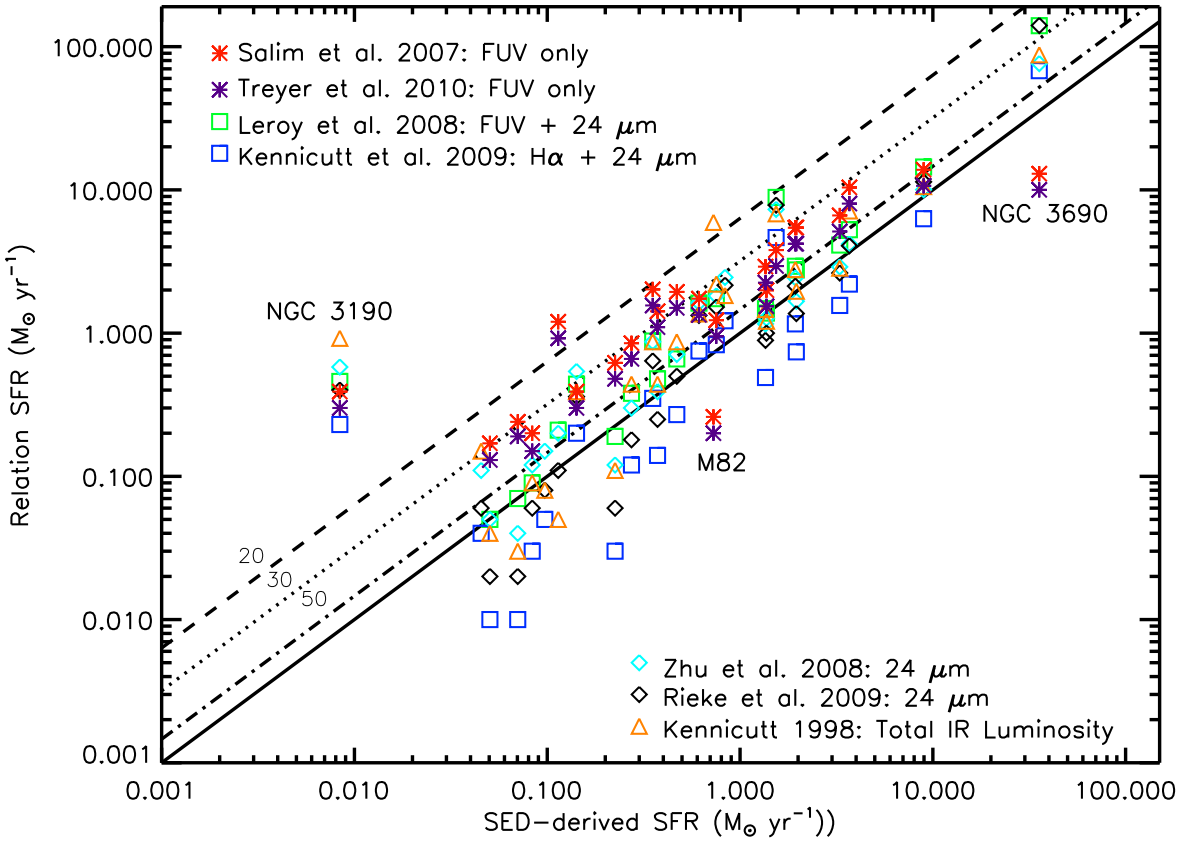

Figure 2.24: Comparison of the SED-derived SFR to those from various SFR proportionality relations from the literature. The solid line shows where the points should lie if the relations agree with the SED-derived values, which is the SFR averaged over 100 Myr. The dotted, dashed, and dot-dashed lines shows SFR averaged over 20, 30, and 50 Myr, respectively. SFR is modeled as an exponential burst with a peak value such that the average over 100 Myr is given by the MAGPHYS SFR and decay times of 20, 30, and 50 Myr. While the relations depending solely or partially on IR emission agree well with the MAGPHYS SFR, the FUV relations are typically high and agree better with a SFR modeled as an exponential burst with a width of 30−50 Myr.

formation within the past 50 Myr, although mid-to-late B stars can also contribute a significant fraction (Calzetti 2012). In contrast, the IR relations typically assume that a fraction of the stellar light is absorbed to heat dust, and as a result, while the youngest and hottest stars dominate the heating of hot dust, the accumulation of low-mass stars contribute significantly to the heating of the more diffuse dust. Hence, the IR relations represent star formation over a longer timescale. The SFRs derived by MAGPHYS are averaged over the last 100 Myr, which is more consistent with the timescales associated with the IR-dependent SFR relations. Figure 2.24 also shows the SFRs averaged over shorter time periods with SFR modeled as an exponential decay with a peak value such that the average over 100 Myr is the MAGPHYS SFR value and decay times of 20, 30, and 50 Myr, respectively. The SFRs estimated from the FUV emission agree better with an exponential decay star formation history with a width between 30 and 50 Myr, which is the expected timescale of a starburst episode.

2.6 Summary

We modeled the FUV−FIR SEDs of fourteen groups of 31 interacting galaxies, typically with 15−25 flux points, to determine the most probable evolution of dust luminosity, SFR, sSFR, dust mass, stellar mass, and dust temperature. The systems were classified as either weakly, moderately, or strongly interacting (Stages 2−4 in the Dopita et al. 2002 scheme). The broad similarities in SED shape between different stages emphasize one key conclusion from this study: as the interaction progresses, and even as bursts of star formation may occur, the changes are most clearly seen not in the distribution of energy broadly but in minor and subtle changes to the SED shapes. Bulk SED properties

change little, and only gradually, in typical interactions. Strongly interacting galaxies typically have SEDs characterized by stronger MIR emission relative to both their NIR and FIR emission and more UV emission relative to their NIR emission.

There are marginally statistically differences (as determined by a K-S Test) in the derived galaxy properties: dust luminosity and mass, SFR, and cold dust temperature increase from Stage 3 to Stage 4, SFR increase from Stage 2 to Stage 4, and dust luminosity, SFR, and cold dust temperature increases from the non-interacting galaxies to the Stage 4 galaxies. In contrast, the sSFR does not show variations with interaction stage. The relative constancy of the sSFR between the different stages suggests that this lack of evolution is not due to uncertainty in stage classification or in the association of interaction stage and progress along the interaction. Rather, our set of interacting galaxies shows no clear evidence for a burst of star formation prompted by the interactions or that such effects occur on timescales such that we see enhancements in both stellar mass and SFR, leaving the sSFR relatively stable. This suggests a need to be circumspect about this canonical activity during the early stages of galaxy mergers.

Different wavelengths have different effects in constraining galaxy parameters in the MAGPHYS SED analysis. UV data strongly inform the stellar population age; moreover, they contribute importantly to the accurate determination of the SFR and sSFR. The stellar mass is primarily determined by UBV-IRAC data. SPIRE data are crucial in determining the dust mass; in its absence the cold dust temperature tends to be underestimated, because the location of the peak is much less constrained without data longward of 170 μm. Cold dust mass, which tends to make up the bulk of the dust mass, goes as T^{-6} (assuming β=2), so the change in the dust mass is large for even a small underestimate in the dust temperature. The possible contributions to the SED

from AGN are modest for this sample and do not affect our conclusions.

The SFRs derived by MAGPHYS agree reasonably well with simple relations based solely or partially on IR photometry. Relations based on corrected FUV emission tended to overestimate SFR compared to the SED-derived SFR, which is averaged over 100 Myr. The SFR estimated from FUV can best be understood if it represents an exponential decay star formation history with a width of 30−50 Myr.

The complete SIGS sample will bring a significant increase in statistical power in determining galaxy property trends. In addition, testing the accuracy of MAGPHYS against simulations of interacting galaxies will help improve the diagnostic power of SEDs. In a future paper, we will examine what kind of simulated interactions and their parameters best reproduce observed systems and their SEDs. Further, we will test how well MAGPHYS recovers galaxy parameters as a function of their interaction details.

Acknowledgements

We are grateful to Gregory Snyder, Maria Koutoulaki, and Flora Stanley for their classifications of our galaxies, Steven Willner for his classifications and helpful comments, Volker Tolls for his assistance in processing *Herschel* data, Don Neill and Susan Neff at the *GALEX* helpdesk for the reprocessing of the observation of NGC 3690/IC 694, Erik Hoversten for his assistance with regards to the UVOT corrections, Christopher Klein for his preparation of the IRAC observations, and Joseph Hora for his assistance with galaxies on the edge of SPIRE observations. This work was based on archival data obtained from the Spitzer Science Archive, the Swift data archive, and the Herschel

Science Archive. This research has made use of the NASA/IPAC Extragalactic Database (NED), which is operated by the Jet Propulsion Laboratory, California Institute of Technology, under contract with the National Aeronautics and Space Administration as well as the the Mikulski Archive for Space Telescopes (MAST).This work was supported in party NASA grant NNX10AD68G and NASA JPL RSA 1369566. A.Z. acknowledges support from AR-12011X Chandra grant and EU IRG grant 224878.

Appendix A to Chapter 2: Classification Scheme

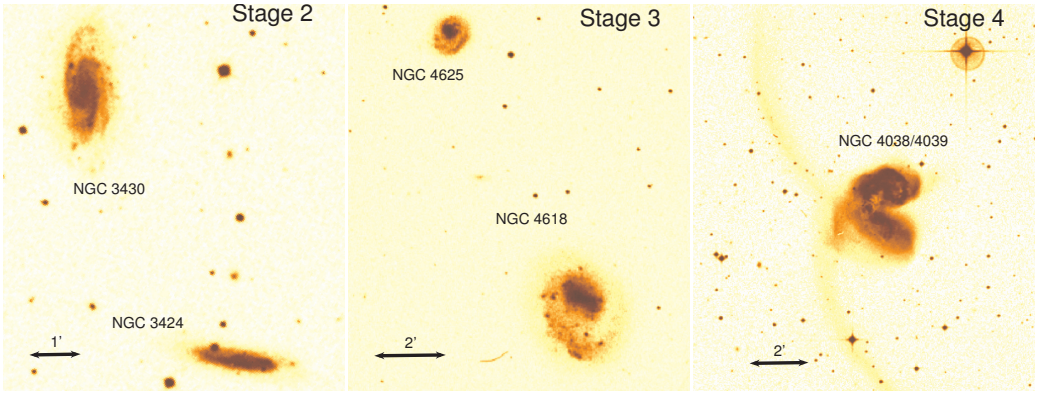

Figure 2.25: Representative examples of Stage 2−4 (left-right) galaxies, showing increasing morphological distortion.

The classification methodology used to determine the interaction stage of each system is based on the Dopita et al. (2002) classification scheme. Stage 1 galaxies are non-interacting and Stage 5 galaxies are post-merger or coalescence systems. Stages 2−4 are weakly, moderately, and strongly interacting systems, based on their degree of morphological distortion. In Figure 2.25, we show a representative system from our sample. The Stage 2 galaxies show little distortion and the galaxies are typically well

separated. The Stage 3 galaxies have a range of proximity and show some degree of distortion and the Stage 4 galaxies show significant morphological distortion and are typically close even in projection.

Appendix B to Chapter 2: Processing Concerns

PACS and High Pass Filters

In the course of processing the PACS photometry, we initially used the PhotProject pipeline scripts to make mosaics. When we compared the measured fluxes to values obtained by the MIPS and *IRAS* instruments at the same wavelengths, we found some were more than a factor of two too low, with M101 having the greatest disagreement. This disagreement is the result of the range of angular extents of the galaxies. The PhotProject pipeline includes a high pass filtering algorithm that removes a significant portion of the extended emission in the field and therefore affects nearby galaxies with more extended emission much more egregiously. As a result, we found it essential for nearby galaxies to use the MADmap (Cantalupo et al. 2010) pipeline.

Swift UVOT and Coincidence Losses

As we noted in Section 2.3.3, the UVOT telescope is vulnerable to coincidence losses. When multiple photons arrive in the same pixel within the same frame, only a single photon is counted. Losses become greater than 1% when the count rate exceeds 0.007 counts per second per pixel. While corrections for these losses and the uncertainties

involved is well determined for point sources (Poole et al. 2008; Kuin & Rosen 2008), there is a lack of similar understanding for extended sources. Although some of the sample galaxies, notably the starburst galaxies M82 and Arp 299, have count rates high enough over most of their surface that would result in significant coincidence losses, even for the rest of the sample have regions of high fluxes, typically limited to the nuclear area and star forming regions. We therefore opted to analyze only those galaxies lacking *GALEX* photometry as well as an additional test case, as described in Section 2.3.3. Fortunately for the two galaxies having UVOT, but lacking *GALEX*, only the nucleus and a few small regions are bright enough to require corrections. We excluded the regions with high count rates and then measured them independently as point sources, correcting them for coincidence losses using the method of Poole et al. (2008). These corrections always account for less than 1.5% of the count rate. Based on our test case of NGC 3424, the agreement between the *GALEX* and UVOT photometry is excellent.

Appendix C to Chapter 2:

Notes on Individual Galaxies

Group 1:

NGC 2976: A small galaxy on the outskirts of the M81 group, NGC 2976 has two active, infrared bright regions at the edges of its disk, whose presence is almost completely missed in the UV and NIR.

NGC 3031: Also known as M81, this galaxy is in our closest system and has very clear spiral arms and filamentary structure seen in all the images across our whole

filter range. Its nucleus is a LINER. The best-fit decomposition of the IR spectrum performed with DECOMPIR has a 4% AGN contribution to the total IR emission and a 16% contribution in the 8−35 μm range.

NGC 3034: M82 is one of the nearest starburst galaxies and has a strong galactic outflow perpendicular to its stellar disk, which is visible in both the UV and *Herschel* images. Its IRAC 5.8 μm, IRAC 8.0 μm, and MIPS 24 μm images are saturated. Its SED is among the worst fit by MAGPHYS with the current set of models. This may be due in part to the high obscuration − its fit has a $< \tau_V >= 2.9$ − or perhaps to the inclusion of some emission from the outflow, which MAGPHYS does not model. We measured the contribution of the outflow above and below the disk of the galaxy within the aperture and found that it contributes $\sim$ 20$−30% of the UV emission and $\sim$ 10%−20% of the emission at wavelengths greater than 150 μm, which does not fully account for the discrepancy in the UV bands. We selected the 3.6 μm-derived aperture to minimize the contribution of the emission from the outflow. The outflow's UV emission is primarily scattered light from the disk, while its IR emission is from the dust in the outflow. Since MAGPHYS cannot model such a feature, its inclusion would tend to bias the best-fit model.

NGC 3077: Another small galaxy in the M81 group, NGC 3077 lies behind a nearby bright star that prevented it from being observed in the UV by *GALEX* and UVOT. Its MIR−FIR images shows evidence of tidal stripping in the asymmetric structure and southwest lobe.

Group 2:

NGC 3185: This Seyfert galaxy shows a circum-galactic ring of star-forming material in both UV and IR images. The DECOMPIR decomposition requires a 3% and a 12%

contribution of the AGN to the total IR luminosity and $8-35\,\mu$m luminosity respectively. Its disk shows up in the FIR image as two bright regions at the opposite ends of the galaxy. It is the most distant member of the triplet it forms with NGC 3190 and NGC 3187 on the sky, but it and NGC 3190 have much closer recessional velocities than NGC 3187 (1217 km s^{-1} and 1271 km s^{-1} versus 1581 km s^{-1}). Group 2 is the only compact group in our sample, although the SIGS sample has several others. Tzanavaris et al. (2010) found a bi-modality for the sSFR distributions of compact groups depending on the slope of the IRAC photometry between $4.5\,\mu$mand $8.0\,\mu$m. NGC 3185 has a negative IRAC slope and its sSFR places it in the relatively quiescent population as expected by Tzanavaris et al. (2010).

NGC 3187: This galaxy has a pair of tidally elongated arms, which are best detected in the UV. This galaxy did not have archival *IRAS* fluxes. NGC 3187 has a positive IRAC slope and its sSFR places on the edge of the distribution of galaxies with positive slopes, argued by Tzanavaris et al. (2010) to indicate active star formation.

NGC 3190: The most massive of the three galaxies in this group, NGC 3190 is a nearly edge on LINER and has a dust lane, that appears prominently in absorption in UV and is correspondingly bright in IR emission. Its SED shows particularly low UV relative to its visible emission, but presumably the geometry of this dust lane explains the poor fit to the UV and the disagreement in the estimates of its SFR. The DECOMPIR best-fit requires no contribution from an AGN. NGC 3190 has a negative IRAC slope, but the low SFR value derived by MAGPHYS places it in the quiescent category of Tzanavaris et al. (2010).

Group 3:

NGC 3226: As an elliptical galaxy, NGC 3226's emission is dominated by its stars,

although there appears to be a faint tidal feature in the 8 μm emission directed roughly to the north. NGC 3226 is particularly faint in the MIR relative to its NIR emission and only has upper limits in the MIR-FIR from *IRAS*. It has a LINER nucleus, but the decomposition of its IR spectrum indicates no significant contribution from an AGN.

NGC 3227: Along with its smaller companion NGC 3226, NGC 3227 was not observed by *GALEX*, so we use UVOT data instead. Its IRS spectrum shows [Ne V] emission consistent with a Seyfert nucleus. Its DECOMPIR fits are the worst of the nine galaxies, but have the highest AGN contribution of 15%−25% to the total IR luminosity and 45%−60% of the MIR luminosity.

Group 4:

NGC 3395/3396: The apertures of this pair of galaxies overlapped sufficiently to make determination of the emission belonging to each galaxy problematic. We therefore opted to treat the system as a combined system. This pair of galaxies is distantly associated with Group 5. This group does not have UBV photometry. The SED shows little attenuation in the UV and strong 60 μm emission relative to the 100 μm emission.

Group 5:

NGC 3424: This edge-on galaxy's central region becomes increasingly bright relative to its disk with increasing wavelength. Similarly to NGC 3190, the other nearly-edge on galaxy, its NUV−FUV slope is quite steep and not particularly well fit by MAGPHYS. We used this galaxy as a test case for analyzing UVOT photometry and found good agreement with the *GALEX* photometry. It lacks UBV photometry.

NGC 3430: Seen nearly face-on, this galaxy has a large and extended UV disk. This system provides a nice example of a system fairly early in the interaction sequence and hence fairly undisturbed morphologically. The IR peak of its SED is not very well

constrained as this galaxy was not observed by PACS and did not have MIPS 70 μm and 160 μm fluxes available.

Group 6:

NGC 3448: This is the larger member of this pair of dwarf galaxies. A bridge of emission extends from NGC 3448 in the direction of UGC 6016, seen most prominently in the NUV.

UGC 6016: This dwarf galaxy is very faint in the IR, but has a large but diffuse UV envelope. Due to its lack of significant detections in several of our filters and in ancillary *IRAS*, we cannot constrain the galaxy parameters very tightly. Its distance is also the most uncertain of the sample as it did not have a distance modulus or a recessional velocity in the PSCz catalog.

Group 7:

NGC 3690/IC 694: Also known as Arp 299, this system is the most active in our sample, with the highest amount of star formation and is our only LIRG, showing a corresponding large amount of UV attenuation. Its 8 μm image is saturated, and it does not have ancillary UBV fluxes.

Group 8:

NGC 3786/88: The galaxies in this pair have very similar UV−NIR fluxes, but NGC 3788, which is more edge-on, has higher fluxes in the *Herschel* bands. However, their best-fit SEDs have similar infrared luminosities, likely due to the relatively high contribution of the warm dust in the model for NGC 3786 compared to NGC 3788. Neither galaxy has ancillary *IRAS* or UBV fluxes. NGC 3786 is a Seyfert galaxy, with a bright nuclear region showing [Ne V] emission in its IRS spectrum and a partial ring of

star-forming regions. Its decomposition requires an AGN contribution of 7% and 26% to the total IR luminosity and MIR luminosity respectively.

Group 9:

NGC 4038/4039: Also known as the Antennae, this pair of galaxies is one of our most evolved systems and, because we cannot separate them, we treat it as a single entity. Its clumpy distribution of star forming regions are clearly apparent at 8 μm and in the UV bands; the two nuclei are most clearly seen in 2MASS and IRAC, a reflection of the relative PAH strengths to warm dust.

Group 10:

NGC 4618: Paired with NGC 4625 in a roughly equal-mass dwarf galaxy interaction, NGC 4618 has an off-center nucleus with a single arm curving to the south-west, features seen in all the images.

NGC 4625: While relatively compact in the infrared, NGC 4625 has a faint, diffuse set of flocculent set of spiral arms observed best in the NUV band.

Group 11:

NGC 4647: This spiral galaxy is located at the edge of the IRAC field, which complicated the measurement of its flux because its aperture, determined on the NUV image, extends past the edge of the IRAC image. We had to manually correct for the edge pixels without flux. We also do not have ancillary UBV fluxes.

NGC 4649: A large elliptical galaxy also known as M60, NGC 4649 is very faint in the mid-infrared and absent in the far-infrared, a dramatic contract to its companion. It has the lowest sSFR of the sample.

Group 12:

M51A: The Whirlpool Galaxy is the larger galaxy in this well-studied system. It has quite consistent morphology across the wavelengths, but with more inter-arm filamentary emission and greater extent in the UV than in the IR. The decomposition of its IR spectrum is best fit without an AGN contribution, despite its LINER nucleus. This is one of the systems where the flux from the smaller galaxy was subtracted from the aperture of the large galaxy.

M51B: The smaller companion to the Whirlpool Galaxy, M51B is dominated by early-type stars and has very little UV emission. Its FIR emission is confined to its nucleus. Its MIPS 160 μm measurement was a factor of three lower than the PACS measurement, and we opted to omit it from the fits.

Group 13:

NGC 5394/95: The smaller galaxy of our most distant pair, NGC 5394 shows a beautiful pair of tidal tails, especially in the UV. NGC 5395 has a LINER nucleus, which requires only a small AGN contributions of 3% and 12% to the galaxy's total IR and MIR luminosities respectively in the DECOMPIR fits. This is the other system where the small galaxy flux needed to be subtracted from the large galaxy aperture.

Group 14:

M101: Another well-studied galaxy, its *GALEX*, *Spitzer*, and *Herschel* images show clumpy star forming region structures along the spiral arms. Its large size made determining a single unbroken aperture with SExtractor complicated. As a result, some of the outermost UV emitting regions were not included.

NGC 5474: A small companion to M101, its core is offset to the north from its center.

Chapter 3

Simulated Galaxy Interactions as Probes of Merger Spectral Energy Distributions

This thesis chapter will be submitted to the Astrophysical Journal

L. Lanz, C. C. Hayward, A. Zezas, M. Ashby, H. A. Smith, N. Brassington, G. G. Fazio, L. Hernquist

Abstract

We present the first systematic comparison of simulated spectral energy distributions (SEDs) from the ultraviolet to the far infrared of a suite of hydrodynamically-modeled galaxy interactions to the SEDs of a local sample of interacting galaxies. We identify the aspects of simulations necessary to reproduce the observed SEDs. Our sample of

interacting galaxies is drawn from the Spitzer Interacting Galaxy Survey, and probes a range of galaxy interaction parameters. We use the 31 galaxies in fourteen systems which have been observed with *Herschel*, *Spitzer*, *GALEX*, and 2MASS. We create a suite of hydrodynamic simulations with stellar masses comparable to those in our sample of interacting galaxies using GADGET-3. Simulated photometry is calculated using the SUNRISE radiative transfer code. From a comparison of the simulated and observed SEDs, we find that the best matches typically originate from same few simulations around the time of coalescence. The best matches recover infrared luminosity and the star formation rate of the observed systems; the more massive systems preferentially match SEDs from simulations of more massive galaxies. While the most morphologically distorted systems in our sample are associated only with simulated SEDs very close to coalescence, other morphological interaction classes match well with SEDs over a wide range of interaction stages, suggesting that an SED alone is insufficient to identify interaction stage, consistent with the evolution of the SED and its frequently degenerate appearance in all the simulations.

3.1 Introduction

Galaxy interactions, particularly in the case of major mergers, are responsible for some of the most dramatic activity seen in galaxies. In the canonical view, interactions stimulate star formation, thereby powering the high infrared (IR) luminosities often seen in such systems (e.g.,Veilleux et al. 2002): driving gas inflows to the central regions, resulting in heightened activity of the central supermassive black hole and local starburst activity (e.g., Di Matteo et al. 2005; Springel et al. 2005), and leading

to significant morphological distortions (e.g., Hopkins et al. 2006; Mihos & Hernquist 1994; 1996). These activities, however, occur on timescales that make detecting any evolution in individual systems or tracing the corresponding development in physical processes impossible. Hydrodynamic simulations of interacting galaxies provide a means of studying the interaction sequence while bypassing the problem of the timescales.

A crucial test of any simulation is its ability to reproduce observations. Hydrodynamic simulations of galaxy interactions have primarily been tested in two ways: how well they reproduce the (optical) morphological distortions seen in such systems, and how closely their simulated emission tracks that of real systems. Some simulations are created to reproduce specific systems (e.g., Privon et al. 2013; Karl et al. 2013), while others compare specific properties, such as colors, of a suite of simulations to observations (e.g., Snyder et al. 2013; Jonsson et al. 2010).

Toomre & Toomre (1972) were the first to systematically model the morphologies of interacting galaxies. They used simple simulations of massless particles around two masses to reproduce the tails and bridges seen in systems like the M51, the Mice (NGC 4676) and the Antennae (NGC 4038/4039). Much more recently, Barnes & Hibbard (2009; see also Barnes, 2011) developed Identikit, a modeling tool that uses N-body simulations to reproduce the morphology and kinematics of tidal tails in interacting systems. Privon et al. (2013) demonstrated Identikit's ability to reproduce the morphology and H I kinematics of NGC 5257/5258, the Mice, the Antennae, and NGC 2623 and to estimate the time since the first pericenter passage and to coalescence.

Morphological analyses like these inherently suffer from an obvious bias: simulations trace mass but observations trace light. A better comparison entails the propagation of

light from the simulated luminous matter to a fiducial observer. SUNRISE (Jonsson 2006) accomplishes exactly that. It is a radiative transfer code that propagates the emission of simulated stars and active galactic nuclei (AGN) through a dusty interstellar medium (ISM) using the hydrodynamic simulations outputs. It is an ideal tool for creating simulated spectral energy distributions (SEDs) for comparison to photometry. Jonsson et al. (2010) simulated the SEDs of seven isolated galaxies, which they compared to Spitzer Infrared Nearby Galaxies Survey (SINGS; Kennicutt et al. 2003) galaxies from Dale et al. (2007). The Jonsson et al. (2010) simulations did not cover all of the parameter space spanned by SINGS; nonetheless, good matches from the SINGS sample were found for each of the simulated galaxies, demonstrating the ability of SUNRISE to produce realistic galaxy SEDs and leading credibility to the simulations overall. Karl et al. (2013) combined both techniques, by creating a set of hydrodynamic simulations to reproduce the morphology of the Antennae and performing radiative transfer to determine the predicted emission in the Herschel Space Observatory's Photodetector Array Camera and Spectrometer (PACS) bands.

There has not previously been a systematic comparison of the observed and simulated SEDs from the ultraviolet (UV) to the far-IR (FIR) for interacting galaxies. Jonsson et al. 2010 tested the realism of their isolated spiral galaxy simulations by finding a SINGS galaxy whose SED were similar. Our study takes a related but different approach. We determine the set of our simulated SEDs which best reproduce the observed SEDs of a sample of interactions and identify the simulation properties, such as stellar mass, SFR, or interaction stage, common to the set.

At low redshifts, the interaction stage is generally determined based on the degree of morphological distortion observed (e.g. Dopita et al. 2002). At high redshift,

morphological details can become impossible to resolve, making this classification method infeasible. A spectral marker for interaction stage would be a powerful tool for examining how interactions at high redshift compares to local interactions. Therefore, we ask whether there is an unambiguous signature of the interaction stage in the SED. While we will not discuss the morphology of the best matches in this chapter, a clear extension of our study is to test whether there is a signature of the morphology in the SED by finding common morphology either within the set of best matches or between the matches and the observation.

In this chapter, we compare the SEDs of a suite of simulations of interacting and isolated spiral galaxies to the SEDs of 31 interacting galaxies to examine the simulation properties necessary to reproduce the SED of an observed system. This chapter is organized as follows. We summarize our sample selection and the photometry in Section 2. In Section 3, we describe the hydrodynamic simulations and the radiative transfer done in post-processing. We discuss our matching methodology and the best matched SEDs in Section 4. Section 5 contains a discussion of the origins of the best and worst matched SEDs, a comparison between the stellar and dust masses, dust luminosity, star formation rate (SFR), specific star formation rate (sSFR) of the observed systems and the best matched simulated counterparts, an analysis of the effectiveness of morphology-based interaction stage classification scheme, and an examination of the evolution of SEDs in major mergers. We summarize our results in Section 6.

3.2 Observations

Our sample and observations are described in detail in Lanz et al. (2013). Here we summarize the selection criteria for our galaxies and briefly describe the photometry and the fitting process that provides the stellar masses, dust masses and temperatures, SFR, and sSFR that we will compare to the simulations.

3.2.1 Sample Selection

Our galaxies are part of the Spitzer Interacting Galaxy Survey (SIGS) (N. Brassington et al. 2013, in preparation). SIGS was selected strictly on the basis of interaction probability and hence cover a broad range of interaction stages. It is a sample of local galaxies because its selection criteria include a requirement that $cz < 4000$ km s^{-1}.

In Lanz et al. (2013), we examine the fourteen systems with the most extensive wavelength coverage, extending from the *Galaxy Evolution Explorer* (*GALEX*; Martin et al. 2005) far-UV (FUV) band at 0.15 μm to the Spectral and Photometric Imaging Receiver (SPIRE) band at 500 μm. This sample spans the range of interaction stages, having galaxies likely to be in their initial approach (e.g., NGC 3424/3430) as well as galaxies in coalescence (e.g., NGC 3690/IC 694). It also covers a wide range of stellar masses ($1.0\times10^8 - 1.5 \times 10^{11}$ $M_\odot$), stellar mass ratios (1:1 − 1:40) and total infrared luminosities ($1.3\times10^{10} - 5.1 \times 10^{14}$ $L_\odot$). Although consisting primarily of spiral-spiral interactions, our sample also contains two spiral-elliptical interactions. In Table 3.1, we list our interacting galaxies along with distance and interaction stage estimates. This sample is used to prepare the 21 interacting pairs that we compare to the simulations.

Table 3.1. Sample Description

Group (1)	Galaxy (2)	R.A. (J2000) (3)	Decl. (J2000) (4)	Distance (Mpc) (5)	Interaction Stage (6)
1	NGC 2976^{+}	09 47 16.3	+67 54 52.0	3.75	2
	NGC 3031	09 55 33.2	+69 03 57.9	3.77	2
	NGC 3034	09 55 52.2	+69 40 47.8	3.89	2
	NGC 3077^{+}	10 03 19.8	+68 44 01.5	3.93	2
2	NGC 3185	10 17 38.7	+21 41 16.2	22.6	2
	NGC 3187	10 17 48.4	+21 52 30.9	26.1	3
	NGC 3190	10 18 05.7	+21 49 57.0	22.5	3
3	NGC 3226	10 23 27.0	+19 53 53.2	23.3	4
	NGC 3227	10 23 30.5	+19 51 55.1	20.6	4
4	NGC 3395	10 49 50.0	+32 58 55.2	27.7	4
	NGC 3396	10 49 55.2	+32 59 25.7	27.7	4
5	NGC 3424	10 51 46.9	+32 54 04.1	26.1	2
	NGC 3430	10 52 11.5	+32 57 05.0	26.7	2
6	NGC 3448	10 54 38.7	+54 18 21.0	24.4	3
	UGC 6016^{+}	10 54 13.4	+54 17 15.5	27.2*	3
7	NGC 3690/IC 694	11 28 31.2	+58 33 46.7	48.1*	4
8	NGC 3786	11 39 42.5	+31 54 34.2	41.7	3
	NGC 3788	11 39 44.6	+31 55 54.3	36.5	3
9	NGC 4038/4039	12 01 53.9	−18 52 34.8	25.4	4
10	NGC 4618^{+}	12 41 32.8	+41 08 44.4	7.28	3
	NGC 4625^{+}	12 41 52.6	+41 16 20.6	8.20	3
11	NGC 4647	12 43 32.6	+11 34 53.9	16.8	3
	NGC 4649	12 43 40.0	+11 33 09.8	17.3	3
12	M51A	13 29 54.1	+47 11 41.2	7.69	3
	M51B	13 29 59.7	+47 15 58.5	7.66	3
13	NGC 5394	13 58 33.7	+37 27 14.4	56.4*	4
	NGC 5395	13 58 37.6	+37 25 41.2	56.4*	4
14	M101	14 03 09.8	+54 20 37.3	6.70	3
	NGC 5474^{+}	14 05 01.2	+53 39 11.6	5.94	3

Note. — Distance moduli were obtained from Tully et al. (2008), Tully (1994), and the Extra-galactic Distance Database. Galaxies marked with $^{+}$ are dwarf galaxies with stellar mass of less than $1 \times 10^9\,M_\odot$. NGC 2976/3077 and NGC 4618 4625 are dwarf pairs. The distances in Column 5 marked with * did not have distance moduli and were calculated based on heliocentric velocities, corrected per Mould et al. (2000) and assuming $H_0 = 72$ km s^{-1} Mpc^{-1}. The determination of interaction stage is described in Section 2.2. In Column 6 we give the median of the Dopita system classifications.

3.2.2 Photometry

For each galaxy in our sample, we use the global photometry in the available subset of 25 photometric datasets from the UV with *GALEX* to the FIR with SPIRE on *Herschel* measured in the larger of the two elliptical apertures necessary to contain all of the *GALEX* near-UV (NUV) and *Spitzer Space Telescope*'s (Werner et al. 2004) Infrared Array Camera (IRAC) 3.6 μm emission. We summarize the available photometry in order of increasing wavelength. *GALEX* photometry was available for all but three of our galaxies (NGC 3226, NGC 3227, and NGC 3077), which could not be observed due to the presence of nearby foreground bright stars. Optical photometry were retrieved from the Third Reference Catalog (RC3; de Vaucouleurs et al. 1991), which had *UBV* for 50% of the sample and *BV* for an additional 25%. The Two Micron All Sky Survey (2MASS; Skrutskie et al. 2006) yielded near-IR (NIR) photometry for the whole sample. *Spitzer*'s IRAC and Multiband Imaging Photometer (MIPS) instruments provided mid-IR (MIR) photometry from 3.6 μm to 24 μm for the whole sample. Measured photometry in the MIR was supplemented by ancillary photometry from *Infrared Astronomical Satellite (IRAS)* (Surace et al. 2004; Sanders et al. 2003; Soifer et al. 1989, Moshir et al. 1990), and MIPS 70 μm and 160 μm data from SINGS (Dale et al. 2005, 2007). Lastly, FIR photometry was measured by PACS for twelve of fourteen systems and by SPIRE for all fourteen systems. Details of the photometry and their reduction can be found in Lanz et al. (2013).

3.2.3 Interaction Stage Classification

Understanding galaxy interactions requires examination of systems at different interaction stages as interactions proceed on timescales much too long for significant evolution to be observed in a single system. However, determining the order of observed systems on the interaction sequence is not necessarily a straight forward process. For example, a pair of galaxies coming in for the first close passage can appear very similar to a pair that has already passed near to each other and separated once more. Additionally, projection effects complicate the determination of the sequence of observed systems.

Here and in Lanz et al. (2013) and Brassington et al. (in preparation), we use the five-stage scheme devised by Dopita et al. (2002). Stage 1 galaxies are non-interacting. Stage 2 galaxies have little or no morphological distortion. These systems are typically expected to be before or after the first passage. Stage 3 galaxies show a moderate degree of distortion, including tidal tails. Stage 4 galaxies show strong signs of disturbance and are expected to be in the more evolved interactions stages. Finally, the Stage 5 galaxies are post-merger systems. Our systems cover Stages 2−4. By contrast, the simulations contain both isolated and interacting pairs, so the simulated systems span all five stages.

3.2.4 Deriving Galaxy Properties of the Observed Systems

We use the SED fitting code MAGPHYS (da Cunha et al. 2008) to estimate the SFR, sSFR, and stellar and dust masses. MAGPHYS fits SEDs with a stellar spectra library derived from the Bruzual & Charlot (2003) stellar population synthesis code and a thermal infrared dust spectrum. The ISM is modeled as a diffuse medium interspersed with denser stellar birth clouds. The dust emission is treated as the sum of four

components: two modified blackbodies of 30-60 K ($\beta = 1.5$) dust and 15-25 K ($\beta = 2$) dust, a MIR continuum consisting of the average of two $\beta = 1$ modified blackbodies at 130 K and 250 K, and a polycyclic aromatic hydrocarbon (PAH) template (Madden et al. 2006) with an 850 K ($\beta = 1$) modified blackbody underlying continuum. MAGPHYS estimates galaxy SFRs, stellar masses, dust masses, and dust temperatures. We provide MAGPHYS with the photometry in our set of 25 filters. We use a slightly modified version that provides SFR and sSFR estimates averaged over 1 Myr and 10 Myr, as well as the 100 Myr average that is output by the code by default.

3.3 Simulations

We based our analysis on a coherent suite of galaxy interaction simulations, described briefly here. We began by creating four simulated spiral galaxies modeled on the properties typical of SDSS galaxies spanning a mass range from $1 \times 10^9\,M_\odot$ to 5×10^{10} $M_\odot$. These objects are referred to as G0, G1, G2, and G3 in Table 3.2. We simulated each progenitor in isolation (four simulations) and also performed binary galaxy merger simulations of each possible progenitor combination (ten simulations). At numerous times during each simulation and from seven different viewing angles, we computed the emergent combined spectra of the interacting and isolated systems. The degree to which these spectra reproduced the SEDs of our sample galaxies was measured for all simulations, snapshots, and viewing angles, and was the basis on which we assessed the simulation's ability to model the SEDs of realistic systems. This complex process is described in detail below.

3.3.1 Hydrodynamical Simulations

We performed our suite of simulations of both isolated and merging galaxies using the TreeSPH (Hernquist & Katz 1989) code GADGET-3, which uses a hierarchical tree method to compute gravitational interactions. An algorithm of this type groups distant particles into increasingly large cells and computes their joint gravitational pull on a given single particle, thereby significantly reducing the number of calculations. Gas dynamics are modeled via smoothed-particle hydrodynamics (SPH; Lucy 1977; Gingold & Monaghan 1977; Springel 2010), a grid-free method that can easily accommodate higher resolution in denser regions. The version of GADGET-3 used for our simulations includes radiative heating and cooling (Springel et al. 2005; Katz et al. 1996).

Each galaxy is modeled as an exponential, rotationally-supported gas and stellar disk embedded in a dark matter halo modeled with a Hernquist (1990) profile. As a result of self-gravity and radiative cooling, the gas in the the simulated galaxies becomes sufficiently dense and cold for the formation of stars. The rate of radiative cooling is primarily dependent of the local gas density and its internal energy. Star formation is assumed to follow a Schmidt-Kennicutt law (Schmidt 1959; Kennicutt 1998) and hence the simulated SFR is proportional to gas density and inversely proportional to the local dynamical timescale. Since SPH particles typically contain $\geq 10^5\,\mathrm{M}_\odot$, individual stars are not created. Instead, gas particles stochastically produce equal-mass star particles such that the SFR averaged over the simulation agrees with the rate given by the Schmidt-Kennicutt law.

We performed fourteen GADGET-3 simulations: one for each of the four progenitor galaxies and one for each of the ten possible pair of galaxies. We summarize the

properties of these simulated galaxies in Table 3.2. The galaxies are modeled to have median properties of SDSS galaxies and increase in mass from G0 (1×10^9 $M_\odot$ of stars) to G3 (5×10^{10} $M_\odot$ of stars). Further details are given in Jonsson et al. (2006) and Cox et al. (2008). Each galaxy was allowed evolve secularly in isolation for 6 Gyr. Since gas is not accreted from the surrounding environment, the SFR decreases as gas is used. For the interactions, each pair of galaxies (G0G0, G1G0, G1G1, G2G0, G2G1, G2G2, G3G0, G3G1, G3G2, or G3G3) were placed on parabolic orbits such that the disks were prograde with initial separations increasing with the mass of the larger galaxy: 50 kpc for G0, 80 kpc for G1, 100 kpc for G2, and 250 kpc for G3. Each interaction is followed as it evolves from first approach through multiple pericenter passage to the final coalescence and post-merger stage. The different interactions take between 2.5 Gyr and 6 Gyr to reach the passively evolving stage at which we end a simulation.

Table 3.2. Galaxy Models for the Simulations

	G3	G2	G1	G0
M_* (10^{10} $M_\odot$)	5.0	1.5	0.5	0.1
Total Mass (10^{10} $M_\odot$)	116.0	51.0	20.0	5.0
M_{Gas} (10^{10} $M_\odot$)	1.22	0.48	0.20	0.06
Metallicity, Z ($Z_\odot$)	1.00	0.56	0.40	0.28
Number of particles	240,000	150,000	95,000	51,000
$N_{Dark\ Matter}$	120,000	80,000	50,000	30,000
N_{Gas}	50,000	30,000	20,000	10,000

Note. — Simulation parameters with further details given in Tables 1 of Jonsson et al. (2006) and Cox et al. (2008).

3.3.2 Radiative Transfer

SUNRISE calculates the emission from stars and AGN in the GADGET-3 simulation and performs radiative transfer calculations through the ISM dust. Starburst99 (Leitherer et al. 1999) SEDs are used to model the stellar emission and the AGN emission is given by the luminosity-dependent templates of Hopkins et al. (2007). The dust distribution within each galaxy is assumed to be traced by the distribution of the ISM metals in the hydrodynamic simulation with a dust-to-metal gas ratio of 0.4 (Dwek 1998; James et al. 2002). We assume that the dust properties are similar to those of Milky Way (MW) dust and assume the $R = 3.1$ model of Weingartner & Draine (2001) as updated by Draine & Li (2007) (hereafter DL07).

SUNRISE uses a Monte Carlo approach to perform the radiative transfer calculations. Photon packets are emitted and then absorbed by dust as their propagation through the ISM is tracked. In order to accurately determine dust temperatures, SUNRISE uses an iterative method. Dust temperatures are calculated assuming thermal equilibrium based on the grain size and radiation field. SUNRISE calculates an SED per pixel (yielding results analogous to integral field unit spectrography). We determined the integrated photometry of each system from seven viewing angles distributed isotropically in solid angle. While the conditions of the hydrodynamic simulations are saved at 10 Myr intervals, the SEDs are primarily calculated with SUNRISE at 100 Myr intervals, but over the most active periods of the most massive interactions, SEDs were calculated at 10 Myr or 20 Myr intervals. The resulting suite of simulated SEDs of the fourteen simulations has 848 snapshots each observed from seven viewing angles distributed isotropically in solid angle for a total of almost 6000 SEDs.

GADGET-3 uses the Springel & Hernquist (2003) multiphase model for the ISM, assigning a fraction of the gas to dense and diffuse phases based on the average gas density. The dense clumps are assumed to be much smaller in size than the resolved elements for the radiative transfer code. As a result, SUNRISE has two options for radiative transfer through a grid cell: it can assume that the dense clumps have a negligible filling fraction and therefore only consider the diffuse medium in the radiative transfer process (default ISM model), or it can spread the contents over the grid cell evenly and determine the radiative transfer through this average ISM (alternative ISM model). In this chapter, we discuss a comparison between the default ISM SUNRISE run and the observed photometry. SUNRISE runs using the alternative ISM model are presently being conducted and will be presented in the revised paper version of this chapter.

Estimating the Uncertainty in the Simulated SEDs

Radiative transfer codes must inherently make assumptions about the material through which photons are propagated and the source of those photons. For example, in our SUNRISE run, we assumed MW dust composition rather than Large Magellanic Cloud (LMC) and Small Magellanic Cloud (SMC) dust compositions. In order to assess the uncertainty in the simulated SED, we examine six SUNRISE runs calculated for an equal-mass spiral-spiral merger similar to our simulated interactions, wherein the hydrodynamic inputs remain constant but the assumptions on the ISM properties and AGN presence were varied. Figure 3.1 shows SEDs (left) at five different times during the interaction for the six different models, as well as the fractional difference (right) between the fiducial model (black) and each test model.

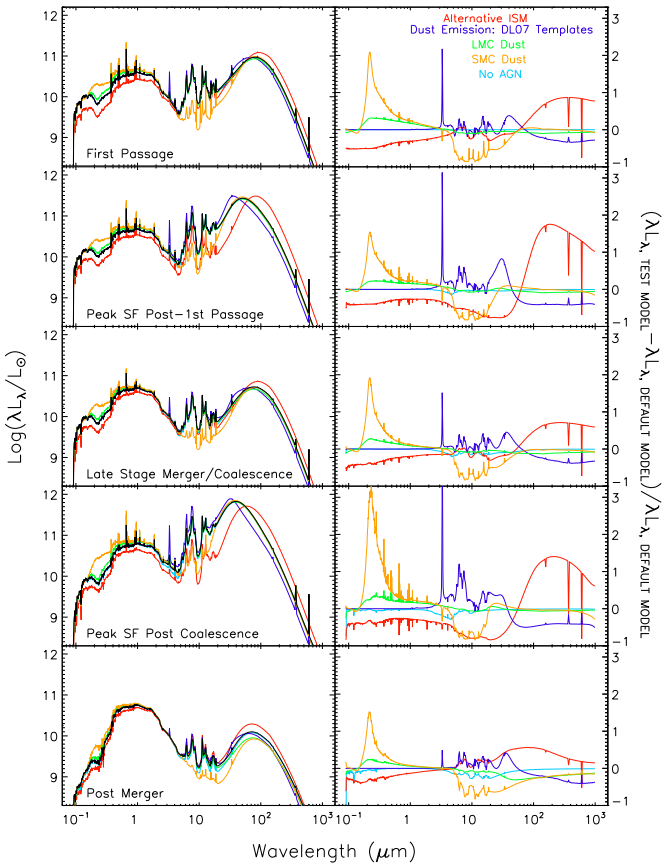

Figure 3.1: SEDs (left) for six different SUNRISE radiative transfer runs at five times of interest (each row) for an equal-mass interaction similar to our simulations. The black line shows the default model SED created with the default SUNRISE parameters, which are the ones used in the SUNRISE processing of our simulations. In the right column, we show the fractional difference between each other model and this fiducial model. The red, alternative ISM SED shows the results when the radiative transfer is calculated through the average ISM in a grid cell rather than only through the diffuse medium, thereby ignoring the cold, dense phase. The dark blue SED is the result of determining the dust emission spectrum using the Draine & Li (2007) spectra parametrized by the interstellar radiation field intensity. The green and yellow SEDs are the result of assuming LMC and SMC dust, respectively, rather than Milky Way dust. The cyan SED demonstrates the effect of removing the AGN contribution.

As we noted, SUNRISE has two possibilities for the treatment of the multiple ISM phases. The black fiducial model uses the default ISM treatment in which dense clumps are ignored. The red line in Figure 3.1 shows the SED derived when the alternative ISM methodology is employed and radiative transfer is calculated through the average ISM content of a grid cell. There are two main effects on the SED: colder dust temperatures (and hence enhanced emission in the SPIRE bands) and an increase in the absorption in the optical and UV.

In green and yellow in Figure 3.1, we show the SEDs that result with the assumption of LMC and SMC dust. The effect of low metallicity, particularly of the SMC dust, is seen in the significantly reduced NUV absorption and the lack of PAH features in the MIR. The dark blue SED shows an alternative method to the radiative transfer: the dust emission is assumed to follow the templates of DL07, which are parametrized with respect to the intensity of the radiation field. In particular, the 3.3 μm PAH is typically much stronger in the template. The effect of the AGN (cyan) is most strongly felt in the MIR around 10 μm, and only becomes apparent in the later interaction stages.

Figure 3.2 shows the uncertainty engendered in the SED produced for each snapshot of this simulation due to the choices made in the radiative transfer process and the viewing angle. Each line is the standard deviation of the five lines shown in one of the right panels in Figure 3.1 as seen from seven viewing angles. To show the evolution of this uncertainty over the course the simulation, the color of the line varies from purple to blue to green to yellow. We find that the NIR and MIR show little evolution with time. Their variation with respect to the fiducial model is typically $\approx$20% and 30$-$40%, respectively. The MIR is dominated by the variety of PAH models, specifically the decrement in the SMC model due to reduced metallicity and the excess in the DL07

model. The significantly lower absorption in the NUV in the SMC model results in the high standard deviation around 0.2-0.3 μm. The standard deviation in the far-IR (FIR) is dominated by the assumption on clumpiness and is typically at least 40%. The FIR also shows the most evolution with time. Its standard deviation rises from 40% to ∼80% during first passage and to 100% during coalescence. If we determine the median uncertainty over all the snapshots and over the whole SED, we find a typical uncertainty of 30% in a single viewing angle and 35% overall.

3.4 Methodology

3.4.1 Matching Criterion

We seek to identify which properties of a simulation are necessary to reproduce the SED of an observed system. We therefore chose to do a brute-force evaluation of all simulated SEDs with the SED of each interacting system by means of the χ^2 statistic between each pair of simulated and observed SEDs:

$$\chi^2 = \sum_{\mathrm{SED}} \frac{(\mathrm{L}_{\nu,\mathrm{Data}} - \mathrm{L}_{\nu,\mathrm{Model}})^2}{\sigma^2_{\mathrm{Data}} + \sigma^2_{\mathrm{Model}}} \tag{3.1}$$

Although the uncertainty in the observed photometry, which is primarily driven by the calibration uncertainty of the instruments, varies with wavelength, we have chosen to use a constant 10% uncertainty on the observed photometry. This is representative of the uncertainty on the *GALEX* and *Herschel* photometry and not excessively conservative for the NIR-MIR data. We are interested in determining the best match to the entire

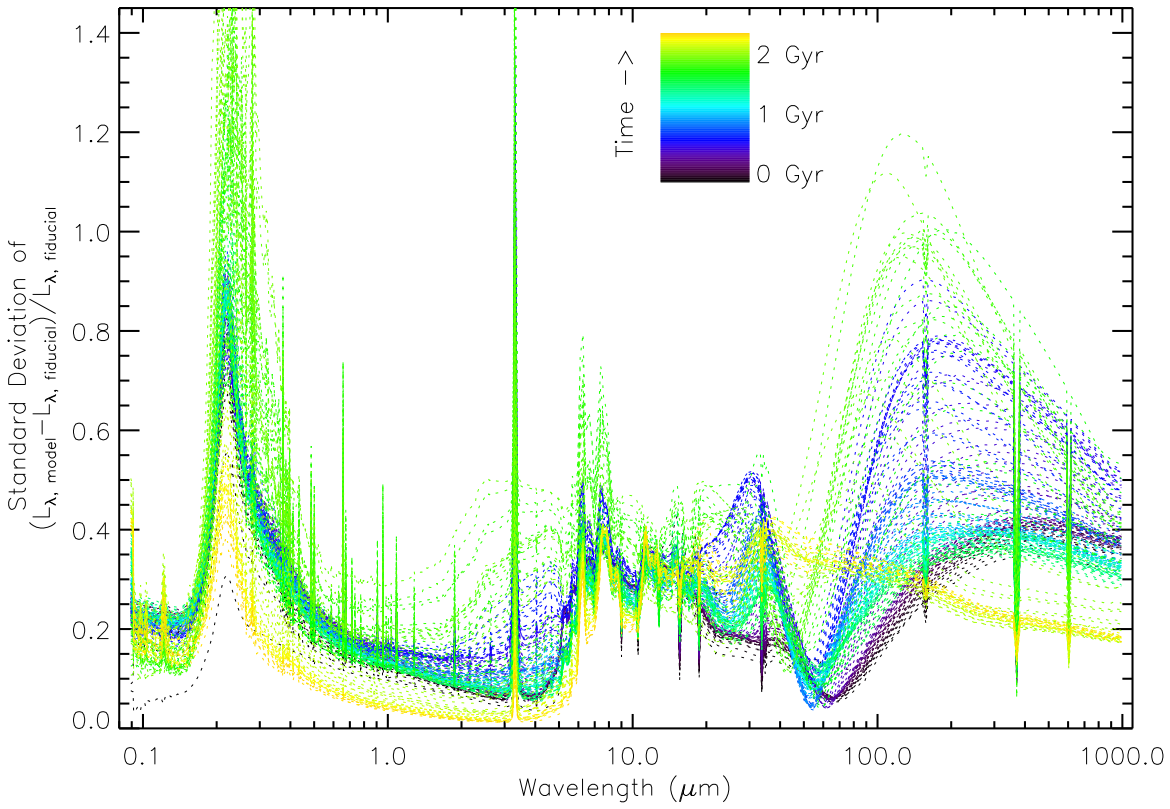

Figure 3.2: Each line shows the standard deviation of the fractional difference between the five test models shown in Figure 3.1 and the fiducial model as seen from seven viewing angles for a single snapshot. Changing colors (from blue to green to yellow) show the evolution of time. For example, the FIR emission is typically about 40% different, rising to 80% and 100% different during the times that correspond to the second and fourth rows of Figure 3.1.

SED, which is a question better answered when the matching methodology is not driven by the NIR-MIR data due to their smaller uncertainties.

For most uses of the χ^2 statistic, the model uncertainty is assumed to be negligible. However, as discussed in Section 3.2.1 there is significant uncertainty in the models, mainly arising from unknown parameters such as the ISM properties regarding which a variety of assumptions must be made for radiative transfer to be effected. Based on our examination of the uncertainty in the simulated SEDs, we determined that a uncertainty of 30% realistically represented our confidence in the simulated SEDs. Since both our observed and simulated galaxies have a large range of luminosities, this uncertainty can be as larger or larger than the uncertainty on the data. Hence, our calculation of the χ^2 statistic must include the uncertainty both the observed and simulated SED. Therefore, the statistic we use to compare the observed and the model SEDs is given by:

$$\chi^2 = \sum_{\text{SED}} \frac{(\text{L}_{\nu,\text{Data}} - \text{L}_{\nu,\text{Model}})^2}{(0.10 \times \text{L}_{\nu,\text{Data}})^2 + (0.30 \times \text{L}_{\nu,\text{Model}})^2} \tag{3.2}$$

3.4.2 Selection of the Best and Worst Matches

In Figure 3.3, we show the reduced[1] χ^2 value for each pairing of an observed and simulated SED ordered by simulation. We used this figure to select the sets of 5 (red) and 100 (cyan) best matching simulated SEDs with the lowest χ^2_ν statistic to examine for trends. The best 5 matches ($\approx 0.1\%$ of the simulated SEDs) generally come from the

[1]Because we examine the trends as a function of simulation, snapshot (or time), and viewing angle, we effectively have three free parameters.

same family of models, and provide a sense of the variation within that family. The best matches do not come preferentially from any particular family of models. The difference in χ^2 between the best and 5th best match is on average 3.3. The best-matched 100 of the simulated SEDs cover the $3-4$ groups of best matches. The larger set of matches provides a sense of the stability of the trends if we relax our definition of the best matches and we consider slightly worse fits. We tested various sizes for both sets of matches and found that these sizes were optimal for providing sets that typically covered the desired number of model families and had sufficient models to assess variation within the set.

We also use the match criterion to select the worst matches. The isolated galaxy simulations of G0 and G1 were systematically the worst matches (see Figure 3.3), because their luminosity (and stellar mass and SFR) are significantly lower than those of our observed systems. So we do not consider them in our determination of the worst matches, as they do not give further insights into the model parameters. We create a set of 100 matches comparable with our 100 best matches, by selecting matches with the largest χ^2_ν for each observed pair.

For each observed system, we also determine the mean and median χ^2_ν as a function of simulation, snapshot, and viewing angle, to determine whether broad areas of parameter space can be deemed unlikely to reproduce the observed SED. We describe the trends in the matches and in these functions in Section 5.1.

Determination of Simulation Parameters

Having established which simulated SEDs were best matched to each observed system, we estimate how accurately we can recover physical parameters such as IR luminosity,

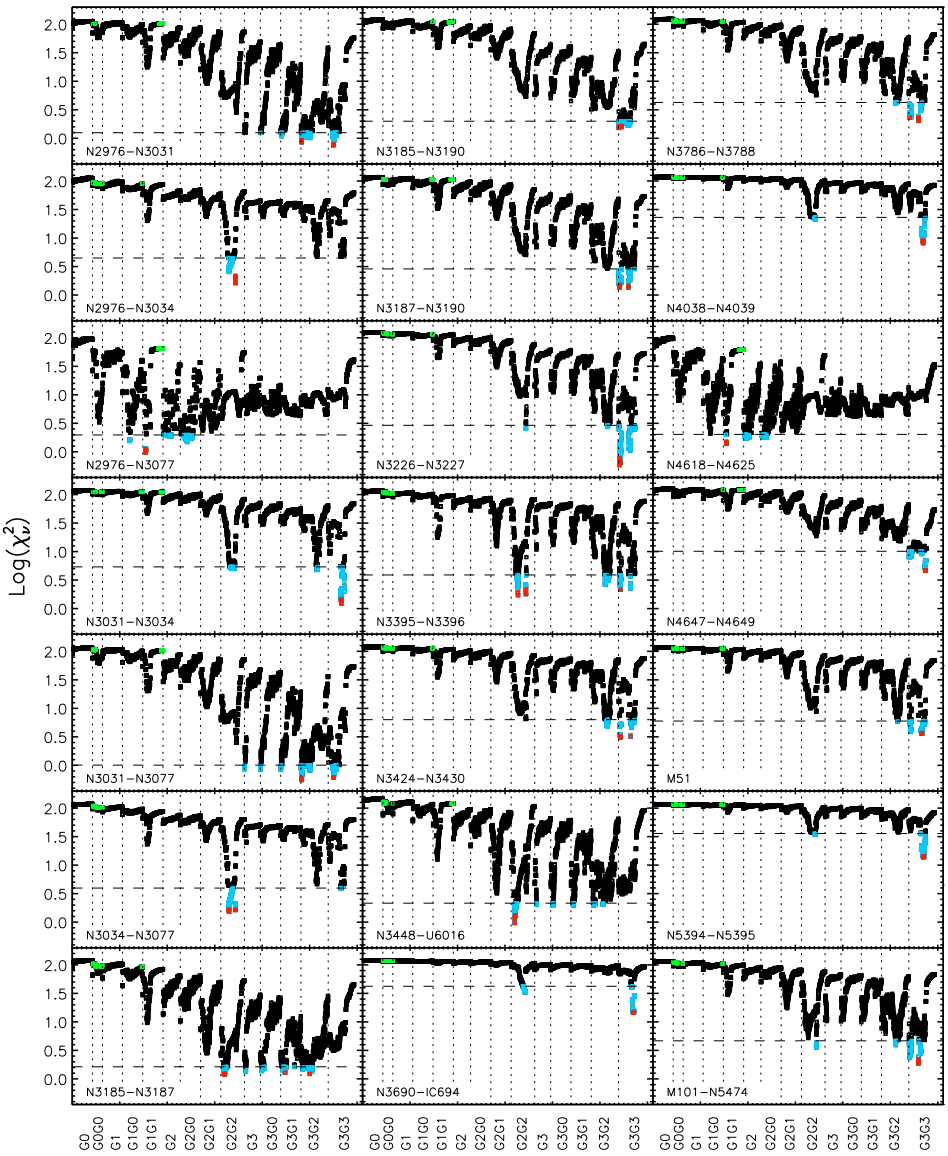

Figure 3.3: Reduced χ^2 for each galaxy for the comparison of the observations with the simulated SEDs. The vertical lines show the separation between each simulation, whose names are given in the horizontal axis. In red, cyan, and green, we show the selected sets of the 5 best matches, the 100 best matches, and the 100 worst matches from both simulations of interacting and isolated galaxies, respectively. The horizontal line indicate cut-off for the best 100 matches.

stellar mass, dust mass, and SFR from the SEDs. Several parameters are recorded at each increment of the hydrodynamic simulation (e.g., stellar mass and SFR). The gas mass and mass of metals therein are tracked during the simulation; the dust mass is assumed to be comprised of 40% of the metals within the gas. The 3-1000 μm luminosity is calculated as part of the SUNRISE post-processing. The results of the comparisons of these parameters for the best matched SEDs and the observations is discussed in Section 5.2. We also compare the dust temperature estimates. Although SUNRISE iteratively computes the dust temperature in each cell, we do not have such highly resolve information for the observations. Therefore, we calculate a typical temperature by fitting both the observed and simulated SEDs with a single β=2 modified blackbody model.

Best-Matched SEDs

In Figure 3.4 we plot the 100 best matched simulated SEDs for each interaction overlaid with the observed photometry. Several systems show interesting behavior. Some of our most evolved systems (e.g. NGC 3690/IC 694, NGC 4038/4039, and NGC 5394/5395) show clear indications of having cooler dust than many of their best matched simulated SEDs, since their FIR emission peaks at longer wavelength. These systems also typically have excess absorption in the UV relative to the observed photometry. In contrast, the pairs with NGC 3034, especially NGC 2976/3034 and NGC 3034/3077, do not have enough UV-optical absorption.

MIPS 24 μm flux estimates frequently shows significant variation among the best matches. Emission of very small, stochastically heated dust grains is often a significant

contributor to the 24 μm flux (e.g., Jonsson et al. 2010) SUNRISE does not currently include a treatment of this process, so it is not surprising that the SEDs do not always match well in this band. The UV is also shows significant variation and generally its absorption is under-estimated, except in our more evolved systems as noted above. In particular, it seems difficult to find a good match to the UV emission of NGC 3185/3190 and NGC 3187/3190, which both include the large edge-on heavily obscured spiral NGC 3190.

Although a fraction of the systems have best-matched simulations whose FIR emission matches well by eye (e.g. NGC 2976/3077), there is tendency for the simulations to underestimate the emission in the SPIRE bands (e.g. NGC 3786/3788, NGC 3424/3430). We expect that the alternative ISM SEDs will match these systems better, since the alternative ISM generally results in colder dust (red line in Figure 3.1).

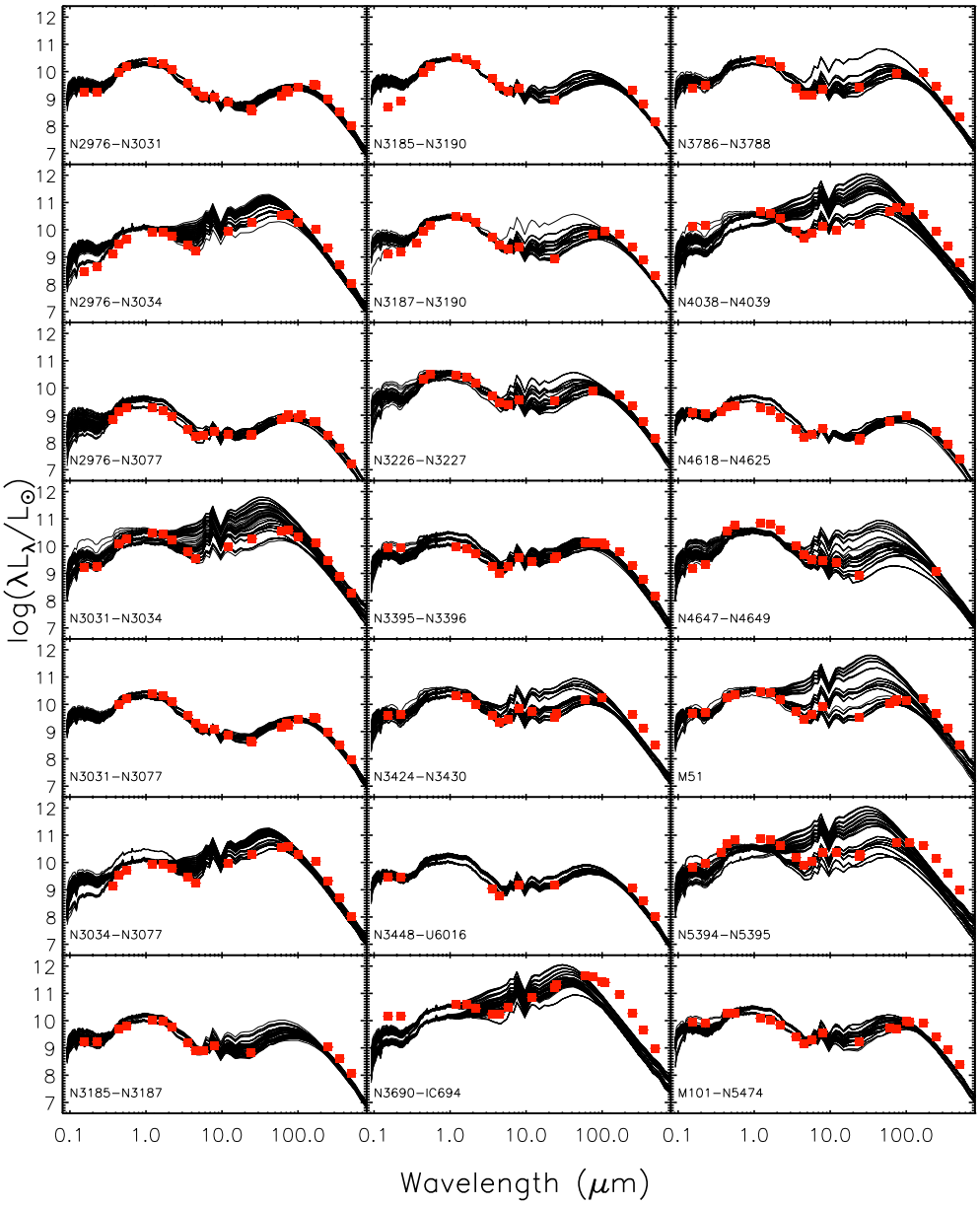

Figure 3.4: Best matched 100 simulated SEDs (black lines) compared to the observed photometry (red) for the 21 pairs of interacting galaxies in our 14 systems.

3.5 Discussion

3.5.1 Where Do the Best Matched SEDs Come From?

In any comparison of a suite of models to observations, two of the most important questions asked are: which areas of parameter space can be ruled out and which areas of parameter space give us the best matches? For the sets of best and worst matches, we examine trends in the distributions of simulations, snapshots, and viewing angles from which the matches originate. For each parameter of interest, we first examine the behavior of the mean and median χ^2_ν as a function of the parameter and then discuss the source distributions.

Matches as a Function of Simulation

Figure 3.5 shows the mean and median χ^2_ν as a function of simulation ordered by increasing mass from G0 to G3G3. We find consistent behavior for many of our interactions, so we plot the typical behavior in the top panel. Eighteen interactions generally have an increased likelihood of matching G2G2 SEDs, of which five also are more likely to match a G3G2 SED. Three outliers consist of NGC 3690-IC 694, which has a much flatter distribution, and the two dwarf pairs (NGC 2976/3077 and NGC 4618/4625), which have much more variable distributions.

Although Figure 3.5 shows the likelihood distribution as a function of simulation, it does not clearly identify from which specific simulations the best and worst matches actually originated. We plot the distribution of the originating simulations ordered by stellar mass for the best and worst sets of matches in Figure 3.6. As expected from the

distribution of red points in Figure 3.3, the best five models typically come from the same simulation, which is never an isolated galaxy simulation. Most of the best matches come from the G3G3 or G2G2 simulation. Interestingly, the two cases where best and worst matches originate from the same simulation are our two dwarf pairs, but from different times within the simulation as can be seen from the separation of the green and red points in Figure 3.3.

Figures 3.5−3.6 together demonstrate the general trends of matches with simulations: (1) the best matches typically come from $1-3$ similar simulations, (2) the most massive major mergers generally yield the most best matches for our observational sample, while the simulations of less massive galaxies generally result in the worst matches, (3) despite the range in mass ratios in the observed systems, only the pairings of NGC 3031/3077 and NGC 2976/3031 have some of their 5 best matches originating from a non-equal-mass merger, and (4) only the dwarf pairs have both best and worst matches from the same simulation.

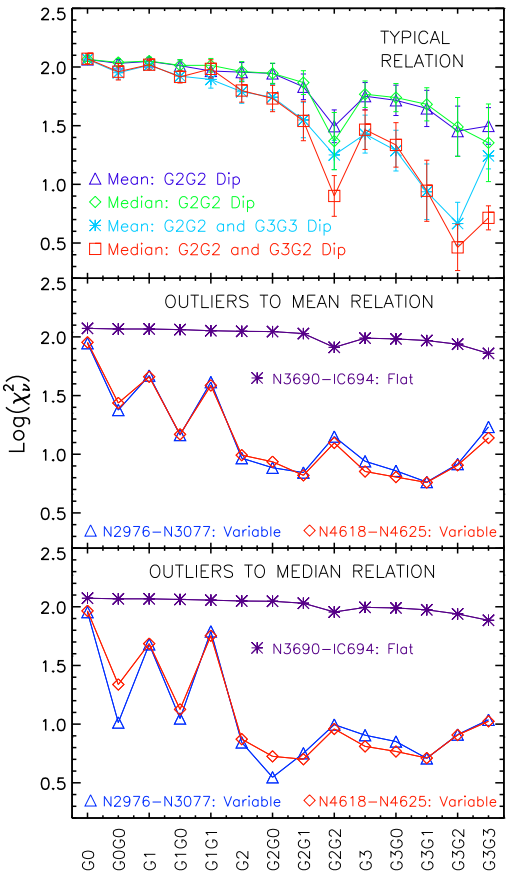

Figure 3.5: Mean and median χ^2_ν as a function of simulation for each interaction. Most systems have the same shape for the mean and median χ^2_ν function, showing dips indicating increased likelihood at G2G2 (18 pairs) and possibly G3G2 (5 pairs). In the top panel, we show the typical mean and median functions for the galaxies whose functions follow these shapes. In the middle and bottom panel, we show the median and mean functions, respectively, with different shapes. NGC 3690-IC 694 has a much flatter shape in both mean and median, although there is a hint that G2G2 and perhaps G3G3 have a higher likelihood. The two dwarfs pairs have quite variable functions, whose minimum generally appears to be around G2G0.

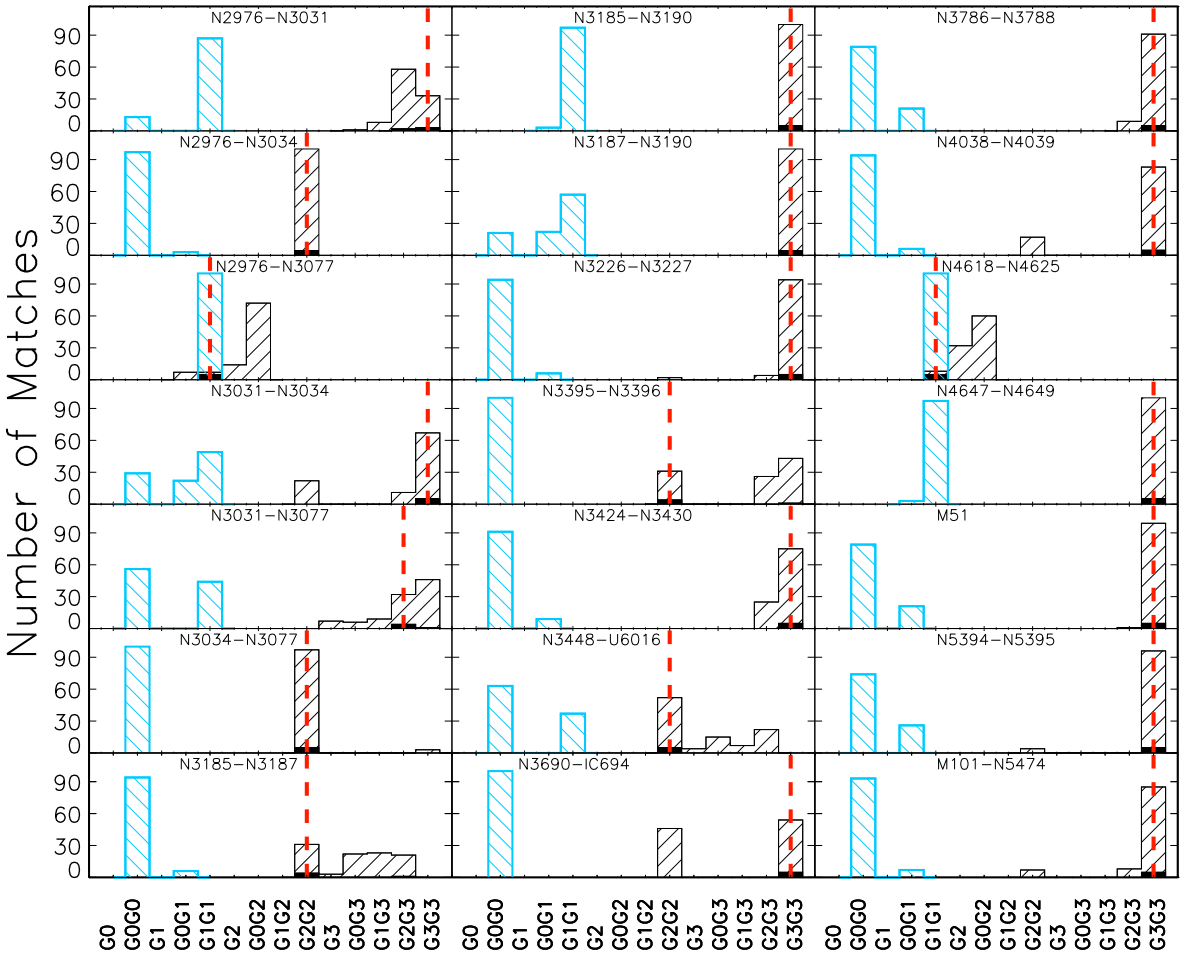

Figure 3.6: Distribution of the simulations from which the best 100 SED matches originate in black compared to the simulations that yield the worst 100 matches (cyan) for the interacting pairs. The best five matches are shown in solid black; the best match is shown in red line and is generally in the same bin as the best five matches.

Matches as a Function of Time

In Figure 3.7 we show the the mean and median χ^2_ν as a function of snapshot number, which correspond roughly to 10 Myr intervals. As in Figure 3.5, we find similar behavior in many observed systems, so we plot, the typical behavior in the top panel. Both the mean and one type of median behavior gradually decrease in likelihood after snapshot ∼100, but the median has a region of heightened likelihood immediately before the decrease begins. Three of the most evolved systems in our sample, also have flat distributions with only a hint of the dip seen in almost all galaxies. In the bottom panel, we show individual outliers from the median. Except for the two dwarf pairs, which are roughly flat distributions with a sharper increase in χ^2_ν after snapshot 400, all our galaxies have indications of a greater likelihood of matching simulations at around snapshot 100.

In order to determine whether matches from different simulations that evolve at different rates nevertheless cluster in the interaction stages that yields best matches, we plot in Figure 3.8 the distribution of the times relative to the coalescence of the supermassive black holes (SMBH) binned in 200 Myr intervals. Many galaxies have a large fraction of their best matches from times close to coalescence. The dwarf pairs show somewhat different behavior: although the best five matches also originate from shortly before coalescence, the bulk of their best 100 matches come from long before coalescence (3−5 Gyr). NGC 4618/4625 has a particularly interesting distribution: its five best matches come from close to coalescence and the remaining best matches come from early in the interaction, while the worst matches come from the post-merger stage of the same simulation (see §5.1.1). Five galaxy pairs have best matches with SEDs from

isolated galaxy simulations: NGC 2976/3077 and NGC 4618/4625 match with G2 within the first Gyr and again around 2 Gyr from the start of the simulation; NGC 3031/3077, NGC 3448/UGC 6016, and NGC 3185/3187 all have a match at several viewing angles within 600 Myr from the start of the simulation.

We find that: (1) best matches often cluster around coalescence and primarily populate times before coalescence, (2) worst matches from simulations of interactions, in contrast, generally originate in the post-merger interaction stages or within the ~ 1 Gyr prior to coalescence, and (3) the most evolved systems (and those including the starburst galaxy NGC 3034) have the narrowest range of times associated with the best matches.

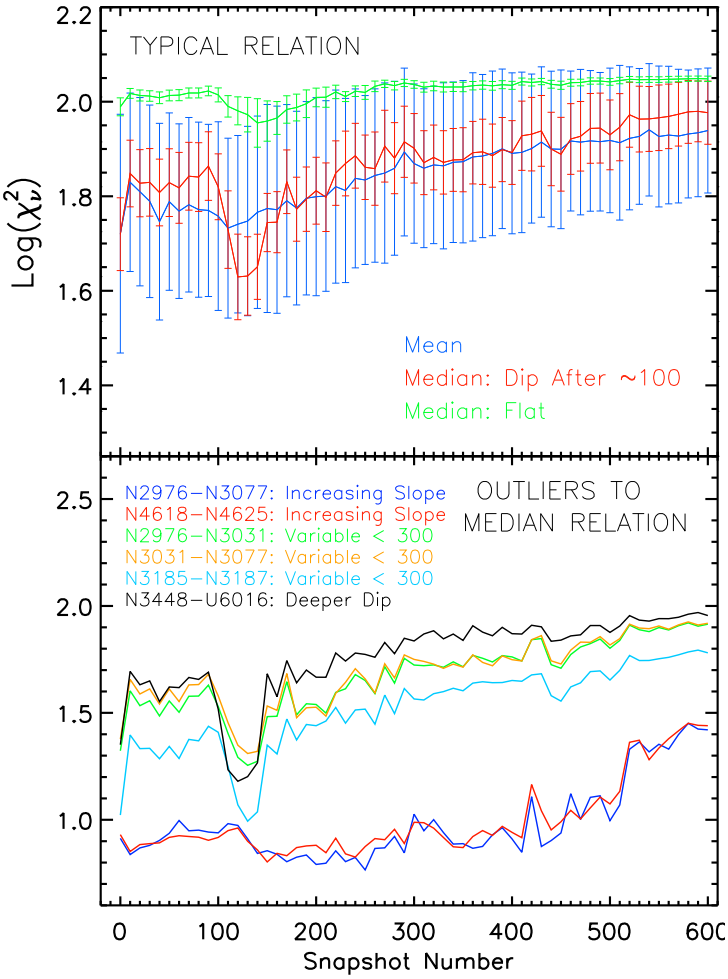

Figure 3.7: Mean and median chi$^2_\nu$ as a function of snapshot. Most systems have a similar shape: all mean chi$^2_\nu$ functions increases slightly from snapshot 100 while the median function is either flat (N3690-IC694, N4038-N4039, and N5394-N5395) or has a region of lower chi$^2_\nu$ shortly after snapshot 100. The galaxies whose median function differ fall into one of three categories. Except for the two dwarf galaxy pairs, the region of increased likelihood after snapshot 100 seems to be found in all galaxies.

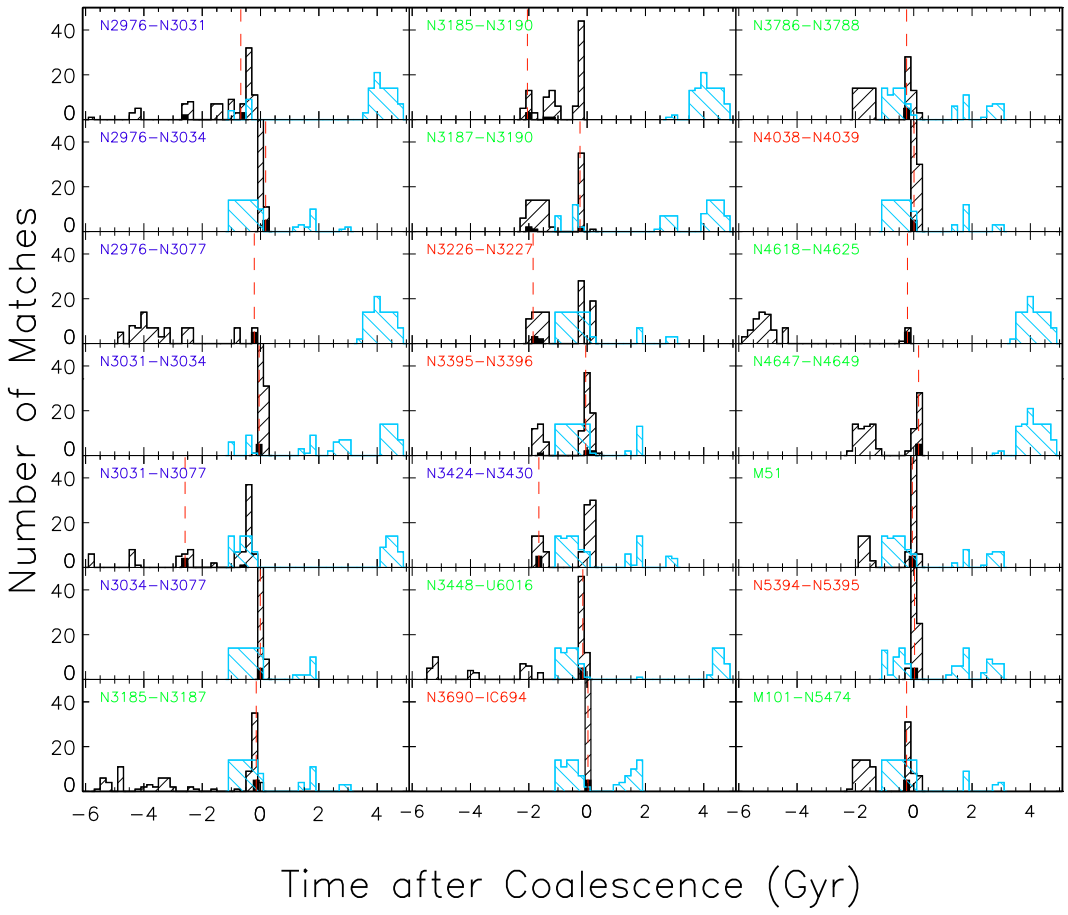

Figure 3.8: Distribution of the times to coalescence in 200 Myr intervals of the best and worst 100 matches using the same color scheme as Figure 3.6. We do not show the matches originating from isolated galaxy simulations, since the time to coalescence would not be definable, therefore N2976-N3034, N2976-N3077, and N4618-N4625 do not have any plotted worst matches. Note that many of the worst matches come from significantly before or after coalescence, but the bulk of the best matches come from close to coalescence. The color of the name indicates weakly (blue), moderately (green), and strongly (red) interacting systems based on the Dopita et al. (2002) classification system (§2.3). Best matches with simulations of interactions not explicitly plotted (e.g., the other 50 best matches for NGC 3690/IC 694) should be assumed to be in the bin which already has at least 50 matches.

Matches as a Function of Viewing Angle

Figure 3.9 show the mean and median χ^2_ν with viewing angle. There is no preference for a particular viewing angle. Since merging spirals are angled with respect to one another, there is no special viewing angle that yields both galaxies edge-on or face-on. Further, except, perhaps, for short periods around coalescence, the galaxies are not optically thick and hence viewing angle should not have a strong impact on the best match. In the bottom panel of Figure 3.9, we show three pairs whose median χ^2_ν with viewing angle have the largest discrepancies with the typical behavior. These discrepancies are small and amount to a slightly lower likelihood at Camera 3. The plots of the distribution of viewing angles from which the matches originate tend to be quite flat (Figure 3.10). The main exception in the interacting systems is NGC 3185/3187.

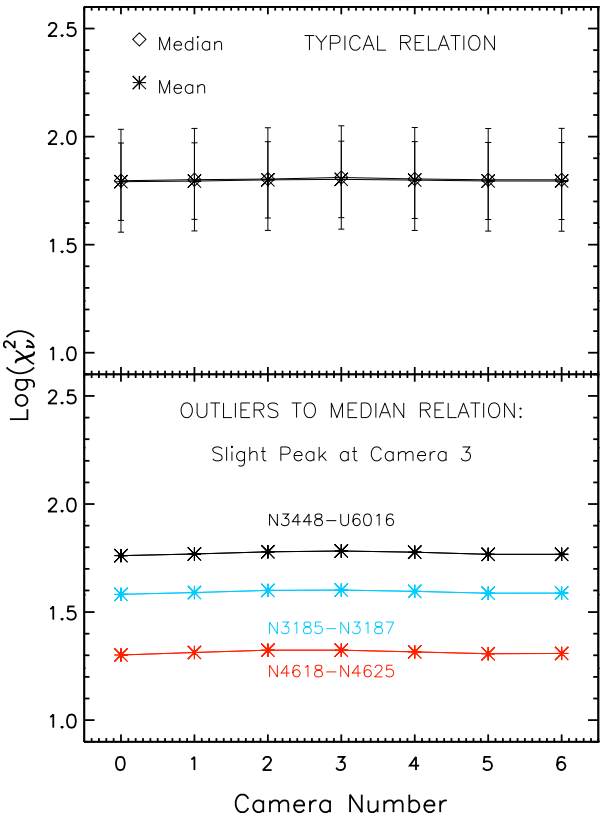

Figure 3.9: Mean and median χ^2 as a function of viewing angle. All the systems have approximately the same shape in median and even more on average, which we show in the top panel. The bottom panel shows median χ^2 per viewing angle with larger deviations from a flat distribution for three systems, with a slightly lower likelihood for Camera 3 in the median χ^2 trace.

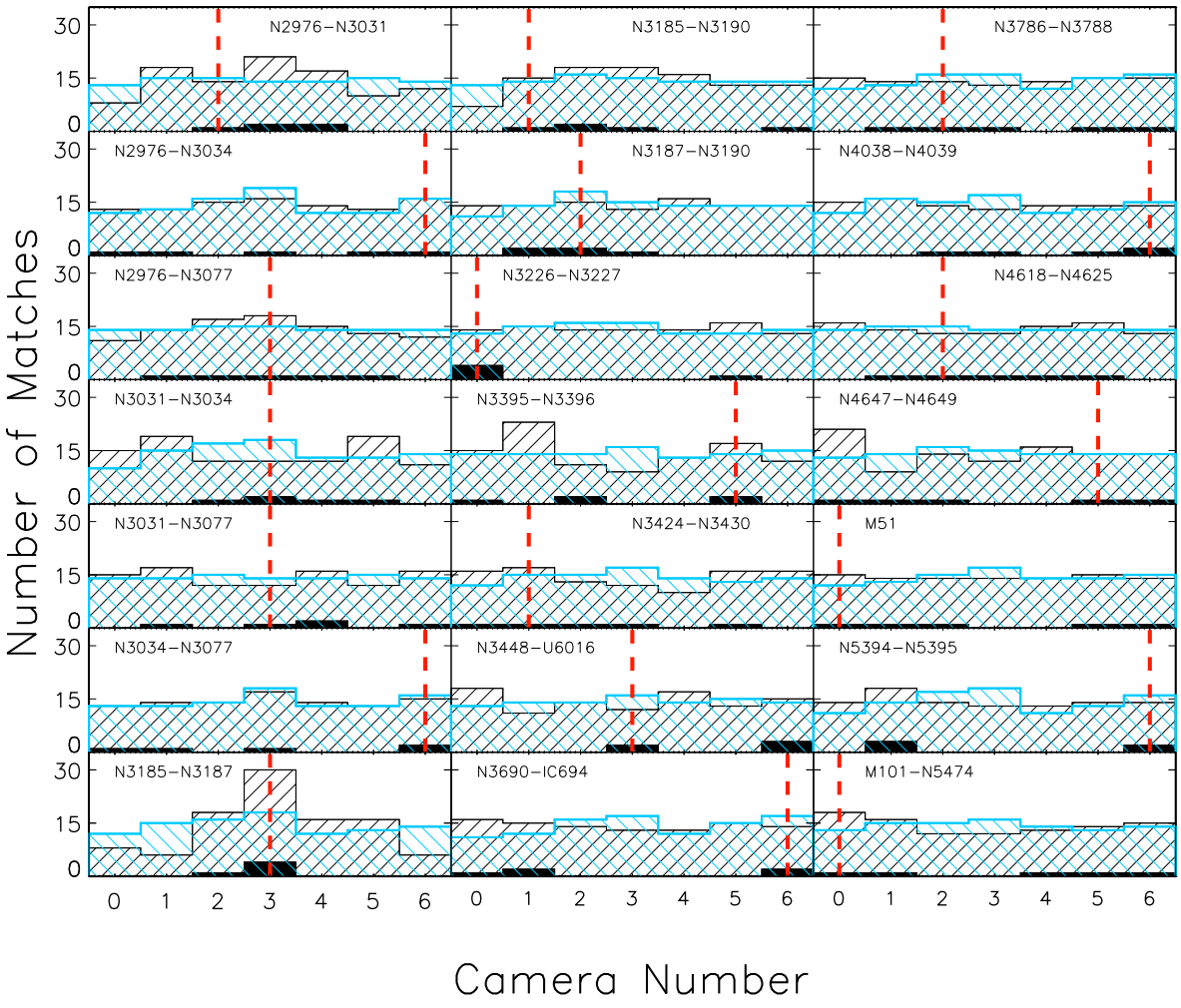

Figure 3.10: Distribution of the viewing angles using the same color scheme as Figure 3.6. Only N3185-N3187 demonstrates a preference for a viewing angle (3) for its best matches.

3.5.2 Recovery of Galaxy Properties

Having determined which simulated SEDs were best matched to each observed system, we estimate how accurately these simulations recover physical parameters such as IR luminosity, stellar mass, dust mass, and SFR from the SEDs. To that end, we compare the best-matched simulations to the quantities derived using the MAGPHYS code. In Figure 3.11 we plot the MAGPHYS-derived value of each of these parameters against the corresponding property from the best-matched simulated SED.

IR luminosity

We find that the IR luminosity (upper left panel of Figure 3.11) is well recovered. Although the best match over-estimates the IR luminosity for some of the brighter galaxies, these systems also have a wider range of IR luminosities associated with their set of 100 best matches. The two systems with the greatest offset in the best match are NGC 4038/4039 and NGC 5394/5395, whose matches originate very close to coalescence.

Stellar Mass

In the upper middle panel of Figure 3.11, we compare the stellar masses of the observed systems to those of their best-matched simulated counterparts. More massive systems are better matched by simulations of more massive galaxies, which is not surprising given the broadly normalizing aspect of stellar mass and its importance in driving the intensity of an interaction. Because the simulated interactions do not gain material from their environment, their stellar mass evolves little over the course of a simulation, as they have a finite gas reservoir out of which to form stars. This results in a sparse coverage of

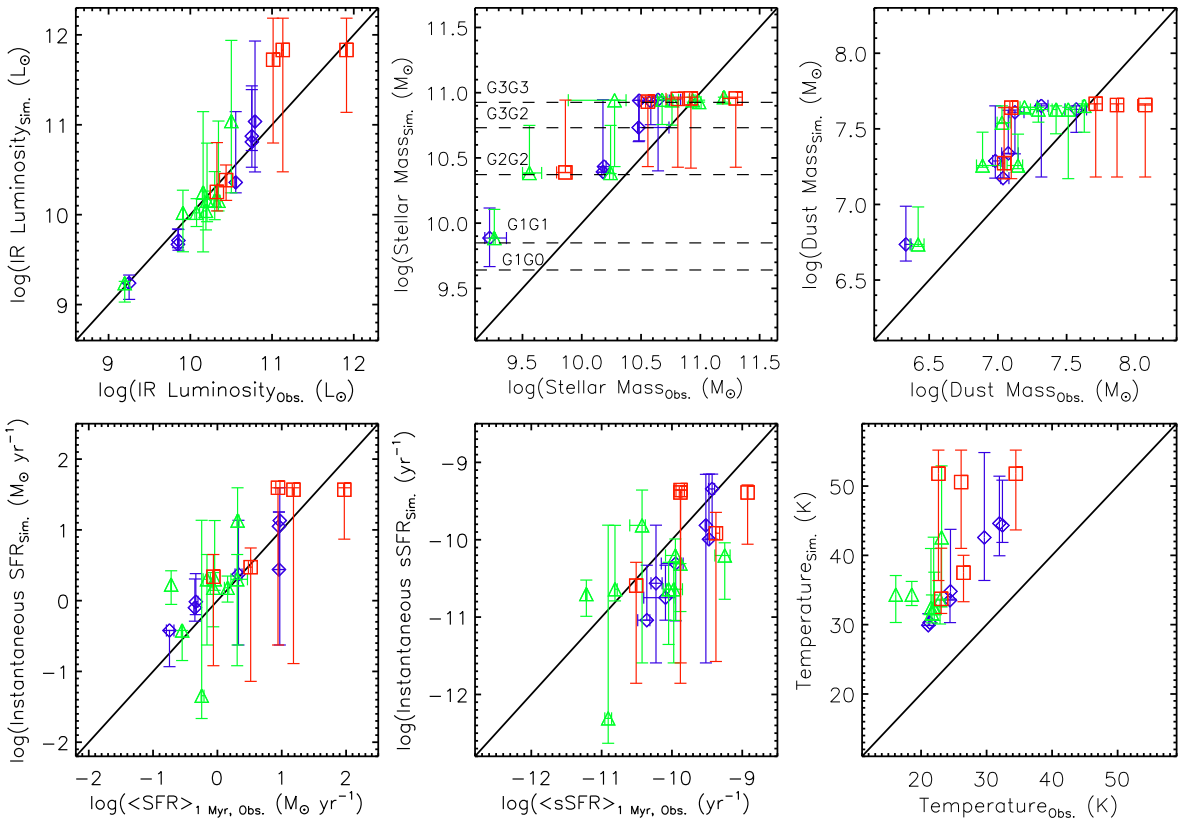

Figure 3.11: Comparison of (upper row): the IR luminosity (left), stellar mass (middle), dust mass (right); and (lower row): SFR (left), and sSFR (middle) derived for the observations with MAGPHYS and the property of the best matched simulated SEDs. The temperatures compared in the lower right panel are the temperatures of $\beta = 1.5$ blackbodies fit to the simulated and observed SEDs. The best matched simulated SED's value is plotted and the error bars show the range of the parameter for the 100 best matched simulated SEDs. Blue diamonds are Stage 2 (weakly interacting) systems, green triangles are Stage 3 (moderately interacting) systems, and red squares are Stage 4 (strongly interacting) systems. The horizontal lines in the stellar mass plot show the mass of the labeled simulations. We find that the parameters are typically well recovered, given the sparsity of our parameter space coverage, except for the temperature, which tends to be too hot in the simulations.

the stellar mass parameter space. Therefore, determining more precisely how well stellar mass is recovered is difficult.

Dust Mass

The upper right panel of Figure 3.11 compares the simulated and observed dust masses. The distribution generally looks similar to stellar mass (i.e., systems with more dust are better matched to simulated SEDs calculated through a dustier environment). Although the simulated dust mass tends to be higher than observed at intermediate masses, it agrees within a factor of $\approx 2-3$, which is typically the level of uncertainty in the determination of dust mass.

Star Formation Rate

We compare SFR in the lower left panel of Figure 3.11. While MAGPHYS can determine several SFR averaged over different timescales, we chose to compare the average over 1 Myr, the shortest available, as being closest to the instantaneous SFR recorded during the hydrodynamic simulation. We find fairly good agreement, although the SFR associated with the simulations best matched to NGC 3690-IC 694 are typically low. The other two highly evolved systems, NGC 4038/4039 and NGC 5394/5395 show a range of over two order of magnitude in the SFR of their matches. However, from Figures 3.3 and 3.4, it should be clear that for these systems, the quality of some of their best 100 matches is significantly lower than their best match.

Several moderately interacting systems (shown in green) also display interesting offsets. The most striking is NGC 4647/4649 whose simulated SFR is particularly low

at around $\log(\mathrm{SFR}/(\mathrm{M}_\odot\ \mathrm{yr}^{-1}))= -1.3$ compared to the observed SFR of $\log(\mathrm{SFR}/(\mathrm{M}_\odot\ \mathrm{yr}^{-1}))= -0.2$. NGC 4649 is a large elliptical galaxy, which we do not have in our simulated galaxies. It was not detected at most MIR-FIR bands, therefore the system has little constraints on that region of the SED It is therefore not surprising that it displays such a large range of SFR. M51, another system with a non-spiral galaxy also shows a large range in its simulation SFR ($\log(\mathrm{SFR}/(\mathrm{M}_\odot\ \mathrm{yr}^{-1}))= [-0.6, 1.5]$. In contrast, NGC 3185/3190 has a fairly constrained simulation SFR range, which is higher than the observed SFR by about a factor of 8. This is likely related to the significant over-estimation in the UV of the best matches (see Figure 3.4), where the best matches were not able to find as heavily obscured a system as one containing the nearly edge-on NGC 3190. The distribution of sSFR (lower middle panel of Figure 3.11) is fairly similar to the distribution of SFR, but with a weaker trend due to the degree of recovery of the stellar mass.

As an additional check on this comparison of observed and simulated SFR, we determine the agreement between an SFR calculated based on simulated photometry using the Kennicutt (1998) L_{IR} prescription and the instantaneous, hydrodynamic SFR. The result is shown in Figure 3.12. We note that for most of the simulated SEDs, there is good agreement between the hydrodynamic and photometric SFR. However, there exists a population whose photometric emission is larger than expected if it was only due to current star formation activity. The population of outliers all come from the major mergers, G1G1, G2G2, and G3G3 and can be divided into two temporal classes. Generally those with instantaneous SFR less than $10^{-4}\,\mathrm{M}_\odot\,\mathrm{yr}^{-1}$ are from the post-merger era and their excess IR luminosity may be due to be from red giants stars that were formed during coalescence. The outliers at higher SFR come from the coalescence

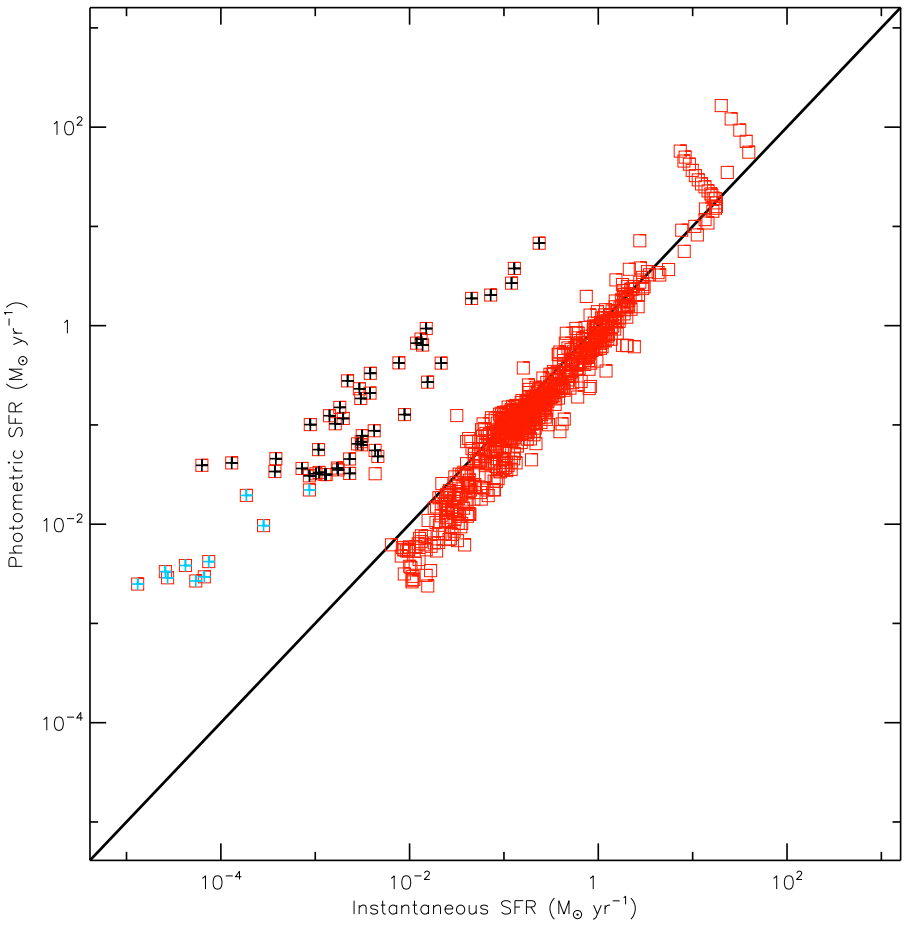

Figure 3.12: Comparison of the SFR calculated for simulated IR luminosities assuming SFR=$2.8\times10^{-44}\,L_{IR}$ (Kennicutt 1998) to the instantaneous SFR recorded during the hydrodynamic simulations (red squares). Blue crosses indicate SFR from the post-merger stages of major mergers and black crosses indicate SFR during the coalescence in major mergers. Although there is general agreement, these two populations have SFR overestimated photometrically.

period, which also experiences heightened AGN emission, which also contributes to the IR luminosity.

Effective Dust Temperature

The lower right panel of Figure 3.11 compares the temperatures of $\beta = 2$ blackbodies fit to the observed and matched simulated SEDs. We find the simulated SEDs always have hotter dust temperatures by about $\sim 10\,\mathrm{K}$. Strongly interacting galaxies and pairs including NGC 3034 show the greatest range in simulated temperatures. We expect that the temperature recovery will be better in the matches from the alternative ISM SEDs, since their FIR emission peaks at longer wavelengths associated with typically colder material.

3.5.3 Effectiveness of Morphology-based Stages Estimates of Interaction

The most common methodology by which interacting systems are organized into a merger sequence is through by the degree of morphological distortion. The Dopita et al. (2002) classification scheme uses this method. Weakly interacting (Stage 2) systems are only mildly distorted if at all, while strongly interacting (Stage 4) systems are significantly distorted. In Figure 3.13 we examine how well this classification works as a proxy for the time along the interaction sequence. Because each simulation proceeds at a pace governed by its particular combination of galaxy masses and mass ratios, the interaction stage associated with any snapshot is not the necessarily the same as that associated with the same snapshot in any other simulation. For instance, 1 Gyr before coalescence,

G3G3 is approximately at the maximum separation after first passage, but G2G2 has not yet had its first pericenter passage. Similarly, the beginning of a simulation is not well defined since it is selected rather arbitrarily for each simulation (e.g.,the initial separation is variable, ranging from 50 to 250 kpc).

However, many interactions share a number of common landmarks along the interaction. We define four signposts to examine the relative location of the best matches. The vertical lines in the top panel of Figure 3.13 indicate the times of our landmarks in the G3-G3 simulation. The first three are defined based on the separation of the central SMBHs, which acts as a proxy for the separation of the galaxies. The first two landmarks are the first close approach and the moment of maximum separation after that initial passage. The simulations have a variable number of close approaches, which tend to increase with stellar mass ratio. The third landmark is the moment at which the two SMBHs coalesce. However, in the major mergers where the increase in IR luminosity is pronounced, the peak luminosity occurs after that coalescence (c.f. Hopkins et al. 2006). Therefore, we define a fourth landmark when the IR luminosity has decreased from its peak and become steady.

We determine where each set of best matches fall between the landmarks. In the bottom panel of Figure 3.13, we plot the range covered by these matches compared to the Dopita system classification. We generally do find that the strongly interacting (strongly distorted) systems originate from the period of black hole coalescence and peak IR emission. This trend is even stronger if we were to subdivide the strongly interacting classification into two subsets: the more distorted (more evolved) systems, NGC 3690/IC 694, NGC 4038/4039, and possibly NGC 5394/5395 have much tighter constraints around coalescence. NGC 3226/3227's best match is associated with a

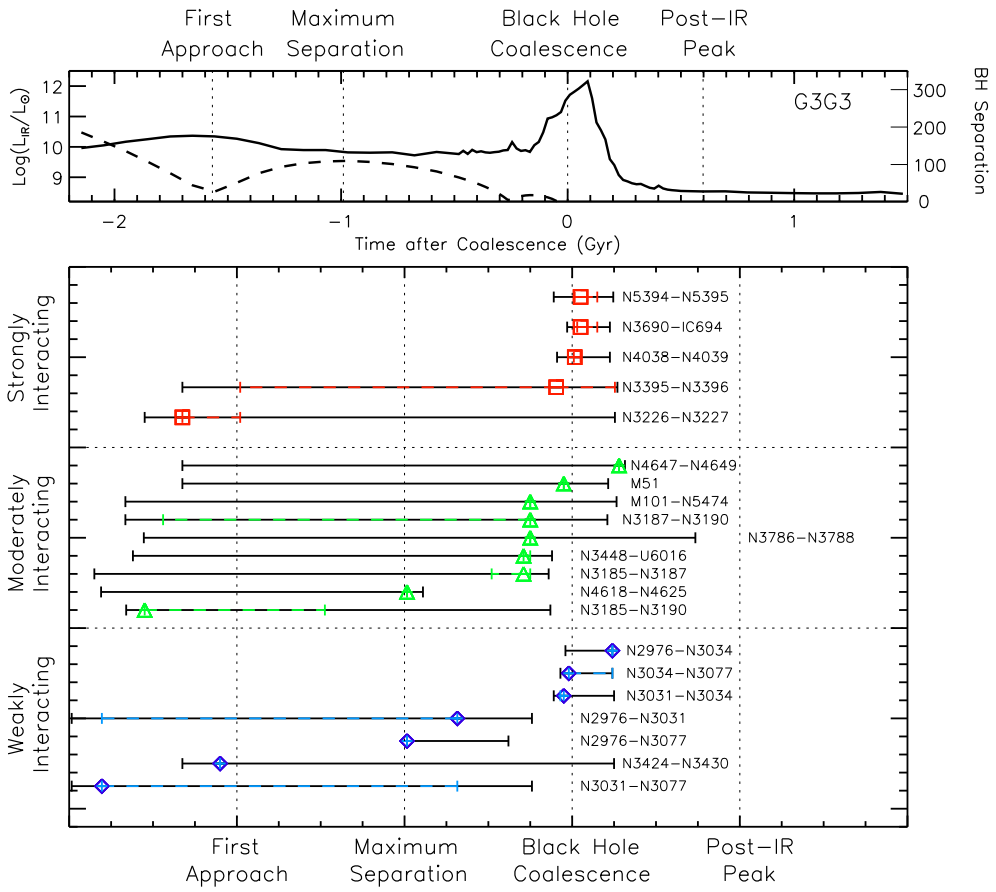

Figure 3.13: Comparison of the Dopita classifications with the timing of the best matched snapshots relative to landmarks of interaction. The top plot shows the evolution of the G3-G3 simulation, showing the IR luminosity (solid line) and the separation of the two SMBH (dashed line). The vertical dotted lines identify the position of the first three landmarks identified from the black hole separation. The fourth landmark is the time at which the IR luminosity has decreased from its peak to a fairly constant value. In the bottom panel, the landmarks are equally spaced, as the time between landmarks varies for each interaction. The data points are plotted at the fractional time between two landmarks from which the best SED match originate. The "error bars" show the range of snapshots from which the best 5 (color) and best 100 (black) SED matches originate. The vertical spread in each class is simply to aid in distinguishing the different systems.

snapshot before the first approach. However, in its best matches, it covers most of the range of the G3-G3 simulation past coalescence. Further, as a spiral-elliptical merger, it is to be expected that it would preferentially tend to match a system with lower IR and lower SFR than the typical spiral-spiral merger. This disparity in gas reservoir between the observed and simulated systems may explain the better matches with the less active interaction stages.

However, for the other "Dopita classes", we do not find a clear trend of evolution along the interaction sequence with the morphologically determined classes, demonstrating that the SED alone is insufficient to uniquely determine the interaction stage. The moderately interacting systems span most of the sequence, as do the weakly interacting systems, which cluster mostly in the same period as the strongly interacting systems. There is, however, a strong caveat: our observational sample is fairly small. Although we have seven pairs of weakly interacting galaxies, six originate from the same system (the NGC 3031-NGC 3034 system), and NGC 3034 is by no means a typical galaxy in the early interaction stages. Similarly, our simulations presents a good effort at spanning the properties of our observed samples, but we would not claim that we are simulating counterparts to our observed system or indeed sampling the possible interaction types with great resolution. Nonetheless, Figure 3.13 demonstrates the inherent weakness of a classification system based on the degree of morphological distortion. In fact, previous simulations of interacting systems have demonstrated that the appearance at a given time during an interaction depends not only on the specific geometry of the encounter, but also on the masses, metallicities, gas contents, and previous interactions of the progenitor galaxies (e.g., Di Matteo et al. 2007).

3.5.4 Evolution of SEDs in Major Mergers

We use the landmarks described in Section 5.2 to define five interaction stages: the initial approach, the first close passage, the separation post-1st passage, coalescence, and the relaxation period after the merger. For each stage, we determine the median SED for each of the equal mass mergers (e.g.,G0-G0) as seen from one of the viewing angles. There is little difference between the median SEDs for different viewing angles because the galaxies do not share an equatorial plane, so there is no preferred viewing angle even early in the interaction. In Figure 3.14, we show the median SEDs for the four equal-mass mergers. We find that the coalescence stage typically has more luminous IR emission than the other stages, although it is also the stage with the highest variation in IR emission. Although the median SEDs are broadly similar in shape, there are a few differences. We find an enhancement in the MIR-FIR after the 1st close passage in the two intermediate mass mergers G1G1 and G2G2. Similarly, the post-merger stage, during which the system has become an elliptical, show noticeably lower UV and FIR in the three massive mergers. However, it should be clear given the large range of variation in the coalescence stage, an SED cannot be used in isolation to determine the interaction stage.

3.6 Conclusions

We present the first systematic comparison of SEDs of observed and simulated interacting galaxies. Our observed sample of 31 galaxies was observed in up to 25 bands with *GALEX*, *Spitzer*, and *Herschel*. We created a suite of GADGET-3 hydrodynamic

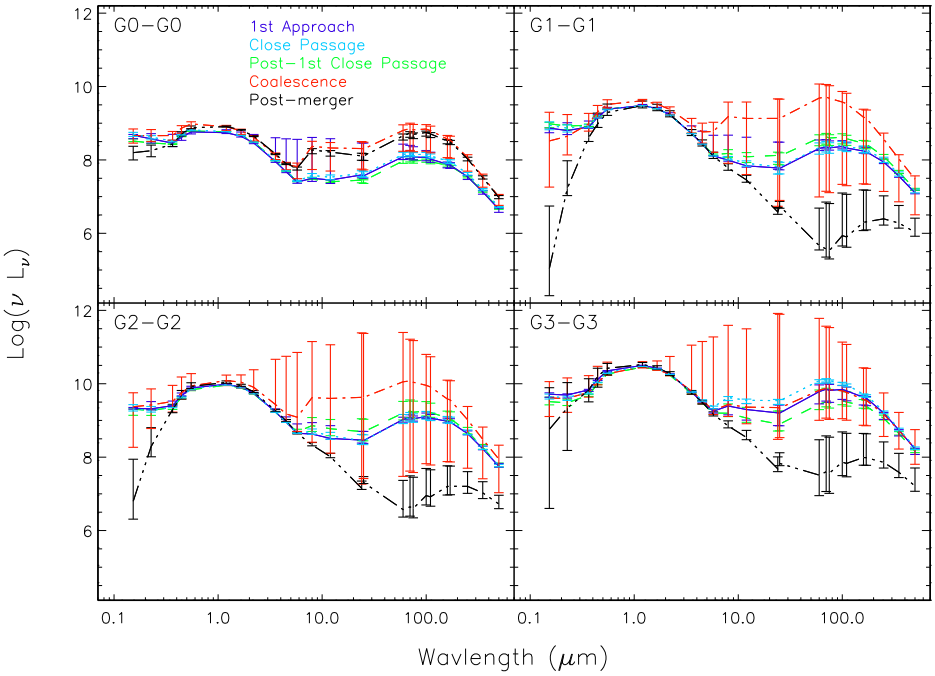

Figure 3.14: Median SED for five stages in the equal mass mergers: the initial approach, first passage, separation after the first passage, coalescence, and post-merger for one of the viewing angles. There is little variation due to viewing angle, since the two galaxies do not share an equatorial plane. The "error" bars show the range over each stage. These SEDs show that even in major mergers, which show the greatest activity, the SED alone is generally insufficient to identify the interaction stage, although the post-merger elliptical typically have significantly lower UV and FIR.

simulation of four galaxies evolving in isolation and the ten pair-interactions evolved from first passage through coalescence to the post-merger stage. Simulated SEDs were calculated using SUNRISE and sets of the best-matching of these SEDs were determined for each observed pair.

We examined the trends in the properties of the simulations that yielded these best matches. The best matches to our observed sample generally come from only 1−3 simulations, often the major mergers. The two dwarf pairs in our sample have their best and worst matches from the same simulation but at opposite ends of the simulation. The best matches tend to cluster around coalescence and the constraint in timing is tightest for the most evolved systems. We do not find, however, that best matches preferentially come from a certain viewing angle.

The best matches recover IR luminosity and SFR fairly well. Stellar and dust masses show indications that more massive (or dustier) systems tend to be matched by simulations of more massive (or dustier) galaxies. We find that the simulations have dust that is typically 10 K hotter than the observed systems. The complexity of the radiative transfer process, however, is such that the simulated SEDs are poorly modeled by a single blackbody.

We examined the effectiveness of the Dopita et al. (2002) classifications of interaction stage and found that the most evolved, strongly interacting systems tend to have tightly constrained interaction stages around coalescence. In contrast, the less strongly interacting classes cover a wide range of interaction stages in their best matches. This suggests that the SED alone is insufficient to identify the interaction stage. This is supported by our examination of the evolution of the SEDs in the major merger

simulations. The SED is so variable in the coalescence stage that given solely an SED, a determination of the interaction stage would be difficult.

Acknowledgements

The simulations in this paper were performed on the Odyssey cluster supported by the FAS Research Computing Group at Harvard University. CCH is grateful to the Klaus Tschira Foundation for financial support and acknowledges the hospitality of the Aspen Center for Physics, which is supported by the National Science Foundation Grant No. PHY-1066293. This work was based on archival data obtained from the Spitzer Science Archive, the Mikulski Archive for Space Telescopes (MAST), the Swift data archive, and the Herschel Science Archive. *Herschel* is an ESA space observatory with science instruments provided by European-led Principal Investigator consortia and with important participation from NASA. *Spitzer* is operated by the Jet Propulsion Laboratory, California Institute of Technology under a contract with NASA. *GALEX* is operated for NASA by the California Institute of Technology under NASA contract NAS5-98034. This research has made use of the NASA/IPAC Extragalactic Database (NED), which is operated by the Jet Propulsion Laboratory, California Institute of Technology, under contract with the National Aeronautics and Space Administration. (TBD: CHECK WITH HAS ABOUT FUNDING FOR ME; CHECK WITH AZ ABOUT SUPPORT)

Chapter 4

Constraining the Outburst Properties of the SMBH in Fornax A through X-ray, Infrared, and Radio Observations

This thesis chapter originally appeared in the literature as

L. Lanz, C. Jones, W. R. Forman, M. L. N. Ashby, R. Kraft, R. C. Hickox

The Astronomical Journal, 2010, 721, 1702

Abstract

Combined *Spitzer*, *Chandra*, *XMM-Newton*, and *VLA* observations of the giant radio galaxy NGC 1316 (Fornax A) show a radio jet and X-ray cavities from AGN outbursts most likely triggered by a merger with a late-type galaxy at least 0.4 Gyr ago. We detect a weak nucleus with an SED typical of a low-luminosity AGN with a bolometric luminosity of 2.4×10^{42} ergs s^{-1}. We examine the *Spitzer* IRAC and MIPS images of NGC 1316. We find that the dust emission is strongest in regions with little or no radio emission and that the particularly large infrared luminosity relative to the galaxy's K-band luminosity implies an external origin for the dust. The inferred dust mass implies that the merger spiral galaxy had a stellar mass of $1 - 6 \times 10^{10}\,M_\odot$ and a gas mass of $2 - 4 \times 10^{9}\,M_\odot$. X-ray cavities in the *Chandra* and *XMM-Newton* images likely result from the expansion of relativistic plasma ejected by the AGN. The soft (0.5-2.0 keV) *Chandra* images show a small $\sim 15''$ (1.6 kpc) cavity coincident with the radio jet, while the *XMM-Newton* image shows two large X-ray cavities lying $320''$ (34.8 kpc) east and west of the nucleus, each approximately $230''$ (25 kpc) in radius. Current radio observations do not show emission within these cavities. The radio lobes lie at radii of $14\farcm3$ (93.3 kpc) and $15\farcm6$ (101 kpc), more distant from the nucleus than the detected X-ray cavities. The relative morphology of the large scale 1.4 GHz and X-ray emission suggests they were products of two distinct outbursts, an earlier one creating the radio lobes and a later one producing the X-ray cavities. Alternatively, if a single outburst created both the X-ray cavities and the radio lobes, this would require that the radio morphology is not fully defined by the 1.4 GHz emission. For the more likely two outburst scenario, we use the buoyancy rise times to estimate an age for the more

recent outburst that created them of 0.1 Gyr and the PV work done by the expanding plasma to create the X-ray cavities to estimate the outburst's energy to be 10^{58} ergs. The present size and location of the radio lobes implies that the outburst that created them happened ~ 0.4 Gyr ago and released $\sim 5 \times 10^{58}$ ergs.

4.1 Introduction

NGC 1316 (Fornax A) is one of the nearest and brightest radio galaxies with radio lobes spanning $33'$ (Ekers et al. 1983). It lies on the outskirts of the Fornax cluster at a distance of 22.7 ± 1.8 Mpc, based on a distance modulus of 31.66 ± 0.17 (Tonry et al. 2001).[1] Early optical observations of NGC 1316 (Evans 1949) revealed dust lanes in the nuclear region, leading Shklovskii (1963) to hypothesize that radio lobes might be powered by accretion of interstellar gas onto the nucleus. More extensive optical observations led Schweizer (1980) to classify NGC 1316 as a D-type galaxy (Morgan 1958) with an elliptical-like spheroid embedded in a large envelope.

Schweizer further suggested that NGC 1316's disturbed morphology may be due to one or more low-mass gas-rich mergers, occurring over the last 2 Gyr. Mackie & Fabbiano (1998) concluded, from more recent optical observations, in combination with *ROSAT* data, that NGC 1316 had undergone either a major merger more than 1 Gyr ago or a merger with a low-mass gas-rich galaxy about ~ 0.5 Gyr ago. NGC 1316 exhibits other signs of at least one merger, including loops of Hα filaments resembling

[1] We adopt $h = 0.70$ and therefore revise the Tonry et al. (2001) distance which used $h = 0.74$. This gives a scale of $9\farcs2\,\mathrm{kpc}^{-1}$ at the distance of NGC 1316.

tidal tails with projected lengths as large as $10'$ (65.4 kpc) and a gas disk rotating much faster than the stellar spheroid and at an angle to it, indicating a likely external origin (Xilouris et al. 2004; Schweizer 1980). Goudfrooij et al. (2001) used globular clusters to date any major mergers to between 1.5 and 4 Gyr ago, but the age and type of merger (or mergers) still remain uncertain.

Multiwavelength observations can set constraints on the merger event. Radio emission, from the radio jet and lobes, is expected to be powered by accretion onto the central supermassive black hole (SMBH), which can be enhanced by the infall of material from a merger. The expanding radio plasma can create cavities in the surrounding hot gas, which are seen as decrements in the X-ray emission. By measuring the PV work done by the expanding radio plasma (McNamara et al. 2000; Churazov et al. 2002), we can constrain the energy produced by the SMBH. Also, since the X-ray cavities rise buoyantly, their distance from the nucleus constrains the age of the outburst. We can set mass-related constraints on the merger galaxy by examining NGC 1316 for dust. As an early-type galaxy, NGC 1316 is expected to be dust poor. Mid-infrared observations permit us to measure the amount of dust present, which, if higher than expected for a galaxy of its size and type, indicates an external origin for the dust.

In this chapter, we report our analysis of the surface brightness distribution of NGC 1316 in the mid-IR with the Infrared Array Camera (IRAC) and the Multiband Imaging Photometer for Spitzer (MIPS) of the *Spitzer Space Telescope* and the resulting determination of the warm dust morphology. We describe our analysis of the X-ray emission imaged both by *Chandra* and *XMM-Newton*. Observations and data reduction are described in §2, and imaging and modeling results are given in §3. We compare the features seen in the infrared and X-ray with the radio emission in the nuclear, inner jet,

and extended emission regions in §4 and examine the constraints these observations place on the mass of the merger progenitor, the outburst and merger ages, and the outburst energies in §5. Finally, we summarize the results in §6. Images have north to the top and east to the left. Angles are given counter-clockwise from west, unless otherwise stated.

4.2 Observations and Data Reduction

4.2.1 *Spitzer* Observations

IRAC (Fazio et al. 2004) observations of NGC 1316 were obtained on 2004 July 19 and 22 as part of the SIRTF Nearby Galaxy Survey (SINGS) Legacy program (Kennicutt et al. 2003; *Spitzer* PID 159) in all four bands. The two visits to NGC 1316 consisted of similar 4×30 s integrations covering the galaxy, its companion NGC 1317, and the nearby field.

For our analysis, we retrieved the Basic Calibrated Data (BCD) version S14.0 pipeline products from the *Spitzer* archive. We corrected the IRAC BCD frames for residual images arising from prior, unrelated observations of bright sources by making object-masked, median-stacked coadds of all science frames not containing significant extended emission from NGC 1316 or NGC 1317. These single-visit coadds were then subtracted from the individual BCDs of the corresponding visit to remove the residual images. For the 8.0 μm observation, light scattered from the galaxy nucleus along the detector array rows was fit and subtracted from the BCD frames using custom software as in Ashby et al. (2009). We then coadded the modified 30 s BCD frames from both observations using version 4.1.2 of `IRACproc` (Schuster et al. 2006) to mosaics having $1\farcs2$

pixels, i.e., the native IRAC pixel size.

The SINGS program also obtained MIPS observations of NGC 1316 (Rieke et al. 2004) on 2004 December 5 and 7. We obtained a combined 24 μm mosaic and coverage map of NGC 1316 from the SINGS website[2].

A $12' \times 12'$ region centered on the galaxy was selected for analysis in each IRAC and MIPS mosaic. The resulting 3.6 μm image, which is very similar to the 4.5 μm image, is presented in Figure 4.1a. The corresponding images for 5.8 μm, 8.0 μm, and 24 μm are shown in the top row of Figure 4.2. Uncertainty maps were created by adding pixel-pixel rms noise and shot noise in quadrature.

[2]http://data.spitzer.caltech.edu/popular/sings

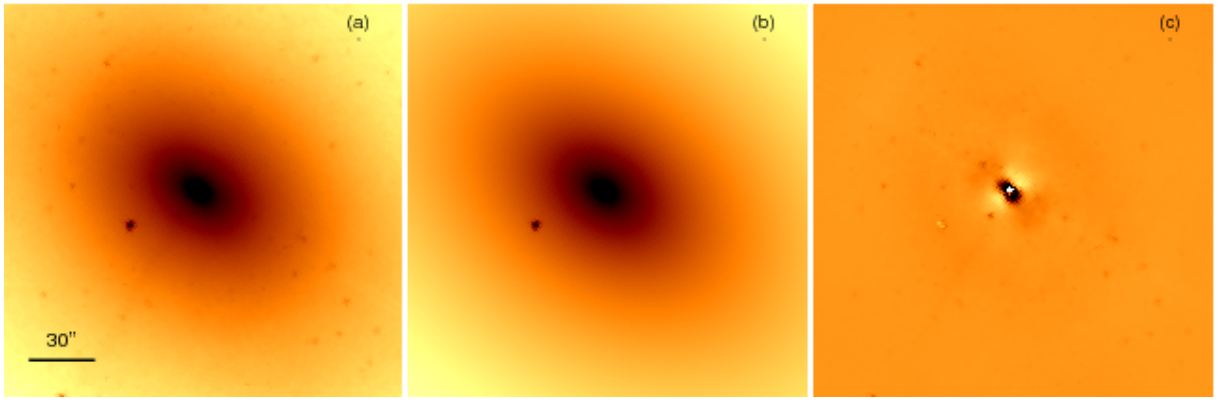

Figure 4.1: The input image used in GALFIT when fitting 3.6 μm (a), the final model combining a Sérsic profile, a point source, and sky (b), and the fit residuals (c). The 4.5 μm images are similar to the 3.6 μm images, and are therefore not shown here. Each image is $3\farcm0 \times 3\farcm0$ with north to the top and east to the left, as are all images throughout this chapter unless stated otherwise. The color scale for all the panels is inverted so bright regions in the residual image (c) are regions where the model is over-subtracted. Panels a and b have logarithmic color scales, while panel c has a linear scale. The dark point source 35″ southeast of the galaxy's nucleus is a foreground star, which we also fit. The scale bar corresponds to 30″ (3.3 kpc).

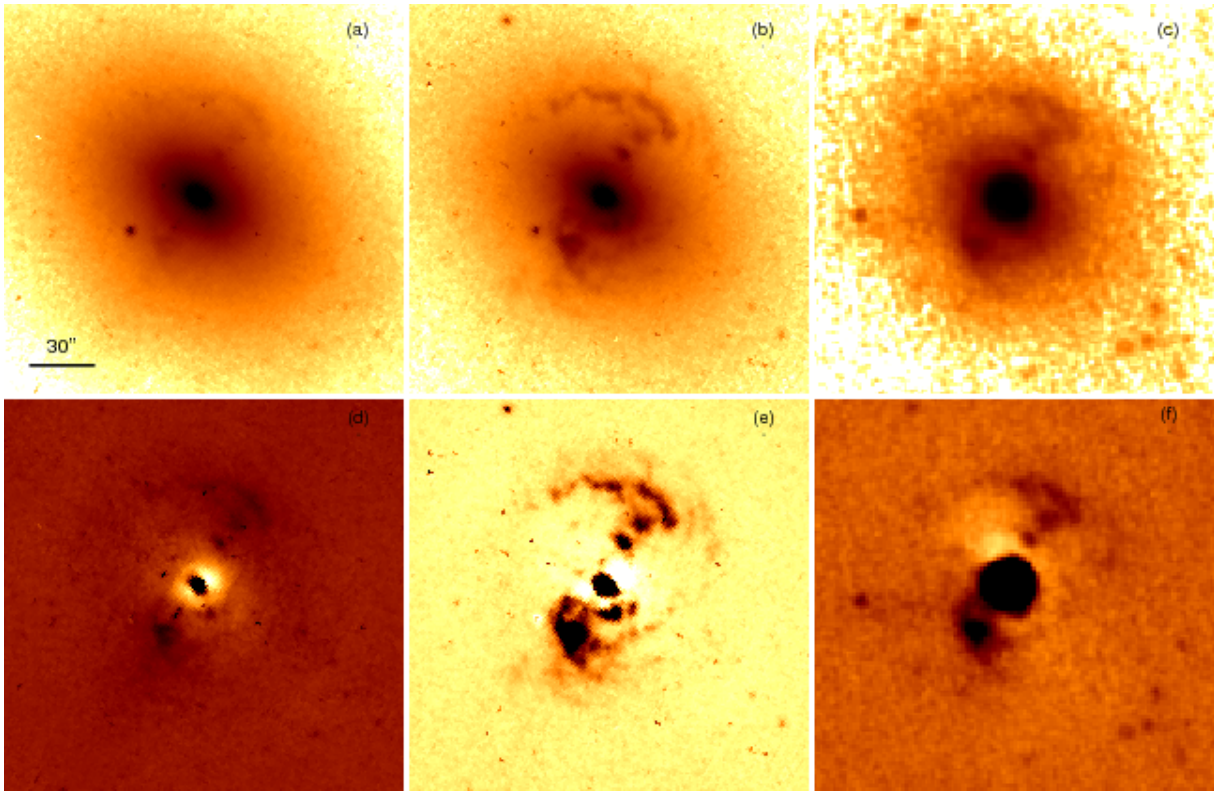

Figure 4.2: The top row shows the input image used in GALFIT when fitting the 5.8 μm (left), 8.0 μm (middle), and 24 μm (right) images. The bottom row are those same images, once a Sérsic model and the foreground star have been subtracted. The image sizes are the same as in Figure 4.1. The color scale is inverted, and the top row has a logarithmic color scale, while the bottom row has a linear color scale. The dark regions in the residual images are excess emission, most likely due to dust. The scale bar corresponds to 30″ (3.3 kpc).

4.2.2 *Chandra* Observations

NGC 1316 was observed for 30 ks on 2001 April 17 (ObsID 2022) with the *Chandra* Advanced CCD Imaging Spectrometer Spectroscopy Array (ACIS-S; Weisskopf et al. 2000). This observation was previously studied by Kim & Fabbiano (2003). We reprocessed this observation applying the latest CTI and time-dependent gain calibrations (see Vikhlinin et al. 2005 for more details). We applied the standard filtering by grade, excluded bad/hot pixels and columns, and removed cosmic ray 'afterglows'. We removed time intervals with background flaring, resulting in an effective exposure time of 23.853 ks. The background files (see Markevitch et al. 2000 for details) were processed in exactly the same manner as the observations.

4.2.3 *XMM-Newton* Observations

XMM-Newton observed NGC 1316 for 107.3 ks on 2005 August 11-12 (ObsID 0302780101). Here we examine the Metal Oxide Semi-conductor CCD (MOS; Jansen et al. 2001) observation. We filtered the data to remove periods of background flaring, resulting in a reduced exposure time of 62.0 ks for MOS1 and 56.3 ks for MOS2. The events were further filtered to retain only events with energies between 0.5 and 7.0 keV and patterns between 0 and 12.

4.2.4 Radio, Optical, and CO Observations

NGC 1316 was observed with the *Very Large Array* (*VLA*) at 4.89 GHz in the AB array configuration on 2002 June 1. We used the Astronomical Image Processing System

(AIPS; version 31DEC09) package to generate a map with a resolution of $1\farcs38 \times 1\farcs02$ (Figure 4.3c). We also obtained a 20 cm *VLA* map from the NASA/IPAC Extragalactic Database (NED) (Fomalont et al. 1989).

The *Hubble Space Telescope* Advanced Camera for Surveys (ACS) observed NGC 1316 on 2003 March 04 through the F555W filter for 6.98 ks (PropID 9409). The WFPC2 instrument on *Hubble* observed it through the F814W filter on 1996 April 07 for 1.86 ks (PropID 5990). ^{12}CO(2-1) intensities at 230 GHz were obtained from C. Horellou and J. H. Black, who observed NGC 1316 with the 15 m Swedish-ESO Submillimeter Telescope (SEST) in 1999 and 2001 with a resolution of $22''$ (Horellou et al. 2001).

4.3 Data Analysis

4.3.1 *Spitzer* Analysis

To measure dust and nuclear emission, we first had to remove the stellar component from the *Spitzer* images. To accomplish this, we modeled the 3.6 μm emission, where the flux from the stars is the greatest of all four IRAC bands, with a two-dimensional Sérsic model (Sérsic 1968) for the stellar contribution. To determine the galaxy model, as well as emission from the nucleus, we used the software package GALFIT (Peng et al. 2002), which is a parametric surface brightness fitting code using χ^2 minimization. We iteratively determined the center for the Sérsic profiles based on the 3.6 μm emission and the position of the central point source based on the 8 μm emission. After confirming that the 4.5 μm emission results in similar parameters, as expected, since this band is also dominated by stellar emission, we held the Sérsic index, effective radius, axis ratio,

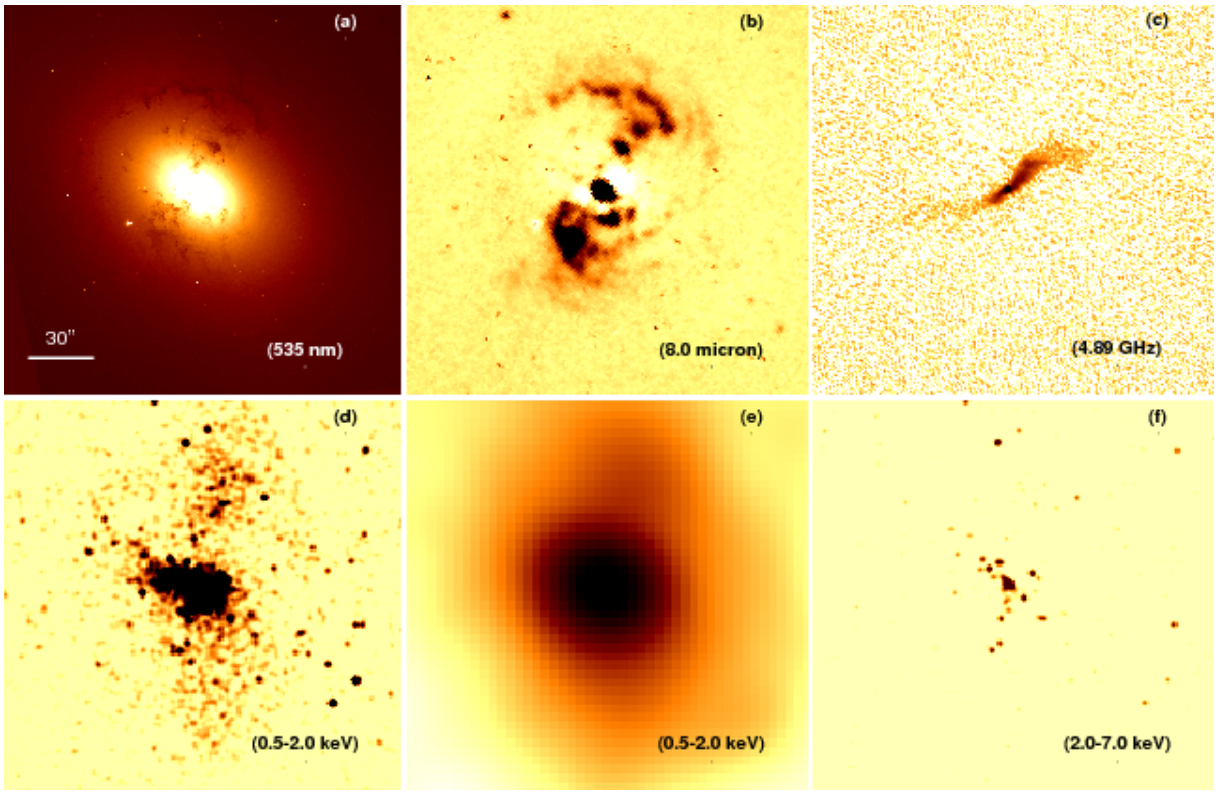

Figure 4.3: $3'.0 \times 3'.0$ images of NGC 1316: (a) *Hubble* ACS visible emission (535 nm), (b) *Spitzer* non-stellar 8.0 μm emission, (c) *VLA* 4.89 GHz emission with a resolution of $1''.38 \times 1''.02$, (d) *Chandra* soft X-ray (0.5-2.0 keV) emission, (e) *XMM-Newton* soft X-ray (0.5-2.0 keV) emission, (f) *Chandra* hard X-ray (2.0-7.0 keV) emission. The *Chandra* images are smoothed with a $5''$ Gaussian and have pixel sizes of $1''$ and $0''.5$ for the soft and hard images respectively. The *XMM-Newton* image is the central region of Figure 4.4, demonstrating the north-south elongation of soft X-ray emission. With the exception of panel a, the darker regions have more emission. Panels a, c, and e have a logarithmic color scale, while panels b, d, and f have a linear color scale. The scale corresponds to $30''$ (3.3 kpc). These images show the variety of morphology present in this galaxy. Optical dust extinction coincides with infrared dust emission, but the distribution of the dust is distinctly different from that of the hot X-ray emitting gas.

position angle, and central position fixed at the 3.6 μm fitted values for subsequent fits to the 4.5 μm, 5.8 μm, 8.0 μm, and 24 μm images. The remaining free parameters were the normalizations of the Sérsic model, central point source, and the foreground star 35″ southeast of the nucleus, as well as a sky model, consisting of a constant offset and gradients in the two array directions. The point response function (PRF) in each band was input to GALFIT in order to fit the emission from the nucleus and foreground star. Masks were used to exclude foreground stars and the bulk of the emission from the neighboring galaxy NGC 1317. The fitted model parameters are given in Table 4.1. The fitted Sérsic index of 6.07 ± 0.10 agrees well with indices of 5.8 and 5.9 determined by Côté et al. (2007) from *Hubble* ACS images of NGC 1316.

Figure 4.1a shows the 3.6 μm mosaic. Figure 4.1b shows the best fitting model obtained from GALFIT of a central point source, foreground point source, and a Sérsic model. Since the residual emission, shown in Figure 4.1c, is on the order of the noise ($\sim 3\%$), outside the nuclear region, our Sérsic model is a good stellar emission model for this galaxy. Since the 4.5 μm image and residuals are similar to those at 3.6 μm, they are not shown.

Figure 4.2 presents the 5.8 μm, 8.0 μm, and 24 μm images (top row) and residuals after the modeled Sérsic profile has been subtracted (bottom row). The 8.0 μm image and contours of its nonstellar emission were previously shown in Temi et al. (2005). The non-axially symmetric, non-stellar component is visible in the top row (a-c) and quite striking in the bottom row (d-f). As we discuss in §4 and §5.1, most of this component is due to dust. In addition to the nucleus, there is a region approximately 11.″8 (1.3 kpc) in radius of dust emission 29″ (3.1 kpc) southeast of the nucleus. There is also dust emission extending 44″ (4.8 kpc) towards the northwest, ending in a clumpy arc that

extends over a $\sim 90^\circ$ angle and containing two knots $21\farcs8$ (2.4 kpc) and $32\farcs0$ (3.5 kpc) from the nucleus.

4.3.2 *Chandra* Analysis

We analyzed *Chandra* observations of NGC 1316 to determine the brightness and morphology of emission due to hot gas and a central nuclear source. We created an image of the soft X-ray emission between 0.5 and 2 keV using the ACIS-S3 CCD. We removed point sources, which we detected using WAVDETECT (Freeman et al. 2002). We then created an exposure map that accounts for all position dependent, but energy independent, efficiency variations across the focal plane (e.g., overall chip geometry, dead pixels or rows, variation of telescope pointing direction). Finally, we made a flat-fielded image by subtracting both the blank-field background and the read-out background and then dividing by the exposure map. We also created an image of the hard X-ray emission between 2 and 7 keV. The resulting images, shown in Figures 4.3d and 4.3f, have $1''$ and $0\farcs5$ pixels respectively and have been smoothed with a $5''$ Gaussian.

4.3.3 *XMM-Newton* Analysis

We analyzed the *XMM-Newton* image to examine features of the extended X-ray emission which were not in the smaller *Chandra* field of view. We created new exposure maps and images, to remove the contribution from the MOS1 CCD with higher background, and we removed point sources. The extended X-ray emission, described in §4.3, includes a pair of cavities $320''$ (34.8 kpc) to the west and southeast of the nucleus. We reprojected

blank sky background files for each of the MOS CCDs[3] to the coordinates of our event file and scaled them appropriately, prior to subtracting the combined background file from the image. We then divided by the exposure map to create an exposure-corrected image with 4″ pixels (Figure 4.4).

[3]http://xmm.vilspa.esa.es/external/xmm_sw_cal/background/blank_sky.shtml

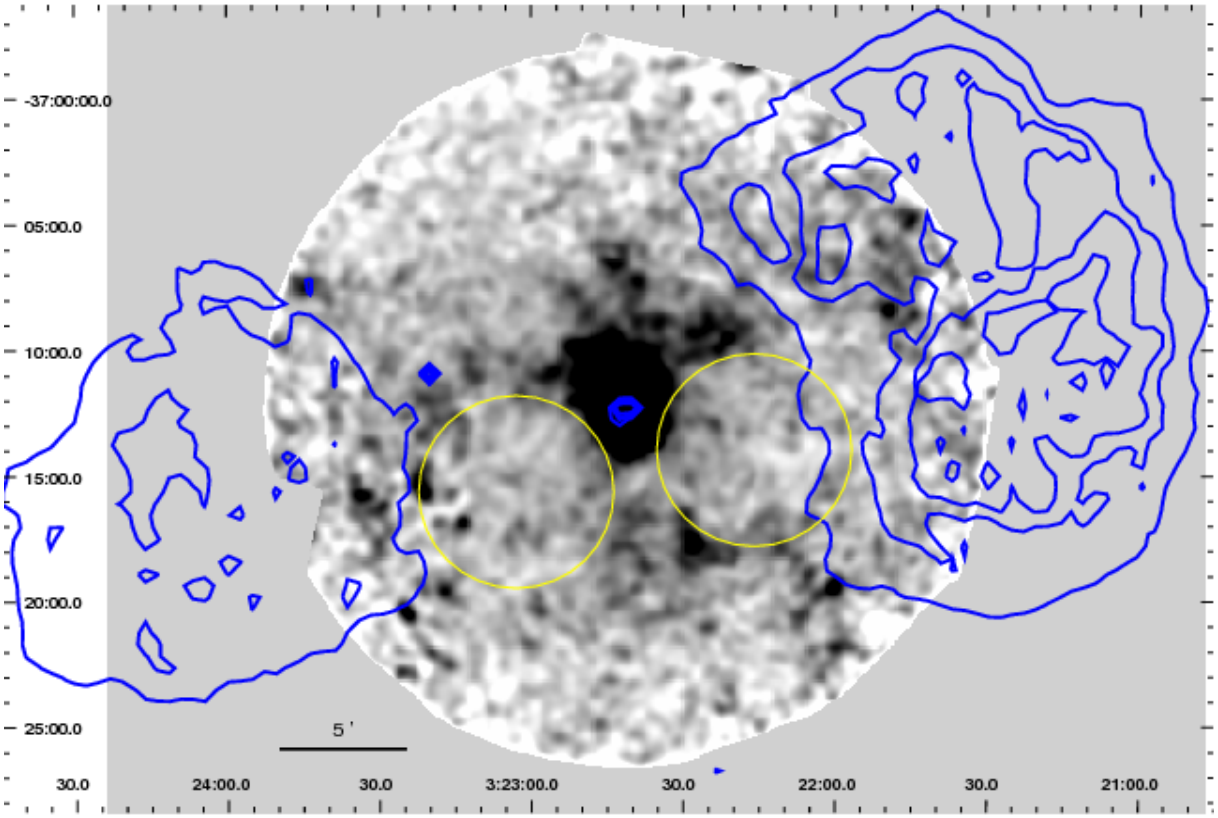

Figure 4.4: 30′ soft (0.5-2.0 keV) exposure-corrected *XMM-Newton* MOS image. Large X-ray cavities (shown by yellow circles) can be seen to the west (right) and to the southeast as lighter regions, centered at ($3^h22^m16^s$, -37°14′00″) and ($3^h23^m3^s$, -37°15′40″) respectively. The edges of the western cavity are marked by emission at ($3^h22^m28.5^s$, -37°17′42″) and ($3^h22^m24^s$, -37°09′35″). The southeastern cavity has a faint edge to its north at ($3^h23^m00^s$, -37°11′33″). These cavities contrast to the brighter emission to the north and south of the nucleus. The blue contours at 6, 11, 15, and 20 mJy/beam are from a 20 cm radio image and show the location of the radio lobes. The scale bar corresponds to 5′ (32.6 kpc).

Table 4.1. GALFIT determined parameters for Sérsic model and nuclear point source

Band (μm)	Sérsic Integrated Flux (mJy)	Sky DC Offset	Nuclear Flux (mJy)	Nuclear Luminosity (10^{41} ergs s^{-1})
3.6	2390 ± 70	-0.10	4.67 ± 0.22	2.40 ± 0.40
4.5	1420 ± 40	0.57	5.63 ± 0.26	2.32 ± 0.38
5.8	1190 ± 40	-0.05	6.78 ± 0.27	2.16 ± 0.35
8.0	560 ± 17	0.11	16.6 ± 0.5	3.85 ± 0.62
24	400 ± 12	-0.20	60.8 ± 1.8	4.69 ± 0.76

Note. — The Sérsic model index ($n = 6.07 \pm 0.10$), effective radius ($r_{eff} = 146\farcs2 \pm 0\farcs6$), axis ratio ($0.688 \pm 0.004$), and position angle ($234.0° \pm 0.2°$ east of north) were all fitted only at 3.6 μm and were held constant for the fits made in the other bands. The central position of the Sérsic profiles and the position of the nucleus were determined iteratively using the 3.6 μm and 8 μm images to be ($03^h22^m41^s.69$, -37°12′28.″8) and ($03^h22^m41^s.71$, -37°12′28.″7) respectively. Note that the Sérsic index determined matches well with the ones obtained by Côté et al. (2007). Luminosities in each photometric band given here are νL_ν in ergs s^{-1}, determined from the luminosity density L_ν. The uncertainty in the luminosities is the result of both the uncertainty in the flux measurement and in the distance to NGC 1316.

4.4 Multiwavelength Comparison of Features

Figure 4.3 shows NGC 1316 in visible (555 nm), non-stellar infrared (8.0 μm), radio (4.89 GHz), *Chandra* soft (0.5-2.0 keV), *XMM-Newton* soft (0.5-2.0 keV), and *Chandra* hard (2.0-7.0 keV) emission. For the 8.0 μm image, we subtracted the stellar emission, as modeled by a Sérsic profile. In Figure 4.5, we show the relative locations of the X-ray, IR, radio, and CO emission. Below, we discuss the nucleus, the jet, and the extended non-stellar emission.

4.4.1 Nuclear Emission

The nucleus is detected in the radio, UV, X-ray, and IR bands. We obtained radio and UV nuclear fluxes from the literature (Geldzahler & Fomalont 1984; Fabbiano et al. 1994). We measured the X-ray spectrum in a 1″ radius circle around the nucleus, using a 1″-2″ annulus to subtract the background thermal emission. We fit the nuclear spectra with an absorbed power law with both a variable n_H and an n_H held constant at the Galactic value of $2.4 \times 10^{20}\,\mathrm{cm}^{-2}$ (Kalberla et al. 2005). The variable n_H fit had a similar power law index to the constant n_H fit and a column density not significantly larger than the Galactic absorption. Therefore, we used the constant n_H spectral fit whose best-fit power law index was $2.09^{+0.41}_{-0.46}$ (90% confidence), which is within the range typically observed for active galactic nuclei (AGN). We converted measured soft (0.5-2.0 keV) and hard (2.0-7.0 keV) X-ray fluxes to luminosities of $6.5 \pm 1.8 \times 10^{38}$ ergs s^{-1} and $5.7 \pm 2.1 \times 10^{38}$ ergs s^{-1}. We measured the X-ray nuclear broadband (0.3-8 keV) flux to be $2.4 \pm 0.7 \times 10^{-14}$ ergs s^{-1} cm^{-2}. Our flux corresponds to a broadband (0.3-8.0 keV) luminosity of $1.5 \pm 0.5 \times 10^{39}$ ergs s^{-1}. We also measured the nuclear flux in the F814W

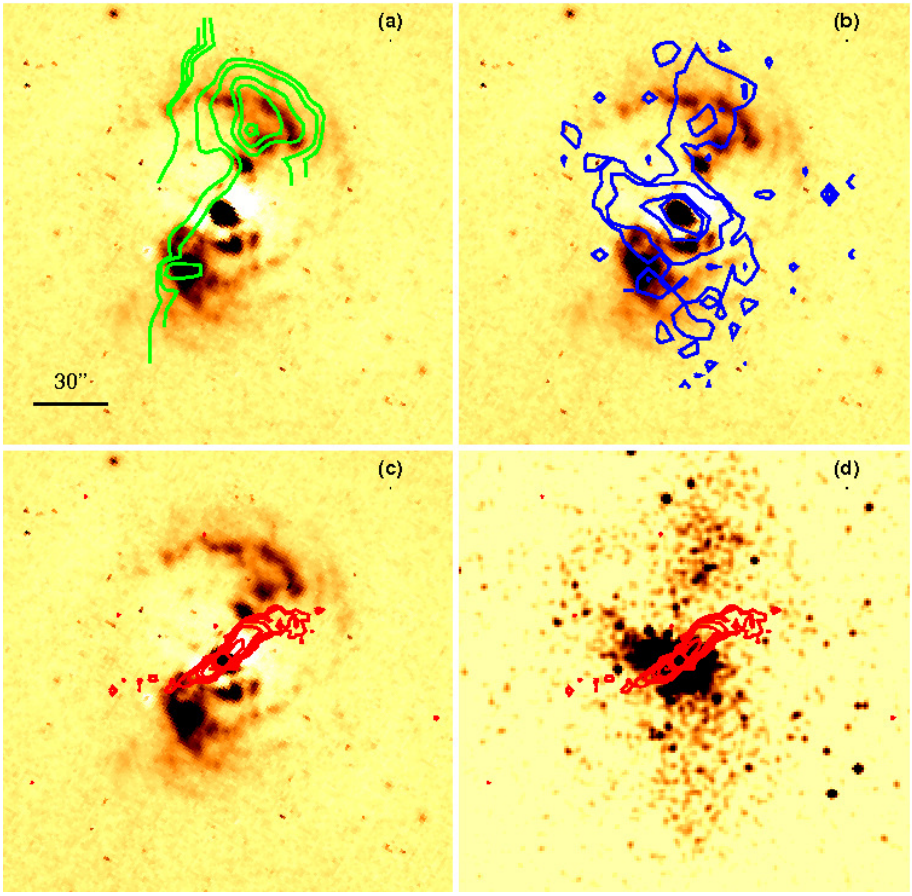

Figure 4.5: $3'.0 \times 3'.0$ images of NGC 1316: (a, b, c) *Spitzer* non-stellar 8.0 μm emission with (a) contours of CO(2-1) (green) (Horellou et al. 2001), (b) flat-fielded soft (0.5-2.0 keV) *Chandra* X-ray contours (blue) at 0.01, 0.02, 0.1, and 0.2 counts/ks/arcsec^2, and (c) radio contours (red) at 0.04, 0.06, 0.10, 0.20, 0.50, 1.0, and 6.0 mJy/beam (rms is 0.03 mJy/beam); and (d) *Chandra* soft X-ray (0.5-2.0 keV) emission with radio contours. The scale corresponds to $30''$ (3.3 kpc). These images show that: 1) infrared dust and molecular emission coincide, 2) the soft X-ray emission shows no indication of absorption due to the dust and cold gas, and 3) that the resolved radio jet does not coincide with dust or soft X-ray emission, but lies in an inner X-ray cavity.

Hubble image in a 0.″15 radius aperture to be $7.8 \pm 0.2 \times 10^{-13}$ ergs s^{-1} cm^{-2}, which we consider an upper limit because of the stellar contribution. Since the F555W image is saturated in the central region, we do not measure the nuclear flux through this filter.

The nucleus is detected in all five *Spitzer* bands. Fluxes and luminosities, νL_ν, in each photometric band from the GALFIT model are given in Table 4.1. We note that the nuclear fluxes were derived from fitting, but that the point source is not directly visible in the IRAC images. To confirm that the galaxy does contain a point-like nucleus, we used the 3.6 μm emission as a stellar model, which was then color corrected and scaled to correct for differences in the apertures and zero point magnitudes between the IRAC bands. The resulting non-stellar images are very similar to those in the bottom row of Figure 4.2. The IR color of NGC 1316's nucleus falls outside, but within 3σ, of the region defined by the mid-IR AGN color selection criteria of Stern et al. (2005) and within the selection region defined by Lacy et al. (2004). We note however that these IRAC selection criteria were developed for Seyfert galaxies and quasars that are significantly more luminous than NGC 1316. Indeed, the spectral energy distribution (SED) of the NGC 1316 AGN (Figure 4.6) is similar to those of other low luminosity AGN (LLAGN) (Ho 1999) in that it lacks the big blue bump found in powerful, optically bright AGN and instead appears to show only a single big red bump and has a larger radio to optical ratio than that of the higher luminosity AGN (Ho 2008). The comparison spectra plotted in this figure are from Figure 7 of Ho (2008) where the purple squares are the LLAGN. Smith et al. (2007b) cited the AGN of NGC 1316 as having the typical peculiar PAH spectrum of LLAGN, which has low ratios of $L(7.7\,\mu\mathrm{m})/L(11.3\,\mu\mathrm{m})$.

We used the supermassive black hole mass of $1.5 \times 10^8\,\mathrm{M}_\odot$ (Nowak et al. 2008) to determine the Eddington luminosity for the AGN to be 2.3×10^{46} ergs s^{-1}. We

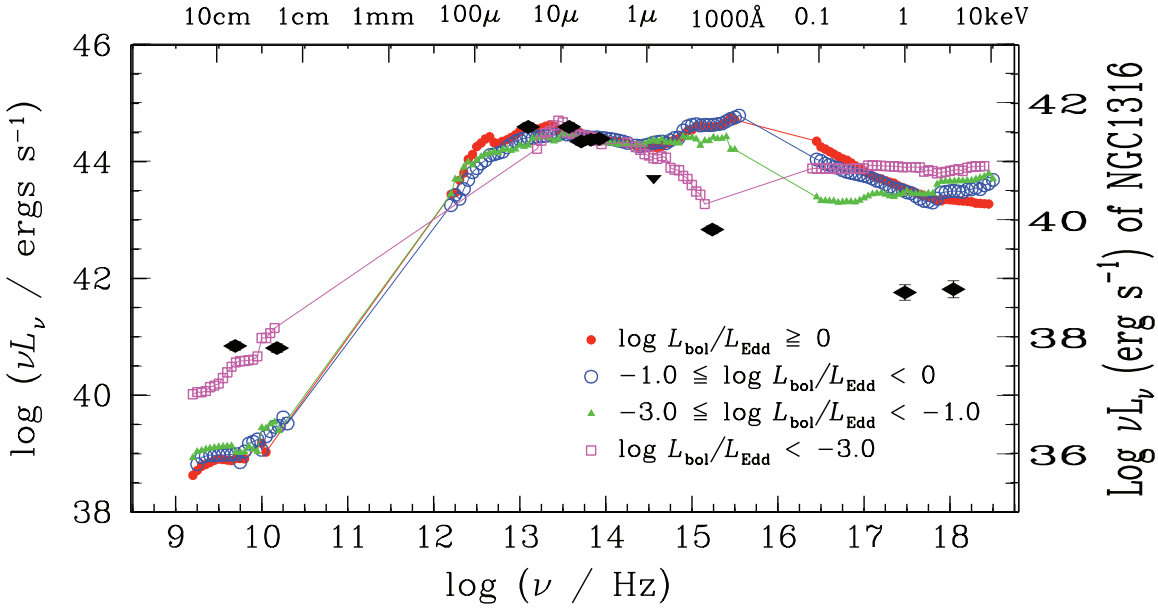

Figure 4.6: Spectral energy distribution of the nuclear emission in the *Spitzer* and *Chandra* bandpasses, through the F814W *Hubble* filter (upper limit), at 4.9 GHz and 15.0 GHz from Geldzahler & Fomalont (1984), and at 1730Å from Fabbiano et al. (1994). The right vertical axis applies to this AGN, and the left axis to the comparison AGN SEDs that are normalized at 1 μm and come from Figure 7 of Ho (2008). The purple squares are the LLAGN with $\log(L_{bol}/L_{Edd} < -3.0)$. NGC 1316's AGN has $\log(L_{bol}/L_{Edd} = -3.9)$. Note the large radio to optical ratio and the lack of the UV-optical big blue bump in the NGC 1316 AGN.

interpolated the SED between the observed photometric points from 10^9 Hz to 10^{18} Hz and derived a bolometric luminosity of $\sim 2.4 \times 10^{42}$ ergs s^{-1}, corresponding to a bolometric correction of ∼6.2 for the 8.0 μm IRAC band. The AGN therefore has a low Eddington ratio of $\sim 10^{-4}$. We also calculated the Bondi accretion rate to be $1.6 \times 10^{-4}\,M_\odot\,yr^{-1}$ (Bondi 1952), based on the black hole mass (Nowak et al. 2008), the 0.77 keV gas temperature (Isobe et al. 2006), and a central gas density of $0.4\,cm^{-3}$ derived from a β model (Cavaliere & Fusco-Femiano 1976) fit to the central 200″ (21.7 kpc) region using *Chandra* data ($a_X = 320$ pc, $\beta = 0.49$, $n_0 = 0.4\,cm^{-3}$) (Jonsson et al. 2010).

4.4.2 Inner Jet

The 4.89 GHz radio emission on small scales (Figure 4.3c) has previously been extensively described by Geldzahler & Fomalont (1984). The northwest jet extends 0.′5 (3.3 kpc) from the nucleus and does not decrease significantly in brightness over the initial 15″ (1.6 kpc). In contrast, the weaker southeast counterjet decreases immediately in brightness away from the nucleus. Unlike the jet in M87 (Shi et al. 2007; Forman et al. 2007) which is clearly detected in all four IRAC bands, the NGC 1316 radio jet is not detected in any IRAC band or at 24 μm. We used an aperture defined by the region of radio emission to the northwest of the nucleus to derive upper limits on the IR emission from the jet, which are given in Table 4.2. Extended aperture corrections were derived and applied.[4] We also calculated the expected fluxes assuming a synchrotron model with a typical spectral index of 0.55 from the radio flux of 29 mJy within the aperture. The expected

[4]IRAC: Extended Source Calibration http://ssc.spitzer.caltech.edu/irac/iracinstrumenthandbook/33

fluxes range from 0.38 mJy to 0.14 mJy, which are below the limits measurable with the present data.

The soft X-ray image (Figure 4.3d and 4.3e and contours on Figure 4.5b) does not show emission from the jet. The resolved northwest radio jet coincides with a region of low X-ray emission, most likely a small $\sim 15''$ X-ray cavity created by the expansion of the radio plasma, previously described by Kim & Fabbiano (2003). As illustrated in Figure 4.5c, the dust emission is faint at the position of the radio jet. The bend in the northwestern jet is located just south of the first IR knot, along the northwestern dust protrusion.

Table 4.2. Jet Infrared Flux Upper Limits

Band (μm)	Flux (mJy)	1σ Unc. (mJy)	Luminosity (10^{40} ergs s^{-1})	1σ Unc. (10^{40} ergs s^{-1})
3.6	<1.05	0.35	<5.94	1.98
4.5	<0.66	0.22	<2.98	0.99
5.8	<0.58	0.19	<2.07	0.69
8.0	<0.39	0.13	<0.97	0.32
24	<0.81	0.27	<0.69	0.23

Note. — Fluxes, given in mJy, are 3σ upper limits and were obtained using an aperture defined by the radio emission northwest of the nucleus applied to each *Spitzer* image. The galaxy flux was removed using the Sérsic model determined from fitting the *Spitzer* images with GALFIT. Luminosities in each photometric band given here are νL_ν in ergs s^{-1}, determined from the luminosity density L_ν.

4.4.3 Extended Non-Stellar Emission

Temi et al. (2005) found that the morphology of the 8.0 μm non-stellar emission was similar to that of the 15 μm emission detected by the *Infrared Space Observatory* (ISO) (Xilouris et al. 2004). They concluded that, while much of the excess emission at 8.0 μm was likely due to PAH emission at 7.7 μm, warm, small dust grains also contributed. The similarity of the features at 5.8 μm and 24 μm supports this interpretation. The extended non-stellar emission has significant structure at all wavelengths as shown in Figure 4.3 and Figure 4.5:

- The *Hubble* ACS image (Figure 4.3a) demonstrates that regions of visible dust extinction have similar morphology to the infrared dust emission described in §3.1 and shown at 8.0 μm in Figure 4.3b. (See similar image in Temi et al. (2005).)

- The CO contours (Horellou et al. 2001) superimposed on the 8.0 μm non-stellar emission in Figure 4.5a demonstrate that the northwestern and southeastern dust emission regions coincide with molecular hydrogen traced by the CO emission, suggesting a common origin for the dust and cold gas.

- The strongest X-ray emission outside the nucleus (Figure 4.5b with soft X-ray contours overlaid on the 8.0 μm non-stellar emission) extends northeast of the nucleus along the major axis of NGC 1316 into a region absent of infrared dust emission. We tested whether the dusty features seen in the infrared and the coincident cold gas result in soft X-ray absorption, but found no indication thereof, although the data is not sufficient to make a conclusive statement.

In the galaxy core, the soft *Chandra* image and the *XMM-Newton* image show a

roughly north-south elongation approximately 1.′25 (8.2 kpc) in each direction (Figures 4.3d, 4.3e), which does not follow the distribution of the stars. Instead, this emission is roughly perpendicular to the major axis of NGC 1316 and may be from hot gas that was moved by the outburst. The larger *XMM-Newton* field of view (Figure 4.4) shows further filamentary emission north of the nucleus and a pair of X-ray cavities. These cavities, likely created by the expansion of radio plasma, are marked with yellow circles of 230″ (25 kpc) radii. The western cavity is centered at ($3^h22^m16^s$, -37°14′00″) and the southeastern cavity is centered at ($3^h23^m3^s$, -37°15′40″). Each cavity lies 320″ (34.8 kpc in the plane of the sky) from the nucleus. There are three regions of enhanced emission along the edges of these cavities, approximately located at ($3^h22^m28.5^s$, -37°17′42″), ($3^h22^m24^s$, -37°09′35″), and ($3^h23^m00^s$, -37°11′33″), which are likely due to increased gas density as the hot ISM is compressed by the expanding cavities. No radio emission is detected in these X-ray cavities, a situation previously seen in Abell 4059 (Heinz et al. 2002), M87 (Forman et al. 2007), and the Perseus cluster (Fabian et al. 2006). While the centers of the radio lobes line up with the AGN, there are indications that this system may be experiencing some sloshing of the hot gas. Specifically, the X-ray cavities are centered 1.′5 and 3.′2 south of the nucleus and Ekers et al. (1983) found low-level radio emission between the lobes $\sim 7'$ south of the nucleus.

To quantitatively measure the significance of the cavities seen in the *XMM-Newton* image, we plot in Figure 4.7 the azimuthal surface brightness of the soft (0.5-2.0 keV) exposure-corrected background-subtracted *XMM-Newton* image (Figure 4.4) taken in an annulus extending from 180″ (19.6 kpc) to 375″ (40.8 kpc) from the nucleus after the image was smoothed with a 28.″2 Gaussian. The azimuthal profile shows that the regions between 190-230°, (i.e. southeast of the nucleus), and between

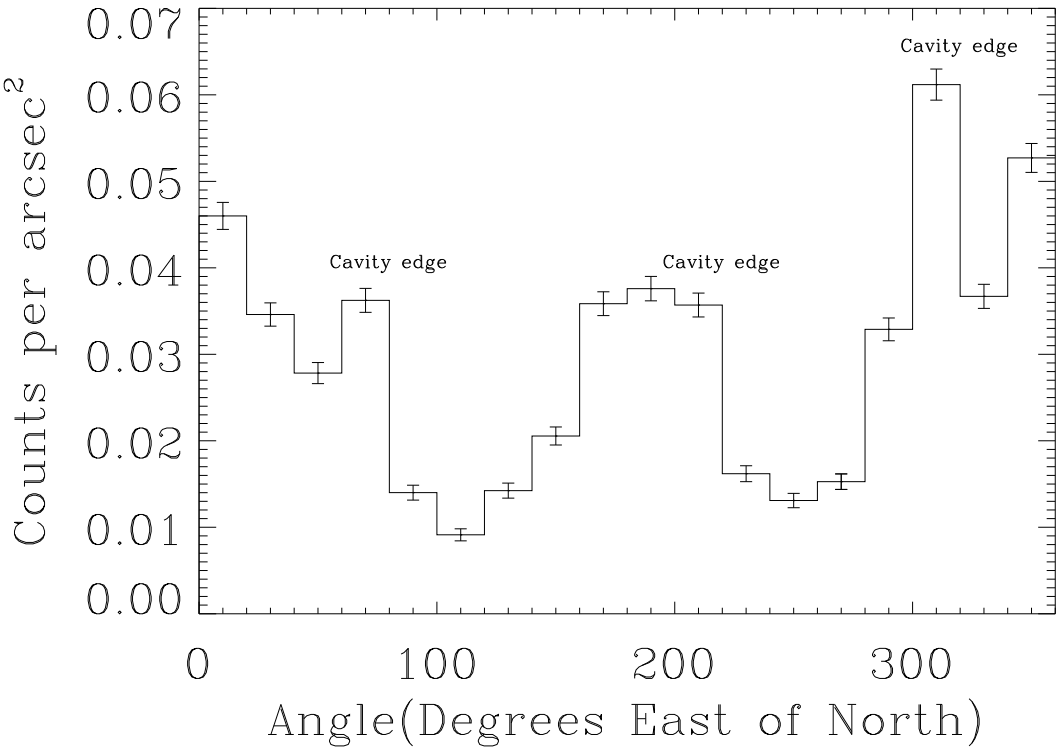

Figure 4.7: Azimuthal profile of background-subtracted counts per square arcsecond for a radial sector with inner and outer radii of 180″ (19.6 kpc) and 375″ (40.8 kpc) from the nucleus in the soft (0.5-2.0 keV) *XMM-Newton* image in Figure 4.4. Angles are given counterclockwise from north. Note that there is less flux to the southeast (120°) and to the west (250°), which corresponds to the locations of the centers of the cavities apparent in Figure 4.4.

330-10°, (i.e. to the west), have significantly lower surface brightness than the rest of the annulus. These regions coincide with the cavities identified (yellow circles) in Figure 4.4. The bright regions north of the nucleus and along the cavity edges in Figure 4.4 coincide with the significantly brighter regions in the azimuthal plot (Figure 4.7). The three regions of enhanced X-ray emission along the cavity edges are noted in Figure 4.7.

We tested whether the variations in azimuthal surface brightness could be the result of abundance or gas density variations. The maximum surface brightness change would require a factor of 2.3 difference in elemental abundance (i.e. the lower surface brightness region would have an elemental abundance 40% that of the brighter regions). While such an abundance gradient would be relatively long lived against diffusion, even if it proceeds as fast as predicted for heavy ions in a fully ionized plasma (Sarazin 1988; Spitzer 1956), such a distribution of metals mimicking cavity structures seems particularly contrived. An alternative explanation for the surface brightness variations is for the isobaric gas to have a density in the regions of lower surface brightness 0.66 times that of the gas to the north and south of the nucleus. Such a difference in density requires either that the lower surface brightness gas is at least 1.5 times hotter than the surrounding gas or that the regions of lower surface brightness would be filled with a relativistic plasma. No indication of emission from a hot plasma is seen in the harder X-ray band (2.0-7.0 keV). Therefore, we expect the regions of lower surface brightness to be cavities filled with a currently undetected relativistic plasma, a morphology seen in other galaxies and galaxy clusters and known as ghost cavities (Heinz et al. 2002). Emission from ghost cavities are generally detected in low-frequency radio data (e.g. Giacintucci et al. 2009).

4.5 Multiwavelength View of the Consequences of the Merger Event

NGC 1316 exhibits signs of a recent merger, including nuclear activity and a disturbed morphology seen in the optical and infrared dust distribution as well as the tidal tails first noted by Schweizer (1980). Each wavelength provides different insights into the merger event and the resulting structure of NGC 1316. Below, we discuss the distribution of the infrared-emitting dust and estimate the mass of the galaxy that collided with NGC 1316 from the measured dust mass. We also use the morphology of the large scale radio and X-ray emission (Figure 4.4) to constrain the recent outburst history of the central SMBH.

4.5.1 Dust Distribution

To measure the dust emission in the *Spitzer* bands, we performed aperture photometry on the infrared images after subtracting a Sérsic model of the stellar emission. Elliptical apertures (Figure 4.8) were chosen to include dust features seen at 8.0 μm. For the southeastern region, we used an ellipse with a major axis of $56\farcs8$, a minor axis of $46\farcs6$, and a position angle of 284° (east of north) centered at ($3^h22^m42^s.75$, -37°13′02$\farcs$1). For the northwestern region, we used an ellipse with a major axis of $86''$, a minor axis of $54''$, and a position angle of 245° centered at ($3^h22^m40^s.47$, -37°11′53$\farcs$0). The counts in each aperture were background subtracted and converted to fluxes, after an extended aperture correction was applied. Columns 2-3 of Table 4.3 list the flux in each aperture. The next two columns give the total fluxes and their uncertainties with and without the nuclear

point source (nuclear fluxes given in Table 4.1). The uncertainties have two components: the uncertainty in the Sérsic model and the uncertainty in the photometric accuracy of *Spitzer* images (Reach et al. 2005; Engelbracht et al. 2007).

Draine et al. (2007) modeled the integrated IRAC, MIPS, and IRAS fluxes of the SINGS galaxy sample with a two-component dust model and determined dust masses. They estimate their models are accurate to 10%. To test whether the dust mass determined for NGC 1316 by Draine et al. (2007) is located within the regions visible in Figure 4.8, we compared our photometry from the two regions of dust emission and the nucleus to their dust model predictions. We convolved the predicted Draine et al. (2007) dust flux SED for NGC 1316 (their Figure 14) through the appropriate response functions to calculate the expected fluxes in the *Spitzer* band passes. Our $5.8\,\mu$m and $8.0\,\mu$m total fluxes for the dust regions and nucleus of 17.4 ± 0.9 mJy and 49.2 ± 0.9 mJy are consistent with the Draine et al. (2007) model values of 13.0 ± 1.3 mJy and 45.4 ± 4.5 mJy, which are the emission for the entire galaxy. The agreement leads us to conclude that the dust mass estimated by Draine et al. (2007) is contained in the non-stellar IR emission regions described in §3.1 and in the nuclear region.

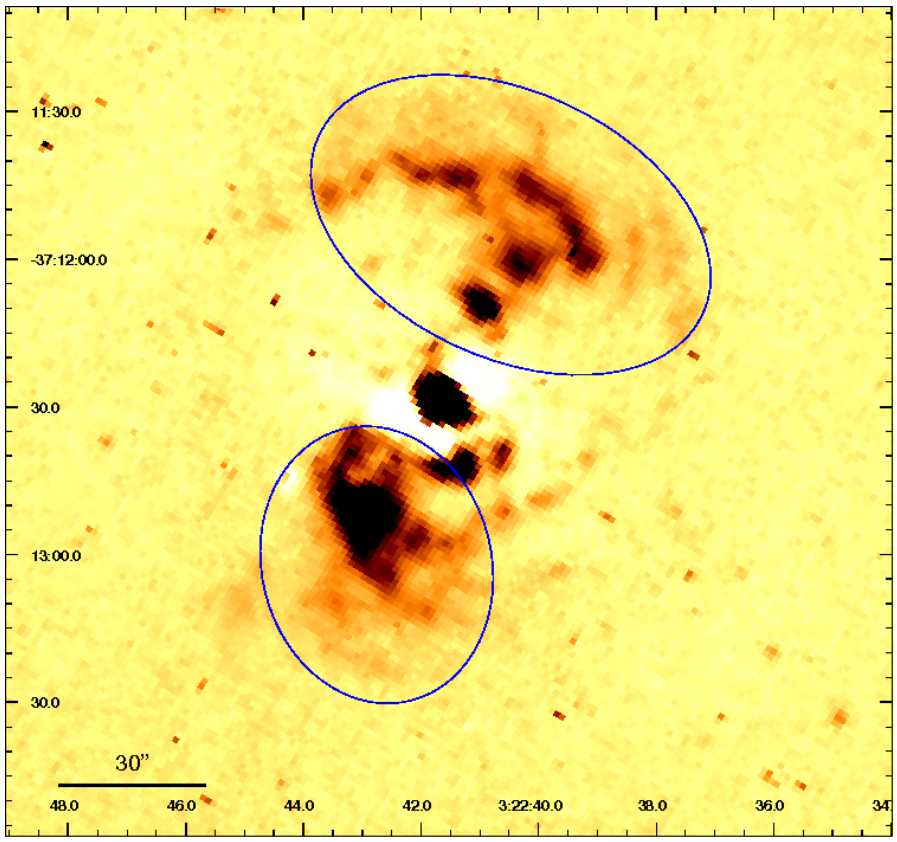

Figure 4.8: 8.0 μm non-stellar image showing the position and size of the apertures used to determine the dust photometry. The southeastern aperture is an ellipse with a major axis of 56.″8, a minor axis of 46.″6, and a position angle of 284° (east of north) centered at ($3^h22^m42^s.75$, -37°13′02.″1). The northwestern aperture is an ellipse with a major axis of 86″, a minor axis of 54″, and a position angle of 245°centered at ($3^h22^m40^s.47$, -37°11′53.″0). The scale bar corresponds to 30″ (3.3 kpc).

Table 4.3. Dust Photometry

Band (μm)	SE Knot $03^h22^m42^s.75$ -37°13′02.″1 (mJy)	NW Knot+Arc $03^h22^m40^s.47$ -37°11′53.″0 (mJy)	Total of knots (mJy)	Total with nucleus[1] (mJy)
5.8	4.16±0.43	6.47±0.70	10.6±0.8	17.4±0.9
8.0	18.8±0.6	13.8±0.5	32.6±0.8	49.2±0.9

Note. — Fluxes (cols 2-3) were obtained using elliptical apertures (Figure 4.8) for the southeast and northwest region on each *Spitzer* image once a Sérsic model had been subtracted.

[1]Nuclear fluxes are given in Table 4.1

4.5.2 Dust Mass and Merger Progenitor Mass

In the following, we show that the dust observed in NGC 1316 is not native to the galaxy and use the dust mass to estimate the mass of the merger galaxy. The clumpy morphology of the dust is significantly different from the smooth elliptical distribution of the stars, so the NGC 1316 stars could not have expelled the dust. In addition, Tang et al. (2009) found for nearby ellipticals that most of the non-stellar 8.0 μm emission is confined to the nuclear region. This also demonstrates that the morphology of the dust emission in NGC 1316 is unusual. Temi et al. (2009) found a correlation between the K-band and 24 μm luminosities of elliptical galaxies. NGC 1316 has a particularly large 24 μm luminosity for its K-band luminosity, about an order of magnitude greater than predicted by the Temi et al. (2009) correlation. While Temi et al. (2009) did not find a correlation between K-band luminosity and either 70 μm or 160 μm luminosity, NGC 1316's integrated luminosities at these wavelengths of 1.4×10^{43} ergs s^{-1} and 1.5×10^{43} ergs s^{-1} (Dale et al. 2007) are also more than an order of magnitude greater than found for the galaxies in the Temi et al. (2009) sample. The large infrared luminosities of NGC 1316 demonstrate an external origin for the dusty emission.

In the following, we estimate the mass of dust in NGC 1316 as well as the dust mass expected to be in an elliptical galaxy the size of NGC 1316. Muñoz-Mateos et al. (2009) provided a formula (A8) for calculating the dust mass of a galaxy from its 24 μm, 70 μm, and 160 μm fluxes and its distance. We calculated that NGC 1316 has a total dust mass of $2.4 \pm 0.9 \times 10^7\,M_\odot$, using the integrated MIPS fluxes from Dale et al. (2007). While emission from the dust is clearly observed, the large uncertainty on the dust mass results from the uncertainties in the distance to NGC 1316 (22.7 ± 1.8 Mpc)

and in the integrated MIPS fluxes (0.43 ± 0.02 Jy at 24 μm, 5.44 ± 0.40 Jy at 70 μm, and 12.61 ± 1.78 Jy at 160 μm). We revised the Draine et al. (2007) dust mass for NGC 1316, which was found on the basis of SED fitting, for our assumed distance of 22.7 Mpc to be $3.2 \times 10^7\,M_\odot$, which is consistent with our dust mass. We used the fluxes for the sample of elliptical galaxies in Temi et al. (2009), along with their B-V colors (de Vaucouleurs et al. 1991) and the color-dependent mass-to-light ratios of Bell et al. (2003), to calculate the stellar and dust masses of the sample. We found that elliptical galaxies typically have dust-to-stellar mass ratios between $0.7 - 5.3 \times 10^{-7}$. Using these ratios, we estimate that NGC 1316 with its stellar mass of $5.3 \times 10^{11}\,M_\odot$ (based on B-V=0.87 (de Vaucouleurs et al. 1991), K = 5.587 (Jarrett et al. 2003), and the relations of Bell et al. (2003)) had an intrinsic dust mass of $0.4 - 3 \times 10^5\,M_\odot$, $\lesssim 1\%$ of the measured dust mass. We conclude that nearly all of the dust currently present in NGC 1316 was contributed by a merger galaxy.

We can constrain the galaxy type and the stellar and gas mass of the merger galaxy from its estimated dust mass of $2.4 \pm 0.9 \times 10^7\,M_\odot$. The merger galaxy had to be a late type galaxy as its stellar mass, were it a typical elliptical, would have been roughly 200 times the present stellar mass of NGC 1316. We calculated the stellar masses of the spiral galaxies in the SINGS sample using NED colors and the color-dependent stellar M/L ratios of Bell et al. (2003). Using the dust masses from Draine et al. (2007), we found dust-to-stellar mass ratios between $0.4 - 3.4 \times 10^{-3}$ for Sa-Sm galaxies with Sc galaxies having the largest ratios. From these ratios and the merger galaxy dust mass, we estimate that the merger galaxy had a stellar mass in the range of $1 - 6 \times 10^{10}\,M_\odot$, approximately 10% of NGC 1316's current stellar mass. Assuming typical galaxy colors (Trimble 2000), we calculated the corresponding L_B to be $0.7 - 2 \times 10^{10}\,L_\odot$ using

the ratios of Bell et al. (2003). We estimate the corresponding cold gas masses based on gas-mass-to-light ratios of Bettoni et al. (2003) to be $2 - 4 \times 10^9\,M_\odot$. Kennicutt et al. (2003) found an upper limit on the mass of neutral hydrogen in NGC 1316 of $5.5 \times 10^8\,M_\odot$, and Horellou et al. (2001) estimate that NGC 1316 has $7.4 \times 10^8\,M_\odot$ of molecular hydrogen gas, resulting in a total cold gas mass of less than $1.3 \times 10^9\,M_\odot$. Since the merger galaxy's estimated cold gas mass of $2 - 4 \times 10^9\,M_\odot$ is larger than NGC 1316's present cold gas mass, some cold gas may have been ionized due to mixing with hot gas or used in star formation in the merger process.

4.5.3 Outburst Ages

The morphologies of the large scale GHz radio emission and the large X-ray cavities in NGC 1316 suggest two possible interpretations of the recent outburst history of the NGC 1316 AGN. Based on the relative location of the X-ray cavities and the radio lobes, we can conclude that either the 1.4 GHz radio features do not fully define the extent of the radio lobes created in conjunction with the X-ray cavities in the course of a single outburst or there were at least two outbursts, one resulting in the radio lobes and a more recent one creating the X-ray cavities seen in the *XMM-Newton* image. In the two outburst scenario, we expect the X-ray cavities, which lie at a smaller radius, to result from the more recent outburst, as they would otherwise have been disrupted by the expanding radio lobes.

Cavity ages can be estimated by assuming that the bubbles that create them rise buoyantly in the gaseous atmosphere (e.g. Churazov et al. 2001). Assuming an approximate buoyancy velocity of $\sim 0.6\,c_s$, where c_s is the sound speed (Churazov et al.

2001), we estimate a buoyancy speed of 270 km s^{-1} in the 0.77 keV medium (Isobe et al. 2006). The X-ray cavities are located 320″ from the nucleus and Wade (1961) measured the separation of the radio lobes to be 33′. If we assume the lobe expansion is in the plane of the sky, for NGC 1316's distance of 22.7 Mpc, the X-ray cavities and the radio lobes are at 35 kpc and 108 kpc from the nucleus respectively. These distances correspond to buoyancy rise times of 0.1 Gyr for the X-ray cavities and 0.4 Gyr for the radio lobes. The age of 0.4 Gyr appears large for radio lobes still emitting at 1.4 GHz, but matches the estimate of the synchrotron age calculated by Ekers et al. (1983). Further, if the lobe is continuously or intermittently connected to the nuclear power supply, fresh injection of electrons or re-energization of existing electron populations could, in principle, supply sufficient high energy electrons so that the lobe is visible at GHz frequencies even after several hundred million years. Finally, Iyomoto et al. (1998) estimated that the nucleus of NGC 1316 was active ∼0.1 Gyr ago, which agrees with our estimate of the age of the X-ray cavities.

Mackie & Fabbiano (1998) estimated a single merger with a low-mass gas-rich galaxy ∼0.5 Gyr ago could be responsible for the optical tidal tail morphology. Such a merger could have provided the material to power the AGN outbursts. A gas-rich merger galaxy would contribute blue young stars, which require about a Gyr to become red and dead. The B-V color of NGC 1316 of 0.87 (de Vaucouleurs et al. 1991) is slightly bluer than the typical B-V color of 0.91 for elliptical galaxies (Trimble 2000), which suggests that NGC 1316 may still contain a small population of early type stars. NGC 1316's color therefore supports a merger within the last Gyr. We also can set a lower limit on the merger age by estimating the free-fall time of the northwestern dust component. We revised the Arnaboldi et al. (1998) total mass within 45″ of the nucleus to be $6.6 \times 10^{10}\,M_{\odot}$ and

used this along with the excess velocity of 70 km s^{-1} for the northwestern clump of molecular gas (Horellou et al. 2001) to estimate a free-fall time for the northwestern dust and molecular gas feature. The estimated free-fall time of 22 Myr is a lower limit on the age of the merger, since the clump likely also has a tangential velocity component and was likely deposited at greater radii by the merger.

4.5.4 Outburst Energies

Churazov et al. (2002) described the energy deposition required to inflate a bubble adiabatically, and thereby create a cavity, as the enthalpy of that bubble, which for relativistic gas is $4PV$. To estimate the energy of the outburst responsible for the X-ray cavities, we used the more clearly defined western X-ray cavity, whose shape we approximate as a sphere of 230″ (25 kpc) centered 320″ (34.8 kpc) from the nucleus. To measure the pressure, we assume an isothermal gas at 0.77 keV (Isobe et al. 2006) and solar abundance and derived the density from the surface brightness. We model the density as a β model (Cavaliere & Fusco-Femiano 1976), whose parameters we derive by fitting the surface brightness profile of the exposure-corrected *XMM-Newton* image in a region not containing the cavities. This method provides a lower limit on the total outburst energy, since it estimates the kinetic energy released in the outburst. Assuming solar abundance, we estimate the kinetic outburst energy is 10^{58} ergs, for equal-sized bubbles created in the plane of the sky on each side of the nucleus. If the abundance is half solar, then the gas density and outburst energy both increase by ∼40 %. Based on the energy needed to create the X-ray cavities and adopting a mass-energy conversion efficiency of $\epsilon = 10\%$, we estimate the mass of material that would have been accreted

onto the SMBH to be:

$$\Delta M_{BH} = \frac{(1-\epsilon)}{\epsilon}\frac{E}{c^2} = 5 \times 10^4 M_\odot \tag{4.1}$$

where E is the total energy output.

Deep X-ray observations are not available for a similar analysis in the regions defined by the radio lobes, and we expect complications due to inverse Compton X-ray emission coincident with the potential cavities (Feigelson et al. 1995). However, if we extrapolate the gas density model to the radio lobes assuming they lie in the plane of the sky and use the 20 cm observation to determine the location and size of the lobes, we can estimate the energy required to evacuate cavities the present size of the lobes and thereby estimate the energy of the outburst required to create them. We approximated the lobes as $24'$ (78.3 kpc) diameter spheres centered at $14\farcm3$ (93.3 kpc) (west) and $15\farcm6$ (101.4 kpc) (east) from the nucleus. We extrapolated the gas density model derived from the *XMM-Newton* surface brightness to the radii of the radio lobes and combined the derived pressure there with the expected cavity volumes created through adiabatic bubble expansion to estimate the required energy of $\sim 5 \times 10^{58}$ ergs. The mass accreted onto the SMBH to produce this energy would be $\sim 2 \times 10^5\,\mathrm{M}_\odot$.

4.5.5 Comparison of the Cen A and Fornax A Jets

Centaurus A (NGC 5128) and NGC 1316 (Fornax A) are both nearby elliptical galaxies, which have recently undergone a merger event that has produced strong nuclear activity. They each host a $10^8\,\mathrm{M}_\odot$ black hole that are low luminosity AGNs and have dust lanes roughly perpendicular to their radio lobes (Marconi et al. 2006; Nowak et al. 2008). However, they differ significantly with regards to the observational characteristics of

their jets. At a distance of 3.7 Mpc (Ferrarese et al. 2007), Cen A has a 1.5 kpc radio and X-ray emitting jet that extends from the nucleus to the northeast radio lobe (Feigelson et al. 1981; Kraft et al. 2002; Hardcastle et al. 2003). In contrast, NGC 1316's $\sim$3 kpc radio jet does not extend to the large radio lobes and coincides not with an X-ray jet, but with a soft X-ray cavity. This phenomenological contrast suggests that, while the jet of Cen A is dissipative (P. Nulsen in preparation), NGC 1316's jet is not or that the NGC 1316 jet has shut off on larger scales.

4.6 Conclusions

We detected considerably more dust emission for NGC 1316 than expected in an early type galaxy with its K-band luminosity and observed evidence of recent AGN outbursts in the form of X-ray cavities and radio lobes. We presented *Spitzer* images of the infrared dust emission, including the first image of dust emission at 5.8 μm. We determined that the dust has a clumpy morphology, mostly confined to two regions, one 28.″8 (3.1 kpc) southeast of the nucleus and a 43.″9 (4.8 kpc) protrusion ending in an arc northwest of the nucleus. Molecular emission is detected from these regions. The resolved radio jet is not detected by *Spitzer*, and it does not coincide with regions of dust emission. Since the dust must be almost entirely external in origin, we use the dust mass to constrain the type and mass of the merger galaxy. We calculated a present dust mass of $2.4 \pm 0.9 \times 10^7\,M_\odot$ based on the integrated MIPS fluxes, which agrees with the dust mass of $3.2 \times 10^7\,M_\odot$ predicted by the model of Draine et al. (2007). We estimate the merger galaxy was a late type galaxy with a stellar mass of $1 - 6 \times 10^{10}\,M_\odot$ and a gas mass of $2 - 4 \times 10^9\,M_\odot$, some of which was likely ionized or used to form stars in the

merger event.

We constrained the age and energy of the merger and outburst events based on the X-ray and radio emission. The *XMM-Newton* image shows a pair of X-ray cavities to the west and southeast of the nucleus, likely created by the expansion of radio plasma, which are closer to the nucleus than the 1.4 GHz radio lobes. The relative locations of these cavities and the radio lobes suggests that either the 1.4 GHz radio emission does not show the full extent of the radio emission from the outburst or that there have been at least two AGN outbursts. We calculate buoyant rise times for the X-ray cavities of 0.1 Gyr and for the radio lobes of 0.4 Gyr, assuming expansion in the plane of the sky at $0.6\,c_s$, which agrees with the synchrotron age estimated by Ekers et al. (1983). Since the age of the radio lobes is close to the 0.5 Gyr age estimated by Mackie & Fabbiano (1998) for the merger, the outburst was likely triggered by the accretion of material onto the SMBH from this merger. Finally, we constrained the kinetic energy of the outbursts based on the energy required to create the *XMM-Newton* cavities and the radio lobes bubbles. We estimate the outburst that created the X-ray cavities had a kinetic energy of 10^{58} ergs and that the creation of the radio lobes required ~ 5 times more power.

Acknowledgements

We are grateful to C. Horellou and J. H. Black for providing us with CO(2-1) intensities and for their comments regarding the molecular gas kinematics, to Zhiyuan Li for his useful discussion on calculating masses, to Dharam Lal for his assistance in creating the 4.89 GHz map, and to Ramesh Narayan for his comments. We thank the anonymous referee for the many comments that improved this work. This work was based on

archival data obtained from the Spitzer Science Archive, the Chandra Data Archive, and the XMM-Newton Science Data Archive. Archived images were also obtained from the Hubble Legacy Archive, the NASA/IPAC Extragalactic Database, and the National Radio Astronomy Observatory Archive. We thank Z. Levay of the Space Telescope Science Institute for his assistance in obtaining the Hubble ACS image. This work was supported by the Smithsonian Institution, the Chandra X-ray Center, and NASA contract NNX07AQ18G.

Chapter 5

Future Directions

There are still many open questions in our understanding of galaxy interactions. The study of the evolution of the star formation and AGN processes has historically been complicated by the selection of samples biased towards more active or evolved systems. In this thesis, we presented the analysis of a sample selected on the basis of interaction probability, and described two new techniques for studying the merger process: systematic comparison of simulated and observed SEDs, and the analysis of post-merger systems. We describe below planned extensions of our study.

5.1 Expanding the Interaction Sample

In Chapter 2, we discussed the evolution of galaxy properties including SFR, stellar mass, and dust properties, over the interaction sequence for a sample of 31 galaxies in fourteen systems. One of the main limitations of our study was the size of our observed sample, which was dictated by the number of objects with available Herschel SPIRE

observations. When divided into three bins by interaction strength, we only had seven weakly and seven strongly interacting galaxies, resulting in very limited statistical significance. The parent sample to ours, SIGS, has 103 galaxies in 48 systems. Since we published our first paper, 12 more systems have been observed with SPIRE and 27 more systems have been observed with PACS. All have also been observed with IRAC, MIPS, GALEX, and 2MASS. We can further extend the sample with the inclusion of systems from the IRAS High Resolution Image Restoration (HIRES) Atlas of All Interacting Galaxies in the IRAS Revised Bright Galaxy Sample (Surace et al. 2004) for a total sample of 180 galaxies in 101 systems. The AKARI mission has also provided a rich archive at FIR wavelengths with increased spatial resolution over IRAS.

Similarly, a refinement of the radiative transfer post-processing on the simulation suite will enhance our understanding of both the simulations and observed interactions. We discussed the comparison of the SEDs of fourteen simulations with those of our observed interactions. For many systems, we noted a discrepancy in the FIR emission: the simulations typically had SEDs indicative of hotter dust and peaked at shorter wavelengths. We are currently preparing a SUNRISE run with an alternative treatment of the ISM. Instead of simply ignoring ISM material in the cold dense phase, light is propagated through the average ISM in a grid cell. For grid cells containing cold ISM, this alternative treatment increases the amount of dust with which the photon packages interact, thereby increasing the attenuation and reducing the typically dust temperature. Comparisons with this set of simulated SEDs will enable us to examine whether this treatment of the ISM yields SEDs that match better than the SEDs from the default ISM run for all or only some of our interactions and whether the treatment of the ISM impacts the recovery of other galaxy properties such as SFR. Initial tests show a

better match in the FIR in the comparisons with the alternative ISM SEDs than in the comparisons with the default ISM SEDs (Chapter 3).

A possible future expansion of hydrodynamic simulation suite probing a larger range of interaction parameters would also permit a more precise determination of parameter recovery and an analysis of the impact of orbital dynamics. The current suite has a limited coverage of the stellar mass parameter space. We noted in Chapter 3 that the limited evolution of stellar mass over an interaction and the small number of simulations means that we can only determine a trend of more massive systems preferentially matching to simulations of more massive galaxies. Similarly, since each interaction is placed on similar initial orbits, it is difficult from the current comparisons to determine whether the dynamics of the interaction are manifested in the set of best-matched SEDs, but this effect could be tested with an expansion of the simulation suite to include a variety of initial orbits.

5.2 Examining Morphology

In Section 3.1, we described the two main means by which the realism of simulations have typically been tested in previous studies, i.e. the recovery of either morphology or emission-based measures such as colors. While our comparison has been based on the comparison of SEDs, SUNRISE also has the capacity of simulating images as would be observed by a variety of telescopes. Since morphology is commonly used to estimate interaction stage in observational studies, it is of interest to discover whether the set of simulations that yield best-matching SEDs have morphologies in common with each other and/or with the observations. Given the variety of morphologies across wavelength

in our observed sample (e.g. the consistent morphology of NGC 3031 in Figure 2.1, the extended UV disks of NGC 3430 in Figure 2.3, and the limited UV and FIR emission of M51B in Figure 2.5), it would also be useful to determine whether some wavelengths are better than others at yielding images that are reflective of interaction stage or determine what is the optimal combination of multi-wavelength data for this measurement. Although we have not yet simulated images for our whole suite of interactions, Figure 5.1 shows NGC 3395/3396 in comparison with a true-color image of a best-matched SED. The simulated image also has the close separation of the two nuclei, although the distribution of its stars and its tidal features are only marginally similar. However, this initial comparison suggests that a morphological analysis may yield interesting fruit.

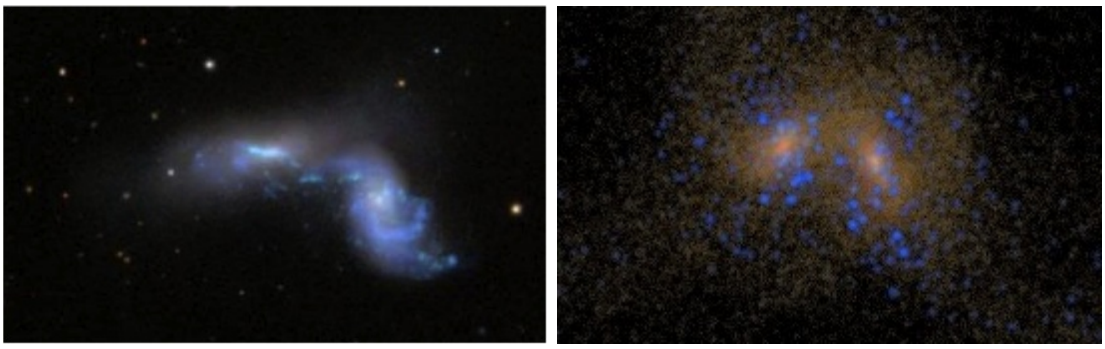

Figure 5.1: SDSS image of NGC 3395/3396 (left) compared to a simulated true-color image from the same simulation, snapshot, and viewing angle as a best-matched SED (right, Chapter 3). Both have a pair of close nuclei, although the simulation's nuclei are a factor of ~ 2 closer at 4.2 kpc compared to the observed projected separation of 9.4 kpc.

5.3 Studying AGN Activity

In our analysis of the SEDs of interacting systems (Chapter 2), we used DECOMPIR to determine the MIR AGN contribution and found a range across the systems but without a tendency to be heightened in the strongly interacting systems. Since the publication of that paper (Lanz et al. 2013), two new developments have occurred to improve our ability to study the AGN activity.

DECOMPIR (Mullaney et al. 2011) determines the contribution of the AGN to the $8-35\,\mu$m emission by fitting the $8-500\,\mu$m SEDs with one of five starburst host galaxy templates along with an intrinsic AGN SED comprised of two power laws (with indices of 1.8 for $6\,\mu\text{m} < \lambda < 19\,\mu$m and 0.2 for $19\,\mu\text{m} < \lambda < 40\,\mu$m) and a $\beta = 1.5$ blackbody for $\lambda > 40\,\mu$m. However, the host galaxy templates provided with the publicly available version of DECOMPIR typically had SEDs indicative of higher SFR and hotter dust than our systems. We have recently obtained a set of host galaxy templates with lower SFR (A. Goulding, priv. comm.). These templates are likely to yield more reliable estimates of the AGN contribution since the new galaxy templates are more representative of the underlying galaxy spectra of our sample.

The second development is a revision of MAGPHYS (Berta et al. 2013) to include emission from dust surrounding the AGN using the Fritz et al. (2006) AGN torus library. S. Berta has agreed to run our galaxies through this version of MAGPHYS, which is currently not publicly available. This would provide a second estimate of the AGN contribution to the IR emission, and give us a means of estimating the uncertainty on the AGN contribution.

References

Aniano, G., et al. 2012, ApJ, 756, 138

Arnaboldi, M., Freeman, K. C., Gerhard, O., Matthias, M., Kudritzki, R. P., Méndez, R. H., Capaccioli, M., & Ford, H. 1998, ApJ, 507, 759

Ashby, M. L. N., et al. 2009, ApJ, 701, 428

Barnes, J. E. 1992, ApJ, 393, 484

—. 2011, MNRAS, 413, 2860

Barnes, J. E., & Hernquist, L. 1996, ApJ, 471, 115

Barnes, J. E., & Hibbard, J. E. 2009, AJ, 137, 3071

Bell, E. F., McIntosh, D. H., Katz, N., & Weinberg, M. D. 2003, ApJS, 149, 289

Berta, S., et al. 2013, A&A, 551, A100

Bertin, E., & Arnouts, S. 1996, A&AS, 117, 393

Bettoni, D., Galletta, G., & García-Burillo, S. 2003, A&A, 405, 5

Blain, A. W., Jameson, A., Smail, I., Longair, M. S., Kneib, J.-P., & Ivison, R. J. 1999, MNRAS, 309, 715

Blanton, E. L., Randall, S. W., Clarke, T. E., Sarazin, C. L., McNamara, B. R., Douglass, E. M., & McDonald, M. 2011, ApJ, 737, 99

Bondi, H. 1952, MNRAS, 112, 195

Boquien, M., et al. 2010, ApJ, 713, 626

Breeveld, A. A., et al. 2010, MNRAS, 406, 1687

Bruzual, A. G. 2007, in IAU Symposium, Vol. 241, IAU Symposium, ed. A. Vazdekis & R. Peletier, 125–132

Bruzual, G., & Charlot, S. 2003, MNRAS, 344, 1000

Calzetti, D. 2012, ArXiv:1208.2997

Calzetti, D., Kinney, A. L., & Storchi-Bergmann, T. 1994, ApJ, 429, 582

Calzetti, D., et al. 2010, ApJ, 714, 1256

Cantalupo, C. M., Borrill, J. D., Jaffe, A. H., Kisner, T. S., & Stompor, R. 2010, ApJS, 187, 212

Casasola, V., Bettoni, D., & Galletta, G. 2004, A&A, 422, 941

Cavagnolo, K. W., McNamara, B. R., Wise, M. W., Nulsen, P. E. J., Brüggen, M., Gitti, M., & Rafferty, D. A. 2011, ApJ, 732, 71

Cavaliere, A., & Fusco-Femiano, R. 1976, A&A, 49, 137

Center, G. S. F. 2004, *GALEX* Observer's Guide

Chabrier, G. 2003, PASP, 115, 763

Charlot, S., & Fall, S. M. 2000, ApJ, 539, 718

Churazov, E., Brüggen, M., Kaiser, C. R., Böhringer, H., & Forman, W. 2001, ApJ, 554, 261

Churazov, E., Sunyaev, R., Forman, W., & Böhringer, H. 2002, MNRAS, 332, 729

Cohen, M., Megeath, S. T., Hammersley, P. L., Martín-Luis, F., & Stauffer, J. 2003, AJ, 125, 2645

Côté, P., et al. 2007, ApJ, 671, 1456

Cox, T. J., Jonsson, P., Somerville, R. S., Primack, J. R., & Dekel, A. 2008, MNRAS, 384, 386

da Cunha, E., Charlot, S., & Elbaz, D. 2008, MNRAS, 388, 1595

Dahari, O. 1985, ApJS, 57, 643

Dale, D. A., & Helou, G. 2002, ApJ, 576, 159

Dale, D. A., et al. 2005, ApJ, 633, 857

—. 2007, ApJ, 655, 863

—. 2009, ApJ, 703, 517

—. 2012, ApJ, 745, 95

David, L. P., et al. 2011, ApJ, 728, 162

de Vaucouleurs, G., de Vaucouleurs, A., Corwin, Jr., H. G., Buta, R. J., Paturel, G., & Fouqué, P. 1991, Third Reference Catalogue of Bright Galaxies. (New York: Springer)

Di Matteo, P., Combes, F., Melchior, A.-L., & Semelin, B. 2007, A&A, 468, 61

Di Matteo, T., Springel, V., & Hernquist, L. 2005, Nature, 433, 604

D'Onghia, E., Vogelsberger, M., Faucher-Giguere, C.-A., & Hernquist, L. 2010, ApJ, 725, 353

Dopita, M. A., Pereira, M., Kewley, L. J., & Capaccioli, M. 2002, ApJS, 143, 47

Draine, B. T., & Li, A. 2007, ApJ, 657, 810

Draine, B. T., et al. 2007, ApJ, 663, 866

Dubinski, J., Mihos, J. C., & Hernquist, L. 1996, ApJ, 462, 576

—. 1999, ApJ, 526, 607

Dunn, R. J. H., & Fabian, A. C. 2006, MNRAS, 373, 959

—. 2008, MNRAS, 385, 757

Dwek, E. 1998, ApJ, 501, 643

Ekers, R. D., Goss, W. M., Wellington, K. J., Bosma, A., Smith, R. M., & Schweizer, F. 1983, A&A, 127, 361

Elbaz, D., et al. 2011, A&A, 533, A119

Ellison, S. L., Patton, D. R., Mendel, J. T., & Scudder, J. M. 2011, MNRAS, 418, 2043

Engelbracht, C. W., Rieke, G. H., Gordon, K. D., Smith, J.-D. T., Werner, M. W., Moustakas, J., Willmer, C. N. A., & Vanzi, L. 2008, ApJ, 678, 804

Engelbracht, C. W., et al. 2007, PASP, 119, 994

Evans, D. S. 1949, MNRAS, 109, 94

Fabbiano, G., Fassnacht, C., & Trinchieri, G. 1994, ApJ, 434, 67

Fabian, A. C. 2012, ARA&A, 50, 455

Fabian, A. C., Sanders, J. S., Taylor, G. B., Allen, S. W., Crawford, C. S., Johnstone, R. M., & Iwasawa, K. 2006, MNRAS, 366, 417

Fazio, G. G., et al. 2004, ApJS, 154, 10

Feigelson, E. D., Laurent-Muehleisen, S. A., Kollgaard, R. I., & Fomalont, E. B. 1995, ApJ, 449, L149

Feigelson, E. D., Schreier, E. J., Delvaille, J. P., Giacconi, R., Grindlay, J. E., & Lightman, A. P. 1981, ApJ, 251, 31

Ferrarese, L., Mould, J. R., Stetson, P. B., Tonry, J. L., Blakeslee, J. P., & Ajhar, E. A. 2007, ApJ, 654, 186

Ferrari, F., Pastoriza, M. G., Macchetto, F. D., Bonatto, C., Panagia, N., & Sparks, W. B. 2002, A&A, 389, 355

Fioc, M., & Rocca-Volmerange, B. 1997, A&A, 326, 950

Fomalont, E. B., Ebneter, K. A., van Breugel, W. J. M., & Ekers, R. D. 1989, ApJ, 346, L17

Forman, W., et al. 2007, ApJ, 665, 1057

Freedman, W. L., et al. 2001, ApJ, 553, 47

Freeman, P. E., Kashyap, V., Rosner, R., & Lamb, D. Q. 2002, ApJS, 138, 185

Fritz, J., Franceschini, A., & Hatziminaoglou, E. 2006, MNRAS, 386, 1252

Gehrels, N., et al. 2004, ApJ, 611, 1005

Geldzahler, B. J., & Fomalont, E. B. 1984, AJ, 89, 1650

Giacintucci, S., Vrtilek, J. M., O'Sullivan, E., Raychaudhury, S., David, L. P., Venturi, T., Athreya, R., & Gitti, M. 2009, in American Institute of Physics Conference Series, Vol. 1201, American Institute of Physics Conference Series, ed. S. Heinz & E. Wilcots, 229–232

Gil de Paz, A., et al. 2007, ApJS, 173, 185

Gingold, R. A., & Monaghan, J. J. 1977, MNRAS, 181, 375

Goudfrooij, P., Alonso, M. V., Maraston, C., & Minniti, D. 2001, MNRAS, 328, 237

Goudfrooij, P., de Jong, T., Hansen, L., & Norgaard-Nielsen, H. U. 1994, MNRAS, 271, 833

Griffin, M. J., et al. 2010, A&A, 518, L3

Hardcastle, M. J., Worrall, D. M., Kraft, R. P., Forman, W. R., Jones, C., & Murray, S. S. 2003, ApJ, 593, 169

Hayward, C. C., Jonsson, P., Kereš, D., Magnelli, B., Hernquist, L., & Cox, T. J. 2012, MNRAS, 424, 951

Hayward, C. C., Kereš, D., Jonsson, P., Narayanan, D., Cox, T. J., & Hernquist, L. 2011, ApJ, 743, 159

Hayward, C. C., Narayanan, D., Kereš, D., Jonsson, P., Hopkins, P. F., Cox, T. J., & Hernquist, L. 2013, MNRAS, 428, 2529

Heinz, S., Choi, Y.-Y., Reynolds, C. S., & Begelman, M. C. 2002, ApJ, 569, L79

Hernquist, L. 1990, ApJ, 356, 359

Hernquist, L., & Katz, N. 1989, ApJS, 70, 419

Ho, L. C. 1999, ApJ, 516, 672

—. 2008, ARA&A, 46, 475

Ho, L. C., Filippenko, A. V., & Sargent, W. L. W. 1997, ApJS, 112, 315

Ho, L. C., Rudnick, G., Rix, H.-W., Shields, J. C., McIntosh, D. H., Filippenko, A. V., Sargent, W. L. W., & Eracleous, M. 2000, ApJ, 541, 120

Hopkins, P. F. 2012, MNRAS, 420, L8

Hopkins, P. F., Cox, T. J., Dutta, S. N., Hernquist, L., Kormendy, J., & Lauer, T. R. 2009, ApJS, 181, 135

Hopkins, P. F., Hernquist, L., Cox, T. J., Di Matteo, T., Robertson, B., & Springel, V. 2006, ApJS, 163, 1

Hopkins, P. F., Hernquist, L., Cox, T. J., Dutta, S. N., & Rothberg, B. 2008a, ApJ, 679, 156

Hopkins, P. F., Hernquist, L., Cox, T. J., & Kereš, D. 2008b, ApJS, 175, 356

Hopkins, P. F., Richards, G. T., & Hernquist, L. 2007, ApJ, 654, 731

Horellou, C., Black, J. H., van Gorkom, J. H., Combes, F., van der Hulst, J. M., & Charmandaris, V. 2001, A&A, 376, 837

Hoversten, E. A., et al. 2011, AJ, 141, 205

Isobe, N., Makishima, K., Tashiro, M., Itoh, K., Iyomoto, N., Takahashi, I., & Kaneda, H. 2006, ApJ, 645, 256

Iyomoto, N., Makishima, K., Tashiro, M., Inoue, S., Kaneda, H., Matsumoto, Y., & Mizuno, T. 1998, ApJ, 503, L31

James, A., Dunne, L., Eales, S., & Edmunds, M. G. 2002, MNRAS, 335, 753

Jansen, F., et al. 2001, A&A, 365, L1

Jarrett, T. H., Chester, T., Cutri, R., Schneider, S. E., & Huchra, J. P. 2003, AJ, 125, 525

Jonsson, P. 2006, MNRAS, 372, 2

Jonsson, P., Cox, T. J., Primack, J. R., & Somerville, R. S. 2006, ApJ, 637, 255

Jonsson, P., Groves, B. A., & Cox, T. J. 2010, MNRAS, 403, 17

Joye, W. A., & Mandel, E. 2003, in Astronomical Society of the Pacific Conference Series, Vol. 295, Astronomical Data Analysis Software and Systems XII, ed. H. E. Payne, R. I. Jedrzejewski, & R. N. Hook, 489

Kalberla, P. M. W., Burton, W. B., Hartmann, D., Arnal, E. M., Bajaja, E., Morras, R., & Pöppel, W. G. L. 2005, A&A, 440, 775

Kaneda, H., Onaka, T., Kitayama, T., Okada, Y., & Sakon, I. 2007, PASJ, 59, 107

Karachentsev, I. D., Kudrya, Y. N., Karachentseva, V. E., & Mitronova, S. N. 2006, Astrophysics, 49, 450

Karl, S. J., Lunttila, T., Naab, T., Johansson, P. H., Klaas, U., & Juvela, M. 2013, MNRAS

Katz, N., Weinberg, D. H., & Hernquist, L. 1996, ApJS, 105, 19

Kaviraj, S., et al. 2012, MNRAS, 423, 49

Keel, W. C., Kennicutt, Jr., R. C., Hummel, E., & van der Hulst, J. M. 1985, AJ, 90, 708

Kennicutt, R. C., et al. 2011, PASP, 123, 1347

Kennicutt, Jr., R. C. 1998, ARA&A, 36, 189

Kennicutt, Jr., R. C., et al. 2003, PASP, 115, 928

—. 2009, ApJ, 703, 1672

Kewley, L. J., Heisler, C. A., Dopita, M. A., & Lumsden, S. 2001, ApJS, 132, 37

Kim, D.-W., & Fabbiano, G. 2003, ApJ, 586, 826

Kocevski, D. D., et al. 2012, ApJ, 744, 148

Kraft, R. P., Forman, W. R., Jones, C., Murray, S. S., Hardcastle, M. J., & Worrall, D. M. 2002, ApJ, 569, 54

Kroupa, P. 2001, MNRAS, 322, 231

Kuin, N. P. M., & Rosen, S. R. 2008, MNRAS, 383, 383

Lacy, M., et al. 2004, ApJS, 154, 166

Lambas, D. G., Tissera, P. B., Alonso, M. S., & Coldwell, G. 2003, MNRAS, 346, 1189

Lanz, L., et al. 2013, ApJ, 768, 90

Laurent, O., Mirabel, I. F., Charmandaris, V., Gallais, P., Madden, S. C., Sauvage, M., Vigroux, L., & Cesarsky, C. 2000, A&A, 359, 887

Leeuw, L. L., Sansom, A. E., Robson, E. I., Haas, M., & Kuno, N. 2004, ApJ, 612, 837

Leitherer, C., et al. 1999, ApJS, 123, 3

Leroy, A. K., Walter, F., Brinks, E., Bigiel, F., de Blok, W. J. G., Madore, B., & Thornley, M. D. 2008, AJ, 136, 2782

Li, C., Kauffmann, G., Heckman, T. M., White, S. D. M., & Jing, Y. P. 2008, MNRAS, 385, 1915

Lotz, J. M., Jonsson, P., Cox, T. J., & Primack, J. R. 2008, MNRAS, 391, 1137

Lucy, L. B. 1977, AJ, 82, 1013

Lutz, D., Maiolino, R., Spoon, H. W. W., & Moorwood, A. F. M. 2004, A&A, 418, 465

Mackie, G., & Fabbiano, G. 1998, AJ, 115, 514

Madden, S. C., Galliano, F., Jones, A. P., & Sauvage, M. 2006, A&A, 446, 877

Magdis, G. E., et al. 2012, ApJ, 760, 6

Makovoz, D., & Khan, I. 2005, in Astronomical Society of the Pacific Conference Series, Vol. 347, Astronomical Data Analysis Software and Systems XIV, ed. P. Shopbell, M. Britton, & R. Ebert, 81

Marconi, A., Pastorini, G., Pacini, F., Axon, D. J., Capetti, A., Macchetto, D., Koekemoer, A. M., & Schreier, E. J. 2006, A&A, 448, 921

Markevitch, M., et al. 2000, ApJ, 541, 542

Martin, D. C., et al. 2005, ApJ, 619, L1

McNamara, B. R., et al. 2000, ApJ, 534, L135

Mihos, J. C., & Hernquist, L. 1994, ApJ, 431, L9

—. 1996, ApJ, 464, 641

Morgan, W. W. 1958, PASP, 70, 364

Moshir, M., & et al. 1990, in IRAS Faint Source Catalogue, version 2.0 (1990), 0

Mould, J. R., et al. 2000, ApJ, 529, 786

Muñoz-Mateos, J. C., et al. 2009, ApJ, 701, 1965

Mullaney, J. R., Alexander, D. M., Goulding, A. D., & Hickox, R. C. 2011, MNRAS, 414, 1082

Narayanan, D., Hayward, C. C., Cox, T. J., Hernquist, L., Jonsson, P., Younger, J. D., & Groves, B. 2010a, MNRAS, 401, 1613

Narayanan, D., et al. 2010b, MNRAS, 407, 1701

Noll, S., Burgarella, D., Giovannoli, E., Buat, V., Marcillac, D., & Muñoz-Mateos, J. C. 2009, A&A, 507, 1793

Nowak, N., Saglia, R. P., Thomas, J., Bender, R., Davies, R. I., & Gebhardt, K. 2008, MNRAS, 391, 1629

Ott, S. 2010, in Astronomical Society of the Pacific Conference Series, Vol. 434, Astronomical Data Analysis Software and Systems XIX, ed. Y. Mizumoto, K.-I. Morita, & M. Ohishi, 139

Paladini, R., Linz, H., Altieri, B., & Ali, B. 2012, Assessment Analysis of the Extended Emission Calibration for the PACS Red Channel, Document: PICC-NHSC-TR-034 (Pasadena, CA: NHSC)

Peng, C. Y., Ho, L. C., Impey, C. D., & Rix, H.-W. 2002, AJ, 124, 266

Pilbratt, G. L., et al. 2010, A&A, 518, L1

Poglitsch, A., et al. 2010, A&A, 518, L2

Poole, T. S., et al. 2008, MNRAS, 383, 627

Press, W. H., Teukolsky, S. A., Vetterling, W. T., & Flannery, B. P. 2007, Numerical Recipes 3rd Edition: The Art of Scientific Computing, 3rd edn. (New York, NY, USA: Cambridge University Press)

Privon, G. C., Barnes, J. E., Evans, A. S., Hibbard, J. E., Yun, M. S., Mazzarella, J. M., Armus, L., & Surace, J. 2013, ApJ, 771, 120

Randall, S. W., et al. 2011, ApJ, 726, 86

Reach, W. T., et al. 2005, PASP, 117, 978

Rich, J. A., Torrey, P., Kewley, L. J., Dopita, M. A., & Rupke, D. S. N. 2012, ApJ, 753, 5

Rieke, G. H., Alonso-Herrero, A., Weiner, B. J., Pérez-González, P. G., Blaylock, M., Donley, J. L., & Marcillac, D. 2009, ApJ, 692, 556

Rieke, G. H., et al. 2004, ApJS, 154, 25

Roberts, M. S., Hogg, D. E., Bregman, J. N., Forman, W. R., & Jones, C. 1991, ApJS, 75, 751

Salim, S., et al. 2007, ApJS, 173, 267

Salpeter, E. E. 1955, ApJ, 121, 161

Sanders, D. B. 1999, Ap&SS, 266, 331

Sanders, D. B., Mazzarella, J. M., Kim, D.-C., Surace, J. A., & Soifer, B. T. 2003, AJ, 126, 1607

Sanders, D. B., Soifer, B. T., Elias, J. H., Neugebauer, G., & Matthews, K. 1988, ApJ, 328, L35

Sarazin, C. L. 1988, X-ray emission from clusters of galaxies (Cambridge: Cambridge University Press)

Saunders, W., et al. 2000, MNRAS, 317, 55

Schiminovich, D., et al. 2007, ApJS, 173, 315

Schmidt, M. 1959, ApJ, 129, 243

Schuster, M. T., Marengo, M., & Patten, B. M. 2006, in Society of Photo-Optical Instrumentation Engineers (SPIE) Conference Series, Vol. 6270, Society of Photo-Optical Instrumentation Engineers (SPIE) Conference Series

Schweizer, F. 1980, ApJ, 237, 303

Scudder, J. M., Ellison, S. L., Torrey, P., Patton, D. R., & Mendel, J. T. 2012, MNRAS, 426, 549

Sérsic, J. L. 1968, Atlas de galaxias australes (Cordoba, Argentina: Observatorio Astronomico)

Shi, Y., Rieke, G. H., Hines, D. C., Gordon, K. D., & Egami, E. 2007, ApJ, 655, 781

Shklovskii, I. S. 1963, Soviet Ast., 6, 465

Silva, L., Granato, G. L., Bressan, A., & Danese, L. 1998, ApJ, 509, 103

Silverman, J. D., et al. 2011, ApJ, 743, 2

Skrutskie, M. F., et al. 2006, AJ, 131, 1163

Smith, B. J., Struck, C., Hancock, M., Appleton, P. N., Charmandaris, V., & Reach, W. T. 2007a, AJ, 133, 791

Smith, J. D. T., et al. 2007b, ApJ, 656, 770

Snyder, G. F., Hayward, C. C., Sajina, A., Jonsson, P., Cox, T. J., Hernquist, L., Hopkins, P. F., & Yan, L. 2013, ApJ, 768, 168

Soifer, B. T., Boehmer, L., Neugebauer, G., & Sanders, D. B. 1989, AJ, 98, 766

Spitzer, L. 1956, Physics of Fully Ionized Gases (New York: Interscience Publishers)

Spoon, H. W. W., Marshall, J. A., Houck, J. R., Elitzur, M., Hao, L., Armus, L., Brandl, B. R., & Charmandaris, V. 2007, ApJ, 654, L49

Springel, V. 2005, MNRAS, 364, 1105

—. 2010, ARA&A, 48, 391

Springel, V., Di Matteo, T., & Hernquist, L. 2005a, MNRAS, 361, 776

Springel, V., & Hernquist, L. 2003, MNRAS, 339, 289

Springel, V., et al. 2005b, Nature, 435, 629

Stern, D., et al. 2005, ApJ, 631, 163

Surace, J. A., Mazzarella, J., Soifer, B. T., & Wehrle, A. E. 1993, AJ, 105, 864

Surace, J. A., Sanders, D. B., & Mazzarella, J. M. 2004, AJ, 127, 3235

Swinyard, B. M., et al. 2010, A&A, 518, L4

Tang, Y., Gu, Q.-S., Huang, J.-S., & Wang, Y.-P. 2009, MNRAS, 397, 1966

Temi, P., Brighenti, F., & Mathews, W. G. 2007, ApJ, 660, 1215

—. 2009, ApJ, 695, 1

Temi, P., Mathews, W. G., & Brighenti, F. 2005, ApJ, 622, 235

Thilker, D. A., et al. 2007, ApJS, 173, 538

Tonry, J. L., Dressler, A., Blakeslee, J. P., Ajhar, E. A., Fletcher, A. B., Luppino, G. A., Metzger, M. R., & Moore, C. B. 2001, ApJ, 546, 681

Toomre, A., & Toomre, J. 1972, ApJ, 178, 623

Torrey, P., Cox, T. J., Kewley, L., & Hernquist, L. 2012, ApJ, 746, 108

Treyer, M., et al. 2010, ApJ, 719, 1191

Trimble, V. 2000, in Allen's Astrophysical Quantities, ed. A. N. Cox (New York: Springer), 569

Tully, R. B. 1994, VizieR Online Data Catalog, 7145, 0

Tully, R. B., & Fisher, J. R. 1977, A&A, 54, 661

Tully, R. B., Shaya, E. J., Karachentsev, I. D., Courtois, H. M., Kocevski, D. D., Rizzi, L., & Peel, A. 2008, ApJ, 676, 184

Tzanavaris, P., et al. 2010, ApJ, 716, 556

Veilleux, S., Kim, D.-C., & Sanders, D. B. 2002, ApJS, 143, 315

Veilleux, S., et al. 2009, ApJS, 182, 628

Vikhlinin, A., Markevitch, M., Murray, S. S., Jones, C., Forman, W., & Van Speybroeck, L. 2005, ApJ, 628, 655

Wade, C. M. 1961, Pub. NRAO, 1, 99

Weingartner, J. C., & Draine, B. T. 2001, ApJ, 548, 296

Weisskopf, M. C., Tananbaum, H. D., Van Speybroeck, L. P., & O'Dell, S. L. 2000, in Society of Photo-Optical Instrumentation Engineers (SPIE) Conference Series, Vol. 4012, Society of Photo-Optical Instrumentation Engineers (SPIE) Conference Series, ed. J. E. Truemper & B. Aschenbach, 2–16

Werner, M. W., et al. 2004, ApJS, 154, 1

Willner, S. P., et al. 2004, ApJS, 154, 222

Wyder, T. K., et al. 2005, ApJ, 619, L15

Xilouris, E. M., Madden, S. C., Galliano, F., Vigroux, L., & Sauvage, M. 2004, A&A, 416, 41

Xu, C. K., et al. 2010, ApJ, 713, 330

Younger, J. D., Hayward, C. C., Narayanan, D., Cox, T. J., Hernquist, L., & Jonsson, P. 2009, MNRAS, 396, L66

Yuan, F.-T., Takeuchi, T. T., Matsuoka, Y., Buat, V., Burgarella, D., & Iglesias-Páramo, J. 2012, A&A, 548, A117

Zhu, Y.-N., Wu, H., Cao, C., & Li, H.-N. 2008, ApJ, 686, 155

Zibetti, S., Gallazzi, A., Charlot, S., Pierini, D., & Pasquali, A. 2013, MNRAS, 428, 1479